Investigation of mammary gland development and resident macrophages by 3D and intravital imaging

Caleb Alexander Dawson

ORCID 0000-0002-6835-6930

a thesis submitted in total fulfilment of the degree of

Doctor of Philosophy

October 2019

The Walter and Eliza Hall Institute of Medical Research
Department of Medical Biology
Faculty of Medicine, Dentistry and Health Sciences
The University of Melbourne

Dedication

This work is dedicated to God, the creator and the source of all good things, and Jesus, who rules in power, grace and truth. I could not achieve anything without his generous blessings. I pray this work will glorify God by truthfully revealing the works of His creation.

> "Since the creation of the world God's invisible qualities — his eternal power and divine nature — have been clearly seen, being understood from what has been made." Romans 1:20 (NIV)

Abstract

The mammary gland is a fascinating organ that develops after birth and is capable of remodelling through multiple rounds of reproduction. The behaviour of mammary epithelial cells and how these interact dynamically with their environment are poorly understood. Cell morphology and arrangement can be addressed by three-dimensional (3D) confocal imaging to provide large-scale, subcellular resolution views of tissue architecture. Further insight can be gained from intravital imaging that allows direct observation of cell behaviour *in vivo,* but this has rarely been implemented for the normal mammary gland.

Mammary ducts are embedded in adipose tissue, making *in vivo* imaging of mammary ducts extremely challenging. Chapter 3 provides a detailed protocol for an intravital imaging method that was adapted and optimised for the mouse mammary gland. This technique enables high-resolution, 3D intravital imaging of the mammary gland for up to twelve hours. The skin flap surgical technique was modified to expose the entire inguinal mammary gland, allowing rare accessible epithelial structures to be identified. Additional fine microdissection of connective tissue maximised the resolution of imaging. Significant measures were taken to achieve as near to physiological conditions as possible, including creating a sealed environment over the exposed tissue. Strategies used for image analysis are then discussed, including image stabilisation, cell tracking and 3D visualisation. This technique advances our ability to observe mammary cell behaviour *in vivo* and will enable future investigation of rare events that are spatially and temporally regulated, such as stem cell behaviour, tumour initiation and microenvironment interactions.

Mammary gland morphogenesis occurs by migration of terminal end buds through the mammary fat pad. Terminal end buds are large, club-like structures comprising a cap layer and a multi-layered body that give rise to bilayered ducts. Epithelial progenitors within terminal end buds generate mature cells of ducts but how these behave and cooperate to generate the bilayer is not well understood. Chapter 4 describes the lineage-specific behaviours of terminal end bud progenitors as observed by intravital microscopy. Cap cell migration into the body was recorded

at high resolution *in vivo* for the first time. High-dimensional image quantification of cap cell behaviour showed that most cap cells that migrate into the body die rapidly but a small proportion survive long term. Progenitors for the luminal lineages were observed to have contrasting behaviours, with hormone-sensing progenitors being highly migratory. Single cell transcriptomic analysis of terminal end buds is described, providing possible molecular drivers of the distinctive behaviour of hormone-sensing progenitors. This work provides an unprecedented view of mammary stem cell behaviour, making an important contribution to our understanding of how cellular behaviour drives organogenesis.

Chapter 5 describes a previously uncharacterised population of resident intra-epithelial macrophages that were revealed by 3D confocal imaging. These cells, termed mammary ductal macrophages, are regularly positioned over the entire mammary gland at all stages of development. They do not migrate but monitor the epithelium by dendrite movement, allowing them to rapidly sense and respond to epithelial damage. Ductal macrophages proliferate in pregnancy to maintain their density on the epithelium in lactation. During involution following weaning, they rapidly phagocytose dying alveolar cells to facilitate remodelling. Breast tumour-associated macrophages are pro-tumorigenic and strongly resemble ductal macrophages, not stromal macrophages. Macrophages are emerging as important targets for breast cancer treatment, therefore, better understanding of parallels between DM function in healthy and perturbed tissue may enable development of improved cancer therapies.

Finally, in Chapter 6, the presented results are summarised and their context within the field, wider implications and possible future directions are discussed. Overall, this thesis presents original research that advances our technical ability to address questions of cell dynamics in the mammary gland, provides important insights into mammary stem cell behaviour during morphogenesis, and characterises a novel tissue-resident macrophage population, finding a key role for these in mammary gland remodelling.

Declaration

This is to certify that:

- This thesis comprises only my original work towards the Doctor of Philosophy except where indicated in the preface.
- Due acknowledgment is made for the work of other authors.
- This thesis is fewer than 100,000 words, exclusive of tables and bibliographies.

Caleb Alexander Dawson
The Walter and Eliza Hall Institute of Medical Research
Department of Medical Biology
Faculty of Medicine, Dentistry and Health Sciences
The University of Melbourne

Preface

In accordance with the regulations of The University of Melbourne, the author's contribution, the publication status and collaborator contributions to each results Chapter are as follows:

Chapter 3: 95%

Unpublished material not submitted for publication.
This Chapter is written in the style of Nature Protocols.

A/Professor Scott Mueller taught Caleb Dawson the skin flap surgery.

Chapter 4: 85%

Unpublished material not submitted for publication.

Dr Raymond Yip assisted with experiment monitoring, Dr Bianca Capaldo assisted with TEB dissection, Dr François Vaillant sorted TEB and duct cells, Dr Bhupinder Pal performed single cell RNA-seq and Professor Gordon Smyth and Dr Yunshun Chen performed bioinformatic analysis.

Chapter 5: 90%

In revision following peer review by Nature Cell Biology. Supplementary movies have not been included.

Dr François Vaillant performed hormone pellet transplant and prepubertal epithelial removal experiments, Dr Camille Bleriot assisted with the Ms4a3 experiment, Zhaoyuan Liu and Professor Florent Ginhoux provided *Ms4a3-Cre* mice, Dr Bhupinder Pal performed RNA-seq, Professor Gordon Smyth and Luke Gandolfo performed RNA-seq bioinformatic analysis, Professor Geoffrey Lindeman provided general guidance, A/Professor Scott Mueller assisted in experiment design, Dr Anne Rios designed experiments and provided general guidance, Professor Jane Visvader designed experiments, provided general guidance and co-wrote the manuscript.

Thus, the author's overall contribution to the work presented in this thesis is 90%.

Funding

Caleb Alexander Dawson was supported by:

Australian Government Research Training Program Scholarships

Avis MacPhee PhD Award

Edith Moffat bridging stipend

Melbourne abroad travel scholarship

Associated publications

Rios A. C., Capaldo B. D., Vaillant F., Pal B., van Ineveld R, **Dawson C. A.**, Chen Y., Nolan E., Fu N. Y., DTCLSM Group, Jackling F. C., Devi S., Clouston D., Whitehead L., Smyth G. K., Mueller S. N., Lindeman G. J. and Visvader J. E. (2019) Intraclonal plasticity in mammary tumors revealed through large-scale single-cell resolution 3D imaging. Cancer Cell, 35.

Michalak E. M., Milevskiy M. J. G., Joyce R. M., Dekkers J. F., Jamieson P. R., Pal B., **Dawson C. A.**, Hu Y., Orkin S. H., Alexander W. S., Lindeman G. J., Smyth G. K. and Visvader J. E. (2018) Canonical PRC2 function is essential for mammary gland development and affects chromatin compaction in mammary organoids. PLOS Biology, 16(8): e2004986.

Dekkers J. F.*, Whittle J. R.*, Vaillant F., Chen H.-R., **Dawson C. A.**, Liu K., Geurts M., Herold M. J., Clevers H., Lindeman G. J. and Visvader J. E. (2019) Modeling breast cancer using CRISPR/Cas9-mediated engineering of human breast organoids. J. Natl. Cancer I. djz196.

Third party copyright material

Acknowledgements

I want to firstly thank Jane Visvader — your knowledge and experience of the scientific process from project direction, experiment design, manuscript writing, and publication has been an invaluable example and an inspiration to me. Thank you for committing enormous amounts of time and energy to mentor me in these areas. You have incredibly high standards and pushed me to the edge of my stamina and ability, allowing me to produce the best work I could possibly achieve. You also encouraged me, acknowledged good work, guided me through difficult situations and fostered my creativity, for which I am extremely grateful.

Thank you to Anne Rios, for having endless faith in me and pouring your heart and soul into your supervision. Our countless spirited discussions, your fervent encouragement and your passion for life and science have significantly shaped and influenced me over this time. Thank you for helping me to find my individual voice and pushing me to aim high.

Thank you to Geoff Lindeman for your support, fostering a great lab environment, and, I imagine, thousands of behind the scenes discussions. Thank you also to my committee: Scott Mueller, Samir Taoudi and Marie-Liesse Asselin-Labat. Having your advice and support readily available was a huge help and comfort to me. Thank you particularly to Scott — your generosity in time and resources to train me in intravital microscopy was crucial to my PhD and I am very grateful for this. Your expertise in immunology turned out to be equally invaluable as we stumbled our way into the macrophage world. Thank you for seeing the potential of this project and for all of your advice.

Thank you to everyone in the breast cancer lab — for your friendship, encouragement, patience, cakes, beers, help and feedback. Thank you Bhupinder Pal for RNA-seq, Felicity Jackling for managing our many mouse lines and doing all of the genotyping, François Vaillant for all of the transplant experiments, Bianca Capaldo for microscopy help and organisation, Ray Yip for assistance with intravital, Jim Whittle for growing organoids, Emma Nolan and Rachel Joyce for processing human samples, Ewa Michalak for telling me to stand up straight, Michael Milevskiy

for TEB chats, and Paul Jamieson for teaching me mammary preps and for defying all the odds and staying strong in the midst of tragedy.

Thank you to all people who provided reagents, mice, advice and collaborations, including Angus, Cam, Casey, Dawn, Gabrielle, Gordon, Holly, Jaring, Jo, John, Kathy, Kim, Lachie, Luke, Maria, Mel, Michael, Nicolas, Sapna and Shalin.

Thank you to Kelly Rogers and the Center for Dynamic Imaging team for building and maintaining the incredible facility that this work relied upon so heavily. I also want to acknowledge the WEHI services that facilitate our research and make working at WEHI an enormous privilege. Thank you to all our mouse techs, particularly Dani, Eren, Hannah, Kim, Krystal, Leanne and Steph for doing fantastic, reliable work.

Thank you to Doug Hilton and Samir Taoudi for your inspiration and encouragement and for giving me my first opportunities in research at WEHI.

Finally, thank you to my family, friends, growth groups, the WEHI bible group and my church. Your love and friendship were great blessings, giving me the strength to persevere and grounding me in the things that matter most. Thanks most of all to Mum, Dad, Mad, Jaim and Coop. You're the best and I wouldn't have achieved this without you.

Table of Contents

List of Tables

List of Figures

List of Supplementary figures

Non-standard Abbreviations

2D	Two-dimensional
3D	Three-dimensional
4D	Four-dimensional
AP	Alveolar progenitor
BM	Bone marrow
bp	Base pair
BSA	Bovine serum albumin
C-B	Cap to body
CAR	Chimeric antigen receptor
CC3	Cleaved caspase 3
cDNA	Complementary DNA
CFP	Cyan fluorescent protein
CLB	Cap-like cell in the TEB body
cMOP	Common monocyte progenitor
CMP	Common myeloid progenitor
C/R	Cyan/Red
Cre	Cre recombinase
d	Days
DAPI	4′,6-diamidino-2-phenylindole
DC	Dendritic cell
DC1	Classical dendritic cell 1
DC2	Classical dendritic cell 2
DE	Differentially expressed
DM	Ductal macrophage
DMEM	Dulbecco's modified eagle medium
DNA	Deoxyribonucleic acid
DNase	Deoxyribonuclease
dL	Days lactation
dP	Days pregnant
DT	Diphtheria toxin
DTR	Diphtheria toxin receptor
E	Embryonic day
E-Cad	E-Cadherin
ECM	Extracellular matrix
EdU	5-ethynyl-2-deoxyuridine
EGTA	ethylene glycol-bis(β-aminoethyl ether)-N,N,N',N'-tetraacetic acid

EMP	Erythro-myeloid progenitor
Eos	Eosinophil
ER	Oestrogen receptor
FACS	Flow activated cell sorting
FCS	Fetal calf serum
FDR	False discovery rate
fl	Flox
FMO	Fluorescence minus one
FUnGI	Fructose, urea and glycerol for imaging
GFP	Green fluorescent protein
GMP	Granulo-myeloid progenitor
GO	Gene ontology
H&E	Haematoxylin and eosin
Hi	High
Hrs	Hours
HR	Hormone receptor
HS	Hormone-sensing
HSC	Haematopoietic stem cell
HSP	Hormone-sensing progenitor
Ig	Immunoglobulin
IGF-1	Insulin growth factor 1
Int	Intermediate
Inv	Involution
i.p.	Intraperitoneal
IVM	Intravital microscopy
K	Cytokeratin
KEGG	Kyoto encyclopedia of genes and genomes
Lact	Lactation
Lo	Low
LP	Luminal progenitor
Lum	Luminal
MØ	Macrophage
MaSC	Mammary stem cell
MEC	Mammary epithelial cell
MFI	Mean fluorescence intensity
MHCII	MHC class II
Min	Minute
ML	Mature luminal
MMTV	Mouse mammary tumour virus

Mono	Monocyte
MPA	Medroxyprogesterone acetate
mRNA	Messenger ribonucleic acid
Myo	Myoepithelium
Neut	Neutrophil
NK	Natural killer
PBS	Phosphate buffered saline
PCR	Polymerase chain reaction
PFA	Paraformaldehyde
PI	Propidium iodide
PR	Progesterone receptor
Preg	Pregnant
PyMT	Polyoma middle T
RFP	Red fluorescent protein
RI	Refractive index
RNA-seq	RNA sequencing
RPM	Revolutions per minute
RT	Room temperature
SHG	Second harmonic generation
SM	Stromal macrophage
TAM	Tumour-associated macrophage
TDLU	Terminal ductal lobular unit
TEB	Terminal end bud
Tx	Transplantation
VEGF	vascular endothelial growth factor
w	Weeks
WEHI	Walter and Eliza Hall Institute
WT	Wild-type
YFP	Yellow fluorescent protein

Chapter 1: Introduction

1.1 Mammary gland development and remodelling

Mammary glands are unique to female mammals and function to deliver nutrients to offspring through milk, a rich source of fat, protein, carbohydrates and immune components that provides tailored nutrition to the young (Jensen and Newburg, 1995). Lactation is essential for the nursing of mammalian young that are underdeveloped at birth and provides adaptational, social and nutritional advantages (Oftedal, 2012). The mammary gland may have evolved from hair follicle-associated apocrine glands that provided moisture for permeable eggs, like those in monotremes (Oftedal, 2002). This is supported by the maintenance of vestigial mammary hair during early marsupial development that is lost in eutherian mammals.

The mammary gland is a bilayered epithelial organ that undergoes dramatic remodelling throughout life (Figure 1.1). The virgin adult mammary gland comprises an extensive ductal tree embedded within an adipose stroma containing fibroblasts, immune cells, nerves and blood vessels. The ductal tree stems from the nipple and branches irregularly through the fat pad, distinct from the orderly sequential branching of the lung and kidney (Hannezo et al., 2017; Scheele et al., 2017). While the murine gland consists of a single epithelial tree with ducts that terminate in simple rounded tips (Figure 1.2a), the human breast is divided into multiple lobes with ducts that end in lobular structures called terminal ductal lobular units (TDLUs) (Figure 1.2b) (Russo and Russo, 2004). This Chapter will focus on mammary gland development in the mouse, as this has been most extensively investigated.

1.1.1 The prepubertal mammary gland

Embryonic development of the mammary gland begins with epidermal specification at embryonic day (E) 10 (Macias and Hinck, 2012). A mammary bud is formed by E12.5 (Figure 1.1)

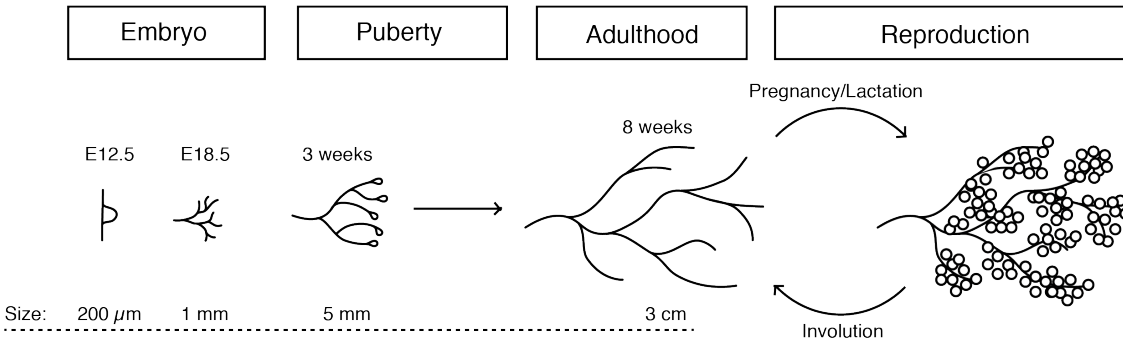

Figure 1.1: Remodelling of the mouse mammary gland

From E10.5–E12.5 a mammary bud forms by epidermal migration into underlying mesenchyme. From E14.5–E18.5, cells in this structure proliferate and branch into the maturing adipose mesenchyme to form a rudimentary branched structure with a lumen at birth. In the prepubertal period, ducts grow allometrically and the fat pad matures. At the onset of puberty, oestrogen stimulates terminal end bud (TEB) formation and branching morphogenesis through the fat pad. In adulthood, the gland is quiescent apart from tertiary branching that occurs in response to progesterone in coordination with the oestrus cycle. Progesterone in pregnancy stimulates, proliferation, budding and branching along ducts, followed by prolactin-driven maturation of alveoli that produce milk in lactation. Upon weaning, alveoli regress through death of alveolar cells, returning the gland to a resting ductal state.

that contains homogeneous undifferentiated cells (Lilja et al., 2018; Lloyd-Lewis et al., 2018) (Figure 1.3a). From E14.5 to E18.5, a small degree of branching occurs and a lumen is developed as the gland grows into the precursor mesenchyme of the fat pad (Macias and Hinck, 2012). The bilayer is established after birth with segregated expression of basal and luminal keratins, but all cells express a basal-like transcriptional signature until about postnatal day 14 (Pal et al., 2017) (Figure 1.3b). From birth until puberty, this structure undergoes allometric growth and branching (Macias and Hinck, 2012).

1.1.2 Morphogenesis in puberty

Puberty-associated oestrogen, growth hormone and insulin growth factor 1 (IGF-1) stimulate the formation of proliferative terminal end buds (TEBs) that drive branching morphogenesis of the

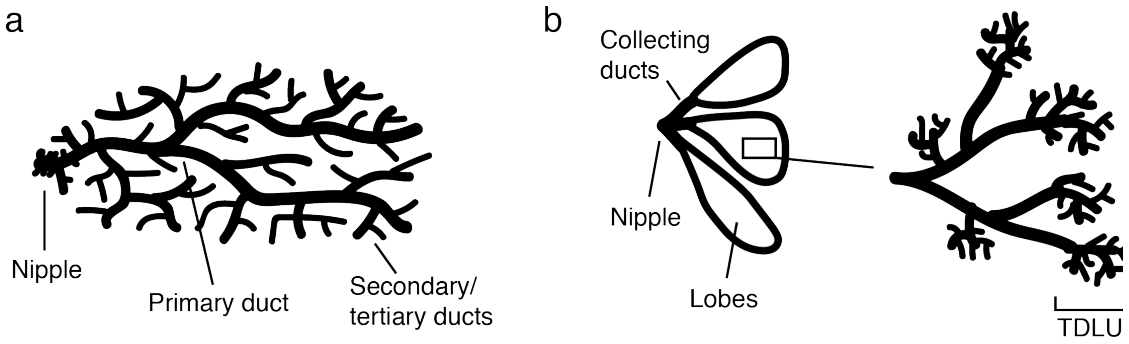

Figure 1.2: Mammary gland architecture in mice and humans

(a) Mammary gland structure in mice. A single ductal tree arises from the nipple and branches from primary ducts into smaller secondary ducts with simple ends.

(b) Mammary gland structure in humans. Multiple collecting ducts stem from the nipple and give rise to separate lobes. On a smaller scale, branching ducts give rise to terminal ductal lobular units (TDLU), which are densely branched regions.

mammary gland through the fat pad (Dulbecco et al., 1982; Howard and Gusterson, 2000) (Figure 1.1). In mice, this process occurs around 3–7 weeks of age, during which time the gland grows from approximately 0.5 cm to 3 cm. Oestrogen signalling occurs through the oestrogen receptor (ER) and is crucial for ductal growth, as the glands of ER knock-out mice do not progress beyond a primitive rudiment (Bocchinfuso and Korach, 1997). Oestrogen stimulates proliferation and ductal growth through paracrine signalling within the epithelium that enables ER knock-out epithelium to grow when co-transplanted with wild-type epithelium (Mallepell et al., 2006). Paracrine signalling is mediated by a population of hormone-sensing epithelial cells that secrete amphiregulin in response to oestrogen to stimulate the proliferation of surrounding epithelial cells (Ciarloni et al., 2007; Mallepell et al., 2006).

These signals generate club-shaped TEBs that house highly proliferative progenitor cells. As the gland grows, these progenitors give rise to the cells of the elongating epithelial bilayer and bifurcation of TEBs creates a branching tree that fills the fat pad by the end of puberty (Macias and Hinck, 2012). TEBs are arranged into a single basal ‘cap’ layer containing rounded ‘cap cells’

that give rise to basal cells of mature ducts, and multiple layers of luminal 'body cells' that give rise to the luminal compartment of mature ducts (Visvader, 2009) (Figure 1.3c).

1.1.3 The adult mammary gland

The resting virgin adult gland is a simple bilayer, with the inner, luminal layer having a typical cuboidal epithelial morphology with tight junctions. The outer, basal layer contains myoepithelial cells that are highly elongated and lie parallel to the duct axis, forming a thin but continuous layer (Rios et al., 2014) (Figure 1.3d).

The adult mammary epithelium undergoes cyclic proliferation, branching and regression in response to the ovarian cycle (every 4–5 days in mice) (Macias and Hinck, 2012). Proliferation occurs during metestrus and diestrus in response to elevated progesterone (Chua et al., 2010; Fata et al., 2001) and leads to the generation of tertiary branches. This is followed by increased apoptosis during diestrus when progesterone levels fall (Andres and Strange, 1999). Progesterone signals through the progesterone receptor (PR) and, similar to oestrogen, induces proliferation through a paracrine mechanism via hormone-sensing cells (Brisken et al., 1998). Progesterone appears to play a more significant role than oestrogen in the adult (Arendt and Kuperwasser, 2015) and is essential for tertiary branching as well as alveolar development. These processes do not occur in PR knock-out mice, which remain a simple epithelial tree (Brisken et al., 1998; Lydon et al., 1995). Progesterone induces a small degree of proliferation in PR^+ cells through cyclin D1 (Beleut et al., 2010) but acts most significantly via paracrine signaling. For example, PR transcriptionally stimulates the RANKL gene (*Tnfsf11*), whose product stimulates the proliferation of PR^- cells (Mukherjee et al., 2010; Mulac-Jericevic et al., 2003; Pal et al., 2013).

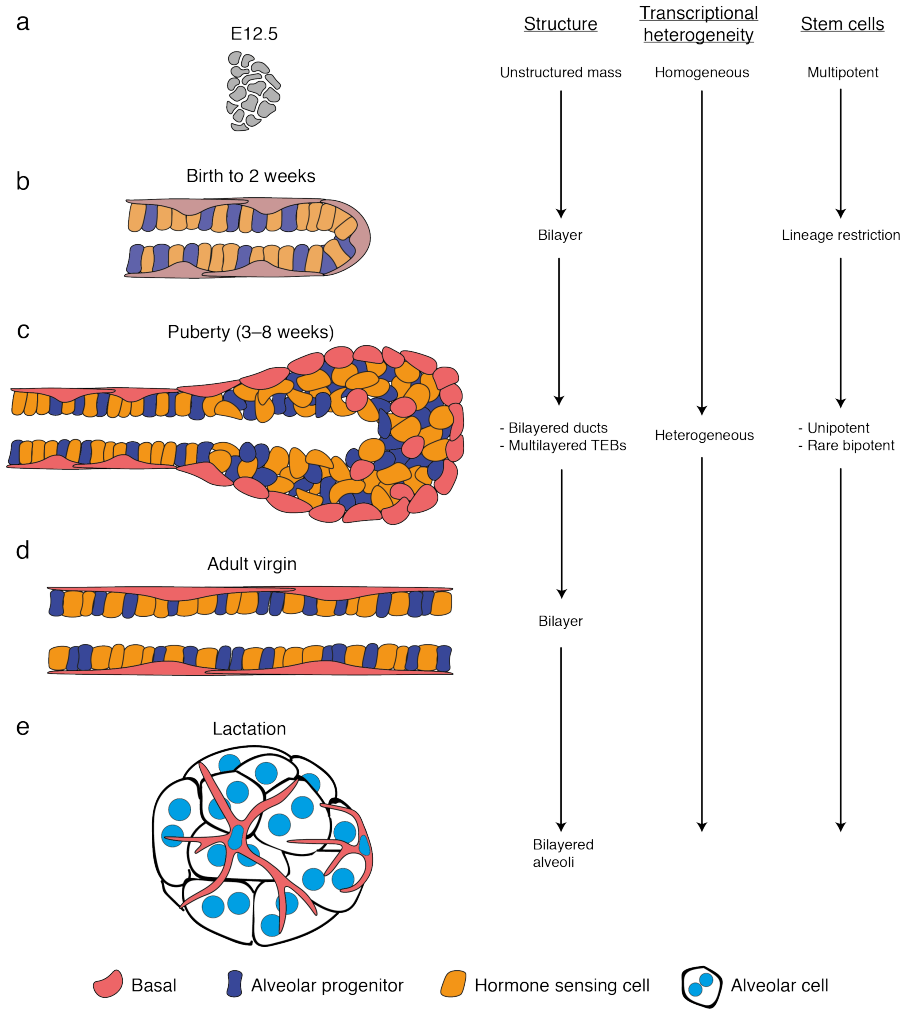

Figure 1.3: Mammary epithelial cell morphology and organisation

(a) The embryonic bud at E12.5 contains undifferentiated cells not yet arranged into a bilayer.

(b) The prepubertal gland forms a bilayer but cells remain transcriptionally homogeneous.

(c) In puberty, TEBs with a cap layer and a multi-layered body grow and give rise to mature bilayered ducts. Cell populations are now transcriptionally heterogeneous and separated into distinct lineages.

(d) The adult gland bilayer comprises highly elongated basal myoepithelial cells and a single luminal layer with tight junctions.

(e) Alveoli in lactation are large and spherical with binucleated, milk-producing alveolar cells surrounded by stellate myoepithelial cells.

1.1.4 The mammary gland during reproduction

During pregnancy, progesterone induces extensive growth and branching to form alveolar buds (Brisken et al., 1998). This occurs though secondary signalling by RANKL (Fata et al., 2000) and Wnt4, which is a direct target of PR (Brisken et al., 2000). Epithelium lacking Wnt4 can form a normal ductal tree in adulthood but has delayed branching and lobule development in pregnancy (Brisken et al., 2000). Prolactin acts in late pregnancy signals through the Jak2/Stat5 and RANKL/RANK pathways (Macias and Hinck, 2012) to drive the maturation of milk-producing alveolar cells in large spherical alveoli (Brisken et al., 1999) (Figure 1.3e). Late in pregnancy and in lactation, alveolar cells undergo binucleation as a result of failed cytokinesis that results in two separate nuclei within each cell (Rios et al., 2016). The switch to lactation also sees the induction of the pro-survival gene *Mcl-1* in alveolar cells by EGF, which is essential for alveolar cell survival (Fu et al., 2015). Myoepithelial cells around alveoli do not form a continuous layer but become stellate and wrap around the alveoli to contract and eject milk (Stevenson et al., 2019). After weaning, the gland remodels back to a resting state through the death of all mature milk-producing cells in a process of involution (Watson and Kreuzaler, 2011).

1.1.5 Alveolar regression during involution

Reproduction is protective against breast cancer in the long term, however, breast cancer arising after parity is more aggressive (Bladström et al., 2003; McDaniel et al., 2006; Schedin et al., 2007; Stanford et al., 2014). Thus, understanding the permanent changes occurring in the epithelium and stroma after parity is important. A significant event in the reproductive cycle is the phase of involution, in which alveolar cells die and the gland returns to a resting ductal state. The involuting gland resembles a wound healing process and inflammation has a strong influence on cancer. Therefore, inflammation during involution may be responsible for increased cancer aggressiveness associated with this stage (Martinson et al., 2015; Schedin et al., 2007).

Involution is typically studied by forcing synchronous weaning of pups at the peak of established lactation (about 14 days). Involution in this scenario occurs in two phases: a first, reversible phase (0–2 days) of milk stasis and epithelial cell shedding driven by local changes from lack of

suckling, and a second, irreversible phase (2–6 days) of cell death, immune infiltration and remodelling driven by systemic changes (Lund et al., 1996; Watson and Kreuzaler, 2011). Alveolar cell death is driven by multiple factors including mechanical force from milk stasis (Quaglino et al., 2009) and signalling by Stat3 (Kreuzaler et al., 2011), Tgfβ3 (Nguyen and Pollard, 2000) and LIF (Kritikou et al., 2003). Stat3 has been shown to induce a non-classical lysosomal-mediated cell death (Sargeant et al., 2014). Stat3 induces a switch from secretion to uptake of milk fat globules, potentially through MFG-E8, a phagocytosis molecule. Accumulation of these globules within cells causes lysosomal leakage that leads to cell death (Sargeant et al., 2014).

Extensive cell death in the second phase triggers immune infiltration that exhibits features of both wound healing (Martinson et al., 2015; Stein et al., 2003) and an immunosuppressive mucosal environment (Betts et al., 2018). Immune infiltrate peaks at 6 days of involution and is dominated by wound healing type macrophages (MØs) (Martinson et al., 2015). Stat3 loss in the epithelium, further to affecting cell death, skews MØs towards a more inflammatory phenotype (Hughes et al., 2012). MØ infiltration is presumed to occur in response to cell death to ensure phagocytosis of epithelial cells and milk (Watson and Kreuzaler, 2011). Moreover, these cells are essential for epithelial cell death, adipose repopulation and proper remodelling of the mammary gland post-lactation (O'Brien et al., 2012).

High protease activity is also a feature of the involuting gland (Green and Lund, 2005), including matrix metalloproteinases, plasminogen and cathepsins. These function to remodel the extracellular matrix and activate growth factors and seem to have relevance to tumour progression, as Cox-2 promotes fibrillar collagen, which increases tumour invasiveness (Lyons et al., 2011).

1.1.6 Phagocytosis by epithelial cells during involution

Interestingly, epithelial cells also phagocytose dying alveolar cells (Monks et al., 2005) and abrogation of this process results in long-term defects in the epithelium such as persistent milk and apoptotic cells (Sandahl et al., 2010). Phagocytosis by epithelial cells is dependent on MerTK

(Sandahl et al., 2010) and autophagy (Teplova et al., 2013) and involves loss of tight junctions (Fornetti et al., 2016). It is not known how the phagocytic activity of macrophages and epithelial cells complement each other to facilitate involution. These may play roles in different phases of involution and in different locations.

1.1.7 Mammary gland remodelling and breast cancer

The remarkable ability of the mammary gland to remodel repeatedly over each reproductive cycle is also associated with high risk of cancer. One in eight women will be diagnosed with breast cancer in their lifetime (DeSantis et al., 2017). Parity has a profound influence on breast cancer risk: the earlier women first give birth, the greater the long-term protection they receive, and protection increases with each subsequent pregnancy (Rosner et al., 1994). Hormones are the main drivers of variation in breast cancer risk (Pike et al., 1983) and the timing of first menstrual period, first full-term pregnancy and menopause are major factors (Miller and Bulbrook, 1980). Breast cancer incidence follows a typical increase with tissue ageing (proportional to proliferation) when variable rates of mammary gland ageing are incorporated throughout life (Pike et al., 1983). In this model, proliferation associated with menstrual cycling and pregnancy hastens tissue ageing thus increasing breast cancer risk. In the long term, parity appears to reduce hormone levels compared to nulliparous women (Yu et al., 1981), which may slow proliferation and thus the rate of tissue ageing. Parity also stimulates differentiation of mammary tissue, decreasing proliferative structures that are more susceptible to carcinogenesis (Russo et al., 1982). Similarly, the loss of ovarian hormone signalling in menopause causes a sharp fall in proliferation and cancer incidence (Pike et al., 1983).

1.2 The mammary gland at the cellular level

1.2.1 Mammary cell populations

The resting adult mammary epithelium consists of three major cell types: luminal progenitors (LPs), mature luminal cells (MLs) (Asselin-Labat et al., 2006) and myoepithelial cells (Visvader, 2009). These cells are differentially regulated by hormones and perform different roles in

homeostasis and lactation. Both luminal populations highly express the junction protein E-Cadherin, as well as keratins (K) 8 and 18 whereas myoepithelial cells highly express K5 and K14 and smooth muscle actin (Gugliotta et al., 1988). Basal cell identity is defined by at least one master transcriptional regulator, p63 (Barbareschi et al., 2001; Carroll et al., 2006), which is required for mammary gland development (Mills et al., 1999; Yang et al., 1999).

Mammary epithelial cells can be identified by flow cytometry (FACS) as CD24 positive cells that are negative for CD45, TER119 and CD31 (Lin^-). Total epithelial cells can then be separated into basal ($CD29^{hi}CD24^+$ or $CD49f^{hi}CD24^+$) and luminal ($CD29^{lo}CD24^{hi}$ or $CD49f^{lo}CD24^{hi}$) populations (Shackleton et al., 2006; Stingl et al., 2006). The luminal compartment is composed of approximately 55% LPs and 45% MLs (Rios et al., 2014), which are arranged in a mosaic fashion (Figure 1.3d). MLs are larger in size, have a round nuclear morphology and are less proliferative, whereas LPs are smaller in size, have a vertically oriented oval nucleus and have greater proliferative potential (Asselin-Labat et al., 2006; Fernandez-Gonzalez et al., 2008; Giraddi et al., 2015; Rios et al., 2014).

LPs give rise to mature alveolar cells during pregnancy and lactation (Visvader, 2009), which are responsible for milk production. A key feature of LPs and alveolar cells is the expression of Elf5, a master transcriptional regulator of alveolar fate and alveolar cell maturation (Choi et al., 2009; Oakes et al., 2008; Rios et al., 2014; Zhou et al., 2005). MLs are distinct in their lack of Elf5, dependence on Gata-3 (Asselin-Labat et al., 2006; Kouros-Mehr et al., 2006) and expression of the ER and PR (Asselin-Labat et al., 2006). This enables MLs to detect hormonal signals during the oestrus cycle and the reproductive phase and relay this information to LPs and myoepithelial cells, which drive subsequent remodelling and alveolar maturation (Asselin-Labat et al., 2010; Brisken et al., 1998; Mallepell et al., 2006; Pal et al., 2013).

Luminal cells with *in vitro* colony forming activity can be enriched by FACS based on expression of CD61 (Asselin-Labat et al., 2006) or CD14 (Asselin-Labat et al., 2011). This observation led to the designation of LP and ML due to the progenitor-like properties of $CD61^+$ cells (LPs) and apparent terminal differentiation of $CD61^-$ cell (MLs) (Asselin-Labat et al., 2006). However, use of an *Elf5-GFP* reporter mouse showed that CD61 also marks a small proportion of MLs (Rios et

al., 2014). It is now emerging that distinct lineages exist for hormone receptor (HR)-negative and HR-positive luminal cells, each with their own committed progenitors (Keymeulen et al., 2017; Wang et al., 2017). While most HR-positive cells are mature/terminally differentiated, they do contain a small progenitor population that has not been well defined. To reflect these developments, luminal cells will here be referred to as belonging to either the alveolar or hormone-sensing (HS) lineage; the alveolar lineage comprising alveolar progenitors (APs) and alveolar cells, and the HS lineage comprising mature HS cells and hormone-sensing progenitors (HSPs).

1.2.2 Mammary stem and progenitor cells

The ability of the mammary gland to undergo repeated remodelling indicates the existence of long-lived undifferentiated stem cells capable of generating large numbers of mature functional cells. This notion was supported by the finding that small fragments of mammary tissue could regenerate an entire mammary gland through serial passages when transplanted into mammary fat pads with no endogenous epithelium (Daniel et al., 1968; DeOme et al., 1959; Hoshino and Gardner, 1967). It was subsequently found that clonal regions could generate entire functional mammary glands on serial transplantation (Kordon and Smith, 1998), strongly suggestive of multipotent stem cells. Finally, mammary glands were generated from transplanted single cells, demonstrating that rare basal cells (approximately 5%) could reconstitute a whole mammary gland (Shackleton et al., 2006; Stingl et al., 2006). Transplantable basal cells are characteristically myoepithelial (Prater et al., 2014) and the discovery of myoepithelial subpopulations based on surface markers or pathway activity has enabled the isolation of cells with increased repopulation potential (Fu et al., 2017; Wang et al., 2015). While these studies highlight the regenerative potential of basal mammary stem cells (MaSCs), transplant conditions are not physiological and may not truly reflect the role of MaSCs in unperturbed tissue (Lu et al., 2019). Genetic lineage tracing that largely preserves physiological conditions has unveiled much of *in situ* MaSC and progenitor function, as well as the link between stem/progenitor cells and breast cancer (Tharmapalan et al., 2019; Visvader and Stingl, 2014).

The longevity of stem cells allows them to accumulate mutations, making them common suspects for cancerous transformation (Visvader, 2011). Thus, understanding the identity and function of MaSCs and mammary progenitors is crucial to identifying the cells of origin of breast cancer subtypes. The identity of mammary stem and progenitor populations has proved difficult to untangle due to the complex phases of growth, homeostasis, cycling and maturation that the organ undergoes throughout life. For this reason, it is best to approach each stage independently. Here MaSCs are defined as cells capable of self-renewal and the generation of both the basal and luminal lineages under normal conditions *in vivo*. Progenitors, on the other hand, may be capable of extensive but limited self-renewal and only generate cells of a single lineage.

1.2.3 Mammary stem cells in the embryo

The mammary gland precursors within the mammary bud are basal-like and until E14 are not committed to any epithelial lineage (Keymeulen et al., 2011; Lilja et al., 2018; Wuidart et al., 2018) (Figure 1.4a). Embryonic MaSCs likely express high levels of Lgr5, Tspan8 (Fu et al., 2017) and S-SHIP (Rohrschneider et al., 2005). Even at E12.5, however, cells begin to show bias towards the luminal or basal lineage (Lilja et al., 2018) and are largely lineage-restricted by E15.5 (Wuidart et al., 2018). Despite this, late embryonic cells (E18.5) have a higher frequency of repopulating cells than early embryonic cells (E13.5-16.5) (Spike et al., 2012).

1.2.4 Pubertal progenitor cells

During morphogenesis in puberty, many progenitors populate each TEB (approximately 170 luminal and 90 basal) and each contribute equally to ductal growth (Scheele et al., 2017). Cap cells of the TEB self-maintain and give rise to mature myoepithelial cells of the duct as the TEB progresses (Sreekumar et al., 2017; Keymeulen et al., 2011; Rios et al., 2014; Scheele et al., 2017) (Figure 1.4b). Similarly, luminal lineage progenitors in the TEB body proliferate to maintain the TEB mass (Paine et al., 2016) and generate luminal cells of the extending ducts (Keymeulen et al., 2011). Within the body, progenitors of the alveolar and HS luminal lineages are distinct and lineage committed (Keymeulen et al., 2017; Wang et al., 2017), suggesting that branching morphogenesis is driven predominantly by lineage-restricted progenitors rather than by highly

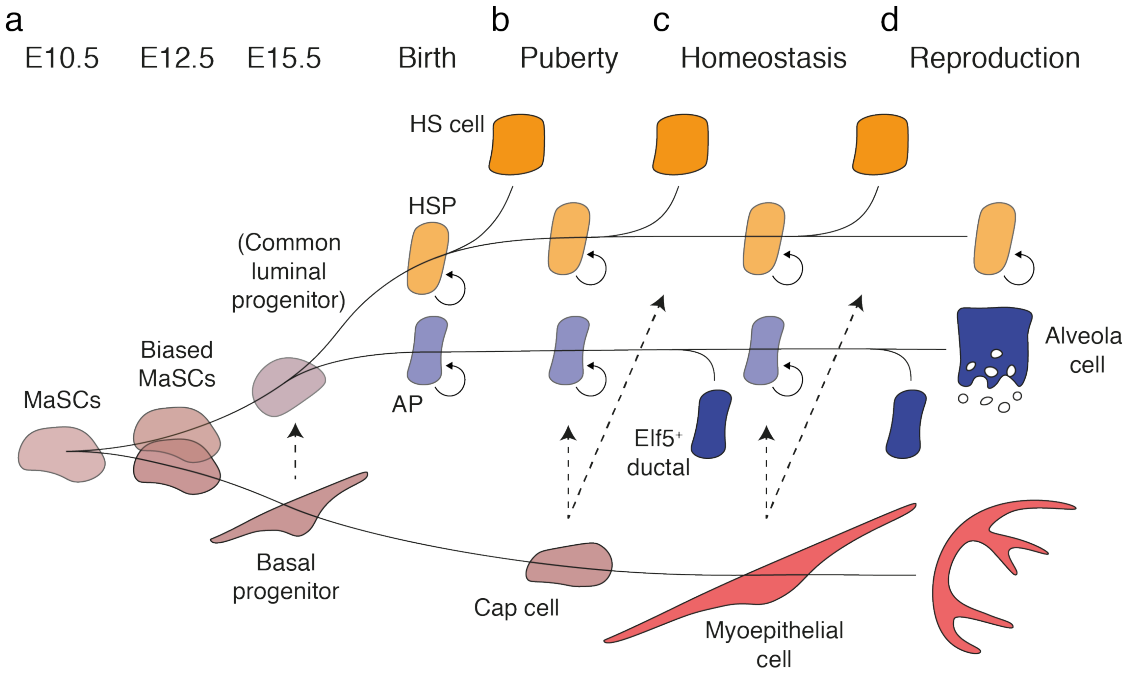

Figure 1.4: The mammary epithelial hierarchy

(a) MaSCs in embryonic development begin as equipotent but become biased and eventually lineage-restricted. The existence of a common luminal progenitor is assumed but has not been definitively identified.

(b) TEB cap cells, APs and HSPs generate ductal cells of their respective lineages with possible low level of cap contribution to the luminal compartment.

(c) Low level cell turnover in homeostasis is sustained by lineage progenitors with rare basal to luminal differentiation.

(d) Reproduction sees the generation and maturation of mature alveolar cells from APs, some of which may originate from basal cells. HS cells do not increase but self-maintain throughout reproduction. MaSC: mammary stem cell, HS hormone sensing, HSP: hormone-sensing progenitor, AP: alveolar progenitor.

active MaSCs. This is supported by unbiased, low frequency labelling of cells in puberty, which leads to labelling of lineage-restricted clones (Davis et al., 2016; Lloyd-Lewis et al., 2018; Scheele et al., 2017). However, if rare MaSCs do function in the TEB, these would be frequently missed by low-density labelling that would heavily favour abundant progenitors.

Cap cells express basal markers but are distinct from mature myoepithelial cells in their rounded morphology and expression of s-SHIP (Bai and Rohrschneider, 2010). Cap cells have long thought to be myoepithelial progenitors (Williams and Daniel, 1983), which has been confirmed by modern lineage-tracing methods (Sreekumar et al., 2017; Keymeulen et al., 2011; Rios et al., 2014). Early histological studies and ex vivo imaging showed invaginations of the cap layer into the body, leading to the hypothesis that they represent MaSCs that give rise to luminal cells (Williams and Daniel, 1983). Cap-like cells that express basal markers are present in the TEB body (Bai and Rohrschneider, 2010; Mailleux et al., 2007; Srinivasan et al., 2003), but the function of these cells and their ability to give rise to luminal cells is unknown, as they do not appear to cycle and frequently undergo apoptosis (Sreekumar et al., 2017; Mailleux et al., 2007; Paine et al., 2016). Migration of cap cells into the TEB body has not been definitively shown, so the presence of an independent population of cap-like body cells is possible. The high rate of death in these cells, however, and the prediction of cap to body migration by mathematical modelling (Paine et al., 2016) suggest constant turnover of this population. Stromal Wnt has been identified as a key survival factor for cap cells, and migration into the body removes them from this source leading to apoptosis mediated by Foxo1 (Sreekumar et al., 2017). Death of cap-like body cells is necessary, as loss of the proapoptotic factor Bim blocks apoptosis and causes lumen filling by highly abnormal squamous-like cells (Mailleux et al., 2007). The purpose of seemingly excessive cap to body migration leading to apoptosis is unknown.

1.2.5 Stem and progenitor cells in adult homeostasis

The resting adult mammary gland is a quiescent organ that undergoes a modest level of proliferation and regression in response to the oestrus cycle (Macias and Hinck, 2012). Epithelial turnover is low and stem/progenitor activity is minimal compared to puberty and pregnancy. Lineage tracing in the adult mammary gland has shown that each epithelial lineage contains progenitors that contribute to maintenance of that lineage (Blaas et al., 2016; Giraddi et al., 2015; Keymeulen et al., 2011, 2017; Lafkas et al., 2013; Rios et al., 2014; Rodilla et al., 2015; Wang et al., 2017; Wuidart et al., 2018), causing a slow drift towards local clonality (Keymeulen et al., 2011; Rios et al., 2014) (Figure 1.4c). Some studies have concluded that basal cells do not give

rise to luminal cells during homeostasis (van Amerongen et al., 2012; Keymeulen et al., 2011; Prater et al., 2014). Others have detected basal cells that give rise to both basal and luminal cells (Rios et al., 2014; Wang et al., 2015), indicating that rare multipotent MaSCs may play a minor role in homeostasis. Furthermore, embryonic-like MaSCs persist in the adult gland proximal to the nipple (Fu et al., 2017; Plaks et al.) that are quiescent but have high regenerative potential and may retain multipotency from their embryonic origin (Fu et al., 2017).

1.2.6 Stem and progenitor cells in pregnancy

Just as in adult homeostasis, conflicting theories are held for MaSC contribution to alveoli during pregnancy, lactation and involution. Committed progenitors have been identified that sustain the HS (Keymeulen et al., 2017), alveolar (Davis et al., 2016; Lloyd-Lewis et al., 2018; Rios et al., 2014; Rodilla et al., 2015) and basal lineages (van Amerongen et al., 2012; Davis et al., 2016; Keymeulen et al., 2011; Lloyd-Lewis et al., 2018; Prater et al., 2014) through multiple rounds of pregnancy (Figure 1.4d). Basal cells do appear to generate a small proportion of alveolar cells (van Amerongen et al., 2012; Rios et al., 2014; Wang et al., 2015) and the importance of this is further supported by a gradual decrease of lineage-traced APs over multiple pregnancies that suggests limited self-renewal ability (Rios et al., 2014).

1.2.7 Caveats of lineage tracing

Many of the lineage-tracing studies mentioned here employ the CreERT2 method of genetic recombination (van Amerongen et al., 2012; Sreekumar et al., 2017; Keymeulen et al., 2011; Prater et al., 2014; Rodilla et al., 2015) that is activated by tamoxifen treatment. Tamoxifen is an inhibitor of ER signalling and even at low doses affects mammary gland development and cell populations (Rios et al., 2014; Shehata et al., 2014). This may be one cause of the conflict in the field over the ability of basal cells to generate luminal cells, as similar approaches that differed by use of tamoxifen (Keymeulen et al., 2011) and the preferable doxycycline (Rios et al., 2014) generated different results.

Other issues may arise from tissue preparation for imaging (Rios et al., 2016a). Approaches that employ partial tissue digestion affect the morphology of mammary cells making

luminal/myoepithelial cell distinction difficult (Rios et al., 2016b; Wuidart et al., 2016). High-resolution 3D imaging techniques that preserve tissue architecture have proven to be invaluable for clonal analyses as they allow detection of exceptionally rare events at subcellular resolution and provide confident cell-type identification (Davis et al., 2016; Lloyd-Lewis et al., 2018; Rios et al., 2014). Whole gland-scale, low resolution imaging has been useful for quantifying global stem cell dynamics from sparse labelling events (Scheele et al., 2017).

The density of cell labelling is also of great importance. If basal to luminal differentiation occurs, it is an extremely rare event. High-density labelling of basal cells is required to capture these events. This complicates clonal analysis because high frequency labelling causes overlap of clonal regions. Thus, with 4-colour labelling such as with the Confetti allele, definitive identification of bi-lineage clones is difficult. Sparse labelling enables the confident determination of a cell's progeny because clones are well separated (Davis et al., 2016; Lloyd-Lewis et al., 2018; Scheele et al., 2017). The limitation to this approach is that it is heavily biased towards more active and numerous progenitors, which may lie downstream of rare MaSCs. Low-density lineage tracing is therefore not able to provide evidence against the existence of rare MaSCs but has strongly established that mammary gland development is driven primarily by lineage-restricted progenitors. Recent advances that allow lineage tracing from many thousands of individual cells, such as cellular barcoding, may overcome this challenge (Lu et al., 2019).

1.2.8 A developmental mammary stem cell hierarchy

Regardless of whether rare MaSCs are active in the mammary gland throughout life, basal cells can generate luminal cells, based on many transplantation studies (Visvader, 2009). The difficulty of detecting this activity *in vivo* suggests that this activity is rarely necessary due the sufficiency of committed luminal lineage progenitors. While there are reports of luminal cells generating basal cells in pregnancy (Song et al., 2019) and rare luminal cells capable of regenerating a mammary gland on transplantation (Rodilla et al., 2015; Shehata et al., 2012), this remains to be confirmed in the absence of tamoxifen as the inducing agent. There may also exist a common luminal progenitor for the HR-positive and HR-negative lineages and while this seems

likely at least during embryonic development, most evidence in adulthood points towards only lineage restricted progenitors (Giraddi et al., 2015; Keymeulen et al., 2017; Wang et al., 2017).

Mammary stem and progenitor activity are developmental stage-specific (Figure 1.4). Early embryonic MaSCs give rise to gradually more lineage-biased progenitors and after birth the lineages appear to be largely maintained by restricted progenitors with rare luminal differentiation from basal cells during ductal morphogenesis, pregnancy and homeostasis. A deeper understanding of the molecular drivers of lineage commitment and behaviour will better enable us to understand breast cancer initiation and implement preventative strategies (Tharmapalan et al., 2019; Visvader, 2011).

1.3 Immune regulation of the mammary gland

1.3.1 The immune system

The immune system plays critical roles in both the detection and eradication of pathogens and the maintenance of tissue homeostasis. Defects in homeostatic immune function can lead to autoimmunity, chronic inflammation (Miyake and Kaisho, 2014) and cancer (Hanahan and Weinberg, 2011). Tissues contain a broad spectrum of immune cell types, including resident immune cells that provide memory and constant surveillance, and circulating cells that rapidly infiltrate tissues in response to infection or injury. Resident immune populations consist predominantly of innate myeloid cells such as MØs and dendritic cells (DCs), neutrophils, eosinophils and mast cells. Resident T, B and innate lymphocytes also patrol tissues but are less numerous. The innate arm of the immune system uses generic receptors for pathogen- and damage-associated molecules to detect abnormalities and trigger subsequent inflammation, wound healing or adaptive immune responses (Medzhitov and Janeway, 2000). The adaptive arm of the immune system is capable of recognising specific antigens and mounting a targeted defense. Adaptive immune responses are potent but take 3-5 days to take effect, so innate immunity provides an important front-line defence (Medzhitov and Janeway, 2000). Under homeostatic conditions, immune cells maintain tissue integrity through a variety of functions:

phagocytosis of apoptotic cells, sustaining tolerance to self, food and commensal bacteria (Chistiakov et al., 2015), regulatory feedback loops with non-immune cells (Schepper et al., 2018), metabolic regulation (Jaitin et al., 2019) and removal of abnormal cells (Cruz-Muñoz et al., 2019).

The immune system has surprisingly important roles in mammary gland development and remodelling (Reed and Schwertfeger, 2010). During mammary gland function in lactation, a mucosal immune environment is established that is immunosuppressive (Betts et al., 2018), and immunological components in milk provide protection for offspring (Stoliar et al., 1976). This section discusses the common immune cell types within the mammary gland and describes their general functions as well as their localisation and function within the mammary gland.

1.3.2 Mast cells and eosinophils

Innate immune populations that regulate mammary gland development include mast cells, eosinophils and MØs (Reed and Schwertfeger, 2010). Mast cells and eosinophils are granulocytes that harbour granule reservoirs of signalling and enzymatic molecules that are released upon activation. Generally, mast cells play important roles in allergic reactions, pathogen clearance, immune tolerance and wound healing (Rao and Brown, 2008), whereas eosinophils regulate tissue remodelling, wound healing and metabolism to resolve pathogenesis (Abdala-Valencia et al., 2018). The pathogenic functions of these cells are far better understood than their homeostatic functions. Mast cell granules contain proteases, cytokines, growth factors and proteoglycans (Rao and Brown, 2008) and are recruited to the surrounding stroma of the TEB during puberty (Reed and Schwertfeger, 2010). c-Kit is essential for mast cell development, as *Kit*$^{W\text{-}sh}$ mutant mice are mast cell deficient (Grimbaldeston et al., 2005). Mammary gland development is perturbed in these mice, with decreased TEB formation, epithelial proliferation and ductal growth that requires degranulation and serine protease activation (Lilla and Werb, 2010). Eosinophils also regulate branching morphogenesis, as TEB formation and branching are affected in both IL5- and eotaxin-null mice, which lack eosinophils (Colbert et al., 2005; Gouon-Evans et al., 2000). Like mast cells, eosinophils surround the TEB, particularly adjacent to the

tip (Gouon-Evans et al., 2000). The signalling pathways used by eosinophils in this context are unknown, but may include TGF-β, TGFα and EGF (Reed and Schwertfeger, 2010).

1.3.3 Dendritic cells

DCs sample the extracellular environment and display antigen on their surface via MHC class II (MHCII). Activated DCs migrate from peripheral tissues to lymph nodes where they present antigen to T cells to initiate adaptive immune responses (Merad et al., 2013). While MØs also present antigen, these do not migrate to lymph nodes and typically express lower levels of T cell co-activation markers. Presented antigens are recognised by antigen-specific $CD4^+$ T helper cells or $CD8^+$ cytotoxic T cells, which react according to integrated activation and suppression signals from DCs and the microenvironment (Chen and Flies, 2013). Immunosuppressive receptors on DCs and anti-inflammatory cytokines skew the T cell response towards regulatory functions indicative of a tolerogenic environment. This is typical of mucosal surfaces, where inflammatory responses to symbiotic bacteria must be suppressed, and tumours, which subvert normal tolerogenic mechanisms in order to evade detection (Woods et al., 2014). Conversely, expression of co-activation receptors on DCs and T cells skews the T cell response to an effector function which promotes elimination of antigen-bearing cells (Chen and Flies, 2013).

DCs typically express CD11c, MHCII, CD26 and CD24, and are negative for the MØ markers F4/80, CD64 and MerTK (Guilliams et al., 2016; Merad et al., 2013; Miller et al., 2012; Tamoutounour et al., 2012). Broadly speaking, peripheral tissue DCs fall into two major populations: classical DC 1 (DC1) that are $CD11b^{low}$, $CD24^{high}$, $CD103^+$ and $Xcr1^+$, and classical DC 2 (DC2) that are $CD11b^+$, CD24-intermediate, $CD103^-$ and $Xcr1^-$ (Calabro et al., 2016; Ginhoux et al., 2009; Guilliams et al., 2016). DC2 are generally more potent activators of $CD4^+$ T helper cells, while DC1 activate $CD8^+$ cytotoxic T cells (Eisenbarth, 2018). Thus, depending on the tissue, spatial localisation and disease context, DCs tune T cell responses to produce appropriate reactions to infections and homeostatic processes.

1.3.4 Dendritic cells in the mammary gland

Little is known about the function of DCs during mammary gland development. Deletion of MHCII in CD11c-expressing cells promotes ductal growth during morphogenesis (Plaks et al., 2015). CD11c is not specific to DCs, so it is not clear whether this is a function of DCs or MØs. However, mice without MØs have decreased growth and branching (Gouon-Evans et al., 2000) so a negative regulatory function of MØs seems unlikely. Inhibition of ductal growth by CD11c-positive cells is carried out by T helper 1 cell-derived Ifn-γ, indicating a role for DC2 as activators. Lactation and involution see the transformation of the mammary gland immune environment into a mucosal system (Betts et al., 2018). Particularly during involution, infiltrating DCs downregulate activation markers and are skewed towards immune suppressive phenotypes (Betts et al., 2018). This may be necessary to prevent immune reaction to milk proteins but appears to have adverse effects due to impaired cancer surveillance, as involution is associated with elevated cancer risk (Martinson et al., 2015; Schedin et al., 2007).

1.3.5 Macrophages

MØs are dispersed throughout all tissues and play essential roles in organ development, function and homeostasis. They are important regulators of pathogenic situations such as infection, injury and cancer (Lavin and Merad, 2013; Varol et al., 2015; Wynn et al., 2013). To account for the diverse stresses and functions of each organ, all tissue microenvironments uniquely program MØs to perform niche-specific functions (Gautier et al., 2012; Gordon and Plüddemann, 2017; Lavin et al., 2014). Under homeostatic conditions, most MØ populations are long-lived and tissue-resident, having the ability to self-maintain through proliferation (Ginhoux and Guilliams, 2016). During injury or infection, however, circulating monocytes enter tissues and differentiate into short-lived MØs that phagocytose pathogens and neutrophils, resolve inflammation and promote wound healing. MØs are dependent on Colony stimulating factor 1 (Csf1) for differentiation, which signals through the Csf1 receptor (Csf1r) (Pollard, 1997). Other cytokines can also regulate the differentiation and function of specific populations, such as IL34 (Wang et al., 2012), IL4 (Jenkins et al., 2013) and IL7 (Leung et al., 2019). Expression of the surface markers CD64, MerTK and F4/80 identifies MØs in all tissues (Gautier et al., 2012; Guilliams et

al., 2016; Scott et al., 2015) but populations vary in expression of other markers such as CD11c, CD11b, Lyve1, Cx3cr1 and MHCII, which can be used to define subpopulations (Chakarov et al., 2019; Gibbings et al., 2017; Gordon and Plüddemann, 2017).

1.3.6 The developmental origin of macrophages

Primitive MØ precursors arise at E7.5 from primitive erythro-myeloid progenitors (EMPs) in the yolk-sac and disseminate throughout the embryo and differentiate into resident MØs (Ginhoux and Guilliams, 2016; Ginhoux et al., 2010). The blood-brain barrier is established shortly after, so brain microglia remain yolk-sac-derived and self-maintain for life (Hoeffel and Ginhoux, 2015). A second wave of MØs originates in the fetal liver at E8.5 through c-Myb-positive EMPs that generate circulating fetal monocytes that seed tissues (Hoeffel et al., 2015; Perdiguero et al., 2014). Definitive hematopoietic stem cells (HSCs) arise late in embryogenesis and seed the bone marrow where they dominate blood production after birth. These generate monocytes by progressive differentiation through common myeloid progenitors (CMPs), granulo-myeloid progenitors (GMPs) and committed monocytes precursors (cMOPs), the final monocyte precursor (Guilliams et al., 2018). After birth, bone marrow-derived MØs gradually replace embryonic MØs at varying rates (Ginhoux and Guilliams, 2016), likely determined by niche accessibility and the longevity of existing MØs (Guilliams and Scott, 2017). MØs in the gut are entirely replaced within the first few weeks after birth (Bain et al., 2014), whereas other populations including lung alveolar MØs, skin Langerhans cells, and liver Kupffer cells are not replaced at all (Ginhoux and Guilliams, 2016). The functional consequence of MØ longevity is unclear and origin seems to have little effect on phenotype or function (Lavin et al., 2014; Scott et al., 2016), likely because the influence of niche programming factors is far greater (Guilliams and Scott, 2017).

1.3.7 Fate mapping of macrophage precursors

The developmental origin of MØs can be determined by mouse models that enable specific labelling of precursor populations. MØs were initially thought to turn over continuously and be maintained by constant differentiation of monocytes (van Furth and Cohn, 1968). Later studies

challenged this model by revealing that populations such as Langerhans cells, Kupffer cells and alveolar MØs were long-lived and capable of proliferation (Hoeffel and Ginhoux, 2015). Fate mapping using a *Cx3cr1-CreER* mouse model demonstrated that many resident MØ populations are fully established during embryogenesis and have little contribution from adult monocytes (Yona et al., 2013).

Generation of blood precursors in the embryo occurs from E7–8.5 by differentiation from haemogenic endothelium and is Runx1-dependent (Tober et al., 2013). Yolk-sac EMPs generated in this manner can be labelled in the *Runx1-Mer-Cre-Mer* mouse model (Samokhvalov et al., 2007). EMPs labelled at E7.5 gave rise to the first MØs in all embryonic tissues (Ginhoux et al., 2010). Only labelled microglia persisted into adulthood, with other populations predominantly generated from precursors arising at E8.5 (Ginhoux et al., 2010). It was subsequently shown that EMPs arising from the haemogenic endothelium at E8.5 migrate to the fetal liver and generate fetal monocytes that produce most adult MØs (Gomez Perdiguero et al., 2014; Hoeffel et al., 2015). An alternative conclusion was drawn from the *Kit-Mer-Cre-Mer* labelling of definitive HSCs at E8.5, which labelled most adult MØs (Sheng et al., 2015). However, this model labelled microglia precursors at E7.5 (known to be EMPs, not HSCs) and therefore likely labelled EMPs at E8.5, which would account for this discrepancy (Ginhoux and Guilliams, 2016).

These fate mapping tools utilised the tamoxifen inducible CreER method for Cre recombination of fluorescent reporter alleles. Tamoxifen treatment during pregnancy often leads to abortion of embryos (Danielian et al., 1998) and affects the health of the mother (Ved et al., 2019). A further limitation is the incomplete labelling of the target population. A mouse model has now been created that expresses *Cre* downstream of *Ms4a3*: a gene uniquely expressed in GMPs (Liu et al., 2019). Combination with a fluorescent reporter labelled all GMP descendants including adult monocytes and MØs but not EMP-derived MØs, enabling easy and robust identification of embryonic MØs. This overcomes the impact of tamoxifen treatment and the inefficiency of other MØ fate mapping models. Thus, the *Ms4a3-Cre* mouse is a valuable new tool that allows unperturbed analysis of resident MØ origin. This has so far enabled the determination of heterogeneous adipose MØ origins in homeostatic and disease settings (Jaitin et al., 2019).

1.3.8 Homeostatic functions of tissue-resident macrophages

Resident MØs receive unique signals within different organ niches and acquire a huge variety of morphologies, molecular phenotypes and functions. Most functions are phagocytic in nature and use scavenger receptors, 'eat me' signal receptors, complement receptors and phagocytic machinery (Gordon, 2016). Apart from the ubiquitous function of dead cell clearance, specific phagocytic functions include clearance of aging red blood cells by spleen red pulp MØs, clearance of particles in the lung by alveolar MØs and clearance of pathogens and blood-borne particles by Kupffer cells (Gordon and Plüddemann, 2017). More specialised functions include synapse pruning by brain microglia (Rosa et al., 2011; Schafer et al., 2012), bone resorption by osteoclasts (Gordon and Plüddemann, 2017), iron recycling by Kupffer cells and spleen red pulp MØs (Gordon and Plüddemann, 2017; Kondo et al., 1988), extracellular matrix (ECM) regulation by arterial MØs (Lim et al., 2018) and electrical conduction by cardiac MØs (Hulsmans et al., 2017).

MØs also display phenotypic and functional heterogeneity within organs – both the heart and lung contain at least four MØ populations with unique phenotypes, gene expression profiles, longevity and functions, likely reflecting differential programming by distinct niches (Chakarov et al., 2019; Epelman et al., 2014; Gibbings et al., 2017). Two MØ subtypes that exist across organs have been identified that reside in blood vessel- and neuron-associated niches (Chakarov et al., 2019). Depletion of blood vessel-associated MØs exacerbated tissue fibrosis, indicating an important role for this population in regulation of ECM and inflammation.

1.3.9 Functions of macrophages in the mammary gland

MØs have an essential role in all stages of mammary gland development and function (Gouon-Evans et al., 2000; O'Brien et al., 2012; Pollard and Hennighausen, 1994). Mice lacking functional Csf1 (*Csf1*$^{op/op}$) do not produce MØs, and have severely impaired ductal outgrowth during morphogenesis in puberty (Gouon-Evans et al., 2000), premature and abnormal formation of alveoli in pregnancy and impaired milk production in lactation (Pollard and Hennighausen, 1994). Csf1 production by the mammary epithelium is required to recruit MØs to

TEBs (Nguyen and Pollard, 2002). Interestingly, *Csf1*$^{op/op}$ mice eventually generate full ductal trees (Gouon-Evans et al., 2000), indicating that MØs may be most important in early puberty, such as in TEB formation. MØs are also important during involution, as conditional depletion of MØs during weaning suppressed of alveolar cell death, delayed milk clearance and reduced adipocyte repopulation (O'Brien et al., 2012). Furthermore, MØs support mammary stem cell activity (Gyorki et al., 2009) through Wnt signalling downstream of Notch activation by basal Dll1 (Chakrabarti et al., 2018).

Mammary macrophages have been reported to fall into F4/80-intermediate (int), CD206-low (lo) adult bone marrow-derived, and F4/80-high (hi), CD206^{hi} fetal liver-derived populations in approximately equal proportions (Jäppinen et al., 2019). This study did not employ markers to exclude DCs and monocytes from MØs and thus the F4/80^{lo} population is not yet established as *bona fide* MØs. This study also performed high-dimensional mass-cytometry on the mammary myeloid compartment but again did not use robust combinatorial markers for differentiation of macrophages, DCs and monocytes. Thus, while this study shows that embryonic macrophages persist in the adult mammary gland, their heterogeneity remains poorly characterised. Embryonic macrophages may be responsible for promoting duct growth during puberty (Jäppinen et al., 2019), as morphogenesis was delayed in Plvap-deficient mice that have perturbed monocyte egress from the fetal liver (Rantakari et al., 2016). Despite this, the identity of MØs that promote morphogenesis is unclear and a mammary-intrinsic role for Plvap has not been ruled out.

Despite the crucial role of MØs in epithelial remodelling, the mechanisms by which MØs support mammary gland development remain largely unknown. MØs are associated with the mammary epithelium throughout development (Chua et al., 2010; Gouon-Evans et al., 2000; Hodson et al., 2013; O'Brien et al., 2010; Plaks et al., 2015; Schedin et al., 2007; Schwertfeger et al., 2006; Sun et al., 2013) and in mammary tumours, where they promote tumour progression and metastasis (Bingle et al., 2002; Franklin et al., 2014; Lin et al., 2001; Linde et al., 2018; Pollard, 2004; Wyckoff et al., 2004). In puberty, MØs are located within TEBs where they phagocytose apoptotic epithelial cells (Gouon-Evans et al., 2000), as well as around TEBs where they organise collagen

fibres (Ingman et al., 2006). Duct-associated MØs are regulated by Tgfβ1, which decreases their number and promotes a dendritic morphology (Sun et al., 2013). They also vary in frequency over the oestrus cycle, peaking in proestrus, and promote both bud formation and regression (Chua et al., 2010).

1.3.10 Macrophage function during involution

The second phase of involution is accompanied by infiltration of MØs, neutrophils, eosinophils, mast cells, DCs and plasma cells (Hughes et al., 2012; Stein et al., 2003). Only MØs have been extensively studied in terms of specific functions in this phase. MØs peak at days 6–8 of involution and are anti-inflammatory, expressing Arg1 but not iNOS (O'Brien et al., 2010). Loss of Stat3, which prevents alveolar cell death (Sargeant et al., 2014), impaired MØ infiltration, increased iNOS and decreased Arg1 expression (Hughes et al., 2012). Muc1 can also enhance the anti-inflammatory MØ signature during involution (Li et al., 2018). Thorough characterisation of immune infiltration revealed parallels with an immunosuppressive wound healing process that facilitated cancer progression (Martinson et al., 2015). Wound healing-type MØs have been implicated in the short-term elevated cancer risk associated with parity (Li et al., 2018; O'Brien and Schedin, 2009; Schedin et al., 2007; Stanford et al., 2014). The involution immune environment has now been characterised as distinctly mucosal, with increases in regulatory, mucosal T cell subtypes, anti-microbial Ig production and immunosuppressive DC phenotypes (Betts et al., 2018).

MØs are required for mammary epithelial cell death, mammary gland remodelling and adipose tissue regeneration during involution (O'Brien et al., 2012). In this study, MØs were depleted in MaFIA mice (Burnett et al., 2004), which express a drug-inducible Fas-based suicide gene under the control of the *Csf1r* promoter. Ablation of MØs from 3 days prior to weaning and throughout involution affected cell death and remodelling even in the presence of Stat3 (O'Brien et al., 2012), indicating that Stat3 may operate through MØs. Tgfβ3, which is essential and sufficient to induce cell death during involution (Nguyen and Pollard, 2000), is not expressed by involution-associated MØs but decreases upon MØ ablation, suggesting that Tgfβ3 is induced downstream

of MØs. Injection of wild-type MØs into MØ-depleted mammary glands at weaning improved cell death and remodelling (O'Brien et al., 2012).

1.4 Breast cancer

One in eight women will develop breast cancer in their lifetime (DeSantis et al., 2017), so improvements in breast cancer prevention and treatment are needed. Breast cancer can be classified into approximately six different diseases, based on hormone and growth factor receptor expression, proliferation rate and gene expression signature (Perou et al., 2000). Each of these is associated with driver mutations (such as P53, PIK3CA and Gata-3) (Koboldt et al., 2012) but are also influenced by the cell of origin within the mammary differentiation hierarchy (Visvader, 2009). Breast cancer can be studied (in order from most to least physiological) by analysing clinical tumour samples, growing human tumours in immunocompromised mice (xenografts), using genetically engineered mouse models of breast cancer or use of cancer cell lines *in vitro*. Of these, mouse models of breast cancer are a valuable tool for investigating the fundamental biology of cancer (Hennighausen, 2000). These are particularly useful for studying the tumour immune environment as they have fully functional immune systems, in contrast to immunocompromised mice required for xenograft models.

1.4.1 Immune regulation of breast cancer

The immune system can control cancer progression by two main mechanisms – adaptive immune response to tumour neoantigens culminating in tumour cell killing by cytotoxic lymphocytes (Schumacher and Hacohen, 2016), and innate killing of tumour cells that downregulate antigen cross-presentation to the adaptive immune system, which is carried out by natural killer (NK) cells (Chiossone et al., 2018). Tumours can evade these attacks through creation of an immunosuppressive environment or by excluding immune cells from the tumour (Gajewski et al., 2013). MØs play a central role in immunosuppression within tumours as a continuation of their homeostatic function within normal tissues (DeNardo and Ruffell, 2019). Immunosuppression can be overcome therapeutically by inhibition of immune checkpoint

receptors (such as PD1/PD-L1 and CTLA-4) that are often highly expressed by tumour cells and tumour infiltrating lymphocytes (Pardoll, 2012). The success of checkpoint inhibitors in activating cytotoxic responses to cancer depend on the neoantigen load of a tumour, which varies greatly between cancer types (Schumacher and Hacohen, 2016). Patient-derived tumour antigen-specific cytotoxic T cells generated *in vitro* (Chimeric Antigen Receptor T cell, CAR T cell) can also produce an effective attack on tumours (Brown et al., 2016; Kahlon et al., 2004). NK cells primarily target metastatic cells and blood cancers and can be potentiated by checkpoint blockade and activating cytokines. Potent NKs can also be generated *in vitro* for adoptive transfer (Krasnova et al., 2017; Souza-Fonseca-Guimaraes et al., 2019).

1.4.2 Tumour-associated macrophages

Tumour-associated MØs (TAMs) promote tumorigenesis through several mechanisms, including promoting tumour cell migration, angiogenesis, immunosuppression and metastasis through programs that resemble wound healing (Qian and Pollard, 2010). Depletion of TAMs by Csf1r inhibition in combination with chemotherapy, immunotherapy or radiation can have robust effects against cancer (Ruffell and Coussens, 2015). Treatments that reprogram TAMs from a typical anti-inflammatory, pro-tumour phenotype to a pro-inflammatory, anti-tumour phenotype have also been shown to decrease tumour growth and metastasis (Guerriero et al., 2017). Furthermore, MØs are capable of phagocytosing non-apoptotic cells that lose expression of 'don't eat me' signals such as CD47 and CD24 – inhibition of these molecules can stimulate TAM phagocytosis of tumour cells (Barkal et al., 2019; Willingham et al., 2012).

1.4.3 Heterogeneity of breast cancer macrophages

The large number of TAMs within tumours, their plasticity and their potential to perform anti-tumour functions makes precise TAM modulation in combination with other therapies a promising goal. Understanding the fundamental biology of TAM programming and development is important to improve our ability to exploit TAMs against cancer. TAMs have been extensively investigated in the *MMTV-PyMT* mouse mammary tumour model and are heterogeneous in this context, comprising $CD11b^{+}$ and $CD11b^{lo}$ populations (Broz et al., 2014; Franklin et al., 2014;

Tymoszuk et al., 2014). CD11b^{lo} TAMs specifically arise during tumourigenesis as only CD11b^{+} MØs are present in normal mammary tissue (Franklin et al., 2014). Compared to CD11b^{+} MØs, CD11b^{lo} TAMs are more phagocytic (Broz et al., 2014) and more proliferative (Franklin et al., 2014; Tymoszuk et al., 2014). These also specifically express CD11c (Broz et al., 2014; Franklin et al., 2014) and VCAM1 but not Ly6C (Franklin et al., 2014). Neither population is capable of activating helper or cytotoxic T cells (Broz et al., 2014). Despite some proliferation, CD11b^{lo} TAMs are derived from monocytes during tumourigenesis (Franklin et al., 2014). These also exhibit a distinct localisation within the tumour environment, with CD11b^{+} TAMs residing in the stroma surrounding the tumour and CD11b^{lo} TAMs lying proximal to the tumour (Broz et al., 2014). CD11b^{lo} TAMs are Notch-dependent and inhibition of Notch signalling in these cells in *CD11c-Cre/RBPJ$^{fl/fl}$* mice inhibited their differentiation and slowed tumour growth (Franklin et al., 2014). It therefore seems that breast TAMs are distinct from normal tissue MØs and are uniquely pro-tumorigenic. When this population arises is not clear, however, intra-epithelial MØs have been observed in hyperplastic ducts. These were suggested to have a role in early cancer dissemination through Wnt signalling (Linde et al., 2018) but it was not determined whether these were a distinct population.

1.5 Three-dimensional confocal imaging

Imaging is an essential tool in biology, as it supplies spatial and temporal information about events that is essential for understanding biological processes. The earliest insights into mammary gland structure and organisation were gained from thin paraffin sections and electron microscopy, which are limited to two-dimensions (2D), and wholemount preparations, which do not provide cellular information. Imaging technology has developed at an incredible rate over the last 20–30 years to provide unprecedented views of biology, including of the mammary gland. Not only have microscopes improved dramatically, but computing and data storage have advanced exponentially to accommodate the increasingly massive and complex datasets generated by modern microscopes. The confocal microscope was invented in the mid-1950s by Marvin Minsky (Minsky, 1988) but only became widespread when engineering, fluorescent dyes

and optics reached sufficient quality for broad application. Confocal imaging uses a pinhole to eliminate out of focus light from a sample and so is capable of imaging thin optical planes through a thick sample that can be subsequently reconstructed in 3D. While confocal technology is relatively old, it remains a laboratory workhorse and provides a good compromise between difficulty of sample preparation, simplicity, resolution, sensitivity and dataset size that make it suitable for everyday use. Advances in microscope optics, computation, sample clearing and analysis software have enabled confocal microscopy to be pushed to the edge of its inherent physical limitations in imaging depth, sensitivity and resolution.

1.5.1 3D cellular imaging of the mammary gland

Biological specimens are opaque because they contain dense, complex mixtures of water, protein and lipid, each of which have different refractive index (RI) values. When light travels between substances with mismatched RIs it is scattered and so cannot travel linearly through tissue (Richardson and Lichtman, 2015). 3D imaging of the mammary gland is especially difficult because it is lipid-rich and strongly refracts light. Additionally, virgin ducts are buried within adipose tissue and so are not easily accessible for imaging. Solutions to these issues have been sought, such as compression of glands between cover slips (Keymeulen et al., 2011; Scheele et al., 2017) or enzymatic digestion (Wuidart et al., 2016) but these affect gland architecture and cell morphology (Rios et al., 2016b).

Various methods for making organs transparent have been used historically but modern tissue clearing that preserves microscopic architecture was pioneered to achieve deep brain imaging for neural network analysis (Chung et al., 2013). There has since been an explosion in new clearing techniques that have been applied to many organs and diverse biological questions. Two categories of clearing agent have been developed; solvent based solutions that remove water and lipids while matching the RI, and aqueous solutions that simply attempt to match the RI of the tissue, while removing lipids in some cases (Richardson and Lichtman, 2015). Solvent-based clearing is the most effective but causes tissue shrinkage, structural deformation and quenching of native fluorescence (Lloyd-Lewis et al., 2016). Organic solvents are also highly toxic, precluding everyday use. Aqueous-based agents, particularly CUBIC (Susaki et al., 2014; Tainaka

et al., 2014) and SeeDB (Ke et al., 2013), are well suited to the mammary gland, as they preserve tissue architecture and native fluorescence while achieving good transparency (Lloyd-Lewis et al., 2016). These clearing methods are simple, single agent and take one week; shorter than many other protocols that are multi-step and take up to two weeks (Richardson and Lichtman, 2015).

In a study in our laboratory, we have developed and published a novel single agent, aqueous clearing method for the mammary gland (Rios et al., 2019). This protocol is based on clearing with a solution of fructose, urea and glycerol for imaging (FUnGI), that clears the mammary gland within hours and preserves tissue structure, cell morphology and native fluorescence. FUnGI has equivalent mammary gland clearing ability to the similar agent Ce3D (Li et al., 2017) and uses a series of permeabilisation and blocking buffers that are highly optimised and effective for whole mammary gland and breast tumour immunostaining (Rios et al., 2019).

1.6 Summary and aims

Overall, understanding of mammary gland biology has progressed rapidly over the past 30 years with the identification of many molecular and genetic regulators, elucidation of the stem cell hierarchy, and development of advanced techniques for deciphering this complex and dynamic system. In turn, these developments have benefitted breast cancer patients through the discovery of new targeted therapies and preventative strategies. Despite this, there remain many outstanding questions and challenges to overcome, including:

- Limited understanding of cell dynamics and a lack of techniques to uncover these.
- How cooperative cell behaviour in the TEB sustains branching morphogenesis.
- How the mammary gland is regulated by heterogeneous immune populations.

These questions form the basis of the experimental investigation of mammary gland biology presented in this thesis. These have been addressed using emerging imaging technology as a primary tool, due to its power in revealing spatial and temporal information that is fundamental to the formation, function and regulation of biological systems.

Chapter 2: Materials and methods

2.1 Experimental animals

2.1.1 Mouse strains

Wild-type C57BL/6 and FVB/N mice were provided by the Walter and Eliza Hall Institute (WEHI) animal facility (Melbourne, Australia). All mice are C57BL/6 unless indicated. *Elf5-rtTA-GFP (Elf5-rtTA)* and *K5-rTTA-GFP (K5-rtTA)* mice (FVB/N) were generated as previously described (Rios et al., 2014) and used as heterozygous. *Tet-O Cre (Tet-Cre)* (bred with K5-rtTA), *CD11c-DTR-GFP (*referred to as *CD11c-GFP* or *CD11c-DTR), CD11c-Cre, CD11b-DTR, CX3CR1-GFP, Csf1r-GFP, UBC-GFP*, *Rosa-TdTomato, MMTV-PyMT* (FVB/N background), *MMTV-Neu* (FVB/N background) and *MMTV-Wnt1* (FVB/N background) mouse lines were originally acquired from Jackson Laboratories (Maine, USA). *MMTV-PyMT/CX3CR1-GFP* and *MMTV-Wnt1/CX3CR1-GFP* mice were on a mixed C57Bl/6, FVB/N background. *Pr-Cre* mice were kindly provided by John Lydon (Soyal et al., 2005); *CD11c-YFP* mice were kindly provided by Scott Mueller; *Irf8-YFP* (Wang et al., 2014) and *Irf8*$^{fl/fl}$ (Feng et al., 2011) mice were kindly provided by Stephen Nutt; *Confetti* mice (Snippert et al., 2010) were kindly provided by Hans Clevers; *Hes1-2dGFP* mice were kindly provided by Toshiyuki Ohtsuka (Ohtsuka et al., 2006); *Ms4a3*^{Cre} mice were generated as described (Liu et al., 2019); *Tet-Cre* mice bred with *Elf5-rtTA* were kindly provided by Kai Schoenig (Schönig et al., 2002). All adult mice were virgin, unless otherwise indicated.

2.1.2 Mouse experiments

Recombination of the *Confetti* allele in *Elf5-rtTA or K5rtTA/Tet-Cre/Confetti* mice was induced by intraperitoneal (i.p.) injection of 1 mg doxycycline (10 mg/mL in PBS) (Sigma) at 28, 29 and 30 days of age and mice were analysed at 5–6 weeks. For analysis of pregnancy time-points, adult mice were mated and females scored for the presence of vaginal plugs. The day of the observed plug was considered P0.5. For involution experiments, weaning was forced at 13-15 days

lactation. Lactation experiments were performed after 14 days of lactation. For cell proliferation analysis with EdU (5-ethynyl-2-deoxyuridine) (Thermo Fisher Scientific), adult or pregnant mice were treated by i.p. injection with 0.1 mg of EdU (100 µl, 1 mg/ml in PBS) 2 hours before collection. Diphtheria toxin (Sigma) was injected at 2 ng/g i.p. (0.5 ng/µl in PBS) for CD11c-DTR and 20 ng/g (4 ng/µl in PBS) for CD11b-DTR. MØ depletion by anti-Csf1r was performed by i.p. injection of 400 µg AFS98 or Rat IgG2a isotype control (WEHI monoclonal antibody facility) at the indicated intervals. For imaging of native fluorescence, transcardiac perfusion was performed immediately following euthanasia using 20 ml of PBS with 10 mg/ml heparin and 5 mg/ml sodium nitrate to remove blood from tissues. The chest cavity was opened, the right ventricle cut, and perfusion buffer injected into the left ventricle using a 26-gauge needle. All mice were bred and maintained in the WEHI animal facility according to institutional guidelines. All experiments were approved by the WEHI Animal Ethics Committee.

2.1.3 Mouse genotyping

Mouse tail samples were digested at 55 °C overnight in DirectPCR Tail lysis buffer (Viagen) with 1 mg/mL Proteinase K, then kept at 85 °C for 1 h. Polymerase chain reactions (PCR) were performed with 1 µl DNA and 19 µl GoTaq Green (Promega) containing the appropriate primers (Table 2.1). PCR amplification products were analysed by gel electrophoresis performed in TAE buffer (40 mM Tris.Acetate pH 8.2, 1 mM EDTA) using 1.5% w/v agarose gels, 60 ng/ml SYBR Safe (Invitrogen) and imaged using ultraviolet light.

2.1.4 Surgical preparation for intravital microscopy

See detailed protocol in Chapter 3.

2.1.5 TEB dissection and sorting for single cell RNA-seq

3 x 5 week-old *Elf5-rtTA-GFP* mice were euthanised then skin was pinned out on an ice-cold board. TEBs and ducts were microdissected under a stereo fluorescence microscope (Leica) and collected in mammary epithelial cell (MEC) media (DMEM-F12 + glutamax (Gibco)

supplemented with 5% fetal calf serum (FCS), 250 ng/ml hydrocortisone (Sigma), 1% penicillin/streptomycin (Sigma) 5 μg/ml insulin (Roche) and 10 ng/ml EGF (Sigma)). The collected tissue was then digested into a single cell suspension and stained for flow cytometry (see 2.4.1 and 2.4.2). To sort total epithelial cells, $CD45^+$, $CD31^+$ and $TER119^+$ cells were excluded, then $CD24^+$ positive cells were collected. Cells were then processed for single cell RNA sequencing (RNA-seq) (see 2.6.2).

2.1.6 Implantation of hormone pellets

After mice were anaesthetised by injection of ketamine/xylazine and given carprofen, 21 day β-estradiol (0.05 mg) + progesterone (35 mg) slow release pellets or carrier compound placebos (HH-115 or C-111, Innovative Research of America) were implanted in the right 3rd mammary gland of mice at 8 weeks. For estrogen plus MPA experiments in bone marrow transplantation mice, estrogen (0.5 mg; in-house) and MPA pellets (15 mg; 21 day release; Innovative Research of America) were co-implanted subcutaneously, and mice were analysed after 3 weeks.

2.1.7 Bone marrow chimera generation

Following euthanasia, bone marrow was flushed from long bones and the pelvis, pooled from 2–3 UBC-$GFP^{Tg/+}$ mice and depleted of red blood cells by incubating with 0.64% NH_4Cl for 3 minutes at room temperature. Ten week-old C57Bl/6 mice were anaesthetised by injection of ketamine/xylazine and were given a single dose of 550 Rads gamma irradiation while shielding the abdomen with a lead shield (custom made). After 3–4 hours recovery, mice were given $2x10^6$ GFP^+ bone marrow cells in PBS by intravenous injection. Only the shielded 4th and 5th mammary glands were collected for analysis.

2.2 Human tissue samples

Fresh human breast tissue from reduction mammoplasties was obtained from consenting individuals through the Victorian Cancer Biobank with approval from the Human Research Ethics Committee of WEHI.

2.3 Microscopy

2.3.1 Wholemount immunostaining

Imaging was performed as previously described (Rios et al., 2019). At 4° C for all steps, tissue was collected and fixed for 1–2 hours in 4% paraformaldehyde (PFA, Sigma) pH 7.4, washed in 0.1% Tween20 (Sigma) in PBS for 30 minutes, then washed in 0.2% Tween20, 0.2% TritonX-100 (Sigma), 0.02% SDS (Sigma) and 0.2% BSA (Sigma) on PBS overnight. Tissue was incubated with primary antibodies (Table 2.3, anti-mouse unless otherwise specified) overnight in 0.1% TritonX-100, 0.02% SDS and 0.2% BSA, washed 3 x 2 hours in staining buffer, then incubated with secondary antibodies overnight before washing 3 x 2 hours and clearing with FUnGI (50% glycerol v/v, 2.5 M fructose, 2.5 M urea, 10.6 mM Tris Base, 1 mM EDTA) for 2 hours at room temp. or at 4°C overnight. During secondary staining, tissue was stained with DAPI (Thermo Fisher Scientific, 4 µg/ml) and/or F-actin was labelled with Phalloidin Alexa Fluor 488, 555 or 647 (Invitrogen, 1:25). For EdU labelling, tissue was incubated with Click-it Imaging 647 kit (Invitrogen) following secondary staining. Cleared tissue was dissected under a fluorescence stereo microscope (Leica), mounted on a glass slide and with slight compression.

2.3.2 Prepration of FUnGI clearing agent

FUnGI was prepared as previously described (Rios et al., 2019): 23.3 ml of Tris-EDTA pH8.0 (100 mM Tris Base (Sigma), 10 mM EDTA (Sigma)) and 110 mL glycerol (Ajax) were mixed, then 100 g fructose (Sigma) and 33.1 g urea (Sigma) were added. The mixture was crudely mixed, then dissolved by placing on an orbital shaker at 40 RPM at room temperature overnight.

2.3.3 Image acquisition

Samples were imaged on inverted Zeiss 780, Zeiss 880 or Leica SP8 confocal microscopes. Zeiss microscopes were equipped with 40x/1.40 Oil DIC or 63x/1.40 Oil DIC objectives and signal was collected by GaAsP array detector using spectral unmixing. Emission spectra were recorded using single stained controls. Airy scan images were captured using a 63x/1.40 Oil DIC objective and

default optimal airy scan settings. Leica SP8 was equipped with an HCX PL APO 40x/1.30 Oil objective and images were acquired using resonance scanning with 6x or 8x averaging.

2.3.4 Image analysis

Image processing and analysis was performed in Zen (Zeiss), LAS X (Leica) and Imaris (Bitplane) for 3D confocal images and FIJI/ImageJ (Schindelin et al., 2012) for other images. Analysis was performed on a Dell Precision T7610 with Dual Intel Xeon Processor E5-2687W v2, 256 GB RAM: (16x16 GB) 1866MHz DDR3 ECC RMIMM, 1 GB NVIDIA Quadro K600. For cell–duct distance quantification, a high-resolution surface was generated using K5 signal, then spots were generated for reporter-positive cells using semi-automated creation with a manually defined quality threshold or by manual spot placement (*Irf8-YFP*). Distances were calculated by creating an artificial channel with values equalling distance from the K5 surface using the Distance transformation XTension, then exporting average intensity of this channel within each spot object. DM density was measured in Imaris by manually placing spot objects on *Cx3cr1*-GFP^{hi} (virgin) or MHCII^{+} (lactation) DM cell bodies beneath the K5^{+} basal layer, using cyan/red (C/R) 3D anaglyph to assist spot placement in 3D. Distance between adjacent DMs was then calculated using the Spot to Spot closest distance module (from center-point). For intravital imaging, movies were manually stabilised, then low resolution (5-10 μm) surfaces of *Elf5*-GFP signal were created and used to mask DM specific MHCII signal. DM coverage of ducts in 3D intravital microscopy (IVM) movies was quantified in ImageJ by measuring the area of an MHCII signal in individual or cumulative time points and calculated as a percentage of *Elf5*-GFP signal area. Percentage DMs EdU^{+} was counted manually in Imaris by scanning optical sections to identify intra-epithelial MHCII^{+} cells and scoring EdU. EdU^{+} epithelial cells were used as a positive reference. Percentage volume of alveoli occupied by DMs was obtained by manually creating alveoli surfaces using the outer edge of the F-actin-high myoepithelium. This was used to mask alveolar MHCII signal, then an alveolar MHCII surface was created and volume occupied calculated as a percentage of total alveolar volume. The percentage of alveolar cells phagocytosed was measured by capturing images of 5 μm optical sections through ~50 alveoli per replicate from 3D images. Alveolar cell counting was assisted by F-actin staining of cell junctions. Alveolar

cells with complete co-staining with low intensity GFP and MHCII were considered phagocytosed. Average alveolar lumen area was measured in ImageJ by manually outlining lumen in four representative 40x regions per replicate. The number of cleaved caspase 3 (CC3)-positive cells and number of $CC3^+$ cells phagocytosed in involution was determined manually by scanning through optical sections. $CC3^+$ cells were considered phagocytosed when completely surrounded by MHCII signal in 3D. Number of $CC3^+$ cells per mm^2 was determined by taking a 20 μm optical section through alveoli, masking CC3 signal within alveoli in ImageJ using F-actin signal, then counting alveolar $CC3^+$ cells and dividing this by the area of the tissue.

TEB cap cell behaviours were quantified in Imaris after tracking each cell by manual spot creation using C/R three-dimensional visualisation. Each cell was associated with a unique Track ID and was individually observed over time and the timing of each behaviour from the beginning of the experiment (or entry into the field of view) was recorded. Tracking ended at the end of the experiment, when a cell moved out of the field of view or when signal became too weak to accurately record behaviour. The morphology of cap cells in the TEB body was quantified by visualisation in C/R three-dimensional mode. Migration speeds were calculated for individual cell tracks by calculating a separate running average for x, y and z coordinates over three time-points (30 minutes) to minimise the effects of tissue movement, then calculating the average speed for each cell for the entire tracking period (minimum 1 hour).

2.3.5 Two-photon image acquisition

Intravital imaging was performed using the FVMPE-RS tow-photon system (Olympus), equipped with MaiTai DeepSee and InSight DeepSee lasers (Spectra-Physics), 2 GaAsP and 2 Multialkali PTMs, SIM scanner and a 25x/1.05 NA water objective (Olympus). Three-dimensional image stacks were acquired with 1–2 μm z-step size every 3, 5 or 10 minutes for up to 12 hours. Site-specific laser damage was induced using the SIM scanner to deliver 800 nm MaiTai laser at 0.3W for 10 seconds in a 10 μm region or a single point while simultaneously imaging with the InSight laser. Laser power was kept below 0.1W for imaging. Green, red and far -red fluorescence was separated by 570 nm (FV30-SDM570) and 650 nm (FF650-Di01) dichroics and 607/70 (FF01-

607/70) and 697/75 (FF01-697/75) bandpass filters (Semrock). Blue/green fluorescence was collected by GaAsP dectector and red/far-red fluorescence by Multialkali photomultiplier tube. GFP and PI were excited at approximately 950 nm and Alexa fluor 647 at approximately 800 or 1200 nm. Imaging of Confetti fluorescence is described in Chapter 3.

2.4 Flow cytometry

2.4.1 Generation of single cell suspensions

Single cells from mammary glands (typically 2 x 3rd and 2 x 4th glands) and tumours were prepared as previously described (Shackleton et al., 2006) after removal of the inguinal lymph node. Tissue was minced using a tissue chopper (Mickle Laboratory Engineering) then digested for 1 hour at 37^{o}C on an orbital shaker (Ratek Laboratory Equipment) at 160 RPM for 1 h in 300 U/m collagenase (Sigma), 100 U/ml hyaluronidase (Sigma) and 100 U/m DNase (Worthington) in MEC media. Tissue was then treated with 0.25% trypsin/EGTA for 2 minutes before quenching with 10% FCS in PBS. No trypsinisation was performed for tumour experiments and for experiments where antibody fluorescence intensity was measured. Cells were passed through a 70 or 100 μm seive (BD-Falcon), followed by blocking and staining. For duct enrichment, whole glands were digested as above without chopping, then pipetted with a 25 ml serological pipette. Ducts were separated from fat by pulse centrifugation, then ducts were manually selected from a dish using a dissection microscope. Ducts were then further digested for 30 minutes and processed to single cells as above.

2.4.2 Antibody labelling and flow cytometry

Immunostaining was performed at 4^{o} C: cells were blocked with 0.1 mg/ml Rat IgG2a then primary antibodies (Table 2.2) were incubated for 30-45 minutes and secondary antibodies for 20 minutes. When biotin-conjugated antibodies were used, cells were labelled with a Streptavidin secondary stain (Table 2.2). Dead cells were identified by resuspending cells in 0.5 μg/ml propidium iodide before analysis or sorting. Flow cytometric analysis was performed on a Fortessa X20 flow cytometer using FACSDiva software (Becton Dickinson). Cells were sorted on

a FACSAria III or a FACSAria Fusion using FACSDiva software (Becton Dickinson). Subsequent analysis was performed using FlowJo (Tree Star). Fluorochrome overlap was compensated using anti-Rat coated beads labelled with the appropriate antibody (for non-rat antibodies, a rat antibody with matching fluorochrome was used) and blank beads.

2.5 Histological analysis

2.5.1 Wholemount carmine staining and analysis

Mammary glands were laid on a slide, fixed in Carnoy's solution (60% ethanol, 30% chloroform, 10% acetic acid), washed with 70% ethanol then stained with carmine stain (0.2% w/v carmine, 0.92% w/v aluminium potassium sulphate dodecahydrate, 0.01% w/v thymol in dH20), dehydrated through 70, 96 and 100% ethanol, then placed in Xylene (Sigma).

2.5.2 Immunohistochemistry

Tissues were fixed in 4% PFA at 4°C, embedded in paraffin and 5 μm sections were cut onto superfrost plus slides. Slides were de-waxed in xylene, re-hydrated, and heat treated (125°C for 30 seconds) in high pH antigen retrieval buffer (Dako). Endogenous peroxidase activity was quenched with 3% hydrogen peroxide in H_2O for 5 minutes. Sections were blocked in 5% goat serum (Merck) and washed in 0.05% Tween20/PBS then stained with primary antibody at 4°C overnight followed by secondary antibody staining. Staining was compared to staining of secondary antibody alone. The streptavidin–biotin peroxidase detection system was used with 3,3'-diaminobenzidine as substrate (DAKO). Slides were then counterstained with haematoxylin, cover slipped and imaged using Nikon Eclipse 50i microscope with Axiovision software (Zeiss). Antibodies: TMEM119 (rabbit, clone 28-3, Abcam), Goat anti-rabbit biotin (Vector Laboratories).

2.6 Molecular biology

2.6.1 Bulk RNA sequencing

Total RNA was extracted using the RNeasy RNA extraction kit (Qiagen) from frozen pellets of sorted macrophage and dendritic cell populations from the mammary glands of 9 week-old C57Bl/6 mice (2 pools of 12 mice), or from sorted macrophage populations isolated from 9 week virgin, pregnant, lactating and post-involution C57Bl/6 mice (individual mice).Total RNA from 400-500 cells (virgin) or 2000 cells (developmental time-course) was used to generate libraries for whole transcriptome analysis following the Clontech v4 low input RNA protocol. Libraries were sequenced on an Illumina NextSeq 500. Between 7 - 38 million 75 bp paired-end reads were generated for each sample. Reads were aligned to the mouse genome mm10 using Rsubread version 1.22.3 (Liao et al., 2013). The number of reads overlapping each Entrez gene were counted using featureCounts and Rsubread's built-in NCBI annotation (Liao et al., 2014). Gene information was downloaded from the NCBI (4 October 2016). Genes were retained for downstream analysis if they achieved at least 1 count per million (CPM) in at least 2 samples. Ribosomal genes, predicted genes, unassembled contigs and obsolete Entrez Gene IDs were removed from further analysis. Counts were converted to log2 counts per million (log2CPM) with prior count 2 using the edgeR cpm function and quantile normalized. Differential expression analysis was performed using the limma package version 3.30.8 (Ritchie et al., 2015) with robust trended empirical Bayes (Phipson et al., 2016). Genes were considered to be differentially expressed if they achieved a false discovery rate (FDR) below 5%. Positive (or negative) signature genes were defined for each population as all genes significantly up-regulated (or down-regulated) in that population vs all the other populations in pairwise comparisons. Canonical pathways were obtained from the Molecular Signatures Database v5.2 (Liberzon et al., 2011). Human genes were mapped to mouse orthologs using HGNC orthology predictions (http://bioinf.wehi.edu.au/software/MSigDB). Overlap analyses of pathways were conducted using hypergeometric tests. Gene set enrichment analysis of pathways was performed using limma's camera function with default settings (Wu and Smyth, 2012). Expression signature

analyses were performed using roast. The multidimensional scaling plot was drawn by limma's plotMDS function with leading log2-fold-change distances. Average Log2-RPKM was computed for each gene and each cell population using edgeR's rpkmByGroup function.

2.6.2 Single cell RNA sequencing

A 10X Genomics Chromium machine was used to capture ~5,000-10,000 single-cells and cDNA prepared according to the Single Cell 3′ Protocol recommended by the manufacturer. Cells were washed and prepared in an ideal concentration (1,000 cells/μl). The 10X machine partitions each cell into a nanoliter-scale Gel Bead-In-EMulsions (GEMs) and a common 10x Genomics Barcode is given to each generated cDNA but a pool of ~750,000 barcodes is used to uniquely index the transcriptome of each cell. The GEM reaction mixture was cleaned up using silane magnetic beads and Solid Phase Reversible Immobilization beads, then barcoded cDNA was amplified by PCR before library construction. The P7 and R2 primers were added during the GEM incubation and the P5 and R1 during library construction via end repair, A-tailing, adapter ligation and PCR. The final libraries contain the P5 and P7 primers used in Illumina bridge amplification. Sequencing was performed using an Illumina Nextseq 500.

The tSNE plots were generated using the Rtsne package. Ternary plots were generated using the vcd package with quantile normalized log2-CPM values. Log2-RPKM values were calculated using edgeR's rpkm function with a prior count of 5. Differential expression analyses used likelihood ratio tests with negative binomial dispersions estimated by the estimateDisp function (Chen et al., 2014; McCarthy et al., 2012). Enrichment for biological process Gene Ontology terms (Mi 2019) was generated using significantly differentially expressed genes with a log fold-change greater than 1.5.

2.7 Statistical analysis

Sample sizes were not predetermined by statistical analysis. Most experiments were performed on at least three biological replicates and most experiments were repeated at least twice, exact *n*, indicating biological replicates, is stated in associated figure legends. Experiments were not

randomised and investigators were not blinded during experiments or analysis of outcome. Error bars are only shown if data was obtained from three or more biological replicates. Error bars shown are mean ± standard error of the mean (s.e.m.) or mean ± one standard deviation (s.d.) as indicated in figure legends. Statistical tests with appropriate corrections are indicated in figure legends and were performed in Prism software (GraphPad). P values were determined by appropriate statistical tests indicated in figure legends. $P<0.05$ was considered significant.

Table 2.1: Genotyping oligonucleotides

Allele	Primer sequence (5' – 3')	Band size (base pairs)
CD11c-Cre	ACT TGG CAG CTG TCT CCA AG GCG AAC ATC TTC AGG TTC TG CAA ATG TTG CTT GTC TGG TG GTC AGT CGA GTG CAC AGT TT	Transgene: 313, 1000 Internal positive control: 200
CD11c-DTR	AAG TTC ATC TGC ACC ACC G TCC TTG AAG AAG ATG GTG CG CTA GGC CAC AGA ATT GAA AGA TCT GTA GGT GGA AAT CTC AGC ATC ATC C	Transgene: 173 Internal positive control: 324
Cx3cr1-GFP	GTC TTC ACG TTC GGT CTG GT CCC AGA CAC TCG TTG TCC TT CTC CCC CTG AAC CTG AAA C	Knock-in: 500 WT: 410
K5-rtTA-GFP	CGT GCT GGT TAT TGT GCT GT TAC AGG GTA GGC TGC TCA AC	650
Elf5-rtTA-GFP	TTG ATG AAA GCG CCT ACC TG GAG TTT CCT TGT CGT CAG GC	550
TetO-Cre	GCG GTC TGG CAG TAA AAA CTA TC GTG AAA CAG CAT TGC TGT CAC TT	100
TetO-Cre (Kai)	GCG GTC TGG CAG TAA AAA CTA TC GTG AAA CAG CAT TGC TGT CAC TT	450
Pr-Cre	TAT ACC GAT CTC CCT GGA CG ATG TTT AGC TGG CCC AAA TG CCC AAA GAG ACA CCA GGA AG	Transgene: 522 Wild type: 302

Confetti	KI: GAA TTA ATT CCG GTA TAA CTT CG KI: CCA GAT GAC TAC CTA TCC TC WT: CTC CTG GCT TCT GAG GAC C WT: CCA GAT GAC TAC CTA TCC TC	Knock-in: 290
MMTV-PyMT	CTC TAG AGG ATC TTT GTG AAG G GGA CAA ACC ACA ACT AGA ATG	600
MMTV-Wnt1	CTC TAG AGG ATC TTT GTG AAG G GGA CAA ACC ACA ACT AGA ATG	800
MMTV-Neu	CTC TAG AGG ATC TTT GTG AAG G GGA CAA ACC ACA ACT AGA ATG	800
Hes1-d2EGP	ATG GTG AGC AAG GGC GAG GA GTA AAC GGC CAC AAG TTC AG TCG TTG GGG TCT TTG CTC AG TCG TCC ATG CCG AGA GTG AT	Transgene: 640

Table 2.2: Flow cytometry antibodies

Target	Species	Clone	Conjugation	Dilution	Supplier
MHCII	Rat	M5/114	Brilliant Violet 711	1/2000	Biolegend
MHCII	Rat	M5/114	Brilliant Violet 421	1/500	Biolegend
Ly6G	Rat	1A8	Brilliant Violet 510	1/50	Becton Dickinson
Ly6C	Rat	HK1.4	PE-Cy7	1/2000	Biolegend
Gr-1	Rat	RB6-8C5	PE-Cy7	1/2000	Life Technologies
CD45	Rat	30-F11	Brilliant Violet 605	1/200	Biolegend
CD64	Rat	X54-5/7.1	Brilliant Violet 421	1/200	Biolegend
CD64	Rat	X54-5/7.1	Brilliant Violet 711	1/200	Biolegend
CD11b	Rat	M1/70	Brilliant Violet 785	1/4000	Biolegend
CD24	Rat	M1/69	PE	1/600	Biolegend
CD24	Rat	M1/69	PerCP-Cy5	1/600	Biolegend
CD24	Rat	M1/69	FITC	1/600	Biolegend
CD11c	Hamster	N418	Alexa Fluor 647	1/200	Biolegend
CD11c	Hamster	N418	Biotin	1/200	Biolegend
CD11c	Hamster	N418	PE	1/200	Biolegend
CD103	Rat	2E7	APC	1/200	Biolegend
CD103	Rat	M290	PE	1/200	Becton Dickinson
B220	Rat	RA3-6B2	APC-Cy7	1/200	Biolegend
F4/80	Rat	BM8	APC-Cy7	1/400	Biolegend
MerTK	Rat	DS5MMER	PE	1/200	eBioscience

Lyve1	Rat	ALY7	FITC	1/50	Invitrogen
CD206	Rat	C068C2	FITC	1/50	Biolegend
Streptavidin	NA	NA	Brilliant Violet 650	1/500	BD Horizon
CD29	Hamster	HMβ1-1	FITC	1/300	Biolegend
CD31	Rat	MEC 13.3	APC	1/40	Biolegend
TER119	Rat	Ter-119	APC	1/80	Biolegend
CD45	Rat	30-F11	APC	1/200	Biolegend

Table 2.3: Immunofluorescence antibodies

Target	Species	Clone	Conjugation	Dilution	Supplier
K8/18	Rat	Polyclonal	NA	1/200	DSHB
K14	Rabbit	Polyclonal	NA	1/400	Biolegend
K5	Rabbit	Polyclonal	NA	1/400	Biolegend
GFP	Chicken	Polyclonal	NA	1/200	Abcam
E-cadherin	Rat	ECCD-2	NA	1/400	Invitrogen
MHCII	Rat	M5/114	NA	10 µg/mL	In house
MHCII	Rat	M5/114	Alexa Fluor 647	1/50	Biolegend
MHCII	Mouse anti-human	L243	NA	1/200	Biolegend
CD11b	Rat	M1/70	NA	1/50	Biolegend
Cleaved caspase 3	Rabbit	5A1E	NA	1/200	Cell Signaling
Anti-rabbit	Donkey		Alexa Fluor 488/555	1/500	Invitrogen
Anti-chicken	Goat		Alexa Fluor 488	1/500	Invitrogen
Anti-rat	Goat		Alexa Fluor 488/555/647	1/500	Invitrogen
anti-mouse IgG2a	Donkey		Alexa Fluor 488/555/647	1/500	Invitrogen

Chapter 3: High-resolution intravital imaging of the mouse mammary gland

3.1 Introduction

Two-photon *in vivo* imaging, or intravital microscopy (IVM), allows cell dynamics to be observed in minimally perturbed tissue. IVM has been applied to studies in immune function (Germain et al., 2012), neuroscience (Zhang et al., 2010), stem cell biology (Ritsma et al., 2014) and cancer (Scheele et al., 2016), providing profound insights into *in vivo* dynamics. Two-photon microscopy causes minimal tissue laser damage by using an excitation laser that is twice the wavelength (half the energy) of single photon technologies such as confocal microscopy. Excitation of fluorescence at a single point is achieved by splitting laser line and converging this at a focal point where the combined energy of two photons can excite fluorescence. As the frequency of two photons interacting is very low, lasers are pulsed at femtosecond scale so that more photons reach the convergence point at the same time. This decreases the total laser power needed to achieve two-photon excitation and so minimises tissue damage. There are also the added benefits of second harmonic generation (SHG) from collagen that provides structural context, better tissue penetration by long wavelength lasers and high efficiency of light collection as no pinhole is needed (Condeelis and Segall, 2003).

Broadly, two approaches have been implemented for IVM of abdominal organs: 1) a terminal procedure involving extensive surgery to expose the tissue of interest, followed by an extended imaging period before euthanasia (Bayarmagnai et al., 2018; Ewald et al., 2011; Kotsuma et al., 2012; Masedunskas et al., 2017; Miller et al., 2003) and 2) non-terminal surgery to insert an imaging window that enables numerous imaging sessions over weeks to months (Ahmed et al., 2002; Kedrin et al., 2008; Shan et al., 2003; Sobolik et al., 2016). IVM has been extensively applied to breast tumours (Condeelis and Segall, 2003; Ellenbroek and van Rheenen, 2014) but rarely to the normal mammary gland. Imaging of the normal gland has focused on lipid droplet

formation in lactation (Masedunskas et al., 2017), MØ motility and association with collagen during puberty (Ingman et al., 2006), and analysis of epithelial migration in TEBs and ducts over time using a mammary window (Scheele et al., 2017).

This Chapter provides a detailed protocol for an adapted and optimised skin-flap approach that allows subcellular resolution of entire duct and alveolar structures in the normal gland. Procedures described include surgical preparation of the skin flap, uncovering mammary ducts by microdissection and image analysis pipelines to generate and fully exploit high-dimensional data. Combination of this technique with multi-coloured fluorescence lineage tracing and antibody labelling allowed observation of single cell behaviour within TEBs and ducts for up to 12 hours. The potential of this technique was demonstrated by characterising epithelial cell–MØ interactions and mammary epithelial cell behaviour, which are described and discussed in more detail in the following chapters.

3.2 Experimental design

3.2.1 Optimising the skin flap for the virgin mammary gland

The mammary imaging window (MIW) (Kedrin et al., 2008; Shan et al., 2003) has enabled high-resolution and long-term IVM of mammary tumours. The only application of this technique to the normal mammary gland allowed observation of cell migration in TEBs and ducts (Scheele et al., 2017). The paucity of virgin mammary duct IVM using the MIW is likely due to the inaccessibility of ducts within the fat pad and impeded tissue access through the window. Mammary tumours and lactating glands displace the mammary adipose stroma, facilitating *in vivo* imaging at high resolution (Ellenbroek and van Rheenen, 2014; Masedunskas et al., 2017) whereas ducts in the adult gland are embedded deep within light-scattering adipose tissue. The skin flap technique does not allow multiple imaging sessions but provides greater tissue access and increased ability to finely manipulate the imaging region (Ewald et al., 2011). Opening of the skin flap primarily involves a midline incision of the skin, which does not cause bleeding or systemic inflammation (Ewald et al., 2011). Previous studies adopting the skin flap method for

the mammary gland used inverted microscopes (Ewald et al., 2011; Masedunskas et al., 2017), requiring the mammary gland to be placed face down on a cover slip with the overlying skin glued to a glass slide. To use the skin flap method while maintaining access to the mammary gland, a method previously employed for imaging the inguinal lymph node (Hor et al., 2015; Miller et al., 2003) was modified. This involved securing the skin flap to a raised square platform skin-side down, placing a cover slip on top of the mammary gland and imaging with an upright microscope. Unfortunately, cauterisation of the 5th mammary gland is necessary for securing the skin flap and fully exposing the inguinal gland. This was performed as far from the inguinal gland as possible and afterwards the tissue was washed thoroughly with PBS. By using mouse models with epithelial fluorescence, the entire inguinal mammary gland could be viewed under a fluorescence stereo microscope for identification of accessible ducts or TEBs prior to transfer to the microscope. Furthermore, direct access to the fully exposed gland enabled removal of poorly vascularized connective tissue from above the region of interest without causing bleeding. This mammary gland-optimised skin flap method enabled high-resolution, stable imaging of virgin ducts and TEBs as well as lactating alveoli for up to 12 hours, after which the stability of mouse anaesthesia was variable and changes in cell behaviour were seen.

3.2.2 Maintaining stable, physiological conditions

To avoid rapid drying out of the exposed skin and abdomen constant replenishing of PBS was required. This was overcome by applying a ring of vacuum grease around the mammary gland, filling this with PBS and placing a cover slip on top, creating a sealed imaging well. Drying out of the abdomen was prevented by laying plastic cling wrap on all exposed areas except for the imaging well. With humidification of the imaging chamber, almost no evaporation occurred, and only occasional application of PBS was required. After many hours of imaging, PBS loss from the imaging well could cause the cover slip to compress the tissue but was a rare occurrence. This potential issue was solved by inserting a needle through the silicone grease ring beneath the coverslip and injecting a small amount of PBS into the well when required. Tissue compression drastically affects cell behaviour (data not shown) and must be strictly avoided. A key and unforeseen advantage of the isolated imaging well is that reagents such as propidium iodide (PI)

or fluorescently conjugated antibodies can be directly added to the media without being lost by media replacement or concentration by evaporation.

As the cover slip is only secured by vacuum grease, there is a high risk of interference by breathing movement that can hinder high-quality image acquisition. The amount of movement varied greatly between experiments, depending on the surgery and the position of the area to be imaged (near or far from the abdomen). Movement was usually lateral, which is difficult to correct post-acquisition. This was minimised by securing the skin flap as far as possible from the abdomen, removing connective tissue from between the skin flap and the torso and placing a brace against the torso (typically a plastic transfer pipette taped to the stage).

3.2.3 Imaging parameters

It is difficult to eliminate lateral breathing movement entirely, but the effects of minor movement can be minimised by resonance scanning and frame averaging (4–8x averaging was typically used, depending on the laser power). Short and rhythmic breathing movement usually affects only one frame and is largely removed by averaging. Resonance scanning has the added benefit of reducing pixel dwell time and thus phototoxicity. To further minimise phototoxicity, laser power was kept below 0.1W and the gain adjusted to optimise the signal to noise ratio. A significant challenge of imaging the mammary gland is the softness of the tissue, which often causes slow and constant drift during imaging. This required frequent manual repositioning of the field of view (every 10–30 minutes, variable per experiment). Olympus FluoView software was useful in this case, requiring only a double click on a central landmark to automatically re-center the field of view without the need to stop and restart acquisition, which can result in many separate files that must be later concatenated. The chosen landmark was also registered at the zero z-position so that z-drift could be easily corrected. Despite these measures, post-acquisition drift correction was essential.

Dual Mai Tai/Insight lasers and a SIM scanner on the Olympus FVMP-RS multiphoton system enabled simultaneous imaging and photoablation. This involves a second set of galvo scanners for the short wavelength laser that can be easily targeted to a single point or a custom region to

deliver defined laser pulses for photoconversion or photoablation. The laser power required varied depending on the depth of the region of interest and the size of the area being targeted. For each experiment, incremental increases in laser power and dwell time were tested at distal sites to determine the parameters for the region of interest.

3.2.4 6-colour imaging with Confetti

Multi-colour fluorescence reporter mice are valuable tools for lineage tracing (Rios et al., 2014) and IVM (Ritsma et al., 2014) because high-density labelling can be induced while maintaining the ability to distinguish single cell morphology and behaviour. The *Confetti* allele contains the *CFP*, *GFP*, *YFP* and *RFP* genes each flanked by loxP sites and preceded by a floxed stop codon (Snippert et al., 2010). Transiently expressed Cre recombines the allele such that the stop codon is removed and a single random fluorescent protein is placed downstream of the promoter. This fluorescent protein is then stably expressed and in all daughter cells.

Collection of standard green, red and far-red fluorescence in combination with SHG is widely performed and required only standard filters. Conversely, collection of distinct CFP, GFP, YFP and RFP fluorescence in *Confetti* mice in combination with SHG and a far-red dye does not appear to have been reported thus far and required extensive filter optimisation. 5-colour two-photon imaging of *Confetti* mice with SHG has been achieved by collecting pairwise overlapping signals that can be subsequently deconvolved (Ritsma et al., 2014). In an alternative approach, 6-colour two-photon imaging in a non-*Confetti* system has been performed through collecting fluorescence across the spectrum and unmixing these post-acquisition (Ricard and Debarbieux, 2014). 6-colour two-photon imaging was achieved here through careful design of filters and excitation wavelengths to collect individual fluorescence signals with minimal overlap (Figure 3.1). Two-photon excitation is non-linear and the excitation spectra are broad, with the maxima often significantly shifted from double that of single photon excitation (Diaspro et al., 2005). Testing of excitation spectra identified specific wavelengths that excited distinct proteins or dyes, allowing collection of multiple distinct signals in the same detector with alternating lasers. Specifically, it was found that GFP, YFP and RFP could be uniquely excited at 970 nm and CFP and multiple far-red dyes uniquely at 830 nm (Figure 3.1a). Therefore, single broad filters could

be used to separately capture CFP and GFP (463–513 nm filter), as well as RFP and far-red dyes (560+ nm filter). A strength of this approach was its ability to collect the relatively dim CFP fluorescence across a wide range, which is normally prevented by overpoweringly bright GFP fluorescence. As SHG fluoresces at half the excitation wavelength, the 970 nm laser used to excite GFP also stimulated SHG in the GFP channel. This was overcome by collecting SHG signal from the 830 nm laser (397–447 nm filter) that could be subtracted from the GFP channel post-acquisition. Collection of GFP, YFP (524–554 nm filter) and RFP were optimised to achieve comparable brightness for each with minimal bleed-through. The utility of this approach was demonstrated by imaging a TEB with Confetti-labelled cap cells and fluorescently conjugated CD45 antibody to observe mammary progenitor cell–stromal interactions (Figure 3.1b).

3.2.5 Visualisation and analysis

Significant challenges were met in the post-acquisition stage, due to the complex four-dimensional (4D: 3D plus time) multi-colour datasets generated. Even small amounts of drift, breathing movement and noise made automated object tracking inaccurate, so manual tracking was preferred. Cells in confetti-labelled TEBs and ducts proved difficult to track and analyse, as position in 3D space is crucial for interpreting epithelial cell behaviour. In densely labelled areas and when migration occurred, cells often passed in front of or behind other cells, impeding tracking. Rotation can aid 3D visualisation but is not ideal for viewing time-lapse data. To overcome this, the cyan/red (C/R) 3D mode in Imaris was used to easily interpret 3D localisation during time-lapse movies for cell tracking and quantification (Figure 3.2). While VR has been applied to similar problems, it is expensive, physically cumbersome and does not yet have advanced cell tracking capability. Polarising 3D was a possible alternative but C/R 3D has the advantage of being cheap and universally compatible. Combination of the C/R 3D and InMotion modes within Imaris during manual channel-specific spot creation enabled accurate 3D placement of objects, even when cell passed over each other. The resulting cell tracks have unique IDs that can be associated with observed behaviours, fluorescence intensities or cellular interactions to generate high-dimensional data that is valuable for dissecting complex cell dynamics (See Chapter 4).

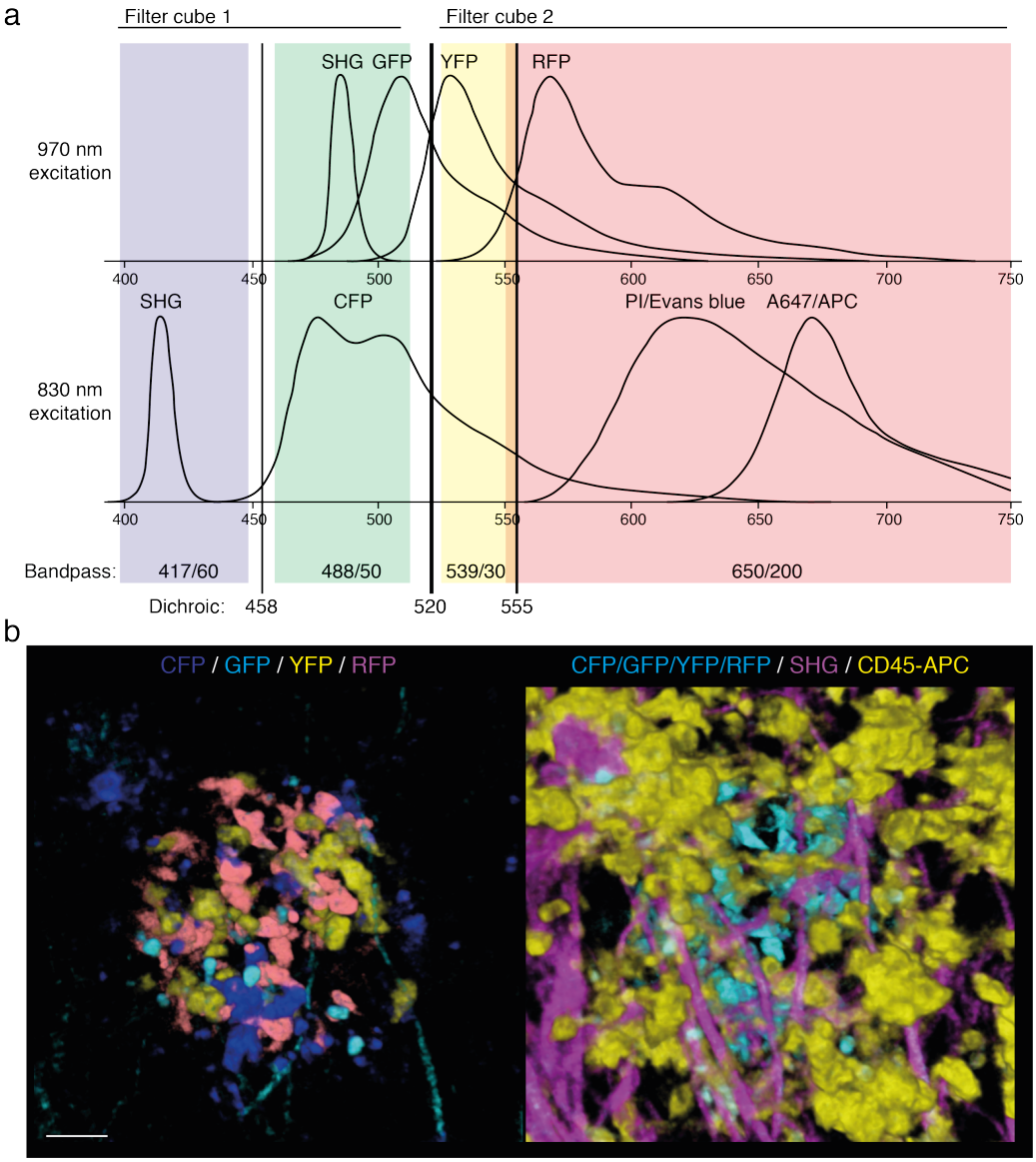

Figure 3.1: 6-channel intravital imaging of fluorescent reporters with antibody labelling

(a) Diagram of emission spectra and filter design for confetti fluorescence separation and simultaneous collection of SHG and far-red fluorescence. A 970 nm laser excites only GFP, YFP and RFP. An 830 nm laser excites CFP and far-red dyes. All numbers are wavelengths (nm) and bandpass filters are notated as centre/width.

(b) 6-colour IVM of a CD45-APC antibody labelled TEB in a 5 week-old *K5/TetCre/Confetti* mouse treated with doxycycline for 3 days at 4 weeks of age. A Gaussian filter was applied, then channel overlap was corrected in Imaris using 'Channel arithmetic'. Scale bar, 30 μm.

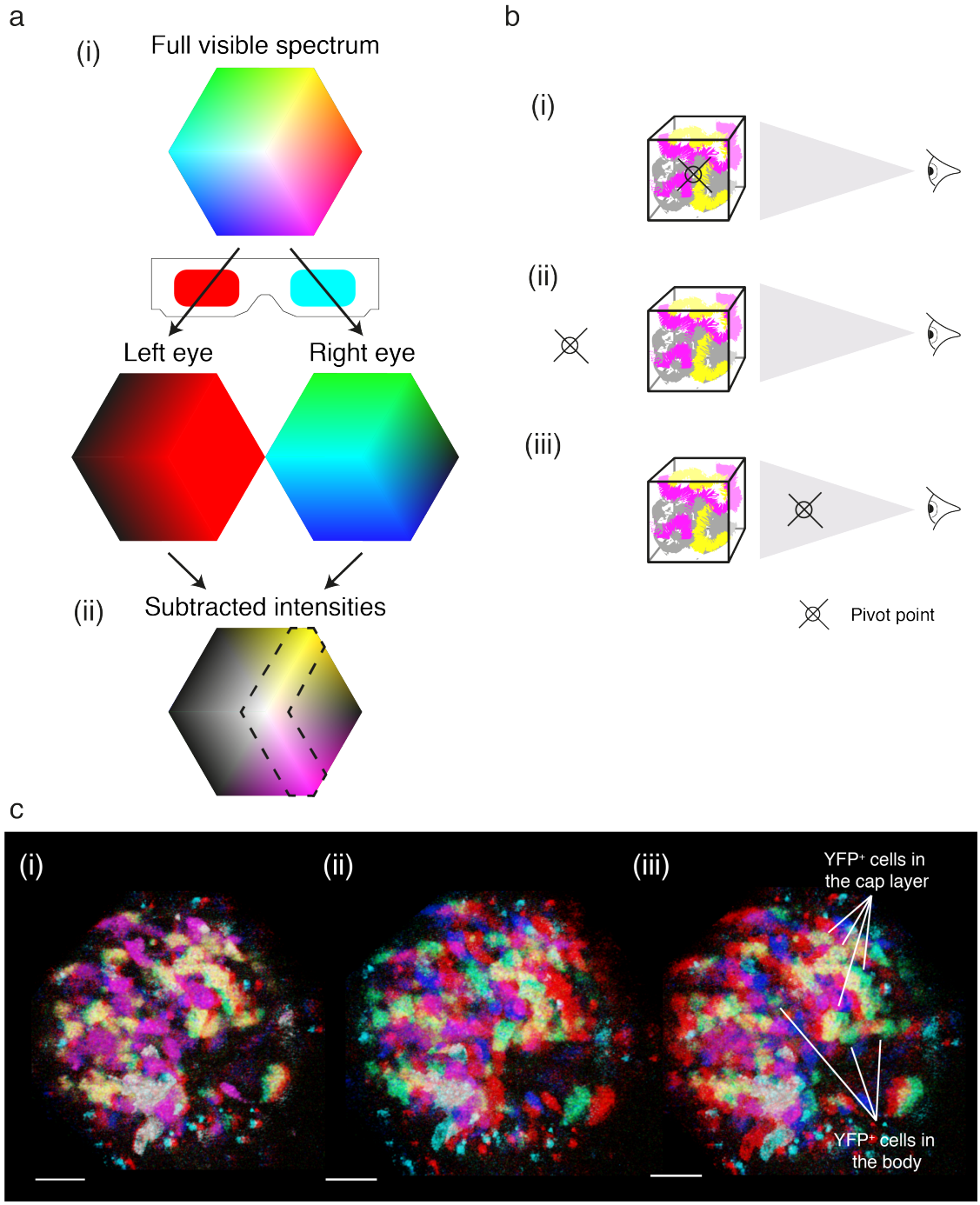
a
(i)
Full visible spectrum
Left eye
Right eye
(ii)
Subtracted intensities
b
(i)
(ii)
(iii)
Pivot point
c
(i)
(ii)
(iii)
YFP+ cells in the cap layer
YFP+ cells in the body

Figure 3.2: Stereo 3D visualisation of microscopy data using cyan/red glasses

(a) Colour consideration for 3D visualisation with C/R 3D glasses. (i) C/R glasses split the visible spectrum into red and green/blue to enable stereo vision. (ii) Objects need to be seen by both eyes to give depth perception and minimise luster effect. Subtracting colours that are only seen by one eye shows that yellow, grey and magenta (and intermediates) are ideal for C/R 3D visualisation.

(b) Depth-perception in 3D visualisation. (i) Pivot point is in the centre of the image volume. The image will appear in front of and behind the page. This is ideal for comfortable viewing and analysis. (ii) Pivot point is behind the image. The entire image volume will jump out of the page at a distance increasing with pivot point depth. This creates visual impact and an immersive experience for presentation but can be tiring and takes time to become accustomed to, so is not ideal for analysis. (iii) Pivot point is in front of the image. The entire image volume will be behind the page at a distance increasing with pivot point displacement. This is a useful visual effect for maximising depth perception and allowing annotations to be comfortably seen 'above' the image.

(c) 3D visualisations of a *K5/TetCre/Confetti* TEB corresponding to **b** (i)–(iii). RFP: magenta, YFP: yellow, CFP: grey. (i) With a central pivot point, the TEB volume extends in front of and behind the page. (ii) With the pivot point behind the image volume, the TEB volume sits entirely out of the page. (iii) With the pivot point in front of the image volume, the TEB volume sits entirely behind the page. Annotations appear above the image and can be viewed easily without affecting the stereo 3D effect. This experiment is further analysed in Chapter 4. Scale bars, 30 μm.

3.3 Materials

Table 3.1: Reagents for intravital microscopy

Reagent	Supplier
DPBS	Sigma, D8662-500ML
Hair removal cream	Veet
MHCII-Alexa Fluor 647 antibody	Biolegend, clone M5/114
CD45-APC antibody	Biolegend, clone 30-F11
Propidium iodide	Sigma, P4864
Silicone grease	Dow Corning, DC976VF
Isoflurane	Pharmachem
Medical oxygen	Mediquip
Saline (154 mM NaCl)	NaCl: Ajax, 465-5KG
Rat anti-K8/18	DSHB
Chicken anti-GFP antibody	Abcam
Rabbit anti-RFP antibody	Rockland
DAPI	Thermo Fisher Scientific

Table 3.2: Equipment for intravital microscopy

Equipment	Supplier
FVMPE-RS two-photon	Olympus
Mai Tai HPDS-OL 690-1040nm	Spectra-Physics
Insight X3-OL 680-1300nm	Spectra-Physics
25x 1.05 NA objective	Olympus, NAFV30-AC25W
Fluorescence stereo microscope	Olympus, SZX16
Custom dichroic filters	Semrock: FF458-Di02, FF520-Di02, FF555-Di03

Custom bandpass/longpass filters	Semrock: FF01-417/60, FF01-488/50, FF01-539/30, FF01-650/200
Redflex Heat Pad	Pet Network
Thermostatic heat pad	FHC, 40-90-8D, 40-90-5D-02 and 40-90-2
Shaver	Wahl
Evo forceps	FTS, 11800-00
Spring scissors 2mm	FST. 15000-03
Spring scissors	ProSciTech, T106
Dissecting scissors	ProSciTech, T1076
Iris scissors	ProSciTech, TS0984
Graefe iris forceps	ProSciTech, T131
Durapore tape	3M, 1538-1
Tissue adhesive	Braun, 1050044
Catheter tubing	Daniels, 1-10338
50 mL Falcon tubes	Fisher Scientific, 14-432-22
20 mL syringe	Terumo, SS+20ES
26-gauge needle	Becton Dickinson, 302002
Plastic transfer pipettes	ThermoFisher Scientific
Isoflurane vapouriser	Mediquip, 98723N
Cauteriser	Antex, RB15
Lacri-Lube eye ointment	Refresh
Lubricant	K-Y
Hydrophobic pen	Dako
Imaging stage (Stainless steel and Perspex)	Custom made
Plastic cling wrap	Beyond red
Square cover slip	ProSciTech, G422
Cyan/red 3D glasses	Oz3D Optics, SKU 629

3.3.1 Reagent setup

Warm up PBS, saline and objective water to 37°C.

Prepare any solutions for the imaging well (eg. PBS with PI or antibody).

3.3.2 Equipment setup

Imaging stage: To a 1 mm thick stainless steel sheet 15 cm long and 10 cm across, glue a 0.5 cm high, 4cm x 4 cm Perspex square in the middle lengthwise and 5 cm from the left edge.

Surgical station: Turn on heat pad, heat lamp and microscope chamber heater (set to 35°C) and allow time for these to warm up. The heat lamp should be approximately 80 cm above the workspace and at a 45° angle.

Anaesthesia: Ensure sufficient isoflurane in the vapouriser for the duration of the experiment.

Surgical kit: Clean surgery area and arrange sterile tools.

Microscope: Turn on laser emission.

3.4 Procedure

3.4.1 Surgery preparation

1. Anaesthetise the mouse in an induction chamber using 3% (4–7 week-old mice) or 4% (adult) (vol/vol) isoflurane in medical oxygen.
2. Once unconscious, transfer the mouse to the heat pad and position a face mask delivering 2% (vol/vol) isoflurane. Slowly decrease isoflurane to 1.5% (vol/vol) throughout surgery and adjust to ensure the mouse continues to breathe steadily. Additional information and guidance on anaesthesia can be found elsewhere (Bayarmagnai et al., 2018; Ewald et al., 2011a; Kotsuma et al., 2012; Masedunskas et al., 2017; Miller et al., 2003).

   CAUTION: The heat lamp should not be pointed directly at the mouse before thermal probe insertion due to risk of overheating.

   CRITICAL STEP: Continuously monitor mouse reflexes to ensure sufficient depth of anaesthesia.

   CAUTION: Position the mouse on the heat pad so that it will eventually be accessible to the dissection microscope.

   TROUBLESHOOTING: See Table 3.3.
3. Moisten eyes with eye ointment.
4. A tail vain injection or catheterisation can be performed at this point if blood vessel labelling is desired.
5. With the mouse laid on its back, shave from above the urethra up to the sternum. Shave the right hind leg and right flank from the tail to the foreleg and around to near the dorsal midline (Figure 3.3).

   CAUTION: Be careful not cut the skin that will form the skin flap. Any incision will result in fluid leakage and tissue dehydration during imaging.

6. Apply hair removal cream to the shaved area and leave for 2 minutes before removing cream and hair.

   CRITICAL STEP: Hair is autofluorescent and stray hairs are difficult to remove following surgery. Remove all hair from the surgery area and tools.

3.4.2 Exposure of the inguinal mammary gland

7. Place the imaging stage underneath the mouse with the raised square immediately to the left of the abdomen.
8. Apply lubricant to the thermal probe and insert into the rectum. Continuously adjust the position of the heat lamp to maintain a temperature of 36–37° C during surgery (Figure 3.3a).

   CRITICAL STEP: Keep the mouse temperature constant. Hypo- or hyperthermia will affect mouse health and anaesthesia depth.

   CAUTION: Secure the rectal probe cord to the tail and the imaging stage to prevent twisting during surgery. This also helps to keep the mouse stable during surgery.
9. Make a skin incision between the 4th and 5th nipples and cut at a 45° angle to the midline then up the midline to the sternum, making sure to avoid cutting the peritoneum or any large blood vessels (Figure 3.3b).

   CRITICAL STEP: Keep tissue hydrated at all times by applying warm PBS with a plastic pipette. Occasionally replace with fresh PBS.
10. From the base of the incision, carefully cut the skin along the right hind leg to halfway between the knee and ankle.

    CAUTION: To avoid cutting the 5th mammary gland and associated blood vessels, use pointed scissors and slide one point between the skin and fat before cutting.
11. Use forceps to gradually lift the edges of the resulting skin flap and cut the connective tissue between the skin and peritoneum. Only separate 0.5 cm of skin at this point and ensure the 5th mammary gland is uncovered.
12. Hold the bottom corner of the skin flap with forceps and lift while sliding pointed scissors under the 5th mammary gland and the associated artery (Figure 3.3c).

    CAUTION: Be careful not to damage the hind leg arteries in these steps.
13. Use the scissors to lift the gland away from the leg and cauterise the 5th mammary gland and the associated artery.

    CRITICAL STEP: Cauterisation should be done as quickly and cleanly as possible to minimise inflammation. Wash the area a few times with PBS afterwards.

    CRITICAL STEP: Cauterise through the center of the 5th mammary gland away from the inguinal mammary gland to prevent any damage near the imaging area.
14. Extend the incision around the hind leg to 1 cm from the base of the tail, ensuring that the inguinal mammary gland is at least 0.5 cm from the edge of the skin flap on all sides (Figure 3.3d).

    CAUTION: Avoid damage to muscle tissue and blood vessels close to the skin on the dorsal side of the leg.
15. Gently pull the skin flap away the abdomen while cutting connective tissue. Separate only enough to enable laying of the skin flap on the raised square.
16. Use tissue adhesive to secure the central edge of the skin flap to the far edge of the raised square (Figure 3.3e), then secure the corners of the skin flap to create a 3 cm by 3 cm flat area with the inguinal mammary gland at the center (Figure 3.3f).


a
b
c
d
e
f
g
h
i
j

Figure 3.3: The skin flap surgery

(a) The anaesthetised mouse is positioned on the imaging stage after shaving, hair removal and rectal probe insertion. Scissors indicate initial incision site and dotted line indicates where the skin should be cut.

(b) An incision is made along the midline and down the leg.

(c) Scissors are inserted under the 5th mammary gland and this is cauterised this along with the associated artery.

(d) The skin flap is lifted while cutting connective tissue.

(e) When enough connective tissue has been removed, the central edge of the skin flap is secured to the raised platform.

(f) The corners of the skin flap are secured to the raised platform.

(g) Plastic cling wrap is placed over the abdomen and a transfer pipette is positioned to prevent interference by breathing movement (arrow).

(h) A ring of vacuum grease is made around the area to be imaged (arrow) and the well filled with PBS.

(i) A cover slip with the edges outlined with hydrophobic pen is placed over the well and gently pressed to seal the well.

(j) Completed surgery with i.p. catheter inserted for saline injection.

CRITICAL STEP: Secure the skin flap as far away from the abdomen as possible. This will minimise breathing movements that hinder imaging and will make TEBs more accessible if imaging in puberty.

CRITICAL STEP: PBS running off the skin flap onto the platform will result in tissue dehydration. To avoid this, ensure that the skin is dry before gluing and leave a 1–2 mm margin of skin unsecured. This margin will curl back and form a barrier to contain PBS.

17. Secure additional points around the skin flap so that it is completely flat and breathing movement is minimised.
18. Position a 50 ml Falcon tube lid to the left of the tail and tape the right hind paw to this to pull the hind leg away from the imaging area (Figure 3.3g).
19. Remove as much connective tissue from between the skin flap and abdomen/leg as possible to minimise interference by breathing movements, particularly directly surrounding the inguinal mammary gland and the torso.
20. Place a small sheet of cling wrap on the abdomen, extending 0.5 cm onto the skin flap.

    CAUTION: Fold in the edges of the cling wrap so that it does not cause PBS to run off the skin flap, as this will lead to tissue dehydration.

21. Take a plastic transfer pipette with the bulb removed and tape the ends to the platform either side of the skin flap so that the abdomen is held away from the mammary gland and interference by breathing movement is minimised (Figure 3.3g).

3.4.3 Selecting and preparing the imaging region

22. Move the heat pad and imaging platform under the fluorescence dissection microscope.

    CAUTION: A dark environment is necessary for dissection by fluorescence. Turn off or dim room lights and position the heat lamp so that the mouse is warmed without illuminating the mammary gland.

    CAUTION: Continuously check that the skin flap is hydrated during dissection and top up PBS if needed.

23. Use white light or green autofluorescence and microdissection tools to pick up and remove a small area (0.5 cm) of the connective tissue that covers the surface of the mammary gland (Figure 3.4a-b).

24. Use fluorescence to identify epithelial structures that are at the surface of the fat pad. Remove connective tissue from a wider area if no structures are apparent.

    CRITICAL STEP: In virgin mice, it is common that no ducts are visible after removal of connective tissue. Folds of fat can be carefully separated by cutting the connective tissue between them, which often reveals underlying ducts (Figure 3.4b).

    CAUTION: Avoid cutting adipose tissue to gain access to mammary ducts as this causes bleeding. If there are no structures at the surface of the fat pad, the experiment may have to be abandoned and the mouse euthanised.

    CAUTION: Do not use UV light for microdissection as this will damage the tissue.

25. Carefully remove any remaining connective tissue overlying the imaging region without damaging the tissue (Figure 3.4c). Multiple areas may be prepared for simultaneous imaging or for selection of the area that provides the best image quality under the two-photon.

26. Move the mouse back to the surgery site and remove PBS from the skin flap.

27. Quickly, before the tissue dries, create a square or ring of silicone grease around the mammary gland approximately 2 cm by 2 cm using a 20 ml syringe (Figure 3.3h).

    CAUTION: Apply silicone grease directly to the skin flap and not the plastic film, otherwise the imaging area will not be sealed and fluid will be drawn out. Leave 1 mm between the ring and the skin flap edge to prevent PBS runoff.

28. Fill the reservoir with PBS. An antibody or dye can be added to PBS before application if desired.

    CAUTION: If the ring does not hold the PBS, remove the PBS and vacuum grease and reapply.

29. Take a small square cover slip and draw around the edge using a hydrophobic pen. Place this on top of the ring (hydrophobic edge face up) and push down gently to form a complete seal with the silicone grease without compressing the mammary gland (Figure 3.3i).

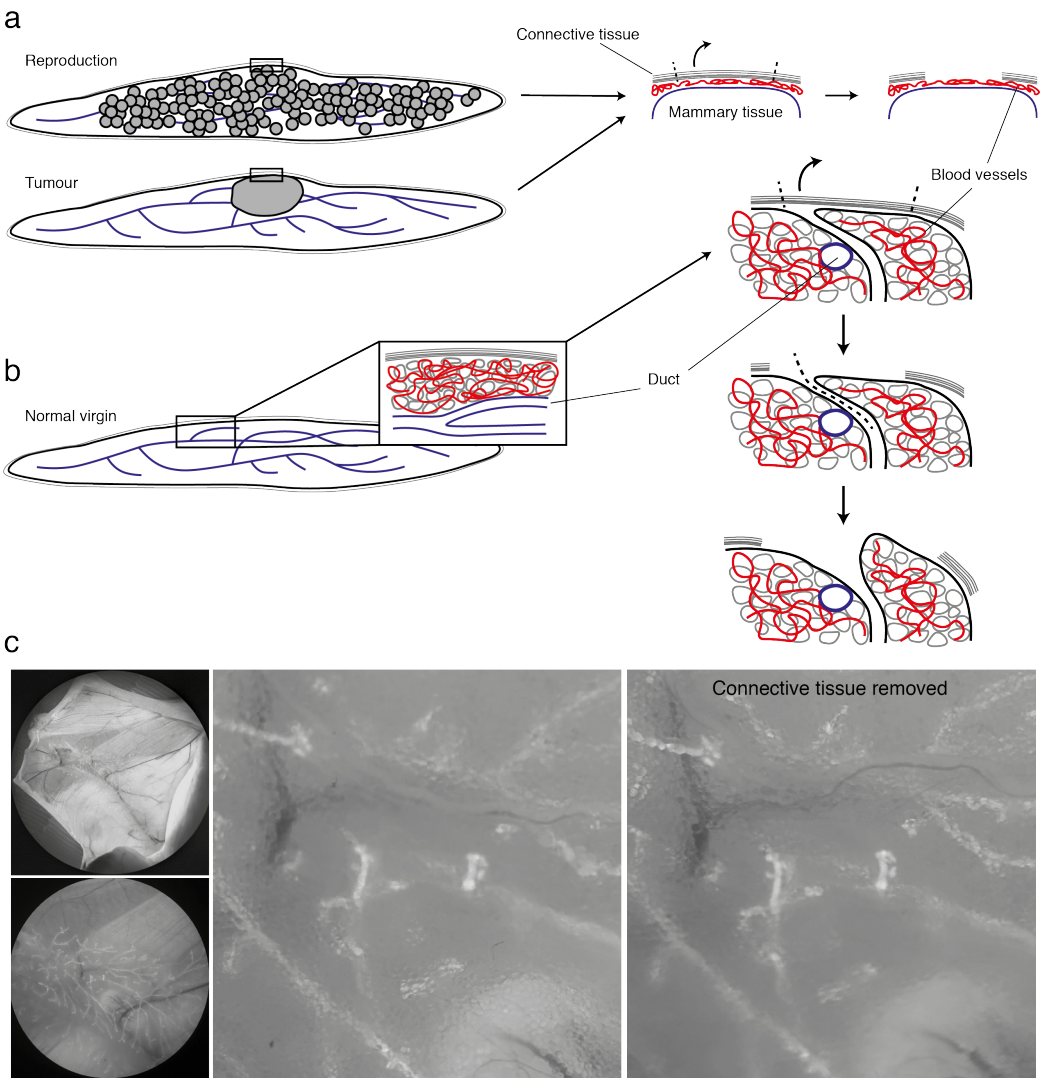

Figure 3.4: Microdissection to remove overlying connective tissue

(a) Diagram of microdissection in reproduction or mammary tumours. Lack of overlying fat aids imaging, but connective tissue can still be removed to improve resolution.

(b) Diagram of microdissection in virgin mice. Ducts can be occasionally found with no overlying fat. If not, folds of fat can be separated by cutting connective tissue to reveal obscured ducts.

(c) Example of improved visibility after removal of connective tissue. Stereo microscope images of a *UBC-GFP* mammary gland at 11 weeks. Top left: whole skin flap, bottom left: zoom of mammary gland, right: zoom of superficial ducts before and after removal of connective tissue.

CAUTION: To prevent compression of tumours and glands in reproduction, alternating O–ring/silicone grease layers can be used to build a deeper well.

CAUTION: Air trapped under the cover slip can interfere with imaging. It can be removed by carefully inserting a needle and syringe into the bubble through the silicone grease and taking up the air.

CAUTION: Imaging is hampered by breathing movement. Any movement can easily be observed at this point by viewing reflections in the cover slip. Breathing movements can sometimes be rectified by ensuring physical separation of the cover slip from other moving objects such as cling wrap, connective tissue or the torso. Moving skin can be stabilised by fixing to the platform with tissue adhesive.

30. Prepare a peritoneal catheter and syringe to deliver saline at 100 µl per hour (Figure 3.3j).
31. Transfer the mouse to the microscope chamber, position the gland under the objective and place a drop of water on the cover slip at the imaging area and away from the edge. Check objective immersion water throughout imaging and top up when required. Humidify the imaging chamber with an open petri dish filled with water to reduce evaporation.

    CAUTION: Water spilling onto tissue from the cover slip will affect osmolarity. If this occurs, remove fluid from the skin flap and reapply PBS.

3.4.4 Imaging

32. Regularly check breathing rate during imaging with a team of 2 or 3 people taking shifts to enable constant monitoring for extended periods. Isoflurane will need to be continuously adjusted from 1.5% to 1% (vol/vol).
33. Through the two-photon viewfinder, use low magnification epifluorescence to find the region to be imaged.
34. Define the imaging region at high resolution and optimise imaging parameters. Up to 6 channels can be imaged simultaneously using carefully designed filter sets and sequential excitation with dual lasers.
35. Acquire images at an interval that facilitates mouse monitoring and adjustment of the imaging region between time-points. If there is significant breathing movement, this can sometimes be removed post-acquisition. Alternatively, frame averaging with resonance scanning can minimise the effects of sharp breathing movements.

    CAUTION: The soft nature of the fat pad allows structures to drift, but this often slows over time. The imaging region will have to be regularly shifted to account for drift, sometimes for each timepoint, particularly early on in the experiment.
36. To induce targeted laser damage using the Olympus FVMPE-RS SIM scanner, deliver 800 nm MaiTai laser at approximately 0.3 W for 10 seconds in a 10 µm region. The laser power required for local damage depends on the depth and area targeted. Optimise laser damage at a distant site before performing in the desired region. Autofluorescence or bleaching can be used as an indicator of damage and can be monitored by simultaneously imaging with the InSight laser.

    CAUTION: Detector over-exposure can occur when simultaneously imaging and inducing laser damage if 800 nm excitable fluorescence is being used.
37. Euthanise the mouse at the end of the desired imaging period or if breathing slows too much.
38. If further analysis by 3D confocal imaging is desired, remove the imaged region then fix, immunostain and clear as described in Chapter 2. Microdissect the imaged region using a fluorescence stereo microscope and mount for imaging.

3.4.5 Image analysis and visualisation

39. If there is overlap between channels, subtract the responsible channel from the contaminated channel. This can be done using Imaris 'Channel arithmetic' and is more effective after application of a Gaussian filter to reduce noise.

40. Image sequences will require stabilisation. This can be achieved by automatic object tracking and movement correction, but IVM datasets are often too noisy or cells move too fast. In these cases, movies can be stabilised by manual spot placement in Imaris followed by movement correction. 5–10 tracks is often sufficient to correct movement.

    CAUTION: Use the 'InMotion' rocking function and channel-specific spot placement in Imaris to facilitate spot placement on objects in 3D. With the cursor on the object, ensure that the image rocks with the centre point at the object before placing the spot. This will prevent spot placement in front of, or behind the object.

41. To view in stereo 3D in Imaris, check 'Enable Stereo Camera Settings' in 'Preferences' > '3D View' and turn on the 'Red/Cyan Anaglyph' option in the 'Camera / Labels' panel. Pseudo-colour channels in yellow, magenta and/or grey (Figure 3.2z).

42. The pivot point, degree of perspective and stereo 'Offset' determine the strength of the stereo effect (Figure 3.2b). Adjust these parameters for optimal viewing. 3D snapshots or movies can be recorded when 'on screen rendering' is enabled in 'Preferences' > 'Display'.

    CAUTION: C/R stereo 3D is tiring for the eyes. Take rests often to avoid eye fatigue.

3.5 Troubleshooting

Table 3.3: Troubleshooting for issues during surgery, imaging and analysis

Step	Problem	Possible reason	Solution
6	Breathing rate changes rapidly before rectal probe is inserted	Temperature is too high or low during hair removal	Observe temperature with rectal probe and adjust heat lamp distance. Note this distance for steps 1–7 in the future.
9	Bleeding	Vascular damage	Remove blood using a cotton swab until bleeding stops or cauterise vessel if bleeding is heavy. Minor adjustments can be made during surgery to avoid blood vessels.
16	Skin flap will not attach to the platform	Platform or skin is wet	Fold the skin flap back over the abdomen and dry the skin and platform before re-attempting to secure the skin flap.
		Tissue adhesive is not setting	Hold each corner of the skin flap in position while the adhesive dries (about 10 seconds).
		Tape is not suitable for tissue adhesive	3M Durapore tape is ideal.
16	Skin flap quickly dries out	There is a hole in the skin flap	Experiment may need to be abandoned and the mouse euthanised.
		PBS is being drawn off the edge of the skin flap	Detach the edge of the skin flap from the platform and dry the skin. Ensure 1–2 mm of skin folds back to act as a barrier.
24	No ducts or TEBs are clearly visible	Obscured by fat	Separating folds of fat by cutting connective tissue in between can uncover structures. If necessary, fat can be held away from a structure by removing PBS and carefully applying a small amount of tissue adhesive.
		Epithelial fluorescence not discernable above skin fluorescence	Green autofluorescence or reporter expression in the skin makes duct identification difficult. Mammary gland specific red reporters are ideal.
	Bleeding	Fat tissue damaged	Fat is highly vascularized and will bleed if cut. Only cut connective tissue and limit manipulation of fat to avoid damage. Inflammation will affect imaging in damaged areas.
29	Breathing causes movement of the cover slip	Cover slip is contacting the abdomen, cling	Move the coverslip away from the moving object. Overhang of the cover slip beyond the skin flap edge is fine.

		wrap, movement brace or hind leg	
		Connective tissue or skin is transferring movement	Cut any connective tissue that is connecting the abdomen to the skin flap or the inguinal mammary gland. Secure any moving skin to the platform and away from the cover slip with tissue adhesive.
		The skin flap is positioned too close to the abdomen	Ensure the skin flap reaches 3–4cm away from the abdomen.
31	Water runs off the cover slip	Hydrophobic ring is not complete	Remove the cover slip, silicone grease ring and PBS from the skin flap. Continue from step 27 using a new cover slip.
		Cover slip water and skin flap PBS came into contact	Remove and replace PBS from the skin flap ensuring it does not flow onto the cover slip. Remove water from the cover slip and allow to dry before re-applying only enough water for objective immersion.
32	Isoflurane is decreased to 1% (vol/vol)	Mouse condition may deteriorate	If breathing continues to slow, imaging may need to be ceased and mouse euthanised. Isoflurane should not be decreased below 1% (vol/vol).
33	Poor signal to noise ratio or blurred signal	Fluorescent signal is weak	Increase laser power while decreasing averaging or imaging frequency to minimise laser damage.
		Overlying fat	Fat is extremely light scattering. Find regions with less or no overlying fat.
		Lasers are misaligned	Re-align lasers if this is a software option or have a technician align them if necessary.
35	Misaligned z-steps or double image with averaging	Breathing movement	Use resonance scanning with 4–8x averaging to minimise minor breathing effects or correct movement post-acquisition or see earlier tips for minimising movement.
	Imaging region shifts	Tissue drift	Manually correct imaging region while drift continues. Identify a stationary reference object and place a marker on the screen to aid repositioning.
		Tissue dehydration	Drying out of the tissue can accelerate drift. Check throughout imaging and ensure tissue is hydrated with PBS.
	Fluorescence dims or disappears suddenly	Evaporation of objective water	Top up water on the cover slip.

		Laser overheating	Check laser status and top up coolant if necessary.
	Cells die during acquisition	Laser power too high	Decrease laser power, averaging or pixel dwell time and increase gain.
		Tissue dehydration	Ensure PBS is maintained on the skin flap and check that PBS is not running off the skin flap.
		Tissue compression	Compression causes cell enlargement and blebbing. Do not compress tissue with the cover slip during preparation. Evaporation and drawing out of PBS from the well can cause tissue compression over time. Occasionally inject PBS under the cover slip if necessary.
39	Channel overlap cannot be corrected	Two-way signal bleedthrough	If two channels bleed into each other, it is difficult to correct. Set up filters so that any signal overlaps are one-way.
40	Automatic stabilisation fails	Objects move too rapidly	Manually track objects in 3D and then correct for movement.
		Poor signal-to-noise ratio	Try reducing noise by applying a Gaussian filter.
41	A channel is only seen by one eye in stereo 3D	Channel colour is not compatible with C/R 3D	Change channel colour to yellow, magenta or grey or an intermediate of these.
	Image doubling caused by stereo channel bleed through	C/R 3D glasses may be of poor quality	Lenses must be true cyan and red. Glasses with a blue or blue-cyan colour will not work.
	Exported snapshots/movies are not 3D	'On screen rendering' is not enabled	Enable this option in Imaris 'Preferences' > 'Display'.

3.6 Anticipated results

3.6.1 Observation of ductal macrophage–epithelium interactions

Chapter 5 describes the identification of a distinct and previously uncharacterised tissue-resident MØ population in mammary ducts. These ductal MØs (DMs) are exclusively localised to the basal–luminal interface and phagocytose apoptotic cells in virgin and involuting glands. 3D confocal imaging revealed their dendritic morphology and regular spacing within the epithelium but provided no information on the dynamics of the DM–epithelium interaction. IVM was performed in 8-week old *Elf5-rTTA-GFP* mice, which express GFP in APs but not HS cells, resulting in a mosaic pattern. DMs were labelled with fluorescently conjugated anti-MHCII antibody introduced to the imaging well. IVM over several hours revealed that DMs do not migrate but extend and retract dendrites to contact each other and monitor the epithelium (Figure 3.5).

3.6.2 Observing immune cell behaviour in response to epithelial damage

To investigate the response of DMs to epithelial damage, we used the Olympus FVMPE-RS SIM scanner to induce targeted damage while imaging DM behaviour. We imaged DMs in a *Cx3cr1-GFP* mouse and labelled apoptotic cells with PI in the imaging well. Damage in a 10 μm area of the epithelium was achieved by ablating a defined region with 800 nm Mai Tai laser while simultaneously imaging with the Insight laser. This led to DM dendrite extension towards the damaged region, then halting of dendrite movement (Figure 3.6a).

DMs surround alveoli during lactation and rapidly phagocytose alveolar cells between 2 and 4 days of involution (Chapter 5). IVM at 3 days involution in *Elf5-rTTA-GFP* mice with fluorescently conjugated anti-MHCII in the imaging well allowed observation of alveolar cell phagocytosis by DMs (Figure 3.6b).

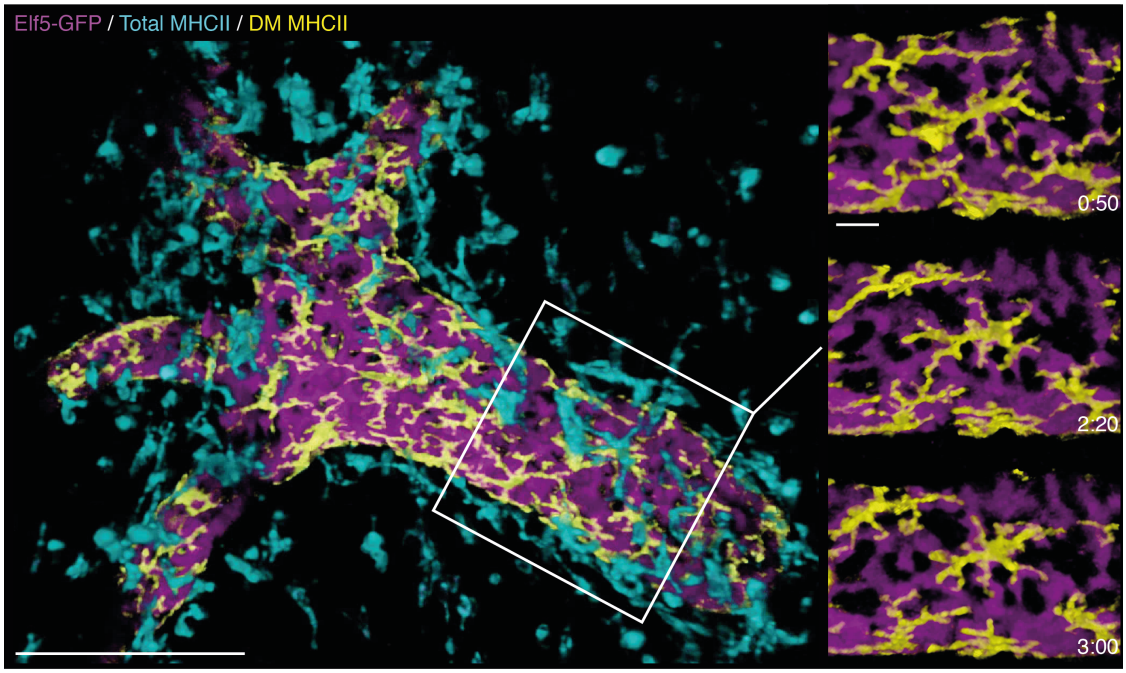

Figure 3.5: Ductal macrophages monitor the epithelium by dendrite movement

Example of IVM from Chapter 5. IVM of a mammary duct in an *Elf5-rtTA-GFP* mouse with immunolabelling with fluorescently conjugated anti-MHCII antibody. DM MHCII signal (yellow) was isolated from total MHCII (cyan) using a GFP (magenta) signal mask (See chapter 2). Enlarged time points show DM dendrite movement over time. This is analysed in greater depth in Chapter 5. Time in hrs:mins. Images were acquired every 10 mins. Scale bar, 100 μm (overview) and 10 μm (enlargements) (n=6 mice).

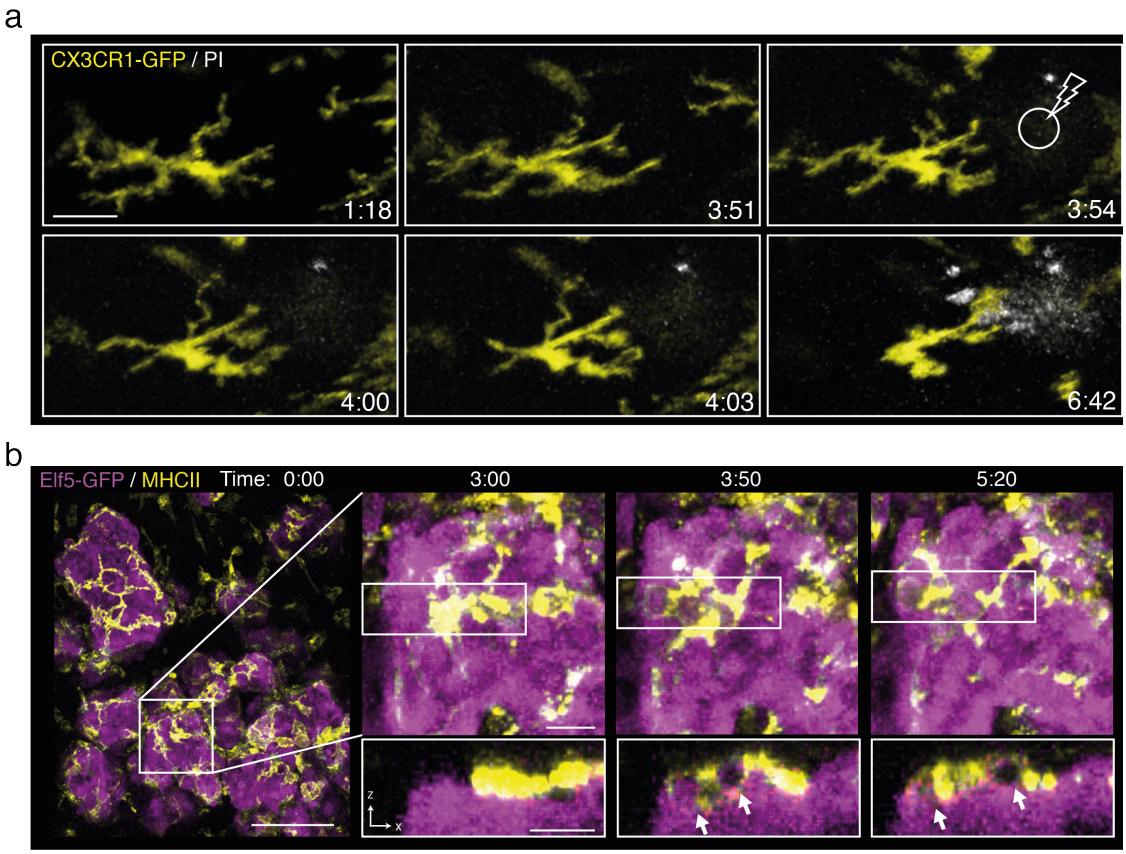

Figure 3.6: Ductal macrophage response to epithelial damage

(a) Example of IVM from Chapter 5. Time-points from an IVM movie in which precise laser damage was induced in the epithelium of a *Cx3cr1*$^{GFP/+}$ mouse after 4 hours of imaging and then observed for another 3 hours (n=3 mice). GFP: yellow, PI: white. DM dendrites stop random surveillance and stably interact with the damaged region. Time hrs:mins. Scale bar, 20 μm.

(b) Example of IVM from Chapter 5. IVM of alveoli in an *Elf5-rtTA-GFP* mouse at 3 days involution showing GFP (magenta) and DMs immunolabelled by fluorescently conjugated anti-MHCII antibody (yellow). Left: overview of alveoli and DMs. Right: enlarged time-points and corresponding horizontal views. Arrows indicate phagocytosed GFP^{+} cells within DMs. Images were acquired every 5 mins (n=3 mice). Scale bars, 100 μm (left), 20 μm (enlargements).

3.6.3 Myoepithelial cells divide longitudinally

Myoepithelial cell dynamics have not been observed *in vivo*. These have a distinctive elongated shape but how this is affected by and changes throughout cell division is unknown. IVM was performed in 8 week-old *K5/TetCre/Confetti* mice treated with doxycycline for three days at 4 weeks of age. Lineage tracing from basal cells in puberty resulted in the labelling of elongated myoepithelial cells and round luminal cells. One basal cell division was observed from three independent imaging sessions (Figure 3.7a). Division occurred longitudinally, involving rounding of the cell body and partial retraction of the arms, then separation of daughter cells lengthwise along the duct axis. Subsequent fixing, immunostaining, clearing and 3D confocal imaging demonstrated that this event generated two myoepithelial cells with distinct cell bodies approximately 50 μm apart with extensions maintaining contact (Figure 3.7b).

3.7 Discussion

This IVM technique is a powerful tool for investigating cell behaviour in the mammary gland. Here a range of biological questions have been addressed, including the dynamics of epithelial–immune interactions and the behaviour of myoepithelial cells in mature ducts. Cell dynamics in the TEB will be addressed in Chapter 4. Many other aspects of mammary gland development could be explored using this approach, such as epithelial remodelling during pregnancy, function in lactation, TEB branching and other epithelial-stromal interactions. *In vivo* imaging of early tumorigenesis has not previously been feasible but should be well suited to this technique. IVM could reveal the behaviour of newly transformed cells, their stromal interactions and immune surveillance of the early events of cancer. Understanding the dynamics of early tumourigenesis will be important for cancer prevention and treatment.

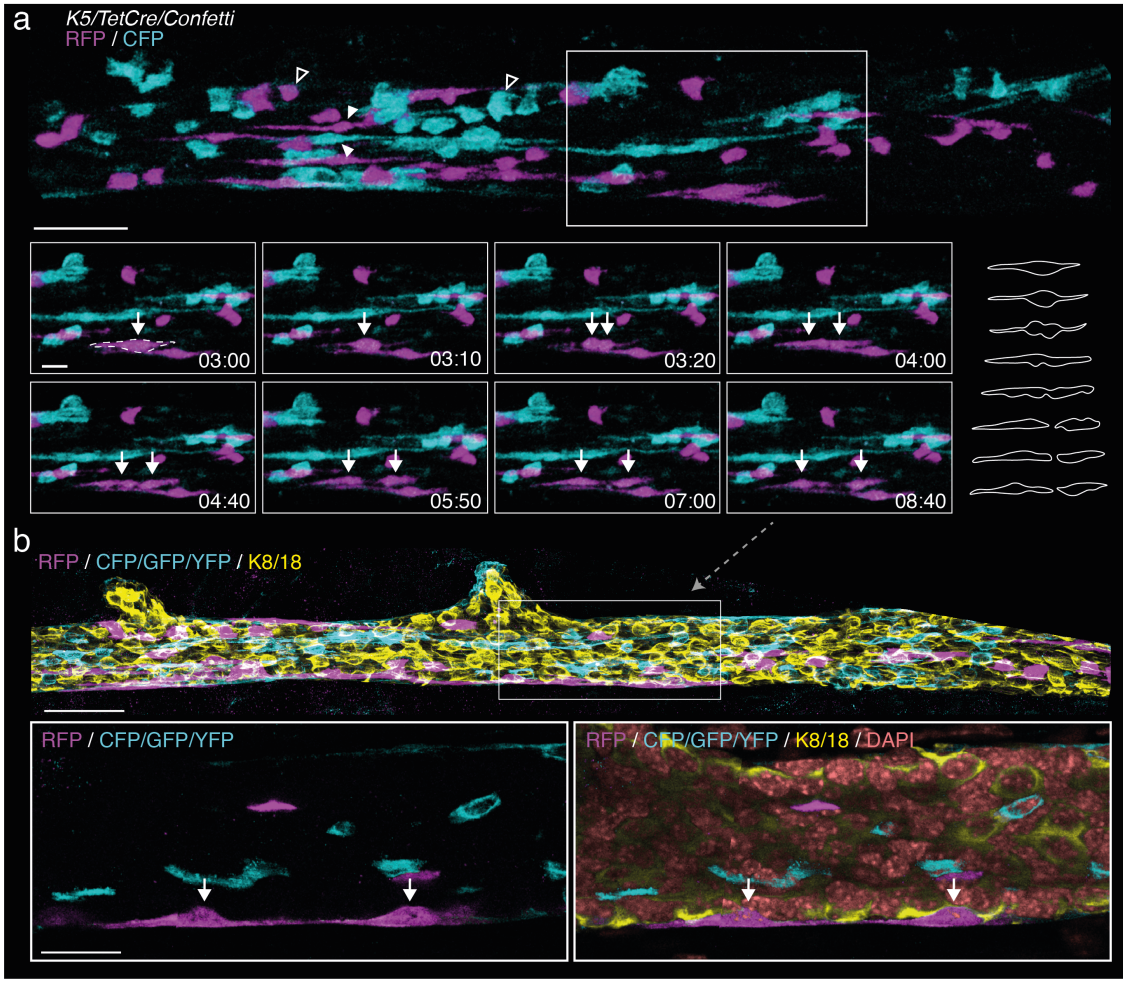

Figure 3.7: Myoepithelial cell division in adult ducts

(a) 3D rendering of an IVM time-point in an 8 week-old K5/TetCre/Confetti mouse duct after treatment with doxycycline at 4 weeks of age (n=3 mice). Enlarged time points: a myoepithelial cell (arrow and outlines) divides longitudinally. Scale bars, 50 µm (overview) and 20 µm (enlargements).

(b) 3D confocal microscopy of the duct imaged in (a) that was fixed, immunostained and cleared post-IVM. Immunostained for RFP (magenta), CFP/GFP/YFP (cyan) and K8/18 (yellow) and DNA labelled with DAPI (Pink). Grey arrow indicates the area enlarged in (a). White arrows indicate myoepithelial daughter cells. Separate nuclei confirm longitudinal myoepithelial division. Scale bars, 50 µm (overview) and 20 µm (enlarged optical sections).

Chapter 4: Imaging single cell dynamics during mammary gland morphogenesis

4.1 Introduction

Ductal growth during puberty occurs by proliferation and rearrangement of epithelial progenitors in TEBs that extend and branch through the fat pad in a process of collective cell migration (Ewald et al., 2008). Understanding this highly regulated growth may provide insight into unregulated cancerous growth. In contrast to bilayered ducts, TEBs comprise a multilayered, poorly polarised body (Ewald et al., 2012) within an outer basal cap layer. Cells of the TEB body lack tight junctions but maintain membranal E-Cadherin and β-Catenin and are connected primarily by desmosomes (Ewald et al., 2008, 2012). This allows individual cell migration within the TEB dowsnstream of receptor tyrosine kinase signalling that drives morphogenesis (Huebner et al., 2016; Neumann et al., 2018) and results in mixing of progenitors within the TEB (Scheele et al., 2017).

Collective migration of the TEB is poorly understood and has been investigated primarily in *ex vivo* organoids (Ewald et al., 2008, 2012; Neumann et al., 2018), which are a valuable tool but do not perfectly recapitulate *in vivo* morphogenesis. TEB progression does not involve actin-rich leading cellular extensions from the TEB in the direction of growth (Ewald et al., 2008). Rather, body cells migrate extensively within the TEB and extend protrusions in the direction of growth (Huebner et al., 2016) before undergoing radial intercalation into the basal-most layer of the TEB body to drive bilayer formation (Neumann et al., 2018). Radial intercalation functions in many developmental systems to narrow and lengthen tissue compartments (Keller, 2002). In the TEB, this follows similar principles to the migration of single cells in culture, with enrichment of Ras, phosphatidylinositol (3,4,5)-trisphosphate and F-actin in leading extensions (Neumann et al., 2018). Computational modelling showed that radial intercalation must be restrained by circumferential hoop stress to result in elongation (Neumann et al., 2018), presumably created

in the TEB neck and duct by maturing basal cells, increased fibroblasts and the thickening basement membrane (Silberstein and Daniel, 1982). These principles apply broadly to TEB dynamics, but how the progenitors of each epithelial lineage behave and cooperate to culminate in collective cell migration remains an open question. Previous *in vivo* imaging showed migration within TEBs and not ducts but did not investigate lineage-specific behaviour of cells and relied upon an anti-apoptotic drug, presumably to prevent excess cell death due to surgery or phototoxicity (Scheele et al., 2017). Thus, 3D IVM of lineage-specific single cell behaviour in minimally perturbed tissue would advance our understanding of TEB function.

Mathematical modelling is a powerful tool for integrating many measured parameters of a system and testing their sufficiency to reproduce known events, such as morphogenic patterns (Takaki, 2005). Adjustments needed to match modelled predictions with actual events can infer new parameters that may correspond to previously unrecognised biological processes. Mammary gland branching morphogenesis has been extensively modelled on the organ scale (Hannezo et al., 2017), revealing that duct elongation and branching occur randomly and terminates when TEBs are in the proximity of other ducts. On the cellular scale, measurement of TEB cell size and number as well as death and division rates enabled generation of a model that recapitulated duct elongation rates (Paine et al., 2016). In this study, TEB and duct compartments were geometrically defined so that net production of cells in the TEB (proliferation > death) predicted the number of cells exiting to give rise to mature ducts. The number and size of the cells generated could then be used to calculate a duct elongation rate that could be compared to experimental measurements. The frequency of cell behaviours such as division and death were inferred from static snapshots of TEBs. Matching this model to experimental data required a steady rate of cap to body (C-B) migration followed by rapid death. It remains to be experimentally determined whether all cap cells that enter the body die or whether some survive and give rise to luminal cells.

This Chapter describes the arrangement and behaviour of lineage-specific TEB progenitors as observed by IVM. This information is then used to construct an updated theory of mammary duct morphogenesis as a culmination of individual cell behaviour.

4.2 Results

4.2.1 Cap cells migrate into the TEB body

To shed light on TEB progenitor dynamics, IVM was performed on TEBs in mouse models that allow lineage-specific fluorescent labelling. This was achieved by lineage-specific *Cre* expression to recombine the *Confetti* allele (Basal/cap cell: *K5-rtTA/Tet-Cre*, AP: *Elf5-rtTA/Tet-Cre*, HS cells: *PR-Cre*). The random expression of one of four fluorescent proteins after *Confetti* recombination enables high labelling density while maintaining the ability to distinguish single cells. This is important, as many cells need to be observed to uncover rare events. Cap cells were labelled in *K5-rtTA/Tet-Cre/Confetti* mice by doxycycline treatment at 4 weeks. All four *Confetti* colours were observed, however, only selected channels are displayed for clarity and nuclear GFP labelled cells were excluded from behavioural analyses. IVM was performed at 5 weeks for up to 12 hours using the modified skin flap method described in Chapter 3. Cap cells migrated within the cap in an amoeboid fashion without long protrusions and occasionally migrated into the TEB body (Figure 4.1). Of the cap cells that migrated into the body, some were observed to rapidly undergo apoptosis, while others survived until the end of the experiment.

4.2.2 Alveolar progenitors transiently send pseudopodia through the cap cell layer

APs were labelled in *Elf5-rtTA/Tet-Cre/Confetti* mice by doxycycline treatment at 4 weeks of age. IVM at 5 weeks revealed that APs are not highly migratory like cap cells (Figure 4.2a i). Rather, these cells sent short, dynamic extensions towards the cap layer. Subsequent 3D super-resolution imaging of these same cells showed that extensions protrude into and through the cap cell layer (Figure 4.2a ii).

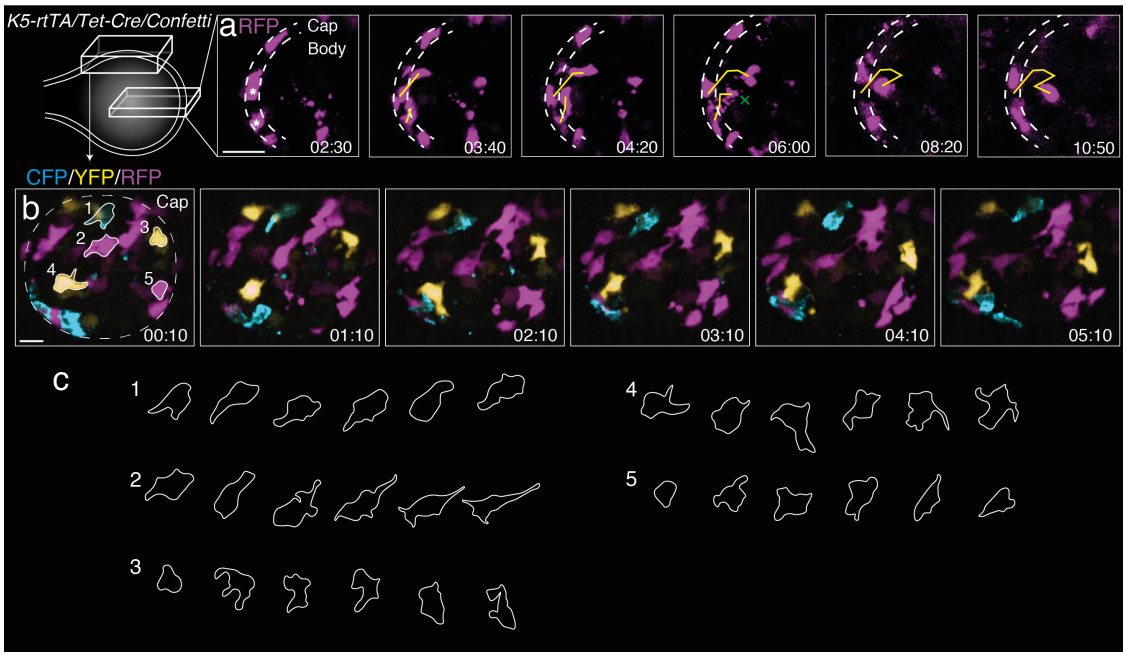

Figure 4.1: Cap cells migrate within the cap layer and from the cap layer into the body

(a) IVM of a TEB at 5 week-old *K5/Tet-Cre/Confetti* mouse treated with doxycycline for 3 days at 4 weeks of age. (i) 3D cross section of the TEB. Two cap cells (asterisks) migrate into the TEB body (yellow lines), where one undergoes apoptosis immediately (green cross), while the other survives for at least 7 hours until imaging ceased (n=2 mice, 1 TEB per mouse). Scale bar, 30 µm.

(b) 3D view of the cap layer from above. Cap cells migrate in an amoeboid fashion. Scale bars, 15 µm.

(c) Outlines of cap cell shape from (b) (n=2). CFP: cyan, YFP: yellow, RFP, magenta.

4.2.3 Hormone-sensing progenitors migrate throughout the TEB

To investigate the behaviour of TEB HS cells, IVM was performed on *PR-Cre/Confetti* mice at 5 weeks of age. As the TEB primarily houses progenitor cells that proliferate to generate mature cells of the extending ducts, HS cells of the TEB will here be referred to as HSPs. Due to constitutive Cre activity, HSPs were densely labelled and many cells expressed two fluorescent

proteins (CFP and RFP or YFP and GFP) due to constant flipping of the *Confetti* cassettes (Snippert et al., 2010). Variation in fluorescence intensity and ratio were sufficient to allow discrimination of the morphology and behaviour of single cells. HSPs migrated extensively throughout the TEB body, often extending thin projections (Figure 4.2b i–iii). Extensions were predominantly oriented radially from the inner to the outer regions of the body and were dynamic. These observations suggest that HSPs but not APs correspond to highly migratory cells previously observed in the TEB (Ewald et al., 2012).

4.2.4 Cap cells and HSPs are more migratory than APs

To quantitatively compare the dynamics of each population, cells were manually tracked using C/R 3D visualisation, giving the average migration speed of each cell. Cap cells demonstrated the greatest motility (median 7.5 μm/hr) and HSPs (median 5.4 μm/hr) migrated faster than APs (median 3.6 μm/hr) (Figure 4.3a). The migration rate of HSPs is remarkably similar to migratory cells in *ex vivo* organoid cultures (5.5 ±1.8 μm/hr) (Ewald et al., 2012). These data suggest that APs play a more passive role in TEB body organisation, in contrast to migratory HSPs.

4.2.5 Modelling cap cell dynamics

To quantify cap cell behaviour, 64 individually tracked cap cells from two TEBs were observed by C/R 3D and the time from first observation to division, death and migration were recorded and plotted (Figure 4.3b). Labelling frequency in the cap was sufficient for the cap layer to be visually determined, allowing the identification of cap cells and C-B migration events. *K5*-traced cells within the body were occasionally spindle-shaped and mesenchymal like, resembling HSPs. The number of these was highly variable and they did not resemble typical cap-like cells in the body (CLB) so they were excluded from this analysis (Figure 4.3c). Due to the large number of censoring events (e.g. death, end of experiment and migration from the cap), a time-to-event Kaplan-Meier plot was ideal for conveying the proportion of cells adopting a fate over time. After 5 hours of imaging, the rate of cap cell death increased and division slowed, so only the first 5 hours of cell tracking were used for subsequent calculations. Linear regression was performed

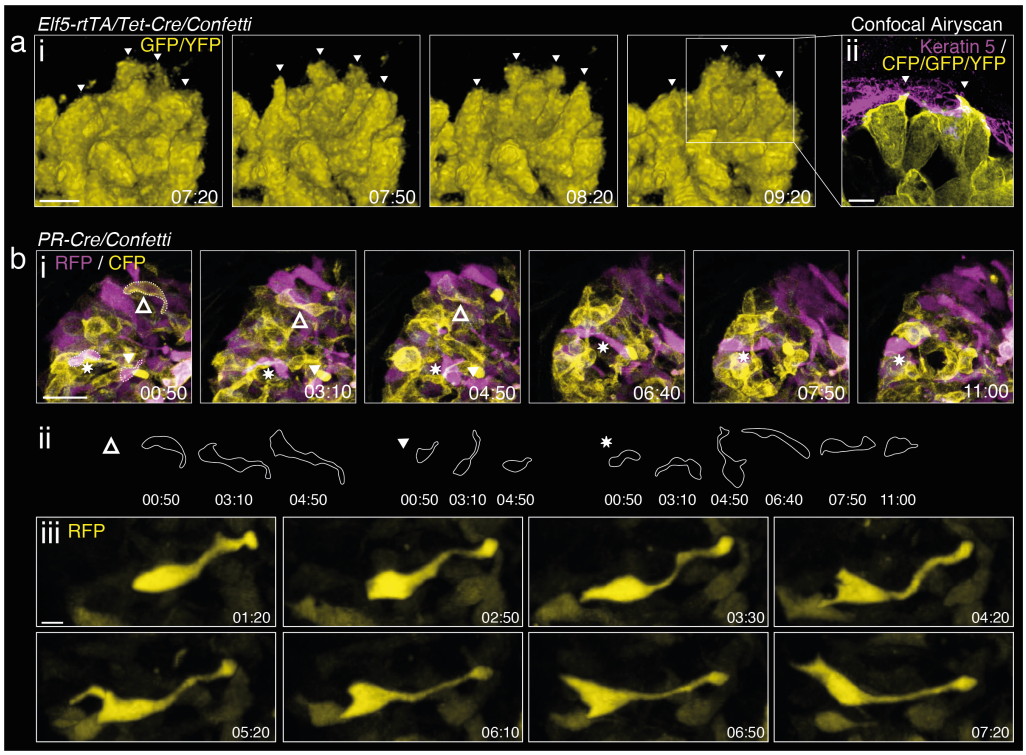

Figure 4.2: Distinct behaviour of luminal lineage progenitors in the terminal end bud.

(a) IVM of a TEB in a 5 week-old *Elf5-rtTA/Tet-Cre/Confetti* mouse treated with doxycycline for 3 days at 4 weeks of age. (i) 3D view of the TEB tip. LPs did not migrate but had dynamic extensions at the TEB edge. (ii) A post-IVM super-resolution AiryScan image of these cells captured after fixation, immunostaining and clearing. This revealed that LP extensions protrude through the K5-positive cap cell layer (n=1 TEB). CFP, GFP and YFP: yellow, K5: magenta. Scale bars, 10 μm (i) and 5 μm (ii).

(b) IVM of a TEB in a 5 week-old *PR-Cre/Confetti* mouse. (i) 3D view of the TEB tip showing highly migratory HSPs with long protrusions that move between the inner and outer regions of the TEB body. Only RFP (magenta) and CFP (yellow) fluorescence is shown. (ii) Outlines of cell shape over time from the cells indicated in (i). (iii) An HSP demonstrating typical migratory behaviour (n=2 mice, 1 TEB per mouse). RFP: yellow. Scale bars, 30 μm (i) and 7 μm (iii).

and extrapolated to 24 hours to give event rates as a percentage of each population undergoing an event per day (Table 4.1).

As the TEB progresses, it generates new cells that are deposited along ducts. Calculation of net change in basal cell number should result in a positive value to reflect maintenance of the cap layer while generating new basal cells that contribute to the growing duct. The net basal change per day was calculated by doubling the division rate to reflect doubling of cell number (+110.4%), then subtracting the death rate (–41.02%) and rate of migration to body (–69.55%) (Table 4.1). This resulted in a net change of –0.17%). This was surprising, as only a positive number would be consistent with the generation of new myoepithelial cells during duct elongation. Previous work showed that cap cells exhibit extremely low rates of apoptosis (~0.65% per day) (Paine et al., 2016), compared to the rate of 41% per day observed here. Assuming that cap cell apoptosis is an artefact of IVM, the net change was re-calculated using a death rate of 0.65% per day. This gave a net change of +40.20% per 24 hours. From an approximated total of 115.7 cap cells per TEB (Paine et al., 2016), this predicts deposition of 46.5 basal cells along the maturing duct per day. These data suggest that cap cells, while resistant to cell death when unperturbed, are particularly sensitive to apoptosis upon disturbance with surgery and IVM. The lack of death of mature myoepithelial cells seen during IVM (Chapter 3) indicates that this sensitivity is specific to cap cells.

4.2.6 Some cap cells may contribute to the luminal compartment

The rate of C-B migration was 69.6% of cap cells per 24 hours (Table 4.1). From a total of 115.7 cap cells, this predicts entry of 80.53 into the body per day, almost twice the number contributing to the basal layer of ducts (46.51). This number seems high but may be reasonable considering that there is a persistent pool of basal-like cells in the TEB body despite their rapid death. Cells that migrated into the body rapidly underwent apoptosis (median survival 3.59 hours) (Figure 4.3b), as previously indicated by cleaved caspase 3 staining (Sreekumar et al., 2017; Paine et al., 2016). Despite the rapid death of 80% of cells following C-B migration, 20% survived the duration of these experiments. The long-term survival of some cap cells that entered the TEB body maintains the possibility of cap cell differentiation into luminal cells. The rate of C-B migration was previously predicted to be 39% per 24 hours (derived from Paine et al., 2016),

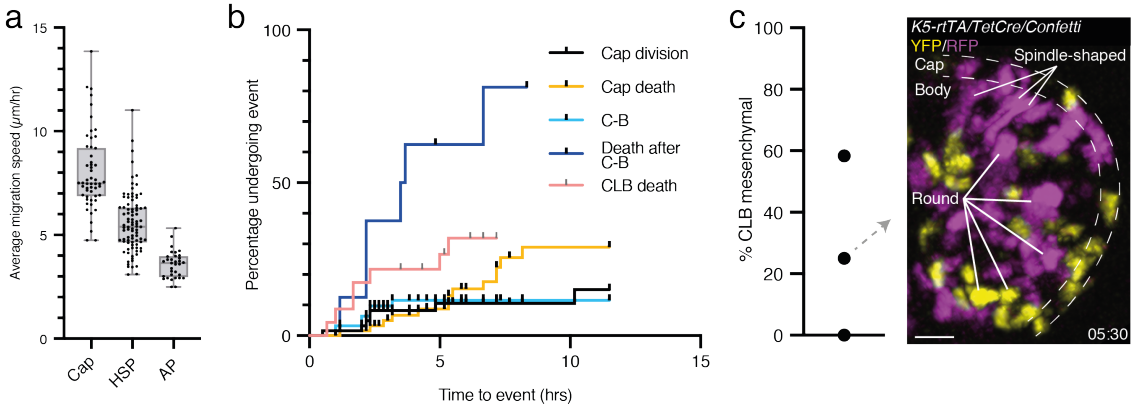

Figure 4.3: Quantification of terminal end bud cell dynamics

(a) Migration speed of individual progenitor cells from IVM of TEBs in 5 week-old mice (From Figure 4.1 and Figure 4.2). Mouse models *K5-rtTA/Tet-Cre/Confetti* (cap), *Pr-Cre/Confetti* (HSP) and *Elf5-rtTA/Tet-Cre/Confetti* (AP). Each cell was manually tracked using C/R 3D. Drift artefacts were reduced by taking a rolling average of position over three time points (30 minutes). Cells with confounding behaviour were excluded: K5-traced cells in the TEB body, dividing cells, cell clusters that could not be distinguished and cells tracked for less than 1 hour. Cap, n=54 cells from 2 mice, 1 TEB per mouse; HSP n=88 cells from 2 mice, 1 TEB per mouse; AP n=33 cells from 1 TEB.

(b) Time to event plot of cap cell behaviour in IVM of TEBs in *K5-rtTA/Tet-Cre/Confetti* mice. 64 cells were tracked manually in 3D, providing a track ID, then cells were observed by C/R 3D and behaviour timing attributed to each ID. Tracking started at the beginning of experiment or when the cell entered the field of view. Cells in the TEB body with HSP-like morphology were excluded. Black points are censoring events listed as follows by Category: censoring event — All categories: end of experiment or exit of cell from field of view. Cap cell division: migration to body or death. Cap cell death: migration to body. Migration to body: cap cell death. Definitions – C-B: Cap to body migration, CLB: Cap-like cell in body at experiment beginning (n=64 cells from 2 mice, 1 TEB per mouse).

(c) Percentage of K5-lineage traced cells in the TEB body with HSP-like radially oriented spindle morphology and an optical section through a TEB by IVM showing spindle-shaped and round morphologies (n=3 mice, 1 TEB per mouse). Scale bar, 20 μm.

compared to the observed rate of 69.6% (Figure 4.3b and Table 4.1). This may be due to a prior overestimation of time to death following C-B migration that would decrease the calculated frequency of C-B events needed to sustain observed CLB numbers.

80.53 cap cells entering the body per day (rate 3.36 C-B/hr) with a median survival of 3.59 hours would generate an equilibrium number of 12.05 CLBs (rate x duration). Paine et al. used imaging to determine that there are approximately 37.72 CLBs per TEB at one time (Paine et al., 2016); far more than the number calculated here (12.05). As 20% of cells survived long term following C-B migration, an arbitrarily longer median survival of 48 hours was attributed to 20% of cells following C-B migration, which increased the equilibrium number of CLBs to 41.91 (Equation 4.1); close to the estimated number of 37.72 (Paine et al., 2016). There are multiple possible fates that could remove these CLBs after extended survival – eventual death within the TEB or loss of basal gene expression (luminal differentiation).

Death following C-B migration may be hastened by IVM, as was apparent for cap cells, so CLB equilibrium number was also calculated using a doubled median survival of 7.18 hours for 80% of cells following C-B migration. Calculation of a reasonable CLB equilibrium required adjustment of the median survival time of the remaining 20% of cells following C-B migration from 48 to 24 hours, giving a CLB number of 35.43 (Equation 4.1). With this conservative estimation, 20% (16.11) of CLBs either die belatedly in the TEB or contribute to the luminal compartment per day. Unfortunately, TEBs cannot be imaged *in vivo* for these timescales, thus long-term fates following C-B migration – death or luminal incorporation – cannot be observed. Additionally, it cannot be excluded that C-B migration was increased as an artifact of IVM, however, this is the first direct observation and measurement of C-B migration *in vivo* and is likely to be more accurate than previous estimates.

Table 4.1: Frequency of cap cell behaviour

Cap cell behaviour (n=64 cells from 2 mice, 1 TEB per mouse)	% per hour (from 1st 5 hours)	% per 24 hours (from 1st 5 hours)
Division	2.30	55.2
Death	1.71	41.0
Migration to body	2.90	69.6
Death after migration to body	13.91	333.8
Death of existing CLBs	5.76	138.2
Net cap change	-0.01	-0.17
Net cap change, death 0.65%/24hr	1.67	40.20

Equation 4.1: Calculating the equilibrium number of cap-like cells in the TEB body

Using a 3.59-hour median survival (shortDuration) for 80%, and a 48-hour median survival (longDuration1) for 20% of cells following C-B migration:

Equilibrium number of CLBs

= (0.8*C-B rate)*shortDuration + (0.2*C-B rate)*longDuration1

= (0.8*3.36)*3.59 + (0.2*3.36)*48 = 41.91

Using a 7.18-hour median survival (2*shortDuration) for 80%, and a 24-hour median survival (longDuration2) for 20% of cells following C-B migration:

Equilibrium number of CLBs

= (0.8*C-B rate)*(2*shortDuration) + (0.2*C-B rate)*longDuration2

= (0.8*3.36)*7.18 + (0.2*3.36)*24 = 35.43

4.2.7 Rare cap cells may give rise to proliferative HS cells

Luminal differentiation of a proportion of cap cells following C-B migration is further supported by the decreased death rate of CLBs present at the beginning of the experiment (5.76 %/hr) compared to following observed C-B migration (13.91 %/hr) (Figure 4.3b and Table 4.1). The death curve for pre-existing CLBs plateaued at 30%, indicating that the majority of these cells survive long term. This suggests that most of the cap cells that entered the body prior to the experiment had already died, leaving a population skewed towards long-term survival and contribution to the luminal compartment. Furthermore, extremely variable numbers of mesenchymal-like *K5*-traced body cells were observed that resembled HSPs and did not undergo apoptosis (Figure 4.3c). These could possibly result from rare CLB to HSP differentiation events that are not reliably captured by low or medium density lineage tracing. The high variability also suggests that HSPs derived from cap cells may be highly proliferative, amplifying the effect of rare differentiation events. This is supported by the clustering of uni-coloured *K5*-traced HSP-like cells, suggestive of clonality (Figure 4.1c).

4.2.8 Migration of HS cells is restricted to TEBs

To further investigate the mesenchymal-like state of HS cells throughout differentiation, we performed IVM on HS cells in mature ducts. Mature HS cells had typical non-migratory, epithelial behaviour, taking on a conical shape with a small apical surface and a large basal surface (Figure 4.4a-c). This suggests that HS cells exiting the TEB cease migration and intercalate into the bilayer. The importance of a migratory to intercalated transition for duct elongation (Neumann et al., 2018) highlights HS cells as potential drivers of mammary gland morphogenesis.

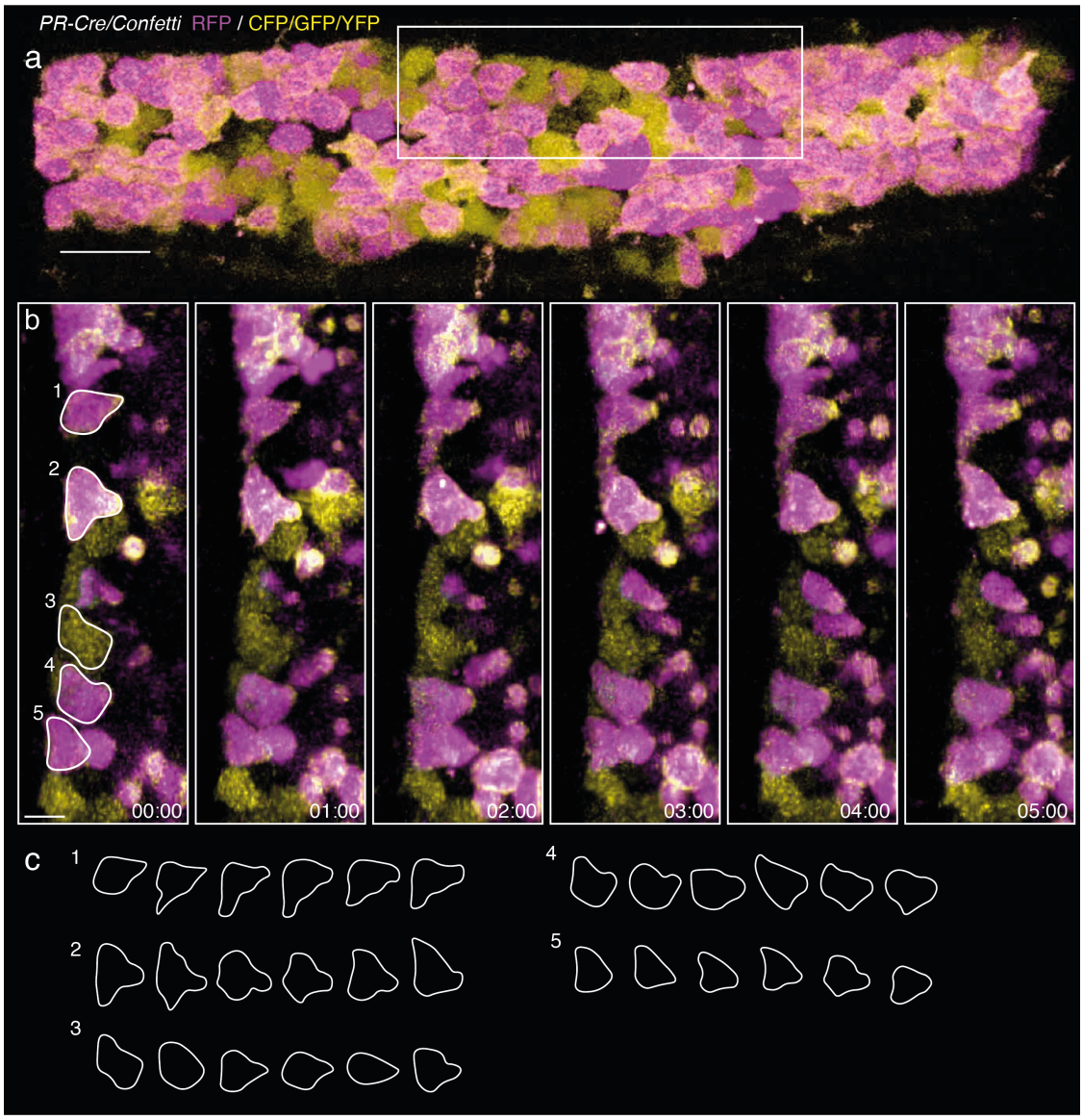

Figure 4.4: Mature hormone-sensing cells are non-migratory

(a) 3D projection of a duct in a 6 week-old *PR-Cre/Confetti* mouse by IVM. The outlined region is enlarged in (b). Scale bar, 30 μm. CFP, YFP and GFP: yellow, RFP: magenta (n=1).

(b) Optical sections at time points throughout imaging. Basal surface is to the left, lumen to the right. Scale bars, 10 μm.

(c) Outlines of cells labelled in (b), showing cell shape at each timepoint shown above (left to right). HS cells in the duct have a conical shape and are not migratory.

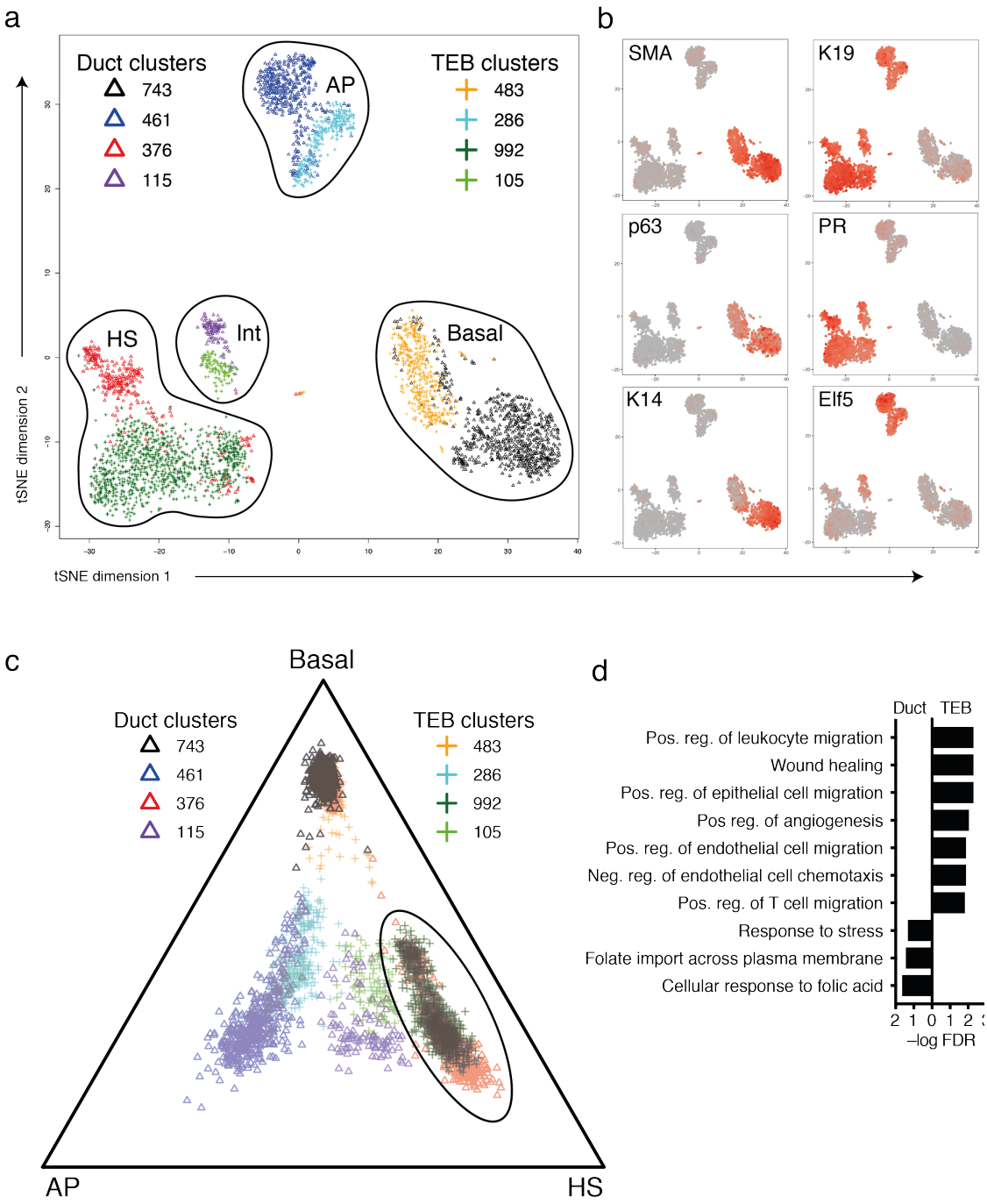
a
Duct clusters
743
461
376
115
TEB clusters
483
286
992
105
AP
HS
Int
Basal
tSNE dimension 2
tSNE dimension 1
b
SMA
K19
p63
PR
K14
Elf5
c
Basal
Duct clusters
743
461
376
115
TEB clusters
483
286
992
105
AP
HS
d
Duct
TEB
Pos. reg. of leukocyte migration
Wound healing
Pos. reg. of epithelial cell migration
Pos reg. of angiogenesis
Pos. reg. of endothelial cell migration
Neg. reg. of endothelial cell chemotaxis
Pos. reg. of T cell migration
Response to stress
Folate import across plasma membrane
Cellular response to folic acid
2 1 0 1 2
–log FDR

Figure 4.5: Single cell RNA sequencing of duct and TEB epithelial cells

(a) tSNE clustering of duct and TEB single cells (n=1 sample, cells pooled from 3 mice). Clusters were labelled based on expression of epithelial lineage markers (b). Triangles: Duct cells. Plus signs: TEB cells. Each cluster is uniquely coloured and the number of cells within each cluster is shown. Int: luminal intermediate.

(b) Expression heatmap of indicated genes overlayed on tSNE plots.

(c) Ternary plot visualisation of single cell gene expression of adult lineage signatures genes. Circle indicates HS cells.

(d) Gene ontology enrichment analysis of genes significantly differentially expressed between duct and TEB HS cells with a log fold change > 1.5.

4.2.9 Single cell RNA-seq implicates Flt1 in HSP migration

To identify possible molecular regulators of HSP behaviour, single cell RNA-seq was performed on epithelial cells from ducts and TEBs separated by microdissection. Single cell profiling has been recently performed (Scheele et al., 2017) but this study only analysed 36 luminal cells and 51 basal cells, which is unlikely to capture the full heterogeneity of TEB populations. Using the 10x Chromium platform, we were able to analyse 1695 cells from ducts and 1866 cells from TEBs. tSNE clustering demonstrated the presence of the 3 main cell types in both TEBs and ducts, as well as a shared luminal intermediate population that was previously identified (Pal et al., 2017) (Figure 4.5a). The basal cluster expressed *SMA, p63* and *K14,* the HS cluster *K19* and *PR*, the AP cluster *Elf5* and the intermediate cluster both *Elf5* and *PR* (Figure 4.5b)*,* as previously described for total epithelial cells in puberty and adulthood (Pal et al., 2017). Within the major clusters defining each lineage, duct and TEB cells were distinct, indicating global transcriptional differences between these regions. Interestingly, the proportion of HS cells in the TEB (53.2%) was increased compared to ducts (22.2%).

To investigate differences between duct and TEB populations, the tSNE clusters were overlaid onto a ternary plot with cells positioned based on expression of genes specific for each of the three epithelial lineages (Figure 4.5c) (Sheridan et al., 2015). TEB basal cells were similarly positioned to duct basal cells but did show some spread towards an HS signature. There was a larger shift in all luminal compartments towards a less defined state. As HS cells displayed the most striking behavioural difference between ducts and TEBs, we compared gene expression in the HS cluster from these regions (Table 4.2, Table 4.3). TEB HS cells showed higher expression of Itgb3/CD61, a known marker of luminal lineage progenitors. We next performed gene ontology enrichment analysis on highly differentially expressed genes (Figure 4.5d). This revealed TEB HS cell enrichment for multiple processes including epithelial migration and angiogenesis. Of interest in relation to angiogenesis is the upregulation of *Flt1* (encodes Vegfr1), which is a potent receptor for vascular endothelial growth factor (VEGF). VEGF is central to angiogenesis, where endothelial tip cells extend filopodia during vessel sprouting and branching in response to VEGF and hypoxia (Risau, 1997). The multilayered structure of TEBs separates body cells from blood vessels by approximately 2–4 cell layers, so the central TEB body is likely to be a hypoxic environment. A role for Flt1 in HS cell migration in response to TEB hypoxia will be an interesting avenue to explore in the future. TEB HS cells expressed higher levels of *Hbegf*, a smooth muscle growth factor that could promote cap cell survival and proliferation.

Table 4.2: Down regulated genes in duct vs TEB HS cells

Gene symbol	Average duct logCPM	Average TEB logCPM	LogFC	FDR
S100a14	8.314	10.846	-2.532	8.37E-160
Wnt5a	8.017	10.088	-2.071	6.69E-129
Basp1	7.901	9.995	-2.094	2.96E-127
Sdc1	8.048	9.733	-1.685	1.90E-103
Golim4	7.726	9.499	-1.773	1.25E-86
Sprr1a	8.793	13.264	-4.470	4.44E-71
Anxa3	7.778	9.494	-1.716	4.28E-66
Prkcdbp	7.682	9.604	-1.922	1.22E-65
Tm4sf1	9.419	10.929	-1.510	3.26E-60
Itih2	7.194	8.845	-1.651	1.28E-59
Fst	7.402	10.200	-2.798	2.84E-58
Serpinb6a	7.587	9.192	-1.605	9.70E-58
Flt1	6.908	9.341	-2.432	5.86E-57
Tenm4	6.886	9.064	-2.178	1.35E-51
Creb5	7.472	9.607	-2.136	3.94E-46
Padi2	7.220	8.840	-1.619	7.41E-46
Itgb3	7.197	9.102	-1.905	5.07E-43
Krt6a	7.088	9.251	-2.163	3.38E-40
Cxcl13	7.119	10.878	-3.759	3.71E-40
Ffar4	7.047	8.846	-1.799	2.70E-38
Cdkn1a	7.817	9.345	-1.528	1.12E-36
Rdh10	7.125	9.029	-1.904	2.90E-36
Fxyd5	6.923	8.503	-1.580	6.32E-35
Ctns	7.106	9.226	-2.120	4.16E-34
Iffo2	7.196	8.748	-1.551	3.05E-33
Hbegf	7.381	9.405	-2.024	7.34E-33
Ctse	7.054	8.690	-1.636	6.29E-31
Thbs1	7.336	9.313	-1.977	3.63E-29

Cacna2d3	6.867	8.694	-1.827	5.31E-29
Sytl2	6.936	8.437	-1.500	5.83E-27
Tnr	6.814	8.335	-1.522	2.02E-25
Isg15	7.169	9.400	-2.231	7.04E-25
Oasl2	6.886	8.426	-1.539	5.47E-21
Ndrg1	7.189	8.705	-1.515	6.19E-21
Bnip3	6.976	8.565	-1.589	1.96E-19
Lmcd1	6.847	8.395	-1.547	1.40E-18
H19	7.020	10.254	-3.234	1.59E-18
Slpi	8.348	10.502	-2.154	1.44E-14
2210407C18Rik	6.825	8.581	-1.756	1.30E-09
Pcp4	8.038	9.671	-1.634	6.83E-09

Table 4.3: Up regulated genes in duct vs TEB HS cells

Gene symbol	Average duct logCPM	Average TEB logCPM	LogFC	FDR
Gpx3	9.633	6.754	2.879	2.30E-185
Col6a3	7.344	4.646	2.698	1.69E-148
Slc7a2	7.209	4.512	2.697	1.63E-143
Nrxn3	7.101	4.470	2.631	9.92E-141
Cxcl17	6.865	3.942	2.923	6.76E-115
Hba-a1	6.848	3.968	2.880	1.10E-76
Folr1	7.172	5.330	1.842	2.47E-64
Lrg1	7.300	5.089	2.211	2.90E-54
Hspa1a	8.042	6.069	1.973	3.91E-53
Fxyd2	7.255	4.318	2.937	5.51E-52
Bex4	6.997	5.101	1.896	1.97E-49
Gadd45g	8.053	6.519	1.534	7.37E-49
Enah	6.975	5.411	1.564	7.06E-48
Dgki	7.000	5.180	1.820	1.50E-47
Igfbp5	9.890	8.132	1.758	1.45E-44
Tagln	9.855	8.075	1.780	3.44E-44
Fgg	7.814	6.069	1.745	3.38E-43
Aoc1	7.161	4.136	3.025	5.73E-43
Folr2	6.842	5.255	1.587	1.70E-40
Agtr1a	6.789	5.200	1.590	3.53E-39
Defb1	6.846	4.138	2.708	2.32E-37
Bex1	7.021	5.470	1.551	3.48E-33
Hp	7.245	5.430	1.815	2.20E-25
Ido1	6.970	4.924	2.047	9.34E-18
Dmbt1	7.006	4.828	2.178	5.45E-08

4.3 Discussion

This study explores how mammary epithelial cell behaviour sustains TEB growth, organisation and duct elongation through the application of high-resolution IVM of TEBs in combination with sophisticated lineage tracing mouse models. IVM of lineage-traced cap cells provided definitive evidence for cap cell migration into the TEB body. The translation of *in vivo* movies into high-dimensional quantitative datasets that tracked individual cell behaviour has led to deeper insights into cap cell biology. The observation that a small proportion of cap cells that enter the TEB body survive long term strengthens the hypothesis that cap cells contribute to the luminal compartment. The highly variable tracing of spindle-shaped migratory cells from cap cells indicates that rare events of cap cell differentiation may generate HSPs with high rates of proliferation. This could possibly be confirmed by longer IVM of *K5*-traced TEBs followed by immunostaining for hormone receptors and basal markers. Even if cap cells do give rise to HSPs, the question of why excess cap cells migrate into the body only to die remains a mystery. Perhaps death following C-B migration is involved in the poorly understood bifurcation process. Bifurcation appears to proceed on a timescale beyond these imaging periods (up to 12 hours), as TEB cleavage was not observed. It is also possible that death following C-B migration is important for MØ recruitment to TEBs where they perform a crucial role (Gouon-Evans et al., 2000).

Expression of fluorescent reporters in distinct luminal subpopulations revealed diverse behaviour of TEB luminal cells. Both Elf5-positive and PR-positive cells within the TEB are presumed to be enriched for progenitor cells as body cells are actively proliferating (Paine et al., 2016; Scheele et al., 2017). Interestingly, APs are relatively static in the TEB, while HSPs are migratory and actively move throughout the TEB body (Figure 4.6). This should lead to greater mixing of HSPs, leading to neutral drift and random cell loss from the TEB, as was shown to be a general feature of TEB progenitors (Scheele et al., 2017). In contrast, APs may rely on a smaller persistent progenitor pool at the TEB tip that gives rise to duct APs in a more linear fashion. Theoretically, this would lead to clonal mixing of HR luminal and basal cells in the duct, but generation of clonal patches of APs. This could be confirmed by large-scale 3D imaging and

analysis of duct clonal patch size in ducts following lineage-specific multi-colour fluorescence tracing.

The motility of HS cells could be an important factor to consider in luminal type cancers that express hormone receptors. It will be of great interest to unravel the molecular drivers of this behaviour and to determine the consequence of blocking HSP migration during morphogenesis and to investigate a role for this in cancer invasion and metastasis. Single cell RNA-seq has pointed to candidate pathways for investigation, particularly Vegf/Vegf1r, which could be stimulated by hypoxia as in angiogenesis. IGF-1 promotes branching during mammary development (Loladze et al., 2006) but may not act specifically on the TEB, as RNA-seq did not did not show differential expression of IGF-1 receptor between the duct and TEB for any population. Region-specific action could still be achieved by local IGF-1 production or differential regulation of the receptor at the protein level. Hypoxia can also promote EMT downstream of HIF1α and is a characteristic of many epithelial tumours (Jiang et al., 2011). Whether tumour hypoxia stimulates HS cell migration in TEBs or luminal cancers is an important question, as mesenchymal-like behaviour is strongly linked to metastasis (Chaffer and Weinberg, 2011).

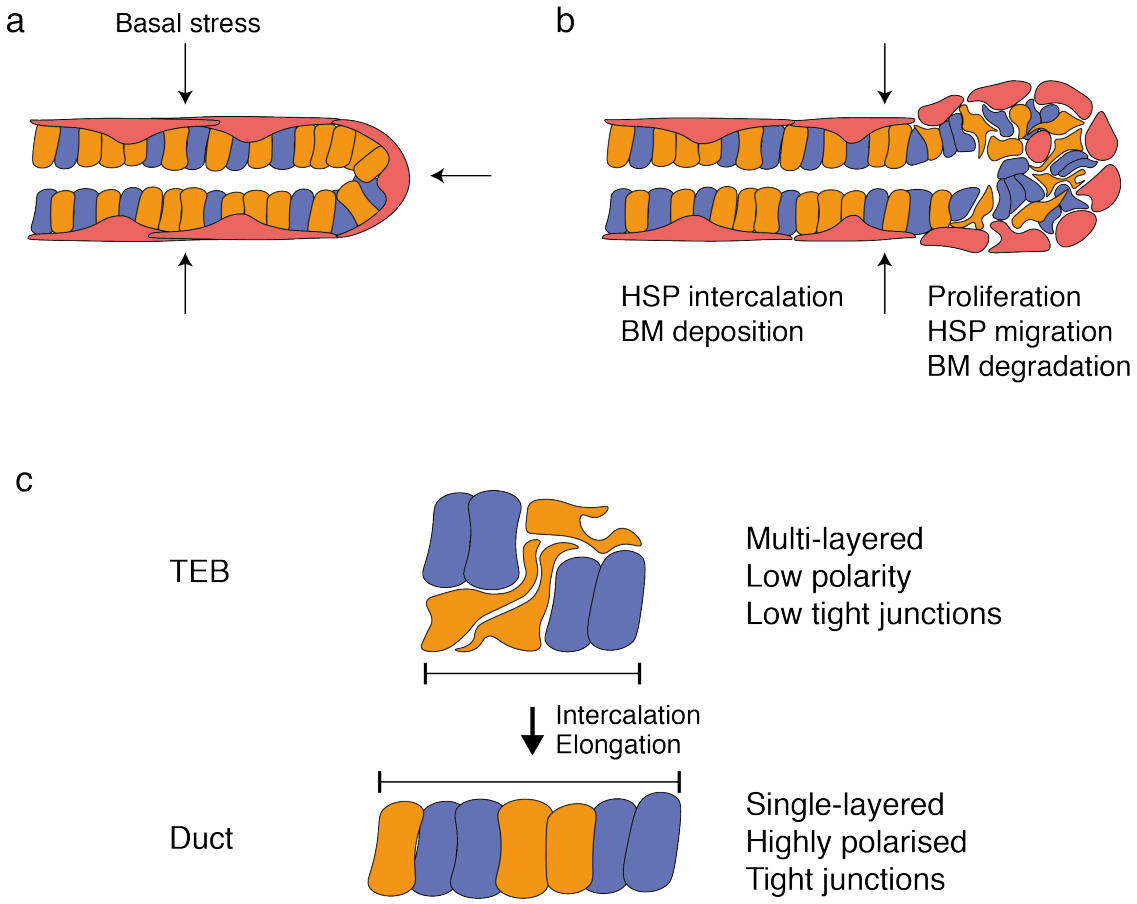

Figure 4.6: Division of labour in TEB formation and duct elongation

(a) Model of a prepubertal terminal duct. The epithelium is arranged in a bilayer with consistent hoop stress (arrows) from the myoepithelium and basement membrane (BM). Red: basal cells, Blue: APs, Yellow: HS cells.

(b) A proposed model of TEB function, where proliferation, HSP migration and basement membrane degradation combine to generate a multilayered bud that allows maintenance of a large progenitor pool. The transition from the TEB to the duct sees increasing hoop stress (arrows) accompanied by HS cell intercalation to create a bilayer.

(c) A proposed model of duct elongation, where HS cell intercalation is the primary force driving duct elongation. The diagram illustrates how HSP migration could maintain a multilayered epithelium and how intercalation of maturing HS cells could result in duct elongation.

Chapter 5: Resident intra-epithelial macrophages survey the entire mammary epithelium and drive remodelling

This Chapter is a manuscript currently under revision following peer review at Nature Cell Biology. It has been included in the submitted form except for changes to formatting and omission of supplementary movies.

Caleb A. Dawson[1,2], Bhupinder Pal[1,2], François Vaillant[1,2], Luke C. Gandolfo[3,4], Zhaoyuan Liu[5], Camille Bleriot[6], Florent Ginhoux[5,6], Gordon K. Smyth[3,4], Geoffrey J. Lindeman[1,7,8], Scott N. Mueller[9,10], Anne C. Rios[1,2,11] and Jane E. Visvader[1,2,11]

[1]Cancer Biology and Stem Cells Division, The Walter and Eliza Hall Institute of Medical Research, Parkville, Victoria 3052, Australia.

[2]Department of Medical Biology, The University of Melbourne, Parkville, Victoria 3010, Australia.

[3]Bioinformatics Division, The Walter and Eliza Hall Institute of Medical Research, Parkville, Victoria 3052, Australia.

[4]School of Mathematics and Statistics, The University of Melbourne, Parkville, Victoria 3010, Australia.

[5]Shanghai Institute of Immunology, Department of Immunology and Microbiology, Shanghai Jiao Tong University School of Medicine, Shanghai 200025, China.

[6]Singapore Immunology Network, Agency for Science, Technology and Research (A*STAR), Singapore 138648, Singapore

[7]Department of Medicine, The University of Melbourne, Parkville, Victoria 3010, Australia.

[8]Parkville Familial Cancer Centre and Department of Medical Oncology, The Royal Melbourne Hospital and Peter MacCallum Cancer Centre, Parkville, Victoria 3050, Australia.

[9]Department of Microbiology and Immunology, The University of Melbourne, at the Peter Doherty Institute for Infection and Immunity, Melbourne, Victoria 3000, Australia.

[10]The Australian Research Council Centre of Excellence in Advanced Molecular Imaging, Melbourne, Victoria 3000, Australia

[11]Joint senior authors

Correspondence should be addressed to J.E.V. at visvader@wehi.edu.au

5.1 Abstract

Macrophages are diverse immune cells that reside in all tissues. Although macrophages have been implicated in mammary gland function, their diversity has not been fully addressed. By exploiting high-resolution 3D imaging and flow cytometry, we have identified a unique population of tissue-resident ductal macrophages (DMs) that form a contiguous network between the luminal and basal layers of the entire mammary gland throughout post-natal development. DMs are long-lived and constantly survey the epithelium though dendrite movement based on advanced 3D intravital imaging. While they initially originate from embryonic precursors, DMs derive from monocytes as they expand during puberty. Moreover, they undergo proliferation in pregnancy to maintain complete coverage of the epithelium in lactation, where they are poised to phagocytose milk-producing cells post-lactation and facilitate remodelling. Interestingly, DMs strongly resemble mammary tumour macrophages and form a network that pervades the tumour epithelium. Thus, the mammary epithelium programs specialised resident macrophages in both physiological and tumorigenic contexts.

5.2 Introduction

Tissue-resident macrophages (MØs) are dispersed throughout all tissues and play essential roles in organ development, function and homeostasis. They are efficient scavengers of apoptotic cells and pathogens and are important regulators of pathogenic conditions such as infection, injury and cancer[1–3]. To account for the diverse stresses and functions of each organ, all tissue microenvironments uniquely program MØs to perform niche-specific functions[4,5]. The broad spectrum of MØ functions include synapse pruning by brain microglia, bone resorption by osteoclasts and clearance of aging red blood cells by spleen red pulp MØs[6]. Tissue-resident MØs initially arise from embryonic precursors in the yolk-sac (microglia) and foetal liver (most other MØs), which generate long-lived resident macrophages with the ability to self-renew[7]. From birth, monocyte-derived MØs gradually replace embryonic MØs at varying rates[8], likely determined by niche accessibility and the longevity of existing MØs[9].

The mammary gland is a highly dynamic organ that undergoes dramatic remodelling throughout life. A rudimentary gland is formed during embryogenesis that remains undeveloped until puberty, when rapid proliferation and migration of terminal end buds (TEBs) culminate in an extensive ductal tree[10]. Mammary ducts consist of a bilayered epithelium of inner luminal cells and outer myoepithelial cells that are embedded in a complex stroma of adipose tissue, extracellular matrix, fibroblasts and immune cells. In pregnancy, further proliferation, remodelling and maturation occur to form milk-producing alveoli that displace the adipose stroma[11]. After lactation, the process of involution returns the gland to its resting state. This phase involves atypical death of alveolar cells[12] and triggers non-inflammatory immune infiltration that is immunosuppressive[13] and resembles wound healing[14], posited to be linked to heightened breast cancer risk[15].

MØs are closely associated with the ductal tree throughout development[16–20] and have been implicated in multiple stages of mammary ontogeny[18,21,22]. Csf1, a growth factor essential for MØ differentiation, is required for proper ductal growth and branching during morphogenesis in puberty[18,23] and alveologenesis in pregnancy[22]. In particular, fetal-derived MØs play a key role in

the promotion of morphogenesis[20]. Mechanistically, MØs within and around TEBs phagocytose apoptotic epithelial cells[18] and organise collagen fibres[24]. Similarly, MØs phagocytose apoptotic alveolar cells during involution[25] and are essential for efficient remodelling, with conditional depletion resulting in delayed death of alveolar cells and reduced repopulation by adipocytes[21]. In the context of the mammary differentiation hierarchy[26], MØs are important for governing stem cell activity[27,28].

The mammary gland is also regulated by other immune compartments: eosinophils promote branching during morphogenesis in puberty[18], while antigen presentation by $CD11c^+$ cells regulates luminal cell differentiation and morphogenesis via T cells[29]. Dendritic-shaped cells that express MHCII[17] and CD11c[29], resembling dendritic cells (DCs) or MØs, have been observed in close association with the epithelium. Analysis of *in vitro* mammary organotypic cultures suggested that these cells could be MØs[29], and while $CD11c^+$ cells were implicated in the regulation of morphogenesis by antigen presentation, the population-specific functions of duct-associated DCs and MØs, their spatial organisation and heterogeneity within the mammary gland have not yet been fully dissected.

Here we use large volume, high-resolution imaging of whole-mount tissue to reveal a unique population of dendritic-shaped, tissue-resident MØs that is exclusively localised to the epithelium. Mammary ductal MØs (DMs) are locally abundant but globally rare in virgin glands compared to stroma-associated MØs, which dominate the mammary MØ landscape. Strikingly, DMs are intercalated between the luminal and myoepithelial layers of ducts and form a contiguous network that actively monitors the entire mammary epithelium through dendrites, thus allowing them to rapidly respond to cell death and execute an essential phagocytic role post-lactation. Finally, DMs share strong similarity with mammary tumour-associated macrophages, implying that the epithelium also programmes MØs to perform a specialised surveillance role during breast tumorigenesis.

5.3 Results

5.3.1 A rare population of macrophages is tightly associated with mammary ducts

To begin to clarify immune regulation of the mammary gland, we explored interactions between the mammary epithelium, dendritic cells (DCs) and MØs by applying large-volume, sub-cellular resolution 3-dimensional (3D) imaging of immunostained and cleared mammary tissue[30]. Whole-mount 3D confocal imaging of adult mammary glands immunostained for the myoepithelial marker Keratin 5 (K5) to label mammary ducts and MHCII to label DCs and MØs showed that these cells are present throughout the stroma and are associated with ducts (Figure 5.1a). To refine the identity of duct-associated cell types, we imaged tissue from *CD11c-GFP* mice co-immunostained for GFP and CD11b (Figure 5.1b), since CD11c marks DCs and some MØs, while CD11b can delineate MØ and DC subtypes[31]. Tissue DCs can typically be subdivided into DC1 ($CD11b^{-}CD103^{+}$) and DC2 ($CD11b^{+}CD103^{-}$), which broadly function to maintain tolerance to self-antigens and induce antigen-specific immune responses[32]. Measurement of $CD11c^{+}$ cell localisation showed that these were frequently associated with mammary ducts (Figure S 5.1a), consistent with previous observations[29]. Duct-associated $CD11c^{+}$ cells had lower levels of CD11b (Figure 5.1b and Figure S 5.1a), suggesting these were either $CD11b^{-}CD103^{+}$ DCs (DC1) or unusual macrophages.

We investigated the phenotype of $CD11c^{+}CD11b^{lo}$ cells by flow cytometric (FACS) analysis of adult mammary glands (Figure 5.1c and Figure S 5.1b). Most DCs ($CD64^{-}$, $F4/80^{-}$ or $MerTK^{-}$, $MHCII^{hi}$ and $CD11c^{+}$) were DC2 (81% of total DCs), while DC1s were rare (3.6% of DCs) (Figure 5.1c). A high proportion (91%) of MØs ($CD64^{+}$ and $F4/80^{+}$) were $CD11c^{lo}CD11b^{+}$ and these could be split into $MHCII^{hi}$ (MØ1) and $MHCII^{lo}$ (MØ2) subsets. We also observed rare $CD11c^{+}CD11b^{lo}Ly6C^{-}$ cells (MØ3: 7.3% MØs), which were likely missed in previous studies due to their rarity and the use of CD11b as a universal myeloid marker. These three MØ populations were positive for the MØ marker MerTK, although MØ3 were $CD64^{lo}MerTK^{lo}$ (Figure S 5.1b), and were confirmed to be MØs and not DCs as they were Csf1-dependent, shown by depletion using anti-Csf1r *in vivo*

(Figure S 5.1c). A previous study identified CD11b^{+}F4/80^{hi}CD206^{+} cells as fetal-derived mammary MØs that were distinct from adult CD11b^{+}F4/80^{lo}CD206^{-} MØs[20]. In our fractionation, we were unable to see discrete F4/80 high and low populations within CD64^{+}MerTK^{+} MØs from 4, 6 or 20–week old females (Figure S 5.1d). Rather, we observed that MØ1 cells were mostly CD206^{+} but contained a minor CD206^{-}MHCII^{hi} population (Figure S 5.1e). MØ2 cells were entirely CD206^{+} and MØ3 were MHCII^{hi}CD206^{-}. In another study, MHCII^{hi}Lyve1^{lo} nerve-associated MØs and MHCII^{lo}Lyve1^{hi} blood vessel-associated MØs were found to exist across tissues[33]. We found that MØ1, MØ2 and MØ3 were Lyve1^{int}, Lyve1^{hi} and Lyve1^{lo}, respectively, indicating possible nerve–association of MØ1/3 and blood vessel-association of MØ2 cells (Figure S 5.1f). Taken together, these findings reveal that mammary MØs are more heterogeneous than expected and indicate that duct-associated MHCII^{+} cells likely comprise rare CD11c^{+}CD11b^{lo} MØs and/or DC1 cells. We also reasoned that the rarity of these populations by FACS could reflect the relatively small volume of ductal tissue in the virgin mammary gland, which is dwarfed in volume and cellularity by the surrounding stromal adipose tissue.

To determine the interaction between DC1 cells and the mammary epithelium, we used *Irf8-YFP* mice, since Irf8 is an established marker of these cells [34,35]. FACS confirmed high expression of YFP in DC1 and low expression in MØ3 (Figure S 5.1g). Co-immunostaining for K5 and YFP and subsequent 3D imaging revealed that Irf8^{hi} DC1 cells were sparse (Figure S 5.1h), however, one third was associated with ducts where they lined the outer myoepithelial surface (0–10 μm, 34%) (Figure S 5.1h-i). Since the frequency of DC1 in contact with the epithelium did not match that seen for CD11c^{+}CD11b^{lo} cells (Figure 5.1b), we imaged mammary tissue from *Csfr1-GFP* mice, which express GFP in MØs[36]. We immunostained for GFP and CD11b to identify CD11b^{lo} MØs (Figure 5.1d). MØs were numerous throughout the tissue but many were in close association with the epithelium (0–10 μm, 32%) (Figure S 5.1j) and these were frequently CD11b^{lo} (Figure 5.1d), closely matching the distribution of CD11c^{+}CD11b^{lo} cells (Figure 5.1b). Overall, these findings indicate that most CD11c^{+} cells associated with the epithelium are CD11b^{lo} MØs.

CD11c^{+} cells were previously shown to negatively regulate branching by antigen presentation to T cells[29] but the identity of these antigen-presenting cells remains unclear. We were not able to

specifically deplete CD11c^{+} MØs to assess their role in this process *in vivo* but explored a role for DC1. CD11c-cre mediated deletion of DC1 in *Irf8*-deficient mice[32,37] led to a modest increase in branching in pubertal female mice (6 weeks) relative to control mammary glands (Figure S 5.2a-b), suggesting that the DC1 subset plays a role in negatively regulating morphogenesis. In addition, we used a cellular ablation model in which cells expressing the Diphtheria toxin (DT) receptor (DTR) are depleted upon DT treatment. CD11b-DTR mice were treated with DT at 5 weeks to deplete a broad range of myeloid cells and mammary glands were analysed at 6 weeks. DT had the largest effect on SMs (50% reduction), presumably because other myeloid populations are quickly replenished (Figure S 5.2c). The ductal tree underwent marked expansion, suggesting that stromal MØs or other myeloid populations also negatively regulate growth. Immune regulation of branching morphogenesis therefore appears to be a complex balance of pro-morphogenic (MØ and eosinophil[38]) and inhibitory (MØ/DC/T cell[29]) factors. Development of tools for specific, long-term ablation of mammary immune populations will be required to fully dissect these phenomena.

5.3.2 Ductal macrophages are entirely dependent on the epithelium

To more precisely define the association between epithelial cells and the different DC and MØ populations, we compared their frequencies in either whole mammary glands, fat pads cleared of epithelium or ducts enriched by partial digestion and manual selection under a dissection microscope. FACS analysis revealed that MØ3 were almost completely absent from fat pads but were enriched 4-fold in isolated ducts (Figure 5.1e). In contrast, no enrichment was seen for other MØs or DCs. Furthermore, implantation of estrogen plus progesterone pellets for 3 weeks, which induces ductal branching and budding (Figure 5.1f), resulted in a 3-fold increase in MØ3 and a slight increase in DC1. Thus, CD11c^{+}CD11b^{lo} MØs are uniquely duct-associated and are responsive to hormone signalling, likely via indirect mechanisms. Given the distinct marker expression and localisation of MØ3, we have termed them mammary ductal MØs or 'DMs', as opposed to their stromal MØ (SM) counterparts (SM1: MHCII^{hi}; SM2: MHCII^{lo}).

5.3.3 CD11c^{+} ductal macrophages possess a distinct gene expression profile implying a unique phagocytic role

To gain further insight into the identity and function of DMs, we sorted DC1, DC2, SM1/2 and DM populations from adult mammary glands for RNA-seq analysis (Figure 5.2a-d and Figure S 5.3a-f**)**. Comparison of populations by multidimensional scaling (MDS) established that DMs possess a gene expression profile that is distinct from the other populations **(**Figure 5.2a). Unique signature genes for each population are shown in Figure 5.2b and Figure S 5.3a-c, as well as genes up- and down-regulated in DMs vs. SM1/2 (Figure S 5.3d). Expression levels of core genes associated with MØs[4] and DCs[39] (Figure S 5.3e, f) affirmed our MØ/DC designations. To identify putative functions for DMs, we performed a canonical pathway enrichment analysis using unique signature genes (Figure 5.2c). DMs were highly enriched for lysosomal genes, indicative of a unique phagocytic role. The lysosomal proteases Hexb, Lgmn and Ctsf were among the top upregulated genes, as well as the matrix metalloproteinase genes Mmp12, 13 and 14, which are important for tissue remodelling (Figure 5.2b). Pathway analysis for DMs versus SM1/2 further revealed that DMs were enriched for Notch signalling (Figure 5.2d). To test for Notch activity, we performed FACS on Hes1-d2GFP mice, which express short half-life GFP only during active Notch signalling[40] (Figure 5.2e). Only DMs exhibited active Notch signalling. Interestingly, MØs have been shown to promote mammary stem cell activity through Wnt signalling downstream of the Notch pathway[28]. DMs are therefore a candidate for this role, although we did not observe specific expression of Wnt pathway genes.

As Cx3cr1 was highly and uniquely expressed by DMs (Figure 5.2b), we assessed GFP expression in *Cx3cr1*$^{GFP/+}$ mice by FACS (Figure 5.2f and Figure S 5.3g). DMs showed very high expression of Cx3cr1-GFP, whereas SM1 and SM2 were mostly Cx3cr1-negative, except for a small population of MHCII^{hi}Cx3cr1^{+} cells. Gene signature comparisons between DMs, SMs and lung macrophage subsets defined by Chakarov et al. [33] revealed that DMs share marked molecular similarity to MHCII^{hi}Lyve1^{lo} lung MØs, while MHCII^{lo}Lyve1^{hi} tissue repair-type macrophages were more aligned with SMs (Figure S 5.3h). To gain insight into potential interactions between DMs and the different epithelial subtypes that constitute the ductal tree, we analysed the

expression of several known ligand-receptor genes that were enriched or highly expressed in DMs (Figure S 5.3i). Of note, the ligand for Cx3cr1, Cx3cl1 was expressed by all epithelial populations, while Csf1 was more highly expressed by basal cells.

5.3.4 Ductal macrophages exclusively occupy an intra-epithelial niche

Whole-mount 3D confocal imaging of mammary tissue from *Cx3cr1*$^{GFP/+}$ mice revealed a contiguous dendritic network of regularly positioned Cx3cr1^{hi} MØs underneath the myoepithelial layer (Figure 5.3a). This localisation was demonstrated by opaque rendering of K5 and GFP signal, which caused the MØ network to be hidden when viewing the outer myoepithelial surface (Figure 5.3a-i) but when the front half of the duct was removed digitally, MØs were clearly visible on the inner myoepithelial surface (Figure 5.3a-ii) and with GFP alone the full 3D network can be seen (Figure 5.3a-iii). This localisation contrasts with DC1 cells, which are not intercalated within the epithelial bilayer but sit outside the basal layer (Figure S 5.1h). By looking through optical sections, we confirmed high *Csf1r-GFP* and *CD11c-YFP*, and low CD11b on MHCII^{hi} intra-epithelial cells, corresponding to DMs (Figure S 5.4a). To further characterise DM–epithelium interactions, we analysed optical sections from 3D images of glands co-immunostained for E-Cadherin, K5 and MHCII (Figure 5.3b). All DMs were sandwiched between the luminal and basal layers, having direct and intimate contact with both the myoepithelial and luminal layers. DMs had no extensions through the myoepithelial layer or into the ductal lumen.

5.3.5 DMs are regularly spaced through the gland during the resting and reproductive phases

Analysis of 3D images of glands immunostained for K5 and MHCII using opaque rendering allowed simple and convenient visualisation of the DM network, without the need for specific fluorescence reporter mice (Figure 5.3c). DMs were present before puberty at 2 weeks (Figure S 5.4b), within TEBs in puberty (Figure S 5.4c), and in alveoli during lactation, where they were tightly associated with stellate-shaped myoepithelial cells (Figure 5.3d and Movie 1) and mirrored the shape of these myoepithelial cells, with dendrites tracking along the myoepithelial

arms. Whole-mount 3D confocal imaging on normal human breast tissue from reduction mammoplasties showed that dendritic-shaped MHCII^{hi} cells were similarly present within the epithelium (Figure 5.3e). We next measured the density of DMs throughout the mouse mammary gland by imaging the nipple, middle and distal regions, as well as the alveoli in lactation, and quantifying the distance between DM cell bodies (Figure 5.3f). DMs were regularly spaced throughout the ducts (mid-region: mean 32 μm) but had a slightly higher density in the nipple region (mean 27 μm) and a lower density around the alveoli (mean 40 μm). Analysis of optical sections through ducts from each region demonstrated that DMs have the same intra-epithelial localisation throughout the entire gland, lying between luminal and basal cells (Figure S 5.4d).

5.3.6 DMs arise from embryonic precursors but are generated from monocytes during puberty

We next sought to determine whether DMs are derived from embryonic precursors and whether they are long-lived. Most fetal MØs (except microglia) are generated from erythro-myeloid progenitor-derived monocytes, in contrast to adult MØs, which are generated from granulocyte-monocyte progenitor (GMP)-derived monocytes[7]. We used the newly developed *Ms4a3-Cre* GMP fate-mapping model that labels all adult-generated MØs while leaving embryonic MØs unlabelled[41,42]. We analysed *Ms4a3-Cre/Rosa-tdTomato* mice at 4, 6 and 20 weeks and found that 80% of DMs were of embryonic origin at 4 weeks (Figure 5.3g). However, as only 46% were of embryonic origin at 6 weeks, DMs arising in puberty must have been seeded by monocytes during the rapid expansion of DMs (6.1-fold change) in this morphogenic phase. Mammary tissue monocytes (93.6%) and neutrophils (97.2%) were efficiently labelled, whereas Kupffer cells, which are embryonic derived, showed only 2.8% labelling (not shown). By 20 weeks, approximately 35% of DMs were of embryonic origin, indicating that seeding by monocytes slows dramatically in adulthood. SM1 and SM2 also displayed a high proportion of embryonic origin before puberty (SM1: 64%, SM2: 73%), however, rather than a rapid increase during puberty, these showed a constant, slow rate of seeding by monocytes that was independent of developmental stage. Interestingly, the proportion of SM1 increased as mice aged after puberty, whereas SM2 cells decreased.

Prepubertal DMs may arise from very few precursors at birth, based on 3D confocal imaging of the entire mammary rudiment at E18.5 and early post-natal mammary glands (day 4 and 7) from Cx3cr1-GFP reporter mice immunolabelled for MHCII and K5. Rare, rounded, Cx3cr1^{+}MHCII^{-} cells were present within the distal tips at E18.5 glands but were completely absent in other regions of the epithelium (Figure S 5.5a). At postnatal day 4, dendritic-shaped Cx3cr1^{+}MHCII^{-} cells were present at the distal tips but were rare in ducts and the nipple region (Figure S 5.5b). By day 7, dendritic-shaped Cx3cr1^{+} cells were more widespread and were MHCII^{+} (Figure S 5.5c). Taken together, these data indicate that DMs may arise from a small number of distal Cx3cr1^{+}MHCII^{-} precursors that gradually migrate towards the nipple and upregulate MHCII in the first weeks of life. However, there were many stromal Cx3cr1^{+} cells in the early postnatal gland and surrounding TEBs that may represent a precursor population.

5.3.7 DMs have a slow rate of turnover in the resting gland

To assess MØ turnover in adulthood, 8 week-old mice were irradiated while shielding the 4th and 5th mammary glands and then transplanted with 2x10^{6} GFP^{+} bone marrow cells (Figure 5.3h). After 3 months, 30.9% of DMs had been replaced (monocyte GFP% normalised to 100%), compared to 55.9% of SM1 and 12.1% of SM2, showing that DMs are indeed long-lived, despite being largely monocyte-derived after puberty. The persistence of abundant embryonic SM1 and SM2 through puberty suggests that these may promote morphogenesis, as loss of embryonic MØs perturbs mammary gland formation[20].

5.3.8 DMs monitor the entire epithelium through dendrite movement

To examine the dynamics of DM-epithelial interactions in their native environment, we implemented 3D sub-cellular resolution intravital microscopy (3D-IVM) of mammary ducts using multiphoton technology. This was achieved through modification of the skin-flap technique[43–45] to expose an entire mammary ductal tree, enabling selection of ducts that had minimal overlying fat and were therefore more accessible for 3D imaging *in vivo* (Figure S 5.6a). High-resolution 3D-IVM of the ductal tree with other techniques such as the mammary window[46]

is problematic due to the challenge of light-scattering fatty tissue and limited tissue access. The skin-flap approach allowed removal of connective tissue overlying the fat pad without impacting the mammary gland. Multiphoton imaging was performed for up to 12 hours and provided sub-cellular resolution to 300 μm depth, spanning entire ducts. To visualise the epithelium, we used *Elf5-rtTA-IRES-GFP* mice (*Elf5-GFP*), which express GFP in luminal progenitor cells[47], while DMs were identified by conjugated anti-MHCII antibody or the use of *Cx3cr1*$^{GFP/+}$ reporter mice. DM-specific MHCII signal adjacent to *Elf5-GFP* signal was isolated post-acquisition by masking using *Elf5-GFP* surface rendering (Figure S 5.6b). Imaging of 3D volumes of ducts at 5 – 10 minute intervals revealed that DMs do not migrate but dynamically move dendrites to transiently contact each other and monitor the epithelium (Figure 5.4a and Movie 2). Anti-MHCII antibody did not affect DM behaviour, as identical behaviour was observed in *Cx3cr1*$^{GFP/+}$ mice (Figure S 5.6c and Movie 3). DM behaviour was quantified through manual tracking of DM cell bodies, dendrites and stromal MHCII^{+} cells in 3D (Figure 5.4b), showing movement of dendrites but not the cell body, in contrast to the migratory stromal MHCII^{+} cells. Calculation of the epithelial area covered by DMs showed that these cells contacted 30% of the epithelium at any given time (Figure 5.4c). A cumulative map of DM area versus time showed a doubling of contact area to 60% within an hour and a further increase to over 80% within 3 hours (Figure 5.4c). Therefore, all luminal and myoepithelial cells across the entire mammary gland are regularly contacted by DMs through dendrite movement.

To address a role for DMs in monitoring the epithelium for damage or cell death, we used a multiphoton laser pulse to induce epithelial damage in exquisitely targeted points in 3D during 3D-IVM (less than 5-10 μm). Immediately following laser damage, DMs migrated or extended dendrites towards the damaged area to form stable interactions (Figure S 5.6c and Movie 3), consistent with 'cloaking' behaviour, which shields tissue damage from inflammatory neutrophils[48]. Furthermore, whole-mount 3D confocal imaging showed that 70% of cleaved caspase 3^{+} (CC3) apoptotic epithelial cells were in direct contact with DMs and these were often partially or fully engulfed (Figure 5.4d). 3D-IVM of ducts with apoptotic cells labelled with propidium iodide allowed observation of rare events when DMs phagocytosed apoptotic epithelial cells (Figure 5.4e and Movie 4).

5.3.9 Proliferation contributes to rapid DM expansion in pregnancy

To quantify the population dynamics of DMs during remodelling of the mammary epithelia we performed FACS analysis on mammary glands during puberty and the reproductive cycle (Figure 5.5a). While DMs were rare in adult glands (0.64% of total cells), they expanded markedly during pregnancy (40–fold) and constituted 25.7% of total cells in lactation, while DCs and other MØs decreased in lactation. Comparison of the DM/epithelial cell ratio in virgin and pregnant glands revealed that DMs increase in proportion relative to the epithelium, suggesting that they respond to pregnancy-specific cues rather than passively filling the expanding niche (Figure S 5.7a). Involution led to a rapid decrease in DMs and an infiltration of SMs, which was resolved post-involution, when proportions were similar to that in virgin glands. To determine whether proliferation underlies DM expansion in pregnancy, we analysed glands from virgin and 16.5 day pregnant mice treated with EdU for 2 hours (Figure 5.5b and Figure S 5.7b). No EdU^+ DMs were observed in young adult mice, however, 5% of DMs were EdU^+ in pregnancy, in accordance with the ability of DMs to proliferate in parallel with epithelial expansion to maintain high density coverage of the ductal tree and alveoli.

Despite this proliferation, monocyte infiltration could also contribute to DM expansion. To address this, we sought to analyse bone marrow chimeras in pregnancy. Even with shielded irradiation, however, females were unable to become pregnant. We therefore induced a pregnancy-like state in bone marrow chimeras after 2 months recovery by implanting pellets containing estrogen and the progestin medroxyprogesterone acetate (MPA) or placebo pellets. Following three weeks of hormone treatment, the proportion of newly generated DMs did not increase, indicating that DM expansion can be driven by proliferation alone (Figure 5.5c). Nonetheless, derivation from monocytes may have a greater role in late pregnancy, when the gland undergoes extensive morphogenesis.

5.3.10 The DM transcriptome changes through the reproductive cycle but returns to a resting state

We next performed RNA-seq on DMs sorted from mammary glands derived from virgin, day 16 pregnancy, lactating and post-involution (1 month) mice (Figure 5.5d-h). Many genes were differentially expressed (DE) between these stages (adjusted P-value <0.01: Virgin vs Preg (day 16.5), 204 genes; Preg vs Lact, 330 genes), whereas there were few DE genes between DMs from virgin versus post-involution glands (38 genes). This was reflected in an MDS plot, which revealed divergent pregnant and lactating states, but a return to a resting state following involution (Figure 5.5e). Interestingly, DMs from both late pregnancy and lactation expressed high levels of milk protein transcripts, potentially indicating phagocytosis of epithelial cells during these phases. Overall, the lactational transcriptome of DMs was markedly different from that of pregnancy: pathway analysis revealed enrichment for cell cycle and estrogen response genes in pregnancy and enrichment of RANKL/NF-κB, Notch, EGF and several immune modulatory pathways in lactation (Figure 5.5g). Moreover, anti-inflammatory (IL-10) and Th17-related (IL-23, IL-1, IL-22, IL17-A) pathways dominated the lactational molecular profile, suggesting a role for DMs in promoting the immunosuppressive mucosal immune environment that is prominent during lactation and involution[13]. Post-involution DMs only displayed weak enrichments, which surprisingly featured mammary epithelial and breast cancer pathways, as well as iron and lipid metabolism pathways (Figure 5.5h).

5.3.11 DMs are essential for alveolar cell phagocytosis during involution

As DMs dominate the immune compartment of lactating mammary glands, and therefore the microenvironment upon weaning, we investigated a possible role for DMs in tissue remodelling accompanying alveolar cell death in early involution. To observe DM morphology through involution, we performed 3D imaging of alveoli in lactation and at 2 and 4 days of involution (Figure 5.6a). At 2 days post-weaning, alveolar lumen had swollen but alveolar structure and DM morphology remained the same. At 4 days of involution, alveoli had collapsed and the lumen were filled by $MHCII^+$ cells that surrounded $CC3^+$ cells. The lumenal $MHCII^+$ cells represented

Cx3cr1^{hi} DMs (Figure S 5.7c). To further characterise DM infiltration of the lumen, we performed 3D rendering of alveoli and DMs. In lactation, when alveoli were large and DMs highly dendritic, alveolar volume occupied by DMs was 5.2% (±1.3 s.d.) (Figure 5.6b-c). At 4 days involution, the alveoli were small and DMs were rounded, forming a large mass that occupied 54.0% (±19.6 s.d.) of alveolar volume. These data suggest that DMs phagocytose alveolar cells in early involution. We reasoned that large-scale phagocytosis might affect DM isolation by FACS, leading to an under-estimation of DM number in early involution (Figure 5.5a), as they were clearly visible in 3D images. To further characterise phagocytic events, we performed 3D imaging of *Elf5-GFP* glands at 3 days involution, when alveoli had not yet collapsed and phagocytosis could be observed more clearly (Figure 5.6d and S7d). 13.84% (±10.27 s.d.) of large GFP$^+$ alveolar cells were surrounded by diffuse MHCII signal in direct contact with DMs. Phagocytosed alveolar cells exhibited lower GFP intensity than viable neighbours but were characteristically binucleated[49], confirming their identity. To investigate the dynamics of alveolar cell phagocytosis, we applied 3D-IVM in *Elf5-GFP* mice at 3 days involution and observed direct engulfment of GFP$^+$ alveolar cells by DMs (Figure S 5.7e and Movie 5). Phagocytosis occurred resulted in areas of lower GFP intensity and dispersed MHCII signal, corroborating our findings by 3D imaging.

To explore the functional importance of phagocytosis by DMs, we used the CD11c-DTR depletion model, which allows short-term depletion of CD11c$^+$ cells. We administered DT immediately upon forced weaning, when DMs represent the vast majority of CD11c$^+$ cells in the mammary gland (94.2%, Figure 5.6a). This led to ablation of DMs and a decrease in DCs by 1 day involution (Figure S 5.7f). At day 4 involution, DMs had not yet recovered and DC1s remained reduced (Figure S 5.7g), accompanied by a marked delay in remodelling and the persistence of large alveolar lumina (Figure 5.6e-f). DCs were surprisingly present 4 days after DT treatment, possibly because involution stimulates DC recruitment in the period[13]. Regardless, whole-mount 3D confocal imaging of DM-depleted alveoli at 4 days involution revealed the absence of MHCII$^+$ cells within alveoli and loss of CC3$^+$ alveolar cell phagocytosis (Figure 5.6g and Figure S 5.7g). DMs were not replaced in the alveoli, indicating that other immune populations are unable to fulfil this role. DMs, therefore, play a crucial and non-redundant role in remodelling post-lactation. Imaging of DMs at 6 days involution revealed CC3 staining, indicating that they

undergo apoptosis after the brief phagocytic event to return to resting-state numbers (Figure S 5.7i).

5.3.12 DMs persist within the epithelium throughout tumorigenesis

Tumour-associated MØs (TAMs) promote breast cancer progression and metastasis and their presence is correlated with poor prognosis[50]. Breast TAMs are heterogeneous and include a major population that is CD11c^{+},CD11b^{lo}[51,52], Cx3cr1^{hi}, VCAM1^{hi}, Notch-dependent[51], highly phagocytic[53,54] and capable of proliferation[51,52]. These features bear strong similarity to DMs. Furthermore, intra-epithelial MØs have been reported in hyperplastic lesions[55] but it was not determined whether these were a distinct population of MØs. Comparison of the gene expression signatures of tumour-associated macrophages (TAMs) and mammary tissue macrophages (MTM) [51] with our data revealed that TAMs closely align with the signature of DMs (roast p-value < 1e-5) (Figure 5.7a). Moreover, the MTM population was more concordant with SMs, suggesting that MTMs are indeed enriched for stromal macrophages while DMs share properties with TAMs.

To explore the possibility that the mammary epithelium continues to program unique intra-epithelial MØs during neoplasia, we profiled the myeloid compartment of preneoplastic mammary tissue and tumours from the *MMTV-PyMT, MMTV-Neu* and *MMTV-Wnt1* transgenic mouse models (Figure S 5.8a-d). CD11b expression on MØs was variable, increasing on CD11c^{+} MØs in tumours (Figure S 5.8a), while Ly6C remained low on CD11c^{+} MØs (Figure S 5.8b), enabling consistent identification. Ly6C^{-}CD11c^{+} DM-like MØs increased in *PyMT* and *Neu* hyperplastic glands and constituted the major population of TAMs in tumours from all models (Figure S 5.8b-c), consistent with previous studies[51,52]. To further characterise phenotypic changes in the MØ compartment during tumorigenesis, we analysed MHCII and Cx3cr1-GFP expression on Ly6C$^{-/+}$CD11c^{-} SM-like TAMs and Ly6C^{-}CD11c^{+} DM-like TAMs (Figure 5.7b and Figure S 5.8d). DM-like TAMs maintained high expression of Cx3cr1-GFP and showed a slight shift towards MHCII-low expression. SM-like TAMs, although rare, underwent a shift from MHCII^{-}Cx3cr1^{-} to MHCII^{+}Cx3cr1^{+}, perhaps reflective of a relationship between rare Cx3cr1^{+} SMs (Figure 5.7b) and the tumorigenic epithelium.

To study the localisation and architecture of TAMs in detail, we performed 3D imaging on *MMTV-PyMT/Cx3cr1*$^{GFP/+}$ and *MMTV-Wnt1/Cx3cr1*$^{GFP/+}$ tumours. DM-like Cx3cr1^{hi} intra-epithelial TAMs were found to create a network within the tumour epithelium (Figure 5.7c and Movie 6). These were not arranged in a planar network as in the normal gland but were dispersed throughout the tumour volume in 3D. Tumours were surrounded by a dense population of Cx3cr1^{+} MØs, which may correspond to SM-like TAMs. To further strengthen the connection between DMs and intra-epithelial TAMs, we sought to find a marker that could specifically identify DM-like TAMs. We identified TMEM119 as uniquely expressed in DMs by RNA-seq (Figure 5.2b) and found that this labelled dendritic-shaped intra-epithelial cells with high specificity (Figure S 5.8e). These data indicate that despite being monocyte-derived[51], epithelial-educated MØs continue to monitor the epithelium throughout oncogenesis as a continuation of the function of tissue-resident MØs in the steady-state gland, rather than representing a *de novo* tumour-educated population.

5.4 Discussion

In this study, we identify a previously uncharacterised tissue-resident MØ population in the mouse mammary gland. The direct contact between DMs and the mammary epithelium throughout ductal morphogenesis and reproduction places DMs in a prime position for surveillance of damaged or dying cells (Figure 5.7d). While some DCs are in close proximity to the epithelium, DMs are uniquely confined to the basal-luminal interface. DMs are initially embryonic, have a low rate of turnover and proliferate during pregnancy, establishing DMs as a *bona fide* tissue-resident MØ population that holds an intimate relationship with the epithelium. Their unique gene expression profile and intra-epithelial niche suggest that these cells are highly adapted to perform mammary gland-specific roles in homeostasis and reproduction. The existence of DMs in human breast ducts implies parallel roles. The similarity of stromal MØs to tissue-repair MØs indicates that these may regulate inflammation in the mammary adipose stroma.

Ductal macrophages initially arise from embryonic precursors and appear to originate from very few cells within the embryonic rudiment. Despite the early presence of DMs, they slowly progress to full coverage of the ductal tree, making them a dominant feature within the epithelium only from puberty, when they rapidly increase in number. From our data, it seems that the passage of monocytes across the basement membrane to generate DMs may be limited. However, TEBs in pubertal glands lack a basement membrane around the cap cell region, and this may allow monocytes to enter during this phase. In adulthood and early pregnancy, DM expansion appears to be reliant on proliferation rather than monocyte infiltration. Whether any embryonic DMs remain in the gland in the longer term or during the reproductive cycle remains an interesting and open question.

One of the key functions of DMs is to rapidly clear alveolar cells during involution to return the mammary gland to its prepregnant state. Targeted ablation of DMs in early involution revealed that other immune populations were unable to compensate and clear alveolar cells in the absence of DMs. The non-redundant requirement of a specialised population for this process implies that the strategic localisation and unique molecular features of DMs are essential for rapid and non-inflammatory resolution of involution. Infiltration of wound healing MØs has been observed during involution, peaking at days 6 and 8[14,19], after the period of phagocytosis mediated via DMs. Therefore, while DMs are the most prevalent and active at the onset of involution, other MØ populations likely play roles in the later stages of involution, including adipose tissue regeneration. Other studies have indicated that phagocytosis of luminal debris is performed by epithelial cells and not macrophages[56,57]. Both phenomena may occur, whereby epithelial cells clear debris from the alveolar lumen and are then phagocytosed by DMs. In the steady-state mammary gland, it is plausible that DMs are responsible for previously reported mammary MØ functions, such as promotion of mammary stem cell (MaSC) activity through Wnt signalling[28], promotion of morphogenesis[18,23] and regulation of alveologenesis[22]. MØs have been suggested to participate in a paracrine loop where epithelial Notch ligand Dll1 induces MØ Wnt signalling to MaSCs[28]. DMs showed high *Hes-1*-driven reporter activity and exhibited a signature enriched for Notch pathway activity compared to SMs and DCs, thus implicating DMs in this process. Wnt signalling, however, was not enriched in DMs but this may reflect temporal or spatial regulation

that was lost in pooling of samples and bulk population analysis. It is yet to be determined whether DMs directly govern stem cell activity.

Both normal and tumour epithelia harbour specialised MØs that perform a surveillance role. Previous studies have found that mammary tumour MØs are distinct from normal tissue MØs[51,55]. Our work helps clarify this observation through the discovery of altered proportions of distinct and pre-existing MØ populations in the adult mammary gland. These changes may reflect altered MØ niches, with expansion of the epithelial DM niche occurring in tumours and pregnancy-lactation with a commensurate decrease in the adipose-rich SM niche during these phases. Given that DMs constantly monitor the epithelium with dendrites to enable rapid detection of damage and apoptotic cells, these cells likely perform the same function in preneoplastic glands, possibly representing the first immune contact in perturbed tissue. Whether DMs can respond to these changes and activate or suppress a subsequent immune response pose important questions for the future. Their central role in involution together with their molecular signature in lactation imply an immuno-suppressive role. Indeed, DM-like TAMs can suppress cytotoxic T cell activity and promote tumour progression[51]. Thus, inhibition of DM function could represent a possible preventive therapy for breast cancer.

5.5 References

1. Lavin, Y. & Merad, M. Macrophages: gatekeepers of tissue integrity. *Cancer Immunology Research* **1,** 201–209 (2013).

2. Varol, C., Mildner, A. & Jung, S. Macrophages: development and tissue specialization. *Annual Reviews Immunology* **33,** 643–675 (2015).

3. Wynn, T. A., Chawla, A. & Pollard, J. W. Macrophage biology in development, homeostasis and disease. *Nature* **496,** 445–455 (2013).

4. Gautier, E. L. *et al.* Gene-expression profiles and transcriptional regulatory pathways that underlie the identity and diversity of mouse tissue macrophages. *Nature* **13,** 1118–1128 (2012).

5. Lavin, Y. *et al.* Tissue-resident macrophage enhancer landscapes are shaped by the local microenvironment. *Cell* **159,** 1312–1326 (2014).

6. Gordon, S. & Plüddemann, A. Tissue macrophages: heterogeneity and functions. *BMC Biology* **15,** 53 (2017).

7. Hoeffel, G. & Ginhoux, F. Ontogeny of Tissue-Resident Macrophages. *Front Immunol* **6,** 486 (2015).

8. Ginhoux & Guilliams. Tissue-resident macrophage ontogeny and homeostasis. (2016). doi:10.1016/j.immuni.2016.02.024

9. Guilliams, M. & Scott, C. L. Does niche competition determine the origin of tissue-resident macrophages? *Nat. Rev. Immunol.* **17,** 451–460 (2017).

10. Daniel, Silberstein & Strickland. Direct action of 17 beta-estradiol on mouse mammary ducts analyzed by sustained release implants and steroid autoradiography. *Cancer Res* **47,** 6052–7 (1987).

11. Macias, H. & Hinck, L. Mammary gland development. *Wiley Inderdisciplinary Reviews: Developmental Biology* **1,** 533 (2012).

12. Watson, C. J. & Kreuzaler, P. A. Remodeling mechanisms of the mammary gland during involution. *Int. J. Dev. Biol.* **55,** 757–62 (2011).

13. Betts, C. B. *et al.* Mucosal Immunity in the Female Murine Mammary Gland. *J. Immunol.* **201,** 734–746 (2018).

14. Martinson, H., Jindal, S., Durand-Rougely, C., Borges, V. & Schedin, P. Wound healing-like immune program facilitates postpartum mammary gland involution and tumor progression. *International Journal of Cancer* (2015). doi:10.1002/ijc.29181

15. Lyons, T. R. *et al.* Postpartum mammary gland involution drives progression of ductal carcinoma in situ through collagen and COX-2. *Nat. Med.* **17,** 1109–15 (2011).

16. Chua, A., Hodson, L., Moldenhauer, L., Robertson, S. & Ingman, W. Dual roles for macrophages in ovarian cycle-associated development and remodelling of the mammary gland epithelium. *Development* **137,** 4229–4238 (2010).

17. Sun, X., Robertson, S. & Ingman, W. Regulation of epithelial cell turnover and macrophage phenotype by epithelial cell-derived transforming growth factor beta1 in the mammary gland. *Cytokine* **61,** 377–388 (2013).

18. Gouon-Evans, V., Rothenberg, M. E. & Pollard, J. W. Postnatal mammary gland development requires macrophages and eosinophils. *Development* **127,** 2269–2282 (2000).

19. O'Brien, J. *et al.* Alternatively activated macrophages and collagen remodeling characterize the postpartum involuting mammary gland across species. *Am J Pathology* **176,** 1241–55 (2010).

20. Jäppinen, N. *et al.* Fetal-derived macrophages dominate in adult mammary glands. *Nat Commun* **10,** 281 (2019).

21. O'Brien, J., Martinson, H., Durand-Rougely, C. & Schedin, P. Macrophages are crucial for epithelial cell death and adipocyte repopulation during mammary gland involution. *Development* **139,** 269–275 (2012).

22. Pollard, J. W. & Hennighausen, L. Colony stimulating factor 1 is required for mammary gland development during pregnancy. *Proceedings of the National Academy of Sciences* **91,** 9312–9316 (1994).

23. Nguyen, A. & Pollard, J. Colony Stimulating Factor-1 Is Required to Recruit Macrophages into the Mammary Gland to Facilitate Mammary Ductal Outgrowth. *Dev Biol* **247,** 11–25 (2002).

24. Ingman, W. V., Wyckoff, J., Gouon-Evans, V., Condeelis, J. & Pollard, J. W. Macrophages promote collagen fibrillogenesis around terminal end buds of the developing mammary gland. *Dev. Dyn.* **235,** 3222–9 (2006).

25. Walker, N., Bennett, R. & Kerr, J. Cell death by apoptosis during involution of the lactating breast in mice and rats. *Am J Anat* **185,** 19–32 (1989).

26. Visvader, J. E. Keeping abreast of the mammary epithelial hierarchy and breast tumorigenesis. *Genes & Development* **23,** 2563–2577 (2009).

27. Gyorki, D. E., Asselin-Labat, M.-L., Rooijen, N. van, Lindeman, G. J. & Visvader, J. E. Resident macrophages influence stem cell activity in the mammary gland. *Breast Cancer Research* **11,** R62 (2009).

28. Chakrabarti, R. *et al.* Notch ligand Dll1 mediates cross-talk between mammary stem cells and the macrophageal niche. *Science* eaan4153 (2018). doi:10.1126/science.aan4153

29. Plaks, V. *et al.* Adaptive immune regulation of mammary postnatal organogenesis. *Developmental Cell* **34,** 493–504 (2015).

30. Rios, A. C. *et al.* Intraclonal Plasticity in Mammary Tumors Revealed through Large-Scale Single-Cell Resolution 3D Imaging. *Cancer Cell* **35,** 618–632.e6 (2019).

31. Yu, Y.-R. A. R. *et al.* A Protocol for the Comprehensive Flow Cytometric Analysis of Immune Cells in Normal and Inflamed Murine Non-Lymphoid Tissues. *PLoS ONE* **11,** e0150606 (2016).

32. Ginhoux, F. *et al.* The origin and development of nonlymphoid tissue CD103+ DCs. *J. Exp. Med.* **206,** 3115–30 (2009).

33. Chakarov, S. *et al.* Two distinct interstitial macrophage populations coexist across tissues in specific subtissular niches. *Science* **363,** eaau0964 (2019).

34. Schiavoni, G. *et al.* ICSBP is essential for the development of mouse type I interferon-producing cells and for the generation and activation of CD8alpha(+) dendritic cells. *J. Exp. Med.* **196,** 1415–25 (2002).

35. Wang, H. *et al.* A reporter mouse reveals lineage-specific and heterogeneous expression of IRF8 during lymphoid and myeloid cell differentiation. *J. Immunol.* **193,** 1766–77 (2014).

36. Sasmono, R. *et al.* A macrophage colony-stimulating factor receptor–green fluorescent protein transgene is expressed throughout the mononuclear phagocyte system of the mouse. *Blood* **101,** 1155–1163 (2003).

37. Feng, J. *et al.* IFN regulatory factor 8 restricts the size of the marginal zone and follicular B cell pools. *J. Immunol.* **186,** 1458–66 (2011).

38. Gouon-Evans, V., Lin, E. Y. & Pollard, J. W. Requirement of macrophages and eosinophils and their cytokines/chemokines for mammary gland development. *Breast Cancer Res.* **4,** 155–64 (2002).

39. Miller, J. C. *et al.* Deciphering the transcriptional network of the dendritic cell lineage. *Nat. Immunol.* **13,** 888–99 (2012).

40. Ohtsuka, T. *et al.* Visualization of embryonic neural stem cells using Hes promoters in transgenic mice. *Mol. Cell. Neurosci.* **31,** 109–22 (2006).

41. Liu, Z. *et al.* Fate mapping via Ms4a3 expression history traces monocyte-derived cells. *Biorxiv* 652032 (2019). doi:10.1101/652032

42. Jaitin, D. *et al.* Lipid-Associated Macrophages Control Metabolic Homeostasis in a Trem2-Dependent Manner. *Cell* (2019). doi:10.1016/j.cell.2019.05.054

43. Ewald, A. J., Werb, Z. & Egeblad, M. Monitoring of vital signs for long-term survival of mice under anesthesia. *Cold Spring Harbor Protocols* **2011,** 174–177 (2011).

44. Ewald, A. J., Werb, Z. & Egeblad, M. Preparation of mice for long-term intravital imaging of the mammary gland. *Cold Spring Harbor Protocols* **2011,** 168–173 (2011).

45. Hor, J. L. *et al.* Spatiotemporally distinct interactions with dendritic cell subsets facilitates CD4+ and CD8+ T cell activation to localized viral infection. *Immunity* **43,** 554–565 (2015).

46. Kedrin, D. *et al.* Intravital imaging of metastatic behavior through a mammary imaging window. *Nature methods* **5,** 1019–1021 (2008).

47. Rios, A. C., Fu, N. Y., Lindeman, G. J. & Visvader, J. E. In situ identification of bipotent stem cells in the mammary gland. *Nature* **506,** 322–327 (2014).

48. Uderhardt, S., Martins, A., Tsang, J., Lämmermann, T. & Germain, R. Resident Macrophages Cloak Tissue Microlesions to Prevent Neutrophil-Driven Inflammatory Damage. *Cell* (2019). doi:10.1016/j.cell.2019.02.028

49. Rios, A. C. *et al.* Essential role for a novel population of binucleated mammary epithelial cells in lactation. *Nature Communications* **7,** 11400 (2016).

50. Qian, B.-Z. & Pollard, J. W. Macrophage diversity enhances tumor progression and metastasis. *Cell* **141,** 39–51 (2010).

51. Franklin, R. A. *et al.* The cellular and molecular origin of tumor-associated macrophages. *Science* **344,** 921–925 (2014).

52. Tymoszuk, P. *et al.* In situ proliferation contributes to accumulation of tumor-associated macrophages in spontaneous mammary tumors. *European Journal of Immunology* **44,** 2247–2262 (2014).

53. Broz, M. L. *et al.* Dissecting the tumor myeloid compartment reveals rare activating antigen-presenting cells critical for T cell immunity. *Cancer Cell* **26,** 638–652 (2014).

54. Engelhardt, J. J. *et al.* Marginating dendritic cells of the tumor microenvironment cross-present tumor antigens and stably engage tumor-specific T cells. *Cancer Cell* **21,** 402–417 (2012).

55. Linde, N. *et al.* Macrophages orchestrate breast cancer early dissemination and metastasis. *Nature Communications* **9,** 21 (2018).

56. Monks, J. *et al.* Epithelial cells as phagocytes: apoptotic epithelial cells are engulfed by mammary alveolar epithelial cells and repress inflammatory mediator release. *Cell Death Differ.* **12,** 107–14 (2005).

57. Monks, J., Smith-Steinhart, C., Kruk, E., Fadok, V. & Henson, P. Epithelial Cells Remove Apoptotic Epithelial Cells During Post-Lactation Involution of the Mouse Mammary Gland. *Biology of Reproduction* **78,** 586–594 (2008).

5.6 Acknowledgements

We thank W Alexander, M Kauppi and A Stock for assistance with chimera experiments, F Jackling for animal management, M Chopin and S Nutt for providing mice, Y Hu for bioinformatic assistance, S Naik, J Schreuder and D Lin for discussions, and C Nowell at the MIPS imaging facility. We are grateful to the WEHI imaging, flow cytometry and animal facilities.

Funding: This work was supported by the Australian National Health and Medical Research Council (NHMRC) grants #461221, #1016701, #1024852, #1054618; NHMRC IRIISS; the Victorian State Government through VCA funding and Operational Infrastructure Support; and the Australian Cancer Research Foundation. C.A.D was supported by an Australian Government Research Training Program Scholarship; A.C.R. was supported by a National Breast Cancer Foundation (NBCF)/Cure Cancer Australia Fellowship; B.P., G.K.S., G.J.L. by NHMRC Fellowships #1042629, #490037, #637307; J.E.V. by NHMRC Fellowships #1037230 and 1102742; S.N.M. by NHMRC Fellowship #1136550.

Author contributions: C.A.D. designed and performed experiments, analysed data and wrote the manuscript. B.P. performed RNA-seq experiments. L.C.G. and G.K.S. analysed RNA-seq data. G.J.L. provided general guidance. S.N.M. designed experiments. A.C.R designed experiments and provided general guidance. J.E.V. designed experiments, provided general guidance and co-wrote the manuscript. Competing interests: The authors declare no competing interests.

Data availability: The RNA-seq data is available as GEO series GSE119869. The imaging datasets generated and analysed in this study are not publicly available due to size but are available from J.E.V. upon reasonable request. Other data are available from J.E.V. upon reasonable request.

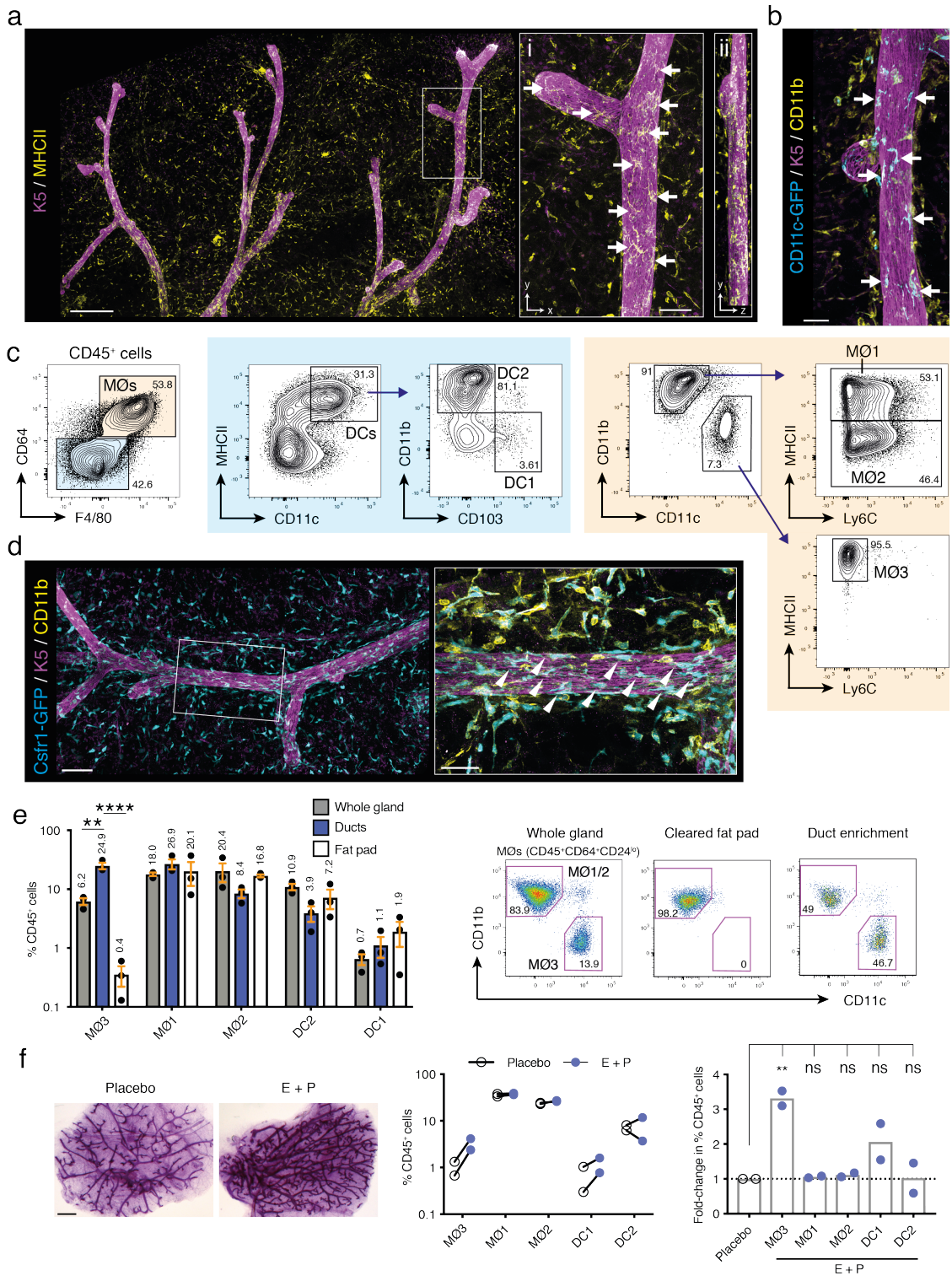
a
K5 / MHCII
i
ii
b
CD11c-GFP / K5 / CD11b
c
CD45⁺ cells
MØs
53.8
42.6
CD64
F4/80
MHCII
31.3
DCs
CD11c
CD11b
DC2
81.1
3.61
DC1
CD103
91
7.3
MØ1
53.1
MØ2
46.4
Ly6C
95.5
MØ3
d
Csfr1-GFP / K5 / CD11b
e
Whole gland
Ducts
Fat pad
% CD45⁺ cells
MØ3
MØ1
MØ2
DC2
DC1
Whole gland
MØs (CD45⁺CD64⁺CD24ʷᵉ)
Cleared fat pad
Duct enrichment
MØ1/2
83.9
98.2
49
46.7
f
Placebo
E + P
Placebo
E + P
Fold-change in % CD45⁺ cells
ns

5.7 Figures

Figure 5.1: Macrophage and dendritic cell populations show differential association with mammary ducts

(a) Whole-mount 3D confocal image of mammary tissue from a mouse at 10 weeks of age (adult virgin), covering large areas of duct and stroma. Glands were immunostained for Keratin-5 (K5) (magenta) and MHCII (yellow). Inset regions are 3D-projections viewed from above (i) and from the side (ii). Arrows indicate $MHCII^{+}$ cells in close association with the duct (n=9 mice). Scale bar, 300 μm. Inset: scale bar, 70 μm.

(b) Whole-mount 3D confocal image of mammary tissue from a *CD11c-GFP* mouse at 10 weeks of age. Glands were immunostained for Keratin-5 (K5) (magenta), CD11b (yellow) and GFP (cyan). Arrows indicate $CD11c^{+}CD11b^{lo}$ cells in close association with the duct (n=3 mice). Scale bar, 40 μm.

(c) Representative FACS plots from a mouse at 10 weeks of age, showing populations of dendritic cells (DCs) and macrophages (MØs) (n=8 mice).

(d) Whole-mount 3D confocal image of mammary tissue from a *Csf1r-GFP* mouse at 10 weeks of age. Glands were immunostained for K5 (magenta), CD11b (yellow) and GFP (cyan). Arrows indicate $CD11b^{lo}Csf1r^{+}$ cells in close association with the duct (n=3 mice). Scale bar, 100 μm. Inset: scale bar, 50 μm.

(e) Frequency of DC and MØ populations and representative plots from FACS of whole mammary glands at 8 weeks, fat pads cleared of epithelium at 3 weeks and aged to 8 weeks and ducts manually isolated after crude enzymatic digestion (n= 3 mice). Error bars: s.e.m. 2-way ANOVA with Tukey correction ****p<0.0001 **p=0.0018, all others non-significant.

(f) Representative carmine stained mammary whole-mounts, frequency and fold-change of DC and MØ populations by FACS, 3 weeks after implantation of either a placebo pellet or a pellet containing estrogen and progesterone (E+P) within the 3^{rd} mammary gland at 8 weeks of age (n=2 pools of 4 mice). One-way ANOVA with Dunnett correction. **p=0.0048. Scale bar, 1 mm.

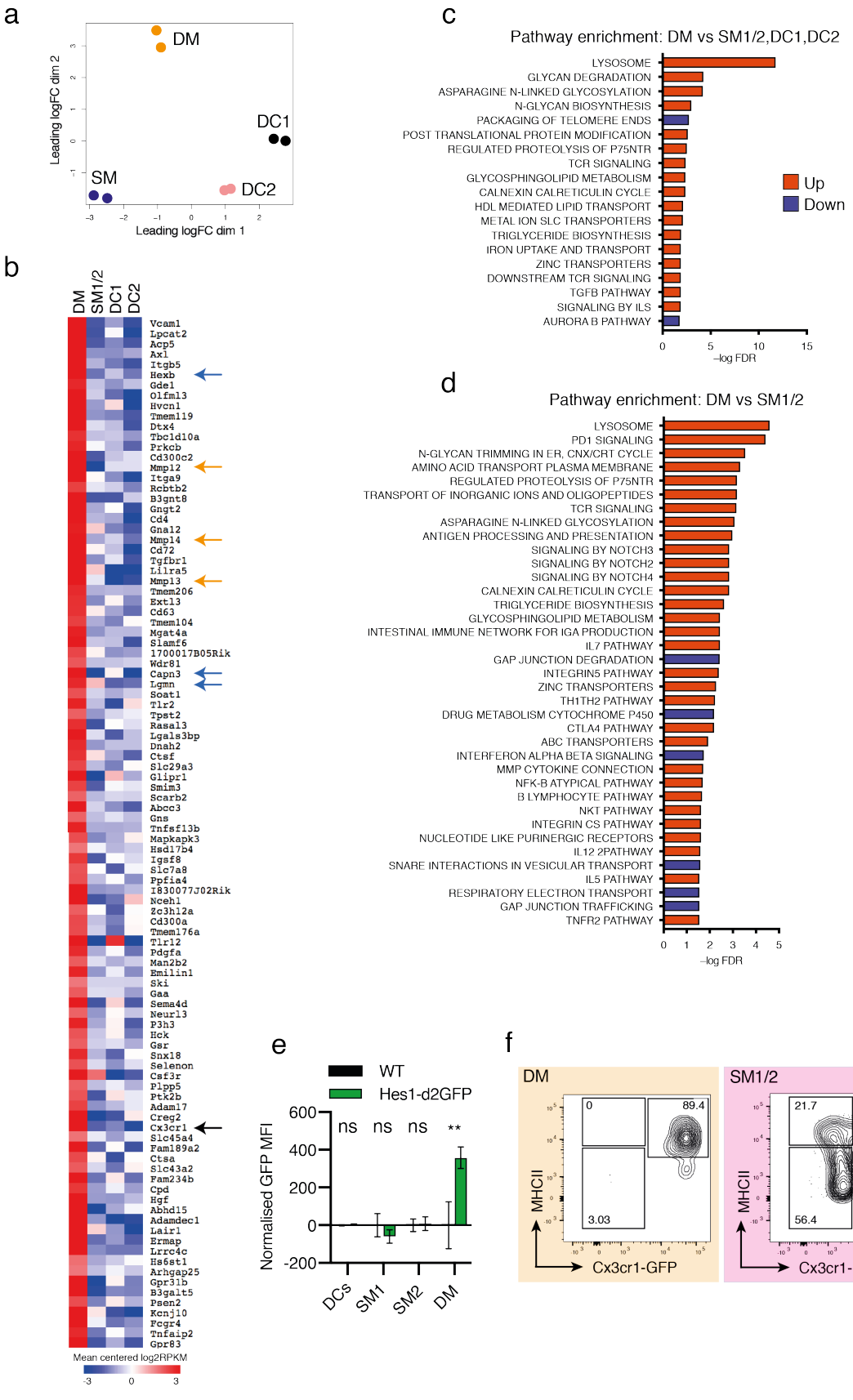
a
DM
DC1
SM
DC2
Leading logFC dim 2
Leading logFC dim 1
b
DM
SM1/2
DC1
DC2
Vcam1
Lpcat2
Acp5
Axl
Itgb5
Hexb
Gde1
Olfml3
Hvcn1
Tmem119
Dtx4
Tbc1d10a
Prkcb
Cd300c2
Mmp12
Itga9
Rcbtb2
B3gnt8
Gngt2
Cd4
Gna12
Mmp14
Cd72
Tgfbr1
Lilra5
Mmp13
Tmem206
Ext13
Cd63
Tmem104
Mgat4a
Slamf6
1700017B05Rik
Wdr81
Capn3
Lgmn
Soat1
Tlr2
Tpst2
Rasal3
Lgals3bp
Dnah2
Ctsf
Slc29a3
Glipr1
Smim3
Scarb2
Abcc3
Gns
Tnfsf13b
Mapkapk3
Hsd17b4
Igsf8
Slc7a8
Ppfia4
1830077J02Rik
Nceh1
Zc3h12a
Cd300a
Tmem176a
Tlr12
Pdgfa
Man2b2
Emilin1
Ski
Gaa
Sema4d
Neurl3
P3h3
Hck
Gsr
Snx18
Selenon
Csf3r
Plpp5
Ptk2b
Adam17
Creg2
Cx3cr1
Slc45a4
Fam189a2
Ctsa
Slc43a2
Fam234b
Cpd
Hgf
Abhd15
Adamdec1
Lair1
Ermap
Lrrc4c
Hs6st1
Arhgap25
Gpr31b
B3galt5
Psen2
Kcnj10
Fcgr4
Tnfaip2
Gpr83
Mean centered log2RPKM
-3
0
3
c
Pathway enrichment: DM vs SM1/2,DC1,DC2
LYSOSOME
GLYCAN DEGRADATION
ASPARAGINE N-LINKED GLYCOSYLATION
N-GLYCAN BIOSYNTHESIS
PACKAGING OF TELOMERE ENDS
POST TRANSLATIONAL PROTEIN MODIFICATION
REGULATED PROTEOLYSIS OF P75NTR
TCR SIGNALING
GLYCOSPHINGOLIPID METABOLISM
CALNEXIN CALRETICULIN CYCLE
HDL MEDIATED LIPID TRANSPORT
METAL ION SLC TRANSPORTERS
TRIGLYCERIDE BIOSYNTHESIS
IRON UPTAKE AND TRANSPORT
ZINC TRANSPORTERS
DOWNSTREAM TCR SIGNALING
TGFB PATHWAY
SIGNALING BY ILS
AURORA B PATHWAY
Up
Down
0
5
10
15
−log FDR
d
Pathway enrichment: DM vs SM1/2
LYSOSOME
PD1 SIGNALING
N-GLYCAN TRIMMING IN ER, CNX/CRT CYCLE
AMINO ACID TRANSPORT PLASMA MEMBRANE
REGULATED PROTEOLYSIS OF P75NTR
TRANSPORT OF INORGANIC IONS AND OLIGOPEPTIDES
TCR SIGNALING
ASPARAGINE N-LINKED GLYCOSYLATION
ANTIGEN PROCESSING AND PRESENTATION
SIGNALING BY NOTCH3
SIGNALING BY NOTCH2
SIGNALING BY NOTCH4
CALNEXIN CALRETICULIN CYCLE
TRIGLYCERIDE BIOSYNTHESIS
GLYCOSPHINGOLIPID METABOLISM
INTESTINAL IMMUNE NETWORK FOR IGA PRODUCTION
IL7 PATHWAY
GAP JUNCTION DEGRADATION
INTEGRIN5 PATHWAY
ZINC TRANSPORTERS
TH1TH2 PATHWAY
DRUG METABOLISM CYTOCHROME P450
CTLA4 PATHWAY
ABC TRANSPORTERS
INTERFERON ALPHA BETA SIGNALING
MMP CYTOKINE CONNECTION
NFK-B ATYPICAL PATHWAY
B LYMPHOCYTE PATHWAY
NKT PATHWAY
INTEGRIN CS PATHWAY
NUCLEOTIDE LIKE PURINERGIC RECEPTORS
IL12 2PATHWAY
SNARE INTERACTIONS IN VESICULAR TRANSPORT
IL5 PATHWAY
RESPIRATORY ELECTRON TRANSPORT
GAP JUNCTION TRAFFICKING
TNFR2 PATHWAY
0
1
2
3
4
5
−log FDR
e
WT
Hes1-d2GFP
Normalised GFP MFI
600
400
200
0
-200
ns
ns
ns
**
DCs
SM1
SM2
DM
f
DM
SM1/2
0
89.4
3.03
21.7
14.8
56.4
MHCII
Cx3cr1-GFP

Figure 5.2: Ductal macrophages have a distinct gene expression signature

(a) Multidimensional scaling plot of bulk RNA-seq from mammary gland DCs and MØs from 9 week-old mice. Distances on the plot represent leading log2-fold changes between samples (n = 2, 12 mice per replicate).

(b) Expression levels of the top 100 DM signature genes across the four populations. Heatmap shows log-expression, mean centred for each gene. Genes are ranked by average false discovery rate (n=2 pools of 12 mice). Blue arrows: lysosomal genes, orange arrows: matrix metalloproteinases, black arrow indicates specific expression of Cx3cr1 by DMs.

(c) Camera gene set enrichment analysis of canonical pathways associated with DMs vs the average of DC1, DC2 and SM1/2. Red: up, Blue: down.

(d) Camera gene set enrichment analysis of canonical pathways in DMs vs SM1/2.

(e) Measurement of GFP fluorescence in populations from 12 week-old *Hes1-d2GFP* mice or FVB controls. The control MFI for each population was subtracted (n=3 mice). Error bars, s.e.m. 2-way ANOVA with Sidak correction. **p=0.0017.

(f) Representative FACS plots of glands from *Cx3cr1*$^{GFP/+}$ *mice* at 8 weeks of age (n=2 mice).

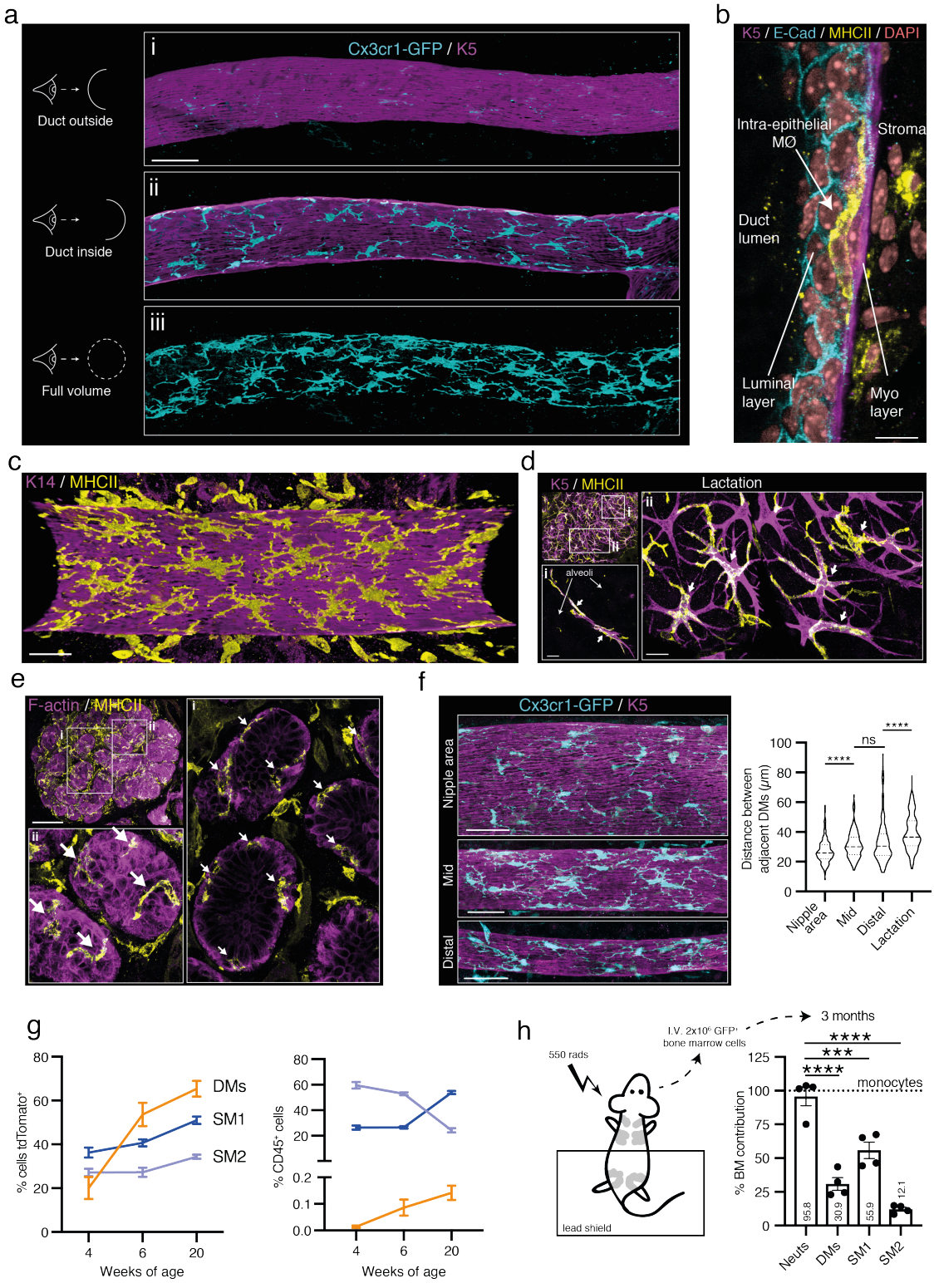
a
Duct outside
Duct inside
Full volume
i
Cx3cr1-GFP / K5
ii
iii
b
K5 / E-Cad / MHCII / DAPI
Intra-epithelial MØ
Stroma
Duct lumen
Luminal layer
Myo layer
c
K14 / MHCII
d
K5 / MHCII
Lactation
alveoli
e
F-actin / MHCII
f
Cx3cr1-GFP / K5
Nipple area
Mid
Distal
Distance between adjacent DMs (μm)
ns
****
Nipple area
Mid
Distal
Lactation
g
% cells tdTomato+
DMs
SM1
SM2
Weeks of age
% CD45+ cells
Weeks of age
h
550 rads
I.V. 2x10⁶ GFP+ bone marrow cells
3 months
lead shield
monocytes
% BM contribution
95.8
30.9
55.9
12.1
Neuts
DMs
SM1
SM2

Figure 5.3: DMs are tissue-resident and occupy an intra-epithelial niche

(a) Whole-mount 3D confocal image of mammary tissue from a *Cx3cr1*$^{GFP/+}$ mouse at 10 weeks of age with opaque signal. Glands were immunostained for K5 (magenta) and GFP (cyan). (i) View of the outer myoepithelial surface showing only the front half of the duct. (ii) View of the inner myoepithelial surface showing only the rear half of the duct. (iii) View of the entire duct volume (n=3 mice). Scale bar, 50 μm.

(b) Confocal optical section through a duct bilayer from a 3D confocal image of a gland immunostained for K5, E-Cadherin (E-Cad) (cyan), MHCII (yellow) and DAPI (pink). Arrow indicates an intra-epithelial MØ, or 'ductal macrophage' (DM), with typical localisation between the luminal and myoepithelial layers. Myo: myoepithelium, Lum: luminal layer. Representative of all DMs within large volume 3D confocal images (n=9 mice). Scale bar, 10 μm.

(c) Whole-mount 3D confocal image of adult mammary tissue immunostained for Keratin 14 (K14) (magenta) and MHCII (yellow) with opaque signal. View of the rear half of the duct showing the inner myoepithelial surface and the intra-epithelial DM network (n=9 mice). Scale bar, 40 μm.

(d) Whole-mount 3D confocal image of alveoli at 2 weeks lactation immunostained for K5 (magenta) and MHCII (yellow). Arrows indicate DMs with intra-epithelial localisation (i) and intimate contact with stellate myoepithelial cells (ii) (n=3 mice). Scale bars, 100 μm (overview), 20 μm (enlargements).

(e) Whole-mount 3D confocal image of a TDLU within nulliparous human mammary tissue from a reduction mammoplasty immunostained for MHCII (yellow) and labelled for F-actin (magenta) (n=3). Scale bar, 100 μm.

(f) Whole-mount 3D confocal imaging of nipple, mid and distal regions of glands from 8 week old *Cx3cr1*$^{GFP/+}$ mice immunostained for GFP (cyan) and K5 (magenta) and quantification of DM–DM cell body closest distance in 3D (n=2 mice, 45–189 cells per region, per replicate). Lactation density was measured in data from Figure 5.3d (n=3 mice). One-way ANOVA with Sidak correction, the pairwise comparisons are shown. ****p<0.0001.

(g) Percentage of tdTomato^{+} cells in mammary MØs in *Ms4a3-Cre/Rosa-tdTomato* mice at 4, 6 and 20 weeks of age and frequency of mammary MØ populations at these stages (n=3-4 mice). Error bars, s.e.m.

(h) Percentage bone marrow contribution to MØs and neutrophils in the 4th and 5th mammary glands, 3 months after shielded irradiation and transplantation of 2x10^{6} *Ubc-GFP* bone marrow cells into wild-type 10 week-old mice (n=4 mice). The percentage GFP^{+} of monocytes was normalised to 100% for each sample. Error bars: s.e.m. Pairwise comparison with neutrophils by one-way ANOVA with Dunnett correction. ****P<0.0001, ***P=0.0005.

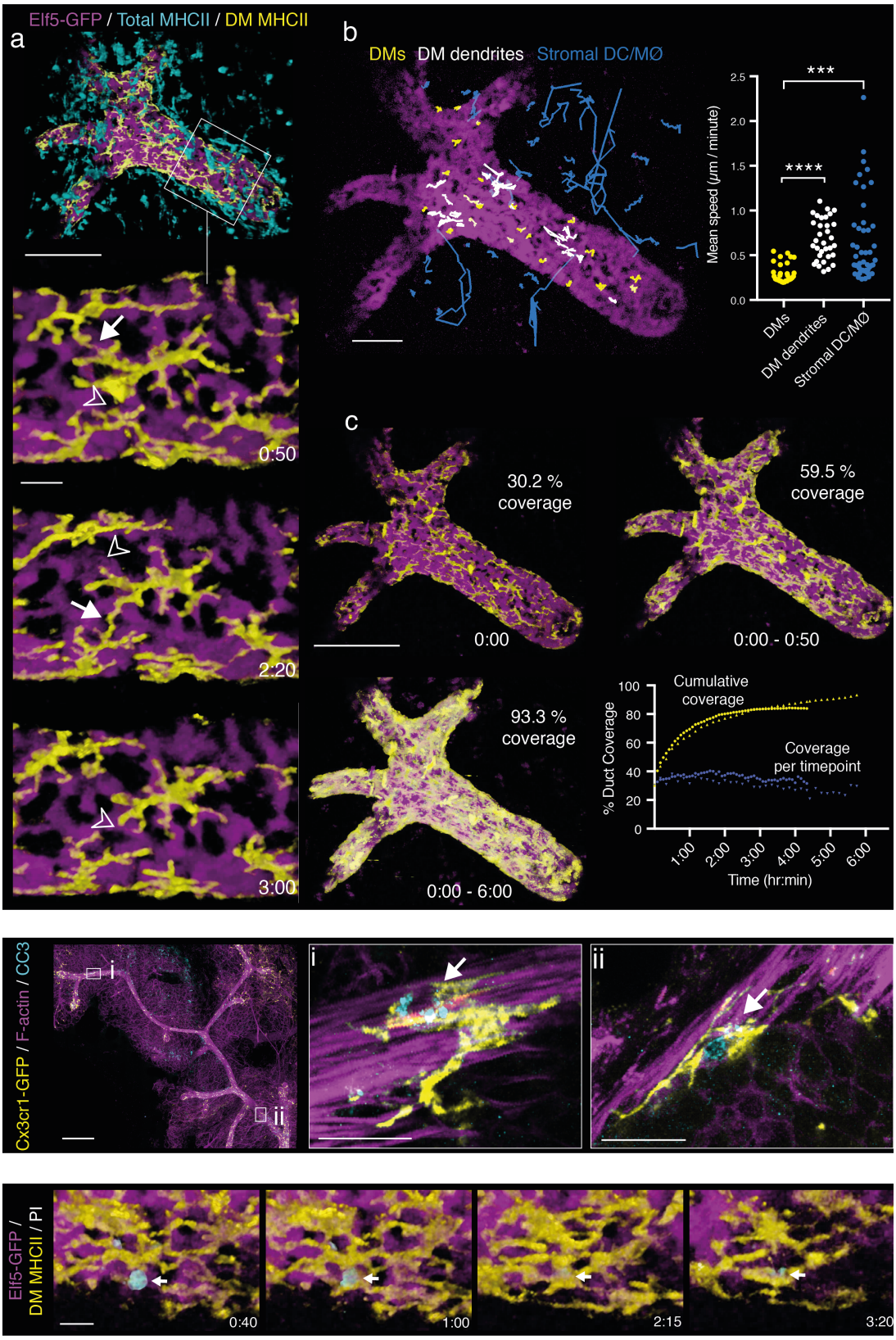
a
Elf5-GFP / Total MHCII / DM MHCII
0:50
2:20
3:00
b
DMs DM dendrites Stromal DC/MØ
Mean speed (μm / minute)
2.5
2.0
1.5
1.0
0.5
0.0
***
****
DMs
DM dendrites
Stromal DC/MØ
c
30.2 % coverage
0:00
59.5 % coverage
0:00 - 0:50
93.3 % coverage
0:00 - 6:00
Cumulative coverage
Coverage per timepoint
% Duct Coverage
100
80
60
40
20
0
1:00
2:00
3:00
4:00
5:00
6:00
Time (hr:min)
d
Cx3cr1-GFP / F-actin / CC3
i
ii
e
Elf5-GFP / DM MHCII / PI
0:40
1:00
2:15
3:20

Figure 5.4: DMs frequently contact all epithelial cells by dendrite movement

(a) 3D intravital microscopy (3D-IVM) of mammary ducts in an *Elf5-GFP* mouse with immunolabelling by fluorescently conjugated anti-MHCII antibody. Luminal progenitor cells are GFP$^+$ (magenta). DM MHCII signal (yellow) was isolated from total MHCII (cyan) using an GFP signal mask (Figure S 5.4b, methods). Enlarged time points show transient DM–DM contact (solid arrows) and separation (arrow heads). Time in hrs:mins. Images were acquired every 10 mins. Scale bar, 100 μm (upper) and 10 μm (lower) (n=6 mice).

(b) Tracking and quantification of *in vivo* MHCII$^+$ cell behaviour. 30 DMs (yellow), 46 stromal DC/MØ (blue) and 33 DM dendrites (white) were manually tracked in 3D and their average speed over time plotted (pooled from n=2 mice). Scale bar, 70 μm. One-way ANOVA with Dunnett correction ****P<0.0001.

(c) Cumulative DM MHCII signal over indicated time periods, quantified as percentage epithelial area covered cumulatively or per time point (n=2 mice) (experiment indicated by circles or triangles). Scale bar, 100 μm.

(d) Whole-mount 3D confocal image of adult mammary ducts (9 weeks) from a *Cx3cr1*$^{GFP/+}$ mouse, immunostained for GFP (yellow) and cleaved Caspase 3 (CC3) (Cyan) and labelled for F-actin (magenta) with conjugated phalloidin. Arrows indicate apoptotic cells in the epithelium in tight association with DMs (n=3 mice). Scale bars, 300 μm (overview), 20 μm (enlargements).

(e) Time-points from a 3D-IVM movie of a mammary duct in a 9 week-old *Elf5-GFP* mouse with immunolabelling by fluorescently conjugated anti-MHCII antibody. A DM phagocytoses an apoptotic epithelial cell (arrow) (3 observations in n=3 mice). GFP: magenta, masked DM MHCII: yellow, PI: propidium iodide (white). Images were acquired every 5 mins. Scale bar, 15 μm.

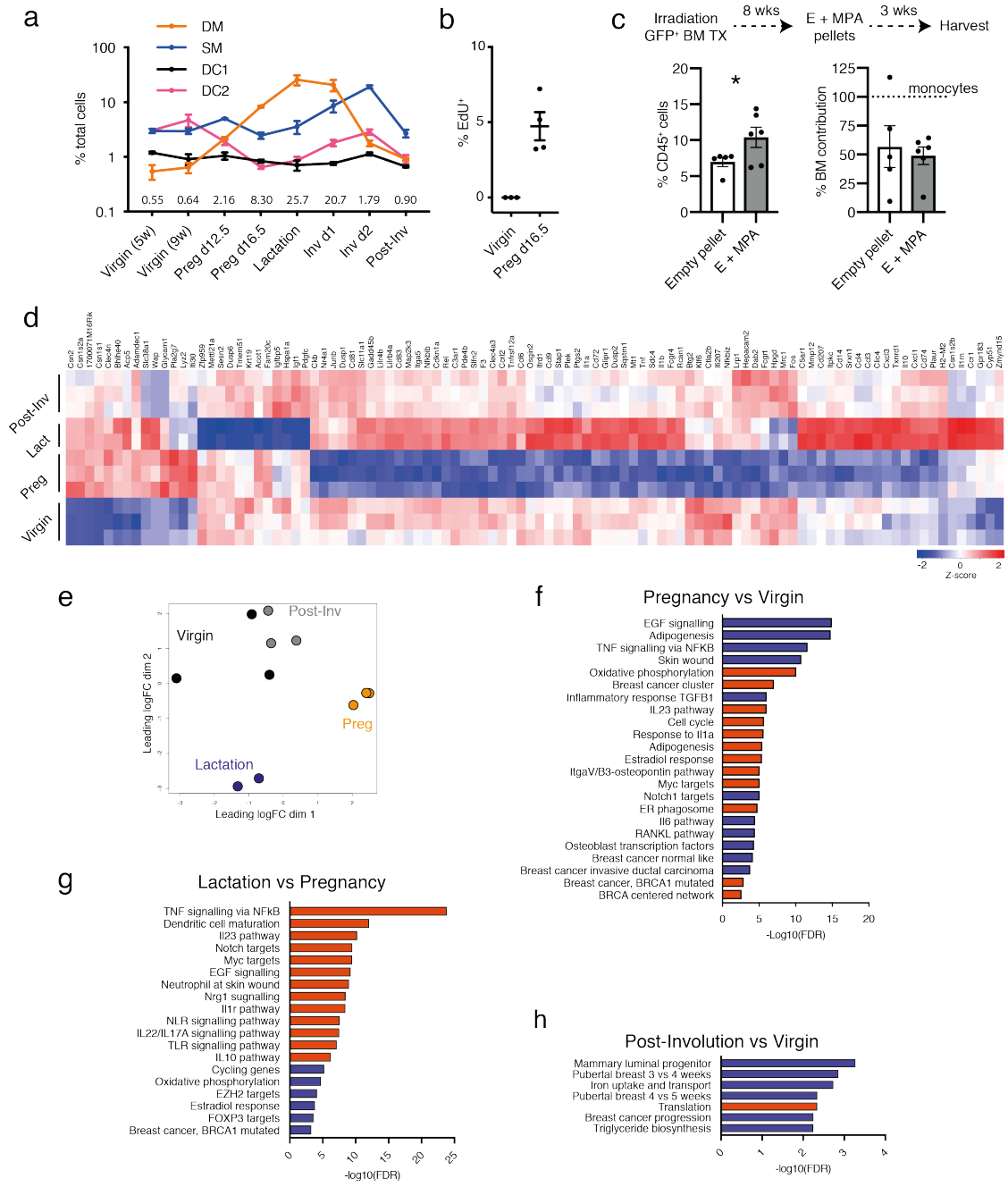
a
DM
SM
DC1
DC2
% total cells
100
10
1
0.1
0.55 0.64 2.16 8.30 25.7 20.7 1.79 0.90
Virgin (5w)
Virgin (9w)
Preg d12.5
Preg d16.5
Lactation
Inv d1
Inv d2
Post-Inv
b
% EdU+
10
5
0
Virgin
Preg d16.5
c
Irradiation
GFP+ BM TX
8 wks
E + MPA
pellets
3 wks
Harvest
% CD45+ cells
20
15
10
5
0
*
Empty pellet
E + MPA
% BM contribution
125
100
75
50
25
0
monocytes
Empty pellet
E + MPA
d
Post-Inv
Lact
Preg
Virgin
-2
0
2
Z-score
e
Post-Inv
Virgin
Preg
Lactation
Leading logFC dim 2
Leading logFC dim 1
f
Pregnancy vs Virgin
EGF signalling
Adipogenesis
TNF signalling via NFKB
Skin wound
Oxidative phosphorylation
Breast cancer cluster
Inflammatory response TGFB1
IL23 pathway
Cell cycle
Response to Il1a
Adipogenesis
Estradiol response
ItgaV/B3-osteopontin pathway
Myc targets
Notch1 targets
ER phagosome
Il6 pathway
RANKL pathway
Osteoblast transcription factors
Breast cancer normal like
Breast cancer invasive ductal carcinoma
Breast cancer, BRCA1 mutated
BRCA centered network
0 5 10 15 20
-Log10(FDR)
g
Lactation vs Pregnancy
TNF signalling via NFKB
Dendritic cell maturation
Il23 pathway
Notch targets
Myc targets
EGF signalling
Neutrophil at skin wound
Nrg1 signalling
Il1r pathway
NLR signalling pathway
IL22/IL17A signalling pathway
TLR signalling pathway
IL10 pathway
Cycling genes
Oxidative phosphorylation
EZH2 targets
Estradiol response
FOXP3 targets
Breast cancer, BRCA1 mutated
0 5 10 15 20 25
-log10(FDR)
h
Post-Involution vs Virgin
Mammary luminal progenitor
Pubertal breast 3 vs 4 weeks
Iron uptake and transport
Pubertal breast 4 vs 5 weeks
Translation
Breast cancer progression
Triglyceride biosynthesis
0 1 2 3 4
-log10(FDR)

Figure 5.5: DMs proliferate during pregnancy and dominate the lactation immune landscape

(a) Frequency of DCs and MØs over post-natal mammary gland development. DC1: $CD11b^-$ DCs, DC2: $CD11b^+$ DCs (n>3 mice). Values shown are DM percentage. Error bars: s.e.m. w: weeks, d: days, preg: pregnancy, Inv: Involution (30 days).

(b) Percentage of DMs EdU^+ after a 2 hr EdU treatment in mice at 10 weeks of age or at 16.5 days pregnancy. Manually counted in whole-mount 3D confocal images (images shown in Figure S 5.3c) (n=4 mice).

(c) DM frequency and bone marrow contribution, 11 weeks after shielded irradiation and transplant of GFP^+ bone marrow, with implantation of pellets containing estrogen and MPA at 8 weeks.

(d) Expression levels of the top DE genes in the DMs across four developmental stages: 9 week-old virgin, 16.5 days pregnancy, 16 days lactation and 1 month post-involution. Heatmaps show z-score (mean centred Log2expression/row s.d.) (n=3 mice for developmental time-points except lactation where n=2).

(e) Multidimensional scaling plot of RNA-seq data for DMs sorted from mammary glands at the four developmental stages. Distances on the plot represent leading log2-fold changes between samples (n = 2-3 mice).

(f) Camera gene set enrichment analysis of enriched pathways associated with DMs in mammary glands from 16.5 days pregnancy vs lactation. Red: up, Blue: down.

(g) Camera gene set enrichment analysis of enriched pathways associated with DMs in lactation vs day 16.5 pregnancy.

(h) Camera gene set enrichment analysis of enriched pathways associated with DMs in 9 week-old virgin vs 30 days post-involution glands.

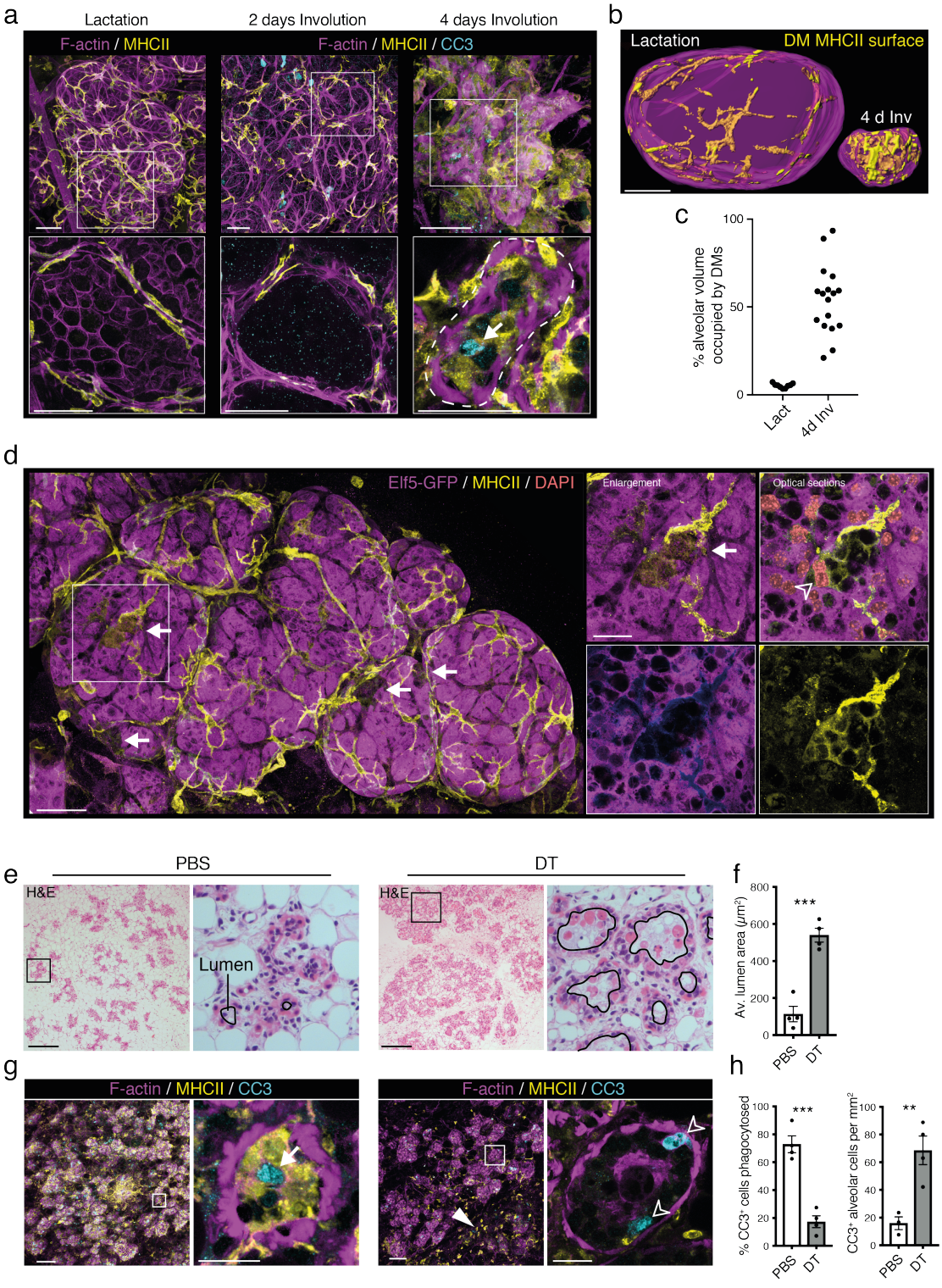
a
Lactation
2 days Involution
4 days Involution
F-actin / MHCII
F-actin / MHCII / CC3
b
Lactation
DM MHCII surface
4 d Inv
c
% alveolar volume occupied by DMs
100
50
0
Lact
4d Inv
d
Elf5-GFP / MHCII / DAPI
Enlargement
Optical sections
e
PBS
DT
H&E
Lumen
f
Av. lumen area (μm²)
800
600
400
200
0
***
PBS
DT
g
F-actin / MHCII / CC3
h
% CC3⁺ cells phagocytosed
***
CC3⁺ alveolar cells per mm²
**
PBS
DT

Figure 5.6: DMs are essential for alveolar cell phagocytosis during involution

(a) Whole-mount 3D confocal images of mammary tissue at 2 weeks lactation, 2 days involution and 4 days involution. Optical sections of the indicated regions are shown below. Glands were immunostained for MHCII (yellow) and cleaved Caspase 3 (CC3) (cyan) and labelled for F-actin (magenta). The dotted line indicates a collapsed alveolus. Arrow indicates phagocytosed apoptotic cell fully surrounded by MHCII signal in 3D (n > 3). Scale bars, 50 μm.

(b) Representative examples of alveolar surface and alveolar MHCII surface renderings in lactation and 4 days involution (n=3). Scale bar, 40 μm.

(c) The percentage of alveolar volume occupied by DMs at 4 days involution (n= 3).

(d) Representative whole-mount 3D confocal imaging of 3 days involution glands from *Elf5-GFP* mice (n=3). 13.84% (±10.27 s.d.) of alveolar cells were phagocytosed (co-stained for GFP and MHCII, 1089 total GFP^+ alveolar cells counted over 3 replicates). Arrows indicate phagocytosed GFP^+ alveolar cells surrounded by MHCII signal. An enlargement of a phagocytic event is shown, along with optical sections indicated by a white border. Scale bars, 50 μm (overview) and 20 μm (enlargements).

(e) Haematoxylin and eosin (H&E) staining of thin sections from *CD11c-DTR* mice at 4 days involution treated with PBS or diphtheria toxin (2 ng/g) immediately upon forced weaning at 14 days lactation (n=4 mice). Scale bars, 100 μm.

(f) Quantification of lumen area from (e). Error bars s.e.m. 2-sided t-test. ***P<0.001.

(g) Whole-mount 3D confocal images from mice in (e) with immunostaining for MHCII (yellow) and CC3 (cyan) and labelling of F-actin (magenta) (n=4). Arrow indicates a phagocytosed $CC3^+$ apoptotic cell fully surrounded by MHCII signal. Hollow arrow-heads indicate non-phagocytosed apoptotic cells. Solid arrow-head indicates presence of stromal $MHCII^+$ cells that have not compensated for loss of phagocytosis caused by DM depletion. Scale bars, 100 μm (overview) and 20 μm (enlargements).

(h) Percentage of $CC3^+$ cell phagocytosed in (g) (completely surrounded by MHCII in 3D) and the number of $CC3^+$ alveolar cells per image area (see Figure S 5.7g) (n=4). Error bars s.e.m. 2-sided t-test. ***P=0.0003, **P=0.0092.

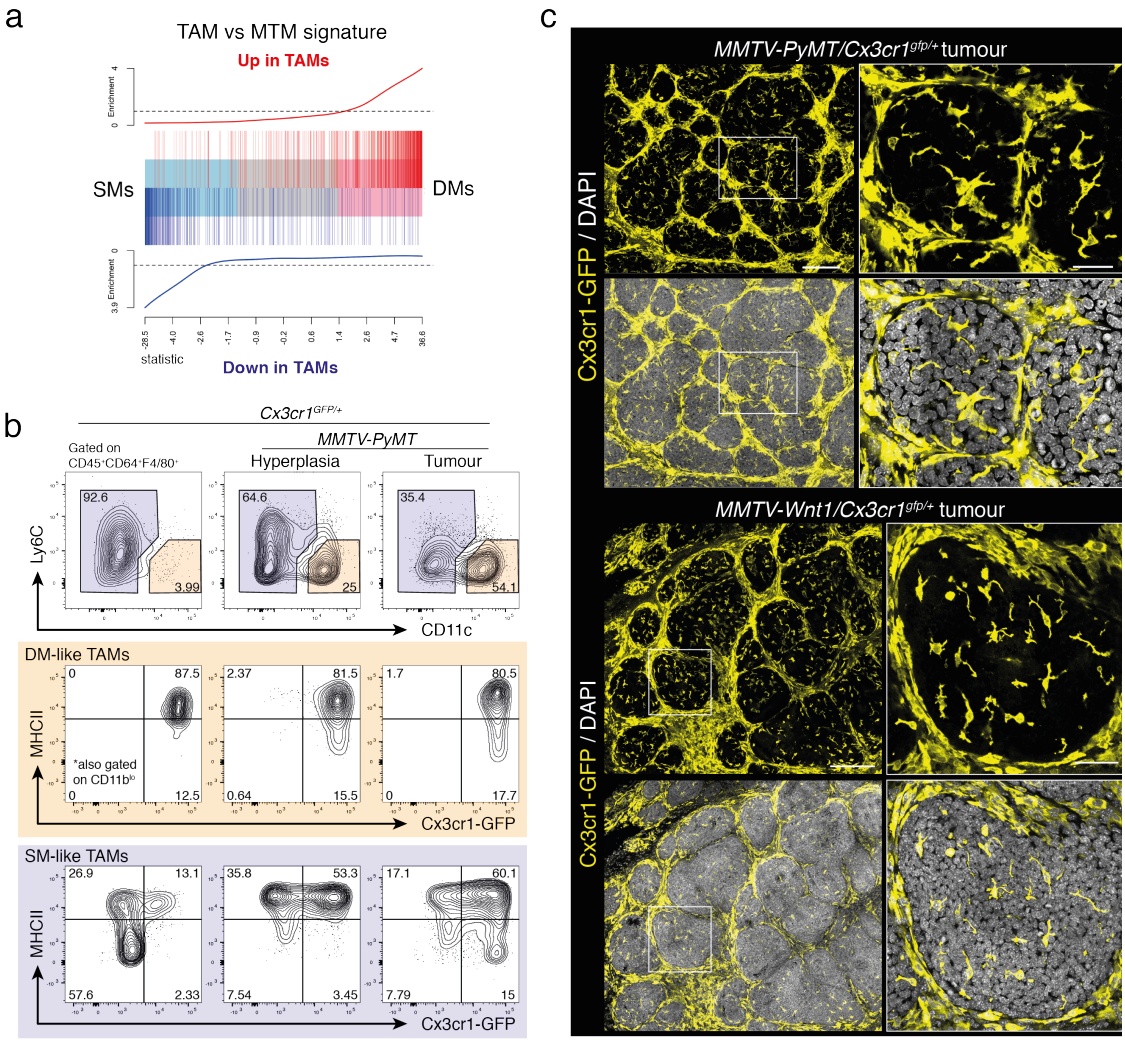
a
TAM vs MTM signature
Up in TAMs
SMs
DMs
statistic
Down in TAMs
b
Cx3cr1GFP/+
MMTV-PyMT
Gated on CD45+CD64+F4/80+
Hyperplasia
Tumour
Ly6C
CD11c
DM-like TAMs
MHCII
*also gated on CD11blo
Cx3cr1-GFP
SM-like TAMs
c
MMTV-PyMT/Cx3cr1gfp/+ tumour
Cx3cr1-GFP / DAPI
MMTV-Wnt1/Cx3cr1gfp/+ tumour

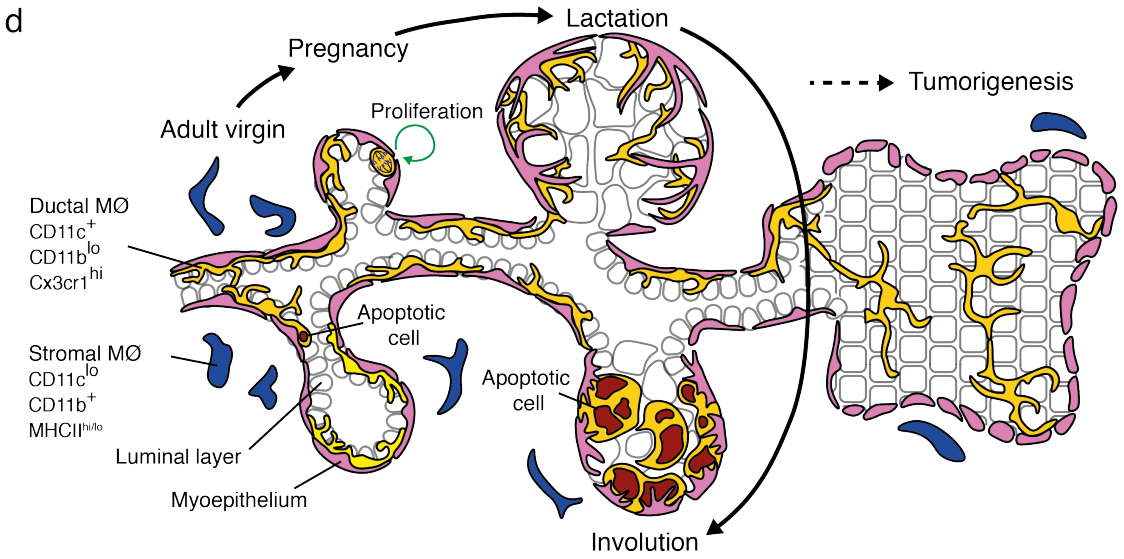
d
Lactation
Pregnancy
Tumorigenesis
Adult virgin
Proliferation
Ductal MØ
CD11c+
CD11blo
Cx3cr1hi
Apoptotic cell
Stromal MØ
CD11clo
CD11b+
MHCIIhi/lo
Apoptotic cell
Luminal layer
Myoepithelium
Involution

Figure 5.7: Mammary tumour-associated macrophages resemble DMs

(a) Barcode enrichment plot showing concordance of tumour-associated macrophages (TAMs [51]) with DMs. The plot shows the expression signature of TAMs compared to mammary tissue macrophages (MTMs [51]) is strongly correlated with that of DMs compared to SMs (ROAST p < 1e-5). Genes are ordered in the plot right to left from most up to most down-regulated in DMs vs SMs. The x-axis shows moderated t-statistics. Vertical red (blue) lines designate genes up-regulated (down-regulated) in TAMs vs MTM. The red and blue worms show relative enrichment of red and blue genes respectively.

(b) Representative FACS plots of *Cx3cr1*$^{GFP/+}$ and *MMTV-PyMT/Cx3cr1*$^{GFP/+}$ mammary glands, tumour-adjacent hyperplastic tissue and tumours (n=2 mice per stage).

(c) Optical sections from whole-mount 3D confocal image of *MMTV-PyMT/Cx3cr1*$^{gfp/+}$ *MMTV-Wnt1/Cx3cr1*$^{gfp/+}$ tumours immunostained for GFP (yellow) and labelled with DAPI (white) (n=4 mice). Scale bars, 100 μm (overview) and 30 μm (enlargements).

(d) Diagram summarising the morphology, localisation, behaviour and function of DMs throughout mammary gland remodelling and oncogenesis. Mammary DMs are unique, long-lived, tissue-resident MØs that exclusively occupy an intra-epithelial niche. DMs create a contiguous network within the mammary epithelium throughout development that allows them to frequently contact all cells. Their strategic localisation allows DMs to rapidly phagocytose dying alveolar cells following lactation. Mammary tumours continue to programme DM-like TAMs in tumours that form a pervasive intra-tumour network.

5.8 Supplementary Figures

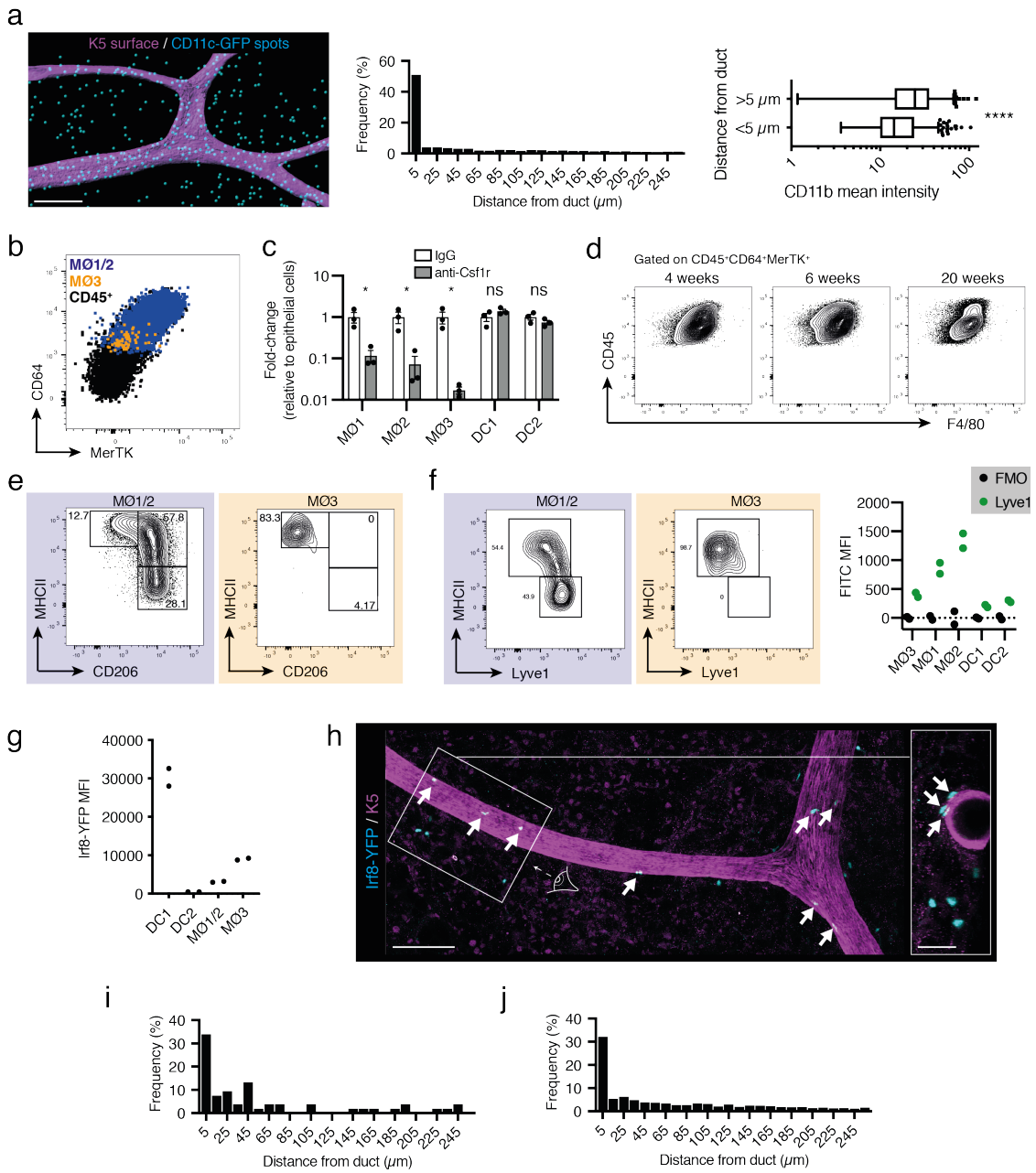

Figure S 5.1: Supporting information for Figure 1

(a) Analysis of a whole-mount 3D confocal image of *CD11c-GFP* tissue immunostained for GFP and Keratin 5 (K5). Surface rendering of K5 signal (magenta) and spots generated from GFP signal (cyan) (left panel). Histogram of distance from spot center to K5 surface edge (middle panel). x-axis shows the center value of 10 μm bins. Boxplot (Tukey) of CD11b mean intensity within GFP spot objects (diameter 10 μm) (right panel), analysed by unpaired t-test (n=2 mice). Scale bar, 200 μm.

(b) Overlay of MØ1/2, MØ3 and $CD45^+$ cells (gated as in Figure 5.1c) showing CD64 and MerTK expression. All MØs were $CD64^+MerTK^+$ but MØ1/2 showed a range of expression and MØ3 were low for both CD64 and MerTK.

(c) FACS quantification of mammary glands from 9-week-old mice treated with 400 μg anti-Csf1r (AFS98) or isotype control by intraperitoneal injection 7, 4 and 2 days before collection (n=3 mice). DC2: $CD11b^+$ DCs, DC1: $CD11b^-CD24^{hi}$ DCs. 2-way ANOVA with Sidak correction. *P=0.0231 (MØ1), *P=0.0159 (MØ2), *P=0.0101 (MØ3)

(d) Representative FACS plots from mice at 4, 6 and 20 weeks of age. No distinct F4/80 high and low populations were observed (n=3-4 mice). Same samples are shown in Figure 5.3g.

(e) Representative FACS plots from 9-week mice (n=2 mice).

(f) Representative FACS plots from 9-week mice and quantification of Lyve1-FITC mean fluorescence intensity (MFI) normalised to autofluorescence in fluorescence minus one samples (FMO) (n=2 mice).

(g) Plot of YFP MFI in *Irf8-YFP* mice, normalised to autofluorescence for each population in YFP-negative control mice. DC1: $CD11b^-$ DCs, DC2: $CD11b^+$ DCs. (n = 2 mice).

(h) Whole-mount 3D confocal image of mammary tissue from an *Irf8-YFP* mouse at 16 weeks of age. Glands were immunostained for K5 (magenta) and YFP (cyan) (n=2 mice). Inset: View along the duct axis. Arrows indicate $Irf8^{hi}$ cells in contact with the outside of the basal layer. Scale bars, 100 μm and 30 μm (enlargement).

(i) Analysis (g): histogram of distance from YFP^+ spot center to K5 surface edge (n=2 mice).

(j) Analysis from a whole-mount 3D confocal image of *Csf1r-GFP* tissue immunostained for GFP and K5 (Figure 5.1d). Histogram of distance from GFP^+ spot center to K5 surface edge (n=2 mice).

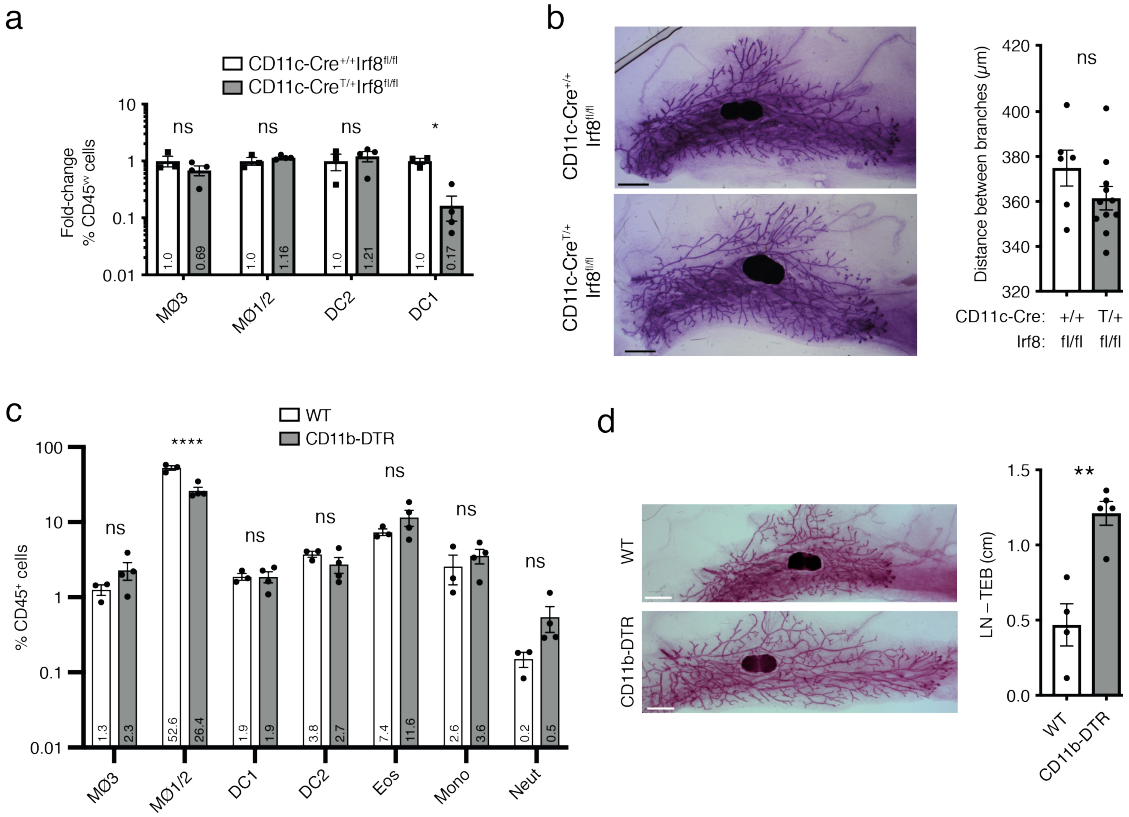
a
CD11c-Cre+/+Irf8fl/fl
CD11c-CreT/+Irf8fl/fl
Fold-change % CD45iv cells
ns
ns
ns
*
MØ3
MØ1/2
DC2
DC1
b
CD11c-Cre+/+ Irf8fl/fl
CD11c-CreT/+ Irf8fl/fl
Distance between branches (μm)
ns
CD11c-Cre: +/+ T/+
Irf8: fl/fl fl/fl
c
WT
CD11b-DTR
% CD45+ cells
****
MØ3
MØ1/2
DC1
DC2
Eos
Mono
Neut
d
WT
CD11b-DTR
LN – TEB (cm)
**

Figure S 5.2: CD11b^{+} cells negatively regulate duct growth during puberty

(a) Quantification of MØs and DCs by FACS in CD11c-Cre$^{T/+}$Irf8$^{fl/fl}$ conditional knockouts and CD11c-Cre$^{+/+}$Irf8$^{fl/fl}$ controls at 6 weeks of age. Fold-change in % CD45^{+} cells was calculated relative to control frequency normalised to 1 (n≥3 mice). Values within bars are means. 2-way ANOVA with Sidak correction. *P=0.0142.

(b) Representative carmine stained mammary whole-mounts from CD11c-Cre$^{T/+}$Irf8$^{fl/f}$ CD11c-Cre$^{+/+}$Irf8$^{fl/fl}$ mice at 6 weeks of age and quantification of branching (n≥6 mice). 2-tailed t tests. Scale, 2 mm.

(c) FACS analysis one day after DT treatment of CD11b-DTR mice (n≥3 mice). Values within bars are means. Eos: eosinophil, Neut: neutrophil, Mono: monocyte. 2-way ANOVA with Sidak correction. ****P<0.0001.

(d) Representative carmine stained mammary whole-mounts from CD11b-DTR or WT mice treated with DT at 5 weeks of age and collected at 6 weeks (n≥4). 2-tailed t test. **P=0.0018. Scale, 2 mm.

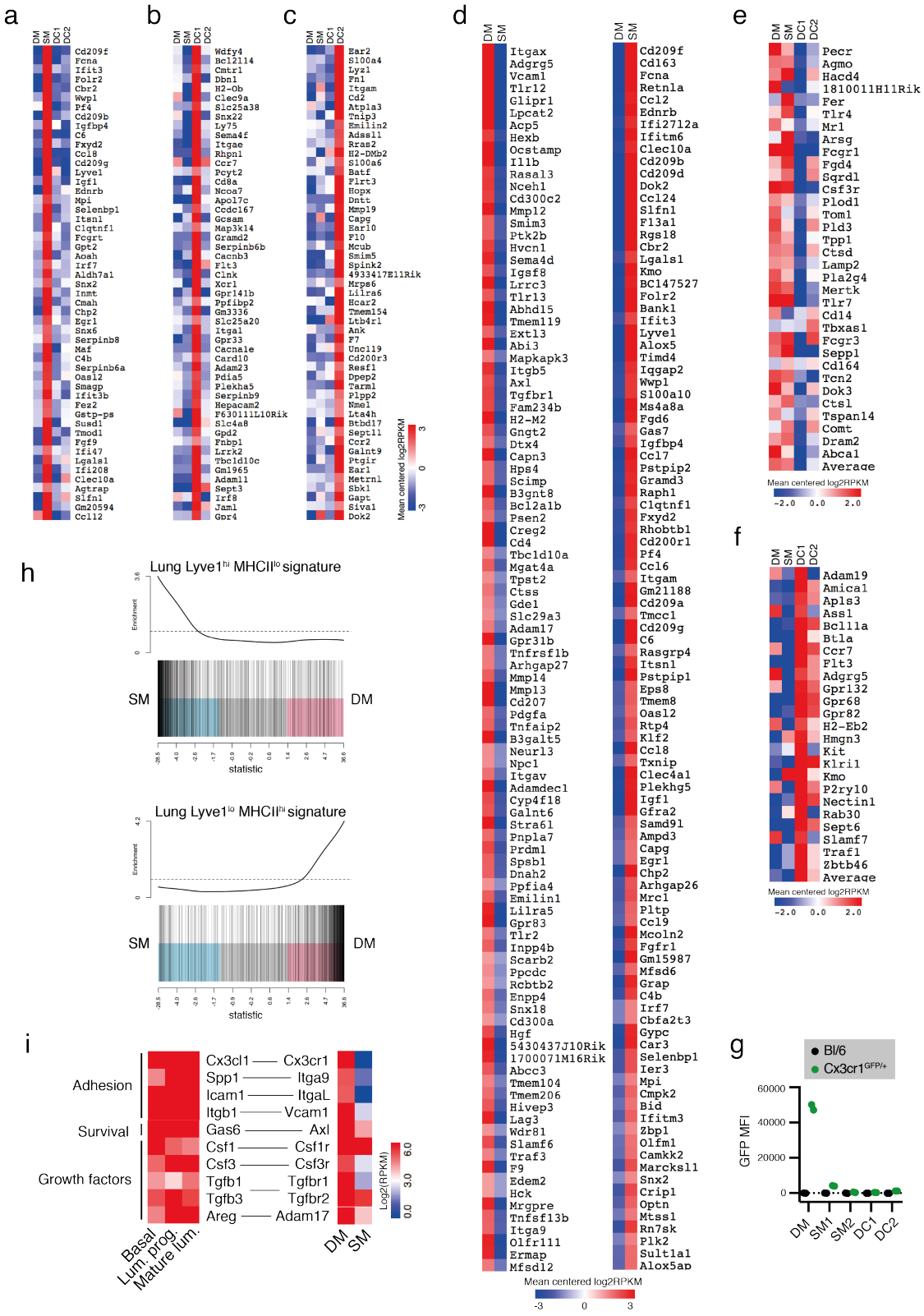
a
b
c
d
e
f
g
h
i
DM
SM
DC1
DC2
Cd209f
Fcna
Ifit3
Folr2
Cbr2
Wwp1
Pf4
Cd209b
Igfbp4
C6
Fxyd2
Ccl8
Cd209g
Lyve1
Igf1
Ednrb
Mpi
Selenbp1
Itsn1
C1qtnf1
Fcgrt
Gpt2
Aoah
Irf7
Aldh7a1
Snx2
Inmt
Cmah
Chp2
Egr1
Snx6
Serpinb8
Maf
C4b
Serpinb6a
Oasl2
Smagp
Ifit3b
Fez2
Gstp-ps
Susd1
Tmod1
Fgf9
Ifi47
Lgals1
Ifi208
Clec10a
Agtrap
Slfn1
Gm20594
Ccl12
Wdfy4
Bcl2l14
Cmtr1
Dbn1
H2-Ob
Clec9a
Slc25a38
Snx22
Ly75
Sema4f
Itgae
Rhpn1
Ccr7
Pcyt2
Cd8a
Ncoa7
Apol7c
Ccdc167
Gcsam
Map3k14
Gramd2
Serpinb6b
Cacnb3
Flt3
Clnk
Xcr1
Gpr141b
Ppfibp2
Gm3336
Slc25a20
Itga1
Gpr33
Cacnale
Card10
Adam23
Pdia5
Plekha5
Serpinb9
Hepacam2
F630111L10Rik
Slc4a8
Gpd2
Fnbp1
Lrrk2
Tbc1d10c
Gm1965
Adam11
Sept3
Irf8
Jaml
Gpr4
Ear2
S100a4
Lyz1
Fn1
Itgam
Cd2
Atp1a3
Tnip3
Emilin2
Adss1l
Rras2
H2-DMb2
S100a6
Batf
Flrt3
Hopx
Dntt
Mmp19
Capg
Emr1l0
F10
Mcub
Smim5
Spink2
4933417E11Rik
Mrps6
Lilra6
Hcar2
Tmem154
Ltb4r1
Ank
F7
Unc119
Cd200r3
Resf1
Dpep2
Tarm1
Plpp2
Nme1
Lta4h
Btbd17
Sept11
Ccr2
Galnt9
Ptgir
Ear1
Metrnl
Sbk1
Gapt
Siva1
Dok2
Mean centered log2RPKM
3
0
-3
Itgax
Adgrg5
Vcam1
Tlr12
Glipr1
Lpcat2
Acp5
Hexb
Ocstamp
Il1b
Rasal3
Nceh1
Cd300c2
Mmp12
Smim3
Ptk2b
Hvcn1
Sema4d
Igsf8
Lrrc3
Tlr13
Abhd15
Tmem119
Ext1l3
Abi3
Mapkapk3
Itgb5
Axl
Tgfbr1
Fam234b
H2-M2
Gngt2
Dtx4
Capn3
Hps4
Scimp
B3gnt8
Bcl2a1b
Psen2
Creg2
Cd4
Tbc1d10a
Mgat4a
Tpst2
Ctss
Gde1
Slc29a3
Adam17
Gpr31b
Tnfrsf1b
Arhgap27
Mmp14
Mmp13
Cd207
Pdgfa
Tnfaip2
B3galt5
Neurl3
Npc1
Itgav
Adamdec1
Cyp4f18
Galnt6
Stra6l
Pnpla7
Prdm1
Spsb1
Dnah2
Ppfia4
Emilin1
Lilra5
Gpr83
Tlr2
Inpp4b
Scarb2
Ppcdc
Rcbtb2
Enpp4
Snx18
Cd300a
Hgf
5430437J10Rik
1700071M16Rik
Abcc3
Tmem104
Tmem206
Hivep3
Lag3
Wdr81
Slamf6
Traf3
F9
Edem2
Hck
Mrgpre
Tnfsf13b
Itga9
Olfr111
Ermap
Mfsd12
Cd209f
Cd163
Fcna
Retnla
Ccl2
Ednrb
Ifi2712a
Ifitm6
Clec10a
Cd209b
Cd209d
Dok2
Ccl24
Slfn1
F13a1
Rgs18
Cbr2
Lgals1
Kmo
BC147527
Folr2
Bank1
Ifit3
Lyve1
Alox5
Timd4
Iqgap2
Wwp1
S100a10
Ms4a8a
Fgd6
Gas7
Igfbp4
Ccl7
Pstpip2
Gramd3
Raph1
C1qtnf1
Fxyd2
Rhobtb1
Cd200r1
Pf4
Ccl6
Itgam
Gm21188
Cd209a
Tmcc1
Cd209g
C6
Rasgrp4
Itsn1
Pstpip1
Eps8
Tmem8
Oasl2
Rtp4
Klf2
Ccl8
Txnip
Clec4a1
Plekhg5
Igf1
Gfra2
Samd91
Ampd3
Capg
Egr1
Chp2
Arhgap26
Mrc1
Pltp
Ccl9
Mcoln2
Fgfr1
Gm15987
Mfsd6
Grap
C4b
Irf7
Cbfa2t3
Gypc
Car3
Selenbp1
Ier3
Mpi
Cmpk2
Bid
Ifitm3
Zbp1
Olfm1
Camkk2
Marcksl1
Snx2
Crip1
Optn
Mtss1
Rn7sk
Plk2
Sult1a1
Alox5ap
Mean centered log2RPKM
-3
0
3
Pecr
Agmo
Hacd4
1810011H11Rik
Fer
Tlr4
Mr1
Arsg
Fcgr1
Fgd4
Sqrdl
Csf3r
Plod1
Tom1
Pld3
Tpp1
Ctsd
Lamp2
Pla2g4
Mertk
Tlr7
Cd14
Tbxas1
Fcgr3
Sepp1
Cd164
Tcn2
Dok3
Ctsl
Tspan14
Comt
Dram2
Abca1
Average
Mean centered log2RPKM
-2.0
0.0
2.0
Adam19
Amica1
Apls3
Ass1
Bcl11a
Btla
Ccr7
Flt3
Adgrg5
Gpr132
Gpr68
Gpr82
H2-Eb2
Hmgn3
Kit
Klri1
Kmo
P2ry10
Nectin1
Rab30
Sept6
Slamf7
Traf1
Zbtb46
Average
Mean centered log2RPKM
-2.0
0.0
2.0
Lung Lyve1hi MHCIIlo signature
Enrichment
3.6
0
SM
DM
statistic
-28.5
-4.0
-2.6
-1.7
-0.9
-0.2
0.6
1.4
2.6
4.7
36.6
Lung Lyve1lo MHCIIhi signature
Enrichment
4.2
0
SM
DM
statistic
-28.8
-4.0
-2.6
-1.7
-0.9
-0.2
0.6
1.4
2.6
4.7
36.6
Adhesion
Survival
Growth factors
Cx3cl1
Cx3cr1
Spp1
Itga9
Icam1
ItgaL
Itgb1
Vcam1
Gas6
Axl
Csf1
Csf1r
Csf3
Csf3r
Tgfb1
Tgfbr1
Tgfb3
Tgfbr2
Areg
Adam17
Basal
Lum. prog.
Mature lum.
DM
SM
Log2(RPKM)
6.0
3.0
0.0
Bl/6
Cx3cr1GFP/+
GFP MFI
60000
40000
20000
0
DM
SM1
SM2
DC1
DC2

Figure S 5.3: Gene expression analysis of adult virgin mammary DCs and MØs

(a) Top 50 positive SM signature genes. Heatmap shows mean-centred log2-expression with genes ranked by average FDR across pairwise comparisons (n = 2 per population, each pooled from 12 mice for a-f).

(b) Top 50 positive DC1 signature genes.

(c) Top 50 positive DC2 signature genes.

(d) Genes differentially expressed in DMs vs. SMs. Left heatmap shows most significant genes up-regulated in DMs, right panel shows most significant down-regulated genes.

(e) Heat map showing relative expression of genes previously associated with MØs [14] in the mammary DC/MØ populations.

(f) Heat map showing relative expression of genes previously associated with DCs[15] in the mammary DC/MØ populations.

(g) GFP MFI from analysis FACS plots of *Cx3cr1*$^{GFP/+}$ mice and wild-type (WT) controls. Control MFI for each population was subtracted (n=2 mice).

(h) Barcode enrichment plots showing that genes associated with MHCII^{lo}Lyve1^{hi} lung MØs are enriched in mammary MØ1/2 (roast p = 4e-5) whereas genes associated with MHCII^{hi}Lyve1^{lo} lung MØs are enriched in DMs (roast p = 5e-5). Genes are ordered in the plot right to left from most up to most down-regulated in DMs vs SMs. The x-axis shows moderated t-statistics. Vertical bars designate MHCII^{lo}Lyve1^{hi} or MHCII^{hi}Lyve1^{lo} lung MØ genes and the worms show relative enrichment.

(i) Epithelial and MØ expression of several known receptor-ligand interactions for genes specifically associated with DMs or of broad significance in MØ programming. Gene expression data for the epithelial populations are from [16]. Lum: luminal, Prog: progenitor.

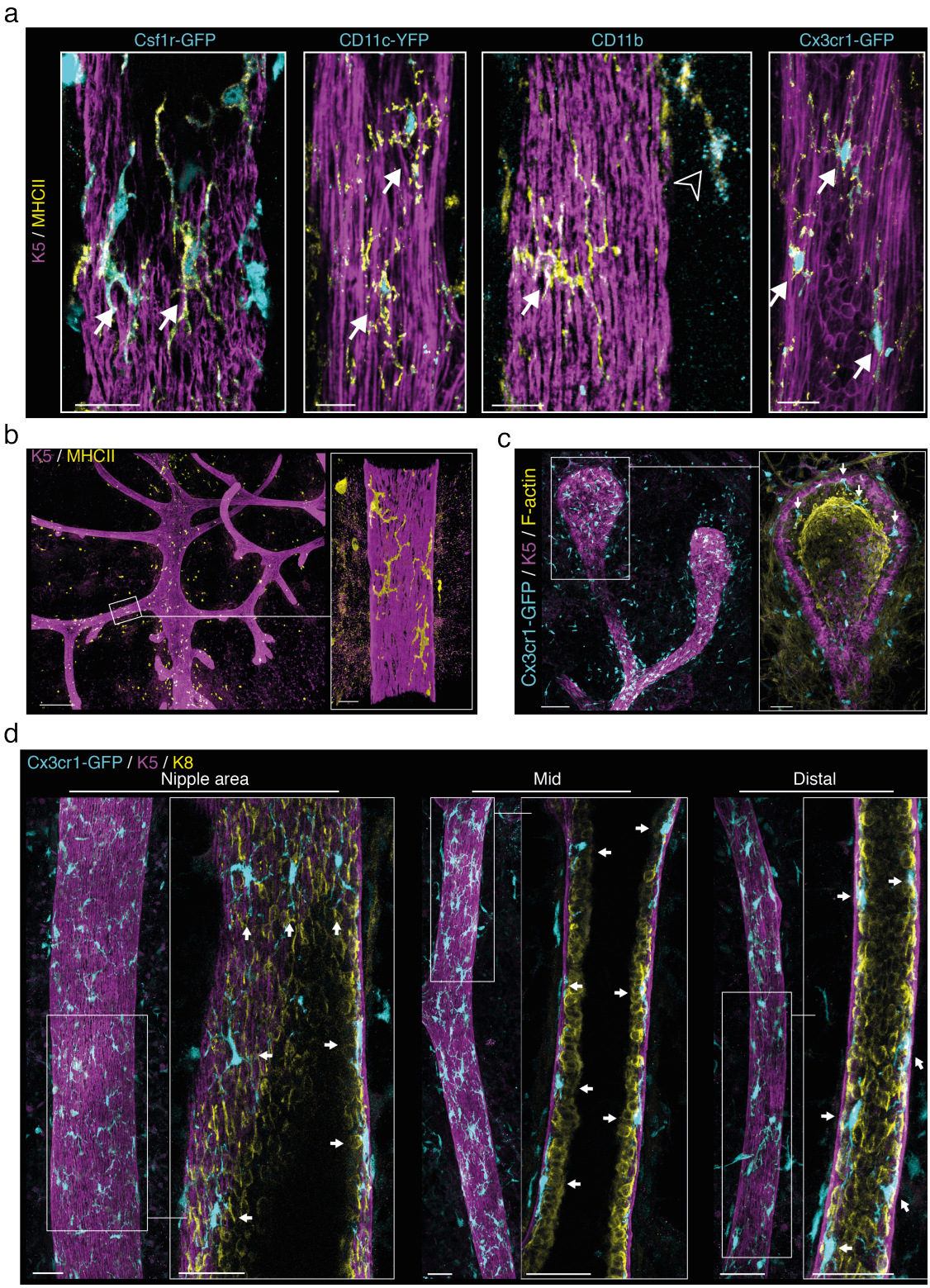
a
Csf1r-GFP
CD11c-YFP
CD11b
Cx3cr1-GFP
K5 / MHCII
b
K5 / MHCII
c
Cx3cr1-GFP / K5 / F-actin
d
Cx3cr1-GFP / K5 / K8
Nipple area
Mid
Distal

Figure S 5.4: Intra-epithelial macrophages are abundant within the mammary epithelium throughout post-natal development

(a) Optical sections from whole-mount 3D confocal images of mammary ducts immunostained for K5 (magenta), MHCII (yellow) and GFP, YFP or CD11b (cyan) in WT or indicated reporter mice. Arrows indicate intra-epithelial MØs. Hollow arrow head indicates a $CD11b^{+}$ stromal cell (n≥3 mice). Scale bars, 20 μm.

(b) Whole-mount 3D confocal image of a 2-week-old gland immunostained for K5 (magenta) and MHCII (yellow). Enlargement: 3D projection of the inner surface of a duct with opaque signal (n=3). Scale bars, 200 μm (overview) and 20 μm (enlargement).

(c) Whole-mount 3D confocal image of TEBs at 5 weeks and enlarged optical section, immunostained for GFP (cyan) and K5 (magenta) and labelled for F-actin (yellow) (n=3). Arrows indicate dendritic-shaped $Cx3cr1^{hi}$ cells within the TEB. Scale bars, 100 μm (overview) and 40 μm (enlargement).

(d) Whole-mount 3D confocal images of ducts of the nipple, mid and distal regions of glands and enlarged optical sections, from 8-week-old *Cx3cr1*$^{GFP/+}$ mice, immunostained for K5 (magenta), GFP (cyan) and Keratin 8 (K8, yellow) (n=2). Arrows indicate $Cx3cr1^{hi}$ DMs between the $K8^{+}$ luminal layer and the $K5^{+}$ basal layer in each region. Scale bars, 50 μm.

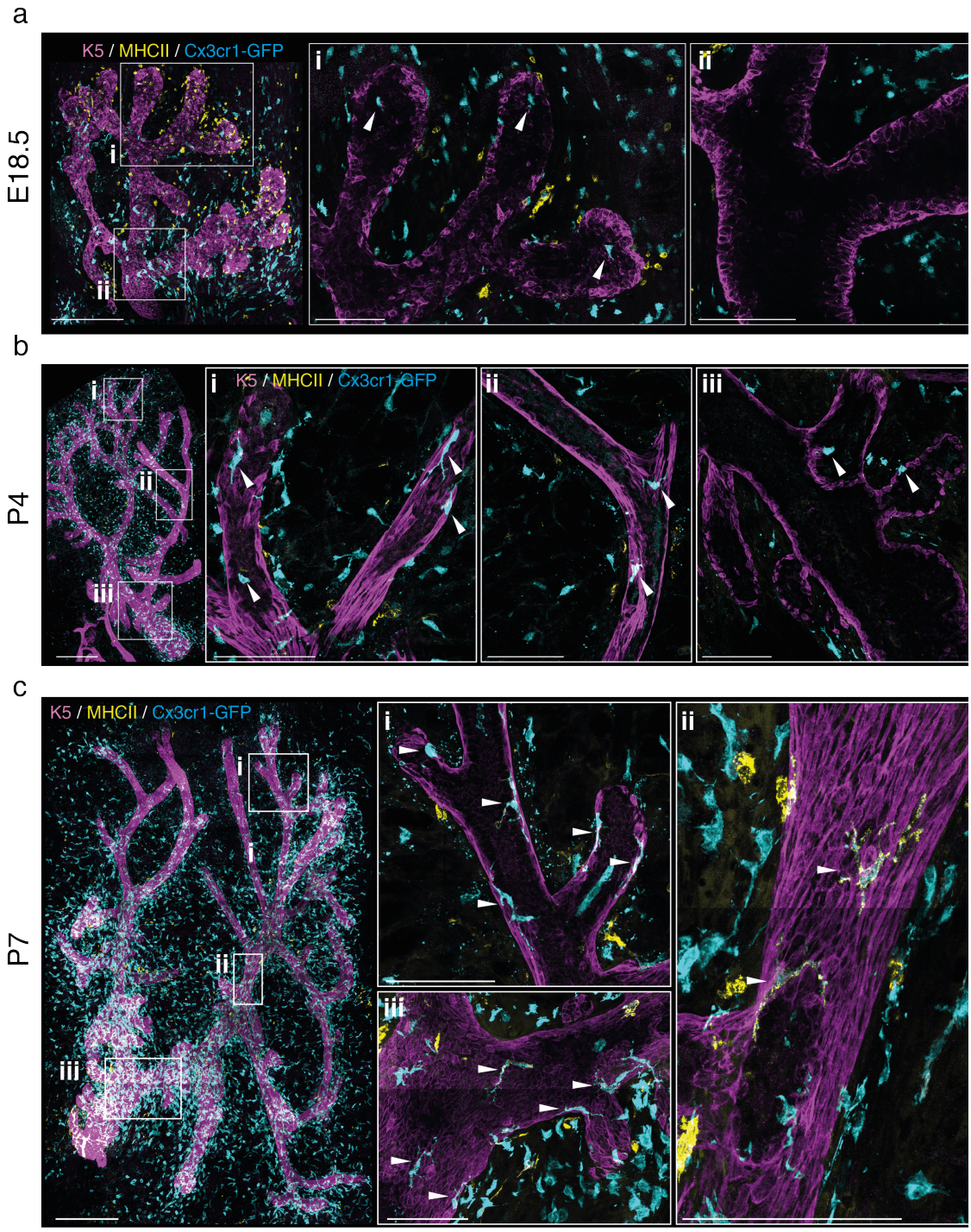
a
E18.5
K5 / MHCII / Cx3cr1-GFP
i
ii
b
P4
K5 / MHCII / Cx3cr1-GFP
iii
c
P7
K5 / MHCII / Cx3cr1-GFP

Figure S 5.5: DMs may arise from rare Cx3cr1^{+} cells in the distal embryonic gland

(a) Whole-mount 3D confocal image of an entire *Cx3cr1$^{GFP/+}$* mammary rudiment at E18.5 with enlarged optical sections of the distal (i) and nipple (ii) regions, immunostained for K5 (magenta), GFP (cyan) and MHCII (yellow) (n=2). Arrows indicate Cx3cr1^{+}MHCII^{-} cells in the distal tips. Scale bars, 300 μm (overview) and 100 μm (enlargements).

(b) Whole-mount 3D confocal image of an entire *Cx3cr1$^{GFP/+}$* mammary gland at post-natal day 4 with enlarged optical sections of the distal (i), mid (ii) and nipple (iii) regions, immunostained for K5 (magenta), GFP (cyan) and MHCII (yellow) (n=2). Arrows indicate Cx3cr1^{+}MHCII^{-} cells that were present in all regions but were more common and dendritic-shaped in the distal region. Scale bars, 300 μm (overview) and 100 μm (enlargements).

(c) Whole-mount 3D confocal image of an entire *Cx3cr1$^{GFP/+}$* mammary gland at post-natal day 7 with enlarged optical sections of the distal (i), mid (ii) and nipple (iii) regions, immunostained for K5 (magenta), GFP (cyan) and MHCII (yellow) (n=2). Arrows indicate highly dendritic Cx3cr1^{+}MHCII^{+} cells that were present in all regions. Scale bars, 300 μm (overview) and 100 μm (enlargements).

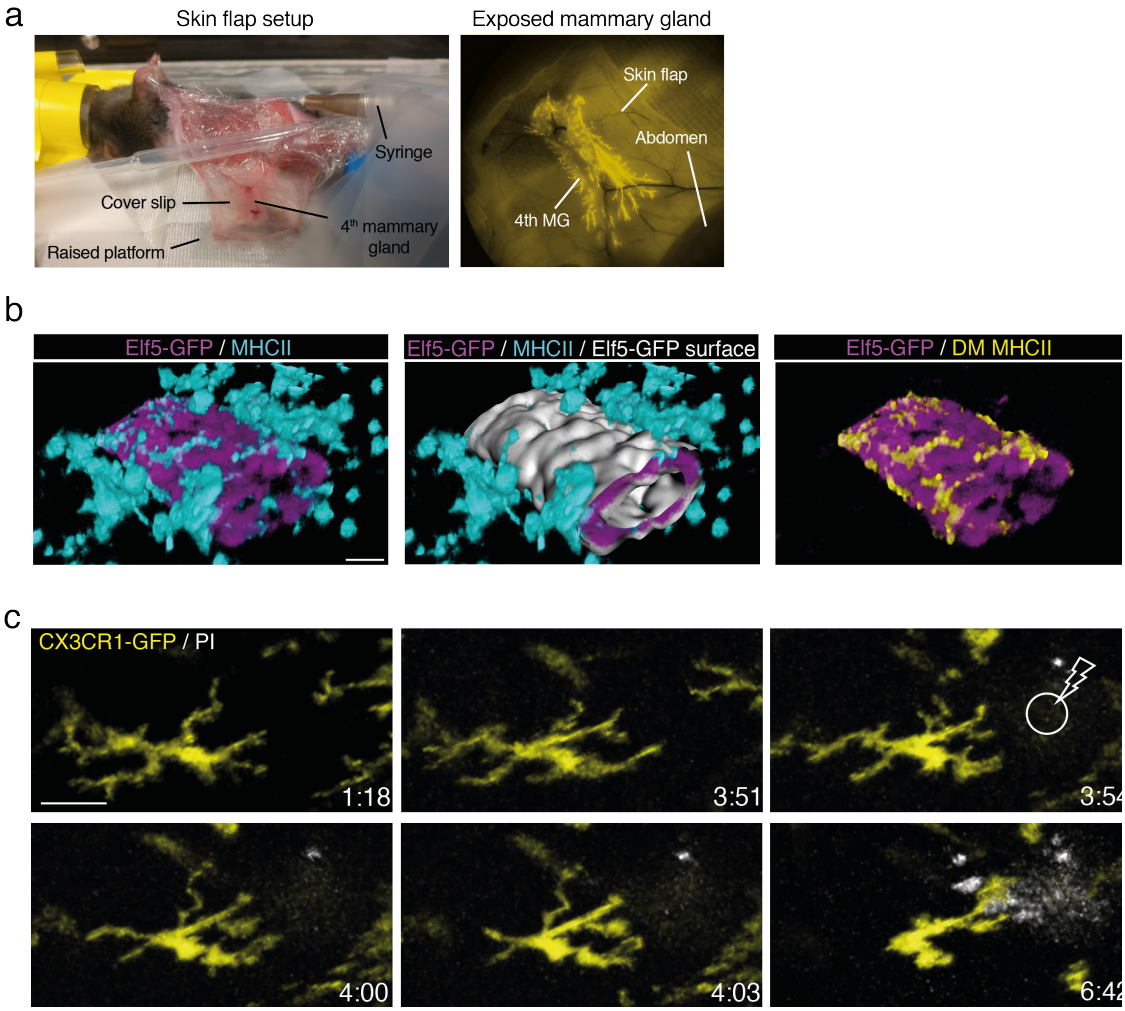
a
Skin flap setup
Exposed mammary gland
Syringe
Cover slip
4th mammary gland
Raised platform
Skin flap
Abdomen
4th MG
b
Elf5-GFP / MHCII
Elf5-GFP / MHCII / Elf5-GFP surface
Elf5-GFP / DM MHCII
c
CX3CR1-GFP / PI
1:18
3:51
3:54
4:00
4:03
6:42

Figure S 5.6: Supporting information for Figures 3 and 5

(a) Photo of a mouse prepared for intravital imaging (left) and the exposed mammary gland after intraductal injection of fluorescent beads prior to surgery (right).

(b) Isolation of DM MHCII signal in 3D-IVM images from *Elf5-GFP* mice. Total MHCII was masked using a low resolution (10 μm) surface of GFP signal in Imaris. Left: raw GFP (magenta) and MHCII (cyan) signal. Middle: addition of GFP surface rendering (white). Right: GFP and masked duct-adjacent DM MHCII signal (yellow) highlighting DM morphology. Scale bar, 30 μm.

(c) Time-points from a 3D-IVM movie (Movie S3) in which precise laser damage was induced in the epithelium of a *Cx3cr1*$^{GFP/+}$ mouse (n=3 mice). DM dendrites stop random surveillance and stably interact with the damaged region. Time hrs:mins. Scale bar, 20 μm.

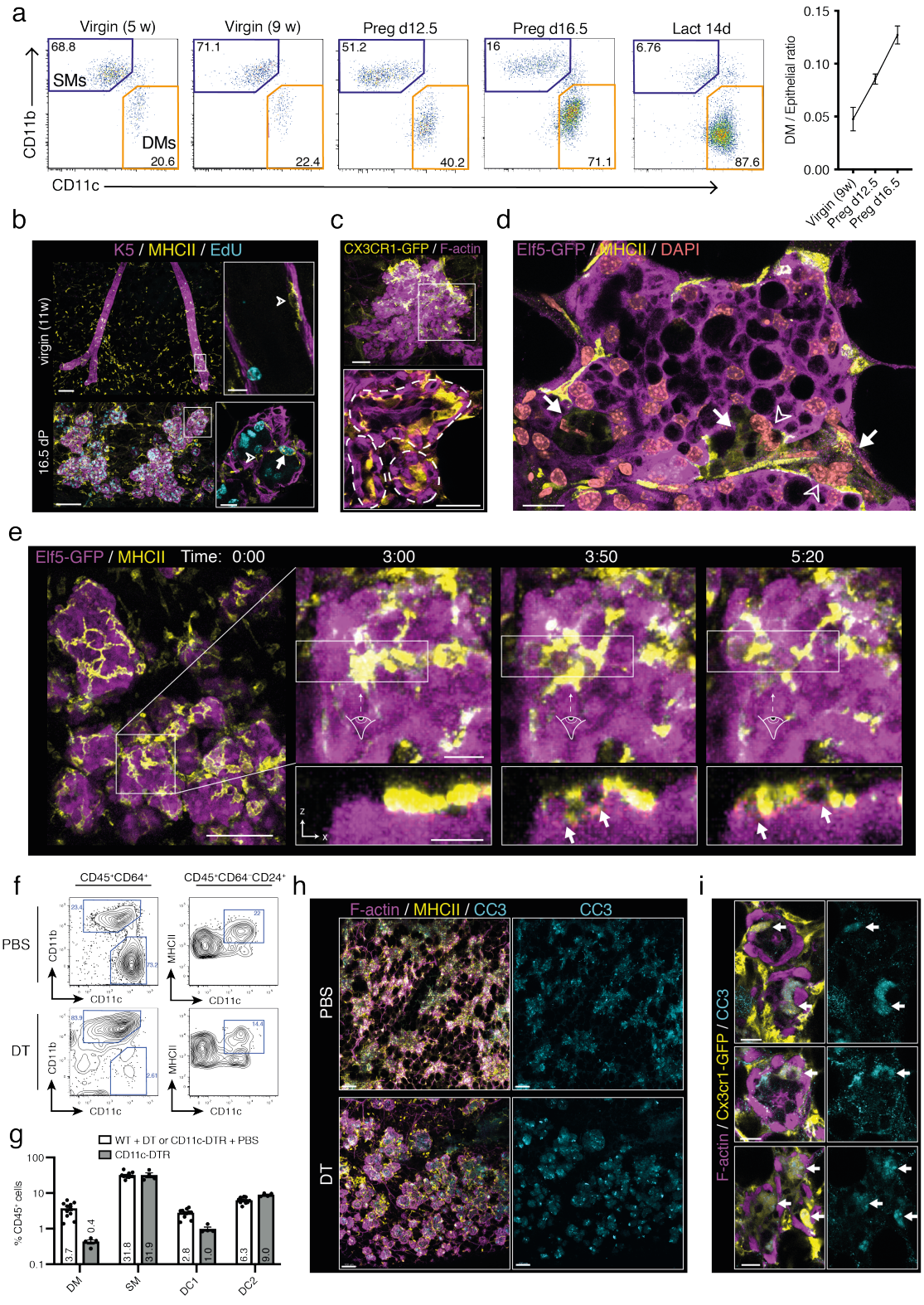
a
Virgin (5 w)
Virgin (9 w)
Preg d12.5
Preg d16.5
Lact 14d
68.8
SMs
DMs
20.6
71.1
22.4
51.2
40.2
16
71.1
6.76
87.6
CD11b
CD11c
DM / Epithelial ratio
0.15
0.10
0.05
0.00
Virgin (9w)
Preg d12.5
Preg d16.5
b
K5 / MHCII / EdU
virgin (11w)
16.5 dP
c
CX3CR1-GFP / F-actin
d
Elf5-GFP / MHCII / DAPI
e
Elf5-GFP / MHCII
Time: 0:00
3:00
3:50
5:20
f
CD45+CD64+
CD45+CD64-CD24+
PBS
DT
CD11b
MHCII
CD11c
g
WT + DT or CD11c-DTR + PBS
CD11c-DTR
% CD45- cells
100
10
1
0.1
3.7
0.4
31.8
31.9
2.8
1.0
6.3
9.0
DM
SM
DC1
DC2
h
F-actin / MHCII / CC3
CC3
PBS
DT
i
F-actin / Cx3cr1-GFP / CC3

Figure S 5.7: Supporting information for figures 5 and 6

(a) MØ FACS profiles throughout post-natal development and comparison of the DM/epithelial cell ($CD45^{-}CD24^{+}$) ratio in virgin and pregnant glands. w: weeks, d: days pregnancy, Lact: lactation (n≥3 mice). Error bars, s.e.m.

(b) Whole-mount 3D confocal images of 11 week adult and day 16.5 pregnant glands and enlarged optical sections, immunostained for K5 (magenta) and MHCII (yellow) and labelled for EdU (cyan). Mice were treated with EdU 2 hrs prior to collection (n=4). Hollow arrow-head indicates an EdU^{-} DM. Arrow indicates an EdU^{+} DM. Scale bars, 100 μm (overviews) and 15 μm (enlargements).

(c) Whole-mount 3D confocal image and enlarged optical section from a *Cx3cr1*$^{GFP/+}$ mouse at 4 days involution, immunostained for GFP and labelled for F-actin (n=2). Dotted lines indicate the outer edge of the F-actin^{hi} basal layer. Cells that infiltrate the alveolar lumen are Cx3cr1^{hi} DMs that have become rounded. Scale bar, 30 μm.

(d) Optical section from a whole-mount 3D confocal image of an *Elf5-GFP* gland at 3 days involution (n=3). Arrows indicate large GFP^{lo} alveolar cells that have been phagocytosed by DMs and are surrounded by MHCII signal. Hollow arrow-heads indicate double nuclei within phagocytosed cells, a characteristic feature of alveolar cells. Scale bar, 20 μm.

(e) 3D-IVM of alveoli in an Elf5-GFP mouse at 3 days involution showing GFP (magenta) and DMs immunolabelled by conjugated anti-MHCII antibody (yellow). Left: overview of alveoli and DMs. Right: enlarged 3D projections at time-points throughout phagocytosis and the outlined volume viewed from the side (indicated by the eyes), demonstrating GFP signal within DMs. Arrows indicate phagocytosed GFP^{+} alveolar cells within DMs. Images were acquired every 5 mins (n=3 mice). Scale bars, 100 μm (left), 20 μm (enlargements).

(f) Representative FACS plots from CD11c-DTR mice at 1 day involution, treated with DT immediately after forced weaning at 14 days lactation. DMs are depleted and DCs reduced (n=2).

(g) FACS quantification MØ and DC frequency at 4 days involution after treatment as in (e). Means are shown

(h) 20 μm thick optical sections from whole-mount 3D confocal images of glands from CD11c-DTR mice at 4 days involution after treatment as in (e) (n=4). Immunostaining for CC3 (cyan) and MHCII (yellow) and labelling for F-actin These were used to quantify the number of $CC3^{+}$ cells per area of mammary tissue (see methods). Note the increased size of alveoli following DT treatment. Scale bars, 100 μm.

(i) Optical sections from a whole-mount 3D confocal image of mammary tissue at 6 days involution in a *Cx3cr1*$^{GFP/+}$ mouse, immunostained for GFP (yellow) and CC3 (cyan) and labelled for F-actin (n=2). Arrows depict DMs, which are $CC3^{+}$, indicating their apoptosis after clearing alveolar cells. Scale bars, 15 μm.

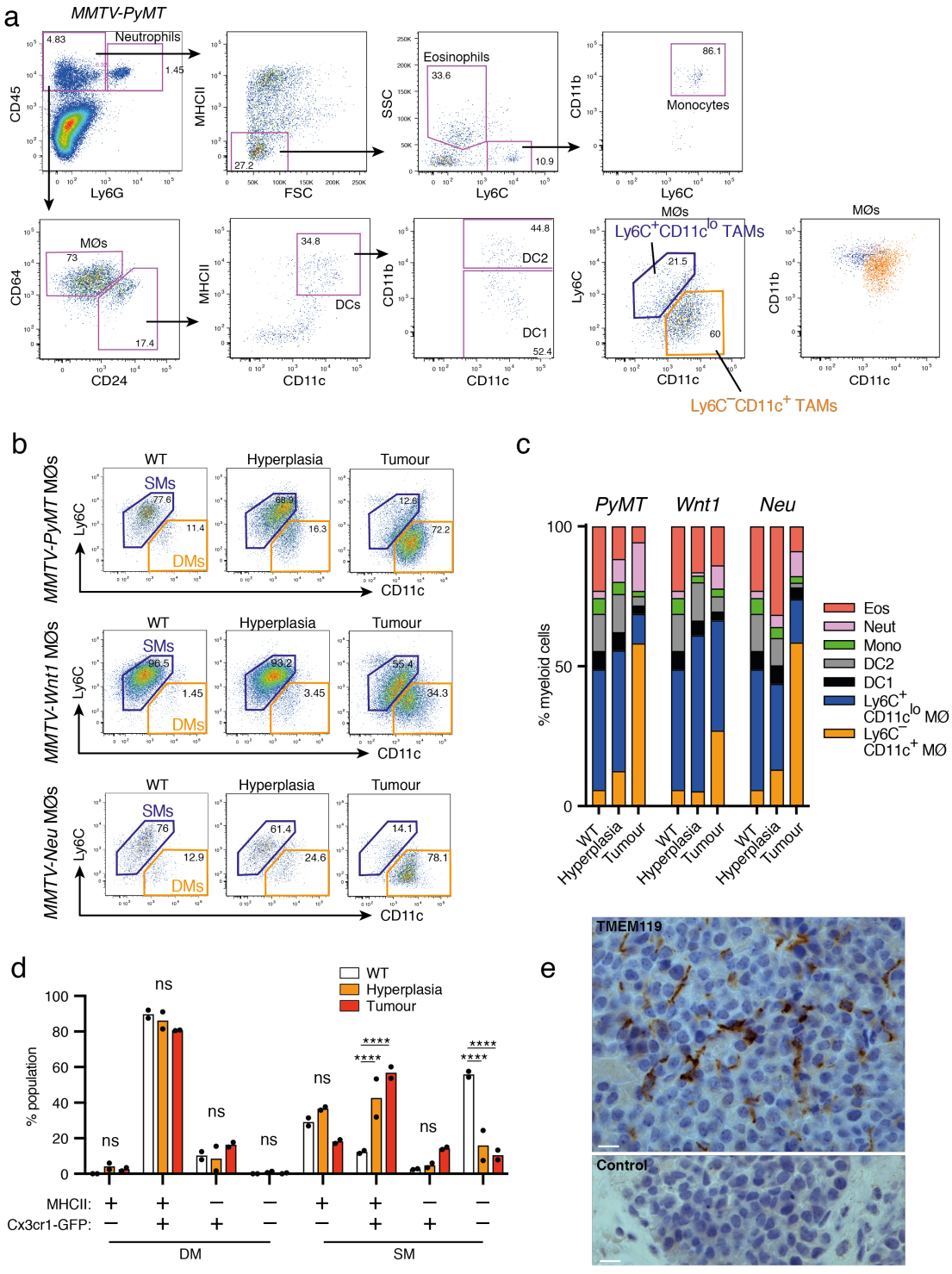
a
MMTV-PyMT
Neutrophils
Eosinophils
Monocytes
MOs
DCs
DC1
DC2
Ly6C+CD11clo TAMs
Ly6C−CD11c+ TAMs
b
WT
Hyperplasia
Tumour
MMTV-PyMT MØs
MMTV-Wnt1 MØs
MMTV-Neu MØs
SMs
DMs
c
PyMT
Wnt1
Neu
% myeloid cells
Eos
Neut
Mono
DC2
DC1
Ly6C+ CD11clo MØ
Ly6C− CD11c+ MØ
d
% population
MHCII:
Cx3cr1-GFP:
DM
SM
e
TMEM119
Control

Figure S 5.8: Resident MØ dynamics throughout tumorigenesis

(a) Representative FACS plots from an MMTV-PyMT tumour, showing typical gating strategy for myeloid profiling (n=4 mice). CD11c+ DM-like TAMs remain Ly6C– but upregulate CD11b.

(b) Representative FACS analysis of MØs (CD45+Ly6G–CD64+CD24lo) in age-matched wild-type FVB mammary glands, tumours and tumour-adjacent hyperplastic tissue from MMTV-PyMT, MMTV-Wnt1 and MMTV-Neu mice (n=4 mice per model).

(c) Quantification of myeloid cell frequencies by FACS in age-matched wild-type FVB controls, tumours and adjacent hyperplastic tissue from MMTV-PyMT, MMTV-Wnt1 and MMTV-Neu models. Eos: eosinophil, Neut: neutrophil, Mono: monocyte. Values are averages (n=4 mice per model).

(d) Quantification of MØ subsets throughout tumourigenesis in MMTV-PyMT/Cx3cr1GFP/+ mice, corresponding to Figure 5.7b (n=2). 2-way ANOVA with Sidak correction. ****P<0.0001.

(e) Immunohistochemistry of a MMTV-PyMT tumour section stained for TMEM119, showing dendritic-shaped intra-tumoral macrophages (n=2). The control panel is shown below. Scale, 10 μm.

5.9 Movie captions

Movie 1: Whole-mount 3D confocal imaging of DMs in lactation.

Animation of a whole-mount 3D confocal image of mammary tissue at 14 days lactation (Figure 5.2e), immunostained for K5 (Magenta) and MHCII (yellow) and labelled for F-actin (pink),

Movie 2: Intravital imaging of steady-state DM behaviour.

Animation of 3D-IVM of mammary ducts in an *Elf5-GFP* mouse with immunolabelling by fluorescently conjugated anti-MHCII antibody (Figure 5.3a-c). Movie cycles over a 6 hr time span with images acquired every 10 mins. GFP: magenta, Masked DM MHCII: yellow (see Figure S 5.4b) and stromal MHCII: cyan. Time in hr:min (n=6 mice).

Movie 3: Intravital imaging of DM response to epithelial damage.

Animation of 3D-IVM of a mammary duct in a *Cx3cr1*$^{GFP/+}$ mouse (Figure S 5.4c). Movie cycles through time-points prior to damage showing the arrangement of GFP^{hi} DMs (yellow) around a duct, then views an optical section through DMs before and after precise multiphoton laser damage at 4 hrs (bolt symbol). Images were acquired every 3 mins (n=3 mice).

Movie 4: Intravital imaging of DM response to apoptosis.

3D-IVM of a mammary duct in an *Elf5-GFP* mouse with immunolabelling by fluorescently conjugated anti-MHCII antibody (Figure 5.3e). GFP: magenta, Masked DM MHCII: yellow. Apoptotic cells are labelled with propidium iodide (PI) (white). Images were acquired every 5 mins (n=3 mice).

Movie 5: Intravital imaging of DM behaviour during involution.

3D-IVM of alveoli at 3 days involution in an *Elf5-GFP* mouse with immunolabelling by fluorescently conjugated anti-MHCII antibody (Figure 5.5d). GFP: magenta, MHCII: yellow. Images were acquired every 5 mins (n=3 mice).

Movie 6: DM-like TAMs form a dendritic network within mammary tumours.

Animation of a whole-mount 3D confocal image of *MMTV-PyMT/Cx3cr1*$^{GFP/+}$ tumour tissue immunostained for GFP (yellow) and labelled with DAPI (white) (Figure S 5.6e) (n=4 mice).

5.10 Materials and Methods

5.10.1 Mice

Wild-type C57BL/6 and FVB/N mice were provided by the Walter and Eliza Hall Institute (WEHI) animal facility. All mice are C57BL/6 unless indicated. *Elf5-rtTA-IRES-GFP* (FVB/N) mice were generated as previously described[1] and used as heterozygous. *CD11c-YFP, CD11c-DTR-GFP (*referred to as *CD11c-GFP* or *CD11c-DTR), CD11c-cre, CD11b-DTR, CX3CR1-GFP, Csf1r-GFP, UBC-GFP*, *Rosa-TdTomato, MMTV-PyMT* (FVB/N background)*, MMTV-Neu* (FVB/N background) and *MMTV-Wnt1* (FVB/N background) mouse lines were originally acquired from Jackson Laboratories; *Irf8-YFP*[2] and *Irf8*$^{fl/fl}$[3] mice were kindly provided by S. Nutt; *MMTV-PyMT/CX3CR1-GFP* and *MMTV-Wnt1/CX3CR1-GFP* mice were on a mixed Bl/6, FVB/N background; *Ms4a3*^{Cre} mice were generated as described[4]. All adult mice were virgin, unless otherwise indicated. Clearing of inguinal fat pads at 3 weeks was performed as previously described[7]. 21 day β-estradiol (0.05 mg) + progesterone (35 mg) slow release pellets or carrier compound placebos (HH-115 or C-111, Innovative Research of America) were implanted in the right 3rd mammary gland of mice at 8 weeks. For estrogen plus MPA experiments in bone marrow transplantation mice, estrogen (0.5 mg; in-house) and MPA pellets (15 mg; 21 day release; Innovative Research of America) were co-implanted subcutaneously, and mice were analysed after 3 weeks. For analysis of pregnancy time-points, adult mice were mated and females scored for the presence of vaginal plugs. The day of the observed plug was considered P0.5. For involution experiments, weaning was forced at 13-15 days lactation. Lactation experiments were performed after 14 days of lactation. For cell proliferation analysis with EdU (5-ethynyl-2-deoxyuridine), adult or pregnant mice were injected intraperitoneally (i.p.) with 0.1 mg of EdU (100 µl, 1 mg/ml in PBS) 2 hours before collection. Diphtheria toxin (Sigma) was injected at 2 ng/g i.p. (0.5 ng/µl in PBS) for CD11c-DTR and 20 ng/g (4 ng/µl in PBS). All mice were bred and maintained in the WEHI animal facility according to institutional guidelines. All experiments were approved by the WEHI Animal Ethics Committee.

5.10.2 3D confocal imaging of whole-mount tissue

Imaging was performed as previously described[5]. Briefly, tissue was collected and fixed in 4% PFA at 4° C, then washed overnight. At 4° C, tissue was incubated with primary antibodies overnight, washed, then incubated with secondary antibodies overnight before washing and clearing with FUnGI. During secondary staining, tissue was stained with DAPI (Thermo Scientific, 4 μg/ml) and/or F-actin was labelled with Phalloidin Alexa Fluor 488, 555 or 647 (Invitrogen, 1:25). For EdU labelling, tissue was incubated with Click-it Imaging 647 kit (Invitrogen) following secondary staining. Cleared tissue was dissected under a Leica M205 A fluorescence stereo microscope, mounted on a glass slide and with slight compression. Primary antibodies: (anti-mouse unless otherwise specified) Keratin-5 (rabbit polyclonal, Biolegend); Keratin-14 (rabbit polyclonal, Biolegend); GFP (chicken polyclonal, Abcam); E-cadherin (rat, clone ECCD-2, Invitrogen); MHCII (rat, Clone M5/114 in house); MHCII (mouse anti-human clone L243, Biolegend); CD11b (rat, clone M1/70, Biolegend); Cleaved caspase 3 (rabbit, clone 5A1E, Cell Signaling). Conjugated antibodies: MHCII Alexa Fluor 647 (rat, clone M5/114, Biolegend). Secondary antibodies: anti-rabbit Alexa Fluor 488 and 555 (Invitrogen); anti-chicken Alexa Fluor 488 (Invitrogen); anti-rat Alexa Fluor 488, 555 and 647 (Invitrogen); anti-mouse IgG2a Alexa Fluor 488, 555 and 647 (Invitrogen). Samples were imaged on Zeiss 780, Zeiss 880 or Leica SP8 confocal microscopes. Zeiss microscopes were equipped with 40x/1.20 Oil DIC or 63x/1.40 Oil DIC objectives and signal was collected by GaAsP array detector using spectral unmixing. Emission spectra were recorded using single stained controls Leica SP8 was equipped with an HCX PL APO 40x/1.30 Oil objective.

5.10.3 Image analysis

Image processing and analysis was performed in Zen (Zeiss), LAS X (Leica) and Imaris (Bitplane) for 3D confocal images and FIJI/ImageJ[6] for other images. For cell–duct distance quantification, a high-resolution surface was generated using K5 signal, then spots were generated for reporter-positive cells using semi-automated creation with a manually defined quality threshold or by manual spot placement (*Irf8-YFP*). Distances were calculated by creating an artificial channel with values equalling distance from the K5 surface using the Distance transformation XTension,

then exporting average intensity of this channel within each spot object. Branch frequency (Figure S 5.2b) was measured using a custom ImageJ macro (available on request). DM density (Figure 5.3f) was measured in Imaris by manually placing spot objects on Cx3cr1-GFP^{hi} (virgin) or MHCII^{+} (lactation) DM cell bodies beneath the K5^{+} basal layer, using cyan/red 3D anaglyph to assist spot placement in 3D. Distance between adjacent DMs was then calculated using the Spot to Spot closest distance module (from center-point). For intravital imaging, movies were manually stabilised, then low resolution (5-10 μm) surfaces of Elf5-GFP signal were created and used to mask DM specific MHCII signal. DM coverage of ducts in 3D-IVM movies was quantified in ImageJ by measuring the area of an MHCII signal in individual or cumulative time points and calculated as a percentage of *Elf5-GFP* signal area. Percentage DMs EdU^{+} (Figure S 5.7b) was counted manually in Imaris by scanning optical sections to identify intra-epithelial MHCII^{+} cells and scoring EdU. EdU^{+} epithelial cells were used as a positive reference. Percentage volume of alveoli occupied by DMs was obtained by manually creating alveoli surfaces using the outer edge of the F-actin-high myoepithelium. This was used to mask alveolar MHCII signal, then an alveolar MHCII surface was created and volume occupied calculated as a percentage of total alveolar volume. The percentage of alveolar cells phagocytosed (Figure 5.6d) was measured by capturing images of 5 μm optical sections through ~50 alveoli per replicate from 3D images. Alveolar cell counting was assisted by F-actin staining of cell junctions. Alveolar cells with complete co-staining with low intensity GFP and MHCII were considered phagocytosed. Average alveolar lumen area (Figure 5.6f) was measured in ImageJ by manually outlining lumen in four representative 40x regions per replicate. The number of CC3^{+} cells and number of CC3^{+} cells phagocytosed in involution (Figure 5.6h) was determined manually by scanning through optical sections. CC3^{+} cells were considered phagocytosed when completely surrounded by MHCII signal in 3D. Number of CC3^{+} cells per mm^{2} was determined by taking a 20 μm optical section through alveoli (Figure S 5.7g), masking CC3 signal within alveoli in ImageJ using F-actin signal, then counting alveolar CC3^{+} cells and dividing this by the area of the tissue.

5.10.4 Mammary gland whole-mount carmine staining

Mammary glands were laid on a slide, fixed in Carnoy's solution, washed with 70% ethanol then stained with carmine stain (0.2% w/v carmine, 0.92% w/v aluminium potassium sulphate dodecahydrate, 0.01% w/v thymol in dH20 (Sigma)), dehydrated through 70, 96 and 100% ethanol, then placed in Xylene (Sigma).

5.10.5 Intravital imaging using the skin-flap technique

In brief, mice were anaesthetised using 3% Isoflurane in 20% O_2 in N_2, which was then decreased to 1-1.5% to maintain stable anaesthesia. Temperature was monitored and maintained at 37° C using a rectal probe and thermostatic heat pad (FHC, Cat. 40-90-8D, 40-90-5D-02 and 40-90-2). The mouse right flank was shaved and remaining hair removed with hair removal cream (Veet). The 4th mammary gland was exposed by making a skin incision along the midline and right hind leg, cauterising the 5th mammary gland and unfolding and positioning the resulting skin flap on a platform. Imaging was aided by fluorescence guided micro-dissection of connective tissue from the top of the fat pad. The exposed torso was covered with cling wrap to prevent dehydration. The exposed mammary gland was labelled with MHCII-Alexa Fluor 647 (5 µl, rat, clone M5/114, Biolegend) and/or 2.5 µg propidium iodide in approximately 200 µl PBS. The imaging area was sealed using a ring of silicone grease (Dow Corning, Cat. DC976VF) and a cover slip. Hydration was maintained by i.p. injection of saline at a rate of 100 µl per hour.

5.10.6 Multiphoton microscopy

Intravital imaging was performed using the FVMPE-RS multiphoton system (Olympus), equipped with MaiTai DeepSee and InSight DeepSee lasers (Spectra-Physics), 2 GaAsP and 2 Multialkali PTMs, SIM scanner and a 25x/1.05 NA water objective (Olympus). Three-dimensional image stacks were acquired with 1µm z-step size every 3, 5 or 10 minutes for up to 12 hours. Site-specific laser damage was induced using the SIM scanner to deliver 800 nm MaiTai laser at 0.3W for 10 seconds in a 10 µm region or a single point while simultaneously imaging with the InSight laser. Laser power was kept below 0.1W for imaging. Green, red and far red fluorescence was separated by 570nm dichroic, 650 nm dichroic and 610/70 and 705/90 filters

(Semrock) and collected by GaAsP or Multialkali photomultiplier. GFP and PI were excited at approximately 950nm and Alexa fluor 647 at approximately 800 or 1200 nm.

5.10.7 Immunohistochemistry

For immunohistochemistry, tissue sections were heat treated in high pH antigen retrieval buffer (Dako), stained with primary antibody at 4°C overnight, followed by secondary antibody staining. Staining was compared to staining of secondary antibody alone. The streptavidin–biotin peroxidase detection system was used with 3,3'-diaminobenzidine as substrate (DAKO). Antibodies: TMEM119 (rabbit, clone 28-3, abcam), Goat anti-rabbit biotin (Vector Laboratories).

5.10.8 Preparation of mammary gland single cell suspensions and flow cytometry

Single cells from glands (typically 2 x 3rd and 2 x 4th glands) and tumours were prepared as previously described[7] after removal of the inguinal lymph node. Briefly, tissue was minced using a tissue chopper (McIlwain), digested for 1 hour in Collagenase/Hyaluronidase/DNase, then treated with trypsin for 2 minutes (no trypsinisation tumour experiments and for experiments where antibody fluorescence intensity was measured) before filtering and staining. For duct enrichment, glands were digested for an hour in collagenase/hyaluronidase then pipetted with a 25 ml serological pipette. Fat was removed by pulse centrifugation, then ducts were manually selected using a dissection microscope and processed to single cells as above. Immunostaining was performed at 4° C: cells were blocked with 0.1 mg/ml Rat IgG2a then primary antibodies were incubated for 30-45 minutes and secondary antibodies for 20 minutes. Primary antibodies: MHCII Brilliant Violet 711 (rat, clone M5/114, Biolegend), MHCII Brilliant Violet 421 (rat, clone M5/114, Biolegend), Ly6G Brilliant Violet 510 (rat, clone 1A8, Becton Dickinson), Ly6C PE-Cy7 (rat, clone HK1.4 Biolegend), Gr-1 PE-Cy7 (rat, clone RB6-8C5, Life Technologies), CD45 Brilliant Violet 605 (rat, clone 30-F11, Biolegend), CD64 Brilliant Violet 421 (rat, clone X54-5/7.1, Biolegend), CD64 Brilliant Violet 711 (rat, clone X54-5/7.1, Biolegend), CD11b Brilliant Violet 785 (rat, clone M1/70, Biolegend), CD24 PE (rat, clone M1/69, Biolegend), CD24 PerCP-Cy5 (rat, clone M1/69, Biolegend), CD11c Alexa Fluor 647 (hamster, clone N418, Biolegend), CD11c Biotin

(hamster, clone N418), CD11c PE (hamster, clone N418, Biolegend), CD103 APC (rat, clone 2E7, Biolegend), CD103 PE (rat, clone M290, Becton Dickinson) B220 APC-Cy7 (rat, clone RA3-6B2, Biolegend), F4/80 APC-Cy7 (rat, BM8, Biolegend), MerTK PE (rat, clone DS5MMER, eBioscience), Lyve1 (rat, clone ALY7, Invitrogen), CD206 FITC (Rat, C068C2, Biolegend). Biotin conjugated antibodies were labelled with Streptavidin Brilliant Violet 650 (BD Horizon). Dead cells were identified by resuspending cells in 0.5 μg/ml propidium iodide before analysis or sorting. Flow cytometric analysis was performed on a Fortessa X20 flow cytometer using FACSDiva software (Becton Dickinson). Cells were sorted on a FACSAria III or a FACSAria Fusion using FACSDiva software (Becton Dickinson). Subsequent analysis was performed using FlowJo (Tree Star). Fluorochrome overlap was compensated using anti-Rat coated beads labelled with the appropriate antibody (for non-rat antibodies, a rat antibody with matching fluorochrome was used) and blank beads.

5.10.9 Bone marrow chimeras

Bone marrow was pooled from 2-3 UBC-GFP$^{Tg/+}$ mice and depleted of red blood cells with 0.64% NH_4Cl. 10 week-old C57Bl/6 mice were anaesthetised by injection of ketamine/xylazine and were given a single dose of 550 Rads gamma irradiation while shielding the abdomen with a lead shield. After 3-4 hours recovery, mice were given 2x10^6 GFP$^+$ bone marrow cells by intravenous injection. Only the shielded 4th and 5th mammary glands were collected for analysis.

5.10.10 RNA sequencing analysis

Total RNA was extracted from sorted macrophage and dendritic cell populations from the mammary glands of 9 week-old C57Bl/6 mice (2 pools of 12 mice), or from sorted macrophage populations isolated from 9 week virgin, pregnant, lactating and post-involution C57Bl/6 mice (individual mice). Total RNA from 400-500 cells (virgin) or 2000 cells (developmental time-course) was used to generate libraries for whole transcriptome analysis following the Clontech v4 low input RNA protocol. Libraries were sequenced on an Illumina NextSeq 500. Between 7 - 38 million 75 bp paired-end reads were generated for each sample. Reads were aligned to the mouse genome mm10 using Rsubread version 1.22.3[8]. The number of reads overlapping each

Entrez gene were counted using featureCounts and Rsubread's built-in NCBI annotation[9]. Gene information was downloaded from the NCBI (4 October 2016). Genes were retained for downstream analysis if they achieved at least 1 count per million (CPM) in at least 2 samples. Ribosomal genes, predicted genes, unassembled contigs and obsolete Entrez Gene IDs were removed from further analysis. Counts were converted to log2 counts per million (log2CPM) with prior count 2 using the edgeR cpm function and quantile normalized. Differential expression analysis was performed using the limma package version 3.30.8[10] with robust trended empirical Bayes[11]. Genes were considered to be differentially expressed if they achieved a false discovery rate (FDR) below 5%. Positive (or negative) signature genes were defined for each population as all genes significantly up-regulated (or down-regulated) in that population vs all the other populations in pairwise comparisons. Canonical pathways were obtained from the Molecular Signatures Database v5.2[12]. Human genes were mapped to mouse orthologs using HGNC orthology predictions (http://bioinf.wehi.edu.au/software/MSigDB). Overlap analyses of pathways were conducted using hypergeometric tests. Gene set enrichment analysis of pathways was performed using limma's camera function with default settings[13]. Expression signature analyses were performed using roast. The multidimensional scaling plot was drawn by limma's plotMDS function with leading log2-fold-change distances. Average Log2-RPKM was computed for each gene and each cell population using edgeR's rpkmByGroup function.

5.10.11 Analysis of Franklin et al microarray data

Normalized log2-expression values were downloaded from GEO series GSE56755. Differentially expressed genes between tumour-associated macrophages (TAMs) and mammary tissue macrophages (MTM) were determined using limma with trended empirical Bayes with robust estimation of the hyperparameters[7]. This yielded 2168 differentially expressed genes with FDR < 0.05. The top 1000 differentially genes were used to represent the TAM vs MTM expression signature.

5.10.12 Human samples

Fresh human breast tissue from reduction mammoplasties was obtained from consenting individuals through the Victorian Cancer Biobank with approval from the Human Research Ethics Committee of WEHI.

5.10.13 Statistics and reproducibility

Sample sizes were not predetermined by statistical analysis. Most experiments were performed on at least three biological replicates and most experiments were repeated at least twice, exact *n*, indicating biological replicates, is stated in associated figure legends. Experiments were not randomised and investigators were not blinded during experiments or analysis of outcome. Error bars are only shown if data was obtained from three or more biological replicates. Error bars shown are mean ± standard error of the mean (s.e.m.) or mean ± one standard deviation (s.d.) as indicated in figure legends. P values were determined by appropriate statistical tests indicated in figure legends. $P<0.05$ was considered significant.

5.11 References for supplementary information

1. Rios, A. C., Fu, N. Y., Lindeman, G. J. & Visvader, J. E. In situ identification of bipotent stem cells in the mammary gland. *Nature* **506,** 322–327 (2014).

2. Wang, H. *et al.* A reporter mouse reveals lineage-specific and heterogeneous expression of IRF8 during lymphoid and myeloid cell differentiation. *J. Immunol.* **193,** 1766–77 (2014).

3. Feng, J. *et al.* IFN regulatory factor 8 restricts the size of the marginal zone and follicular B cell pools. *J. Immunol.* **186,** 1458–66 (2011).

4. Liu, Z. *et al.* Fate mapping via Ms4a3 expression history traces monocyte-derived cells. *Biorxiv* 652032 (2019). doi:10.1101/652032

5. Rios, A. C. *et al.* Intraclonal Plasticity in Mammary Tumors Revealed through Large-Scale Single-Cell Resolution 3D Imaging. *Cancer Cell* **35,** 618–632.e6 (2019).

6. Schindelin, J. *et al.* Fiji: an open-source platform for biological-image analysis. *Nature Methods* **9,** 676 (2012).

7. Shackleton, M. *et al.* Generation of a functional mammary gland from a single stem cell. *Nature* **439,** 84 (2006).

8. Liao, Y., Smyth, G. K. & Shi, W. The Subread aligner: fast, accurate and scalable read mapping by seed-and-vote. *Nucleic acids research* **41,** e108 (2013).

9. Liao, Y., Smyth, G. K. & Shi, W. featureCounts: an efficient general purpose program for assigning sequence reads to genomic features. *Bioinformatics (Oxford, England)* **30,** 923–930 (2014).

10. Ritchie, M. E. *et al.* limma powers differential expression analyses for RNA-sequencing and microarray studies. *Nucleic Acids Res.* **43,** e47 (2015).

11. Phipson, B., Lee, S., Majewski, I. J., Alexander, W. S. & Smyth, G. K. Robust hyperparameter estimation protects against hypervariable genes and improves power to detect differential expression. *The annals of applied statistics* **10,** 946–963 (2016).

12. Liberzon, A. *et al.* Molecular signatures database (MSigDB) 3.0. *Bioinformatics (Oxford, England)* **27,** 1739–1740 (2011).

13. Wu, D. & Smyth, G. K. Camera: a competitive gene set test accounting for inter-gene correlation. *Nucleic acids research* **40,** e133 (2012).

14. Gautier, E. L. *et al.* Gene-expression profiles and transcriptional regulatory pathways that underlie the identity and diversity of mouse tissue macrophages. *Nature* **13,** 1118–1128 (2012).

15. Miller, J. C. *et al.* Deciphering the transcriptional network of the dendritic cell lineage. *Nat. Immunol.* **13,** 888–99 (2012).

16. Sheridan, J. M. *et al.* A pooled shRNA screen for regulators of primary mammary stem and progenitor cells identifies roles for Asap1 and Prox1. *BMC Cancer* **15,** 221 (2015).

Chapter 6: Discussion and Conclusions

The localisation, arrangement and dynamics of cells are central to their function in health and disease. Through 3D and intravital imaging, this thesis has interrogated the 3D landscape of the mammary gland to reveal mammary progenitor cell behaviour and a previously uncharacterised resident MØ population.

6.1 Intravital imaging of the mammary gland

A skin flap method previously used to image breast tumours, the lymph node and the lactating mammary gland (Bayarmagnai et al., 2018; Ewald et al., 2011a; Masedunskas et al., 2017; Miller et al., 2003) was adapted to allow high resolution, long-term IVM of the virgin mammary gland. Many challenges were overcome to achieve this, particularly the high proportion of adipose tissue surrounding the ductal network that causes light-scattering. Exposure of the entire inguinal mammary gland enabled rare exposed regions of the epithelium to be found and imaged. Extensive measures were taken to ensure conditions were as physiological as possible, including creation of a sealed imaging well over the gland and protecting exposed regions from dehydration. This maximised resolution and tissue access for additional fluorescent labels but limited imaging to a single session. Imaging was affected by tissue drift and occasional breathing movement but these could be resolved during imaging and post-acquisition processing.

6.1.1 Myoepithelial cell dynamics

Observation of myoepithelial cell division in the longitudinal axis provides novel insight into mammary epithelial cell biology. This has implications for interpreting clonal expansion in lineage tracing experiments – more weight should be given to the clonal relationship of longitudinally aligned basal cells. Conversely, clonality of adjacent lineage-traced basal cells may need to be excluded, even when cell bodies are in direct contact. Basal cells rarely divided in adulthood as only one division event was seen in three independent long-term IVM experiments.

More observations of basal cell division will need to be made before broad and confident conclusions can be drawn.

6.1.2 Future applications of intravital microscopy

A small proportion of adult basal cells can produce luminal cells during duct homeostasis (Rios et al., 2014). This could occur either by asymmetric division to directly generate a luminal daughter cell and a self-renewed MaSC, or by symmetric division of a MaSC followed by luminal differentiation of one daughter cell. Whether luminal cells arise from basal cells has been disputed (Wuidart et al., 2016), but it is anticipated to be rare and thus difficult to observe by IVM. Basal-to-luminal differentiation or asymmetric division was not observed in IVM of adult ducts. Despite this, skin flap IVM is ideal for clarifying this issue. The ability to fix, immunostain and image a region following IVM would be particularly powerful in this endeavour — observation of basal-to-luminal differentiation could be subsequently confirmed by expression of luminal markers in a cell that was originally basal and elongated. Many experiments would be required to observe even one event. This frequency might be improved by imaging near the nipple, where MaSCs are more prevalent (Fu et al., 2017).

6.2 Visualisation of 3D microscopy

Tissue structure and cell morphology are commonly investigated by two-dimensional (2D) imaging of thin tissue sections and imaging of cells in culture. Traditional methods of scientific data presentation in journals is well suited to these techniques, as data can be shown in its original 2D form. The transition to 3D and 4D imaging with many fluorescence channels far exceeds the ability of 2D images to truly communicate modern imaging data (Fan et al., 2015). Flattening of 3D data to 2D also creates artefacts that misrepresent the original data (Shihavuddin et al., 2017). Animation of microscopy data can convey 3D information and the shift to online reading of papers makes multimedia incorporation simpler (Ruthensteiner et al., 2010), however, their inclusion in publications as supplementary information is cumbersome.

6.2.1 Interactive presentation of microscopy data

The development of virtual reality (VR) and augmented reality (AR) is revolutionising the way that people interact with the digital world. VR uses a headset to provide an immersive experience, where a person can feel as though they were inside a digital world. This is being successfully used in science education (Johnston et al., 2018) and in the clinic (Rizzo et al., 2019). VR has been developed commercially as a tool for science communication and microscopy data analysis (Pidhorskyi et al., 2018) but public outreach through VR is limited, as headsets are not widely accessible due to cost. It is also a private experience typically enjoyed by one or a few people at one time, even when accessed in a public space. Thus, VR is unsuitable for large-scale communication of scientific data such as on social media or in conference presentations.

AR provides a less immersive view of digital objects but places them in real-world context within the view of a camera. Movement of the camera around the digital object creates a 3D impression caused by the changing perspective. Users can interact with the virtual object, typically via a touch screen on a smartphone. The ubiquity of smartphones makes AR a highly attractive option for interactive data presentation but has not been explored for visualisation of microscopy data. AR has been implemented for educational purposes, such as for teaching 3D protein structure in molecular biology (Safadel and White, 2019).

6.2.2 Communicating depth in 2D formats

While 3D animation, VR and AR are the best available methods for communicating 3D information, science communication remains heavily reliant on simple 2D images that can be printed in physical journals and stored as simple files (Ruthensteiner et al., 2010). Further challenges lie in conveying 3D information in live imaging, where a static viewpoint is desirable so that movement within the sample can be appreciated. This makes animation, VR and AR undesirable as these rely on movement to generate 3D perception. 3D information can be conveyed in 2D format by depth-coded colourisation and the separate display of xy, xz and yz projections. Both methods limit the display of important information such as multiple channels

and spatial interactions, and their interpretation is not intuitive. Depth-coded colourisation also discriminates against colour-blind viewers.

6.2.3 Cyan/red 3D for analysis and visualisation

Stereo 3D can better achieve depth communication by four methods of separating stereo images: polarisation, lens shuttering, manual cross-eyed overlaying and two-coloured anaglyphs. Of these, anaglyphs require the least specialised equipment while being easy to view. The C/R anaglyph option provides good colour perception and is colour-blind accessible. Anaglyph 3D has been implemented for viewing of scientific data in a few instances, including for neuroanatomy (Hirsch and Kramer, 1999), brain MRIs (Rojas et al., 2014), endomicroscopy (Orth et al., 2019) and electron microscopy (Heuser, 2000; Postek and Steffens, 1979). In rare applications for laser scanning microscopy, anaglyph 3D has been limited to single channel monochrome (Gilbert et al., 1995; Lucas et al., 1996; Wagner et al., 1994; Wang et al., 2005).

Implementation of C/R 3D through Imaris was surprisingly beneficial for 3D image visualisation, intuitive quantification and communication through posters and oral presentations. In movies of the TEB, cells move extensively in 3D, making analysis of migration and cell fate in 2D projections almost impossible. C/R 3D allowed observation of single cell behaviour in 3D in a crowded environment. While still challenging and slow, the comparative ease and intuitiveness of this approach enabled manual tracking of 175 TEB progenitors to measure their rate of migration, and the observation of 64 cap cells over many hours to determine their fate. Information gained by future applications of 3D cell tracking will provide important insights into cell dynamics within complex and crowded tissue environments.

6.3 Progenitor dynamics in the terminal end bud

The TEB is a highly tractable model of organogenesis, but how each cell type behaves within the TEB to culminate in duct elongation is unknown. This work describes in vivo lineage-specific morphology and behaviour in the TEB, providing an advance in our understanding of how the mammary gland is formed (Figure 6.1).

Combining 3D IVM of TEBs with lineage-specific multi-colour fluorescent labelling revealed diverse single cell dynamics. Cap cells migrated within the cap in an amoeboid fashion and migrated into the TEB body, after which a small proportion survived long term to possibly contribute to the luminal compartment. The cap cell dynamics observed may have been affected by artifactual cell death that was induced by IVM. Cap cells were uniquely sensitive to apoptosis in these experiments, possibly due to laser damage or dilution of important survival factors when the gland is bathed in PBS. More experiments are needed to confirm that this is a consistent observation and not only an issue with these imaging sessions. Increased cell death may have resulted in underestimation of rates of division and migration into the TEB body, or perhaps overestimation of the rate of migration into the body, since this process is associated with cell death. Quantification of individual TEB progenitor cell behaviour demonstrated that APs are less migratory than HSPs, which migrate in a mesenchymal-like fashion throughout the TEB body. Thus, HSPs seem to have a more active role in TEB cellular rearrangement and therefore may be the primary drivers of duct elongation by radial intercalation. The variable generation of mesenchymal-like cells from *K5* lineage-traced cells provides evidence that these cells surviving after cap to body migration may contribute to the HSP pool. More replicates need to be collected for these analyses (particularly for *Elf5*$^{+}$ APs) to confirm that the results are reproducible.

6.3.1 Branching during morphogenesis

Branching was not observed during IVM of TEBs. This may be due to TEB bifurcation occurring on a longer timescale than observable by skin flap IVM. Alternatively, the increased cell death that occurred after many hours of IVM may prevent sufficient growth for branching. Other possibilities are that anaesthesia and surgery affect signals that are critical for branching, or that bifurcation is diurnally regulated and occurs only at night – there is some evidence of a role for cell-intrinsic clocks in duct formation (Rossetti et al., 2012).

Decreased branching was observed upon IGF-1 deletion (Richards et al., 2004) and loss of eosinophils (Gouon-Evans et al., 2000). Other factors that are important for morphogenesis such as TGF-β, RELN, mast cells and MØs seem to promote proliferation or TEB initiation more than branching (Gouon-Evans et al., 2000; Khialeeva et al., 2011; Lilla and Werb, 2010; Silberstein

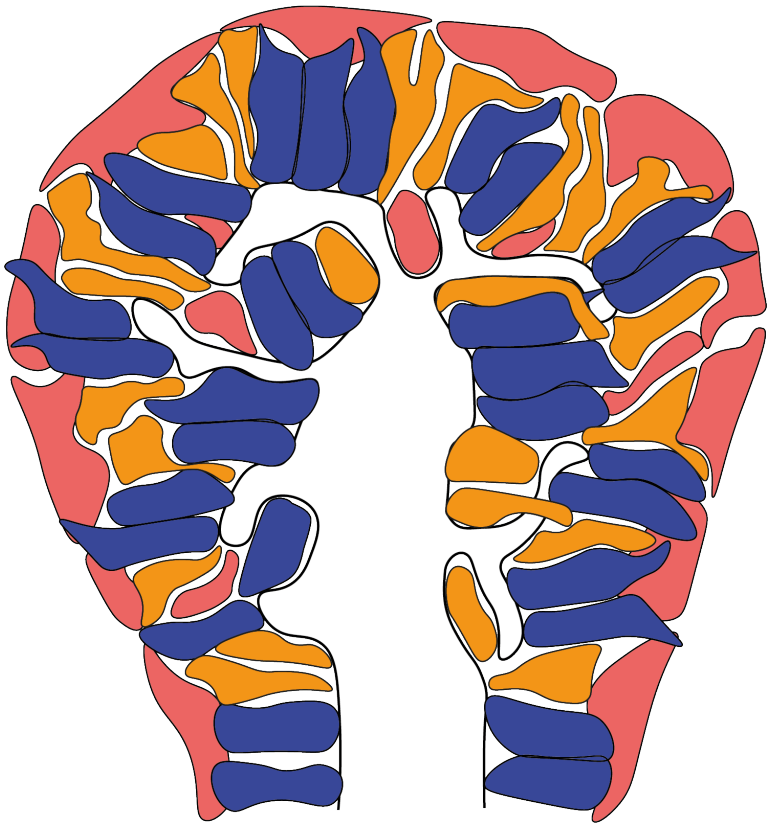

Figure 6.1: Cellular organisation of the terminal end bud

A revised model of TEB morphology. The TEB lumen is complex and cells are poorly polarised without tight junctions. Hormone-sensing progenitors (orange) migrate throughout the TEB and have a radially oriented spindle-like morphology. Alveolar progenitors (blue) are less active but extend short protrusions through the cap layer. Cap cells (red) migrate into the TEB body, where most die but some survive long term.

and Daniel, 1987). Branching of the lung requires localised smooth muscle differentiation at the growing tip (Kim et al., 2015). A similar mechanism may lie behind TEB bifurcation, where cap cell differentiation at the tip could initiate branching. Perhaps IGF-1 signalling or eosinophils adjacent to the cap layer influence this process. Eosinophils could potentially act through alteration of the basement membrane by proteases released from granules upon activation.

The random nature of duct branching (Scheele et al., 2017) suggests that branching is initiated by complex interactions involving multiple factors. Another intriguing possibility is that surface

curvature influences myoepithelial differentiation, as is the case for lung smooth muscle (Xu et al., 2011). In this scenario, small TEBs would have high curvature that promotes an undifferentiated state, whereas large TEBs would have lower curvature that could induce differentiation of myoepithelial cells at the tip. Indeed, myoepithelial cell morphology seems to be highly dependent on duct architecture based on the 3D imaging performed for this project: these cells appear less elongated around duct buds in adulthood and at branch points where the epithelium is curved.

6.3.2 3D cell-based computational modelling

Previous mathematical modelling of the TEB was very useful in linking rates of cell proliferation, death and migration to duct growth (Paine et al., 2016). This approach enforced geometric constraints upon the model but did not address how these geometries are generated and maintained. Morphogenic processes can be modelled in 3D at the single cell level by incorporating cell–cell interactions, biophysical forces and signalling gradients. These models reveal how individual cell behaviours and external forces cooperate during tissue formation and function, such as in the *Caenorhabditis elegans* germline or intestinal crypt homeostasis (Atwell et al., 2015; Buske et al., 2011; Dunn et al., 2013). The lineage-specific behaviour of TEB cells, combined with previous modelling (Paine et al., 2016) and biophysical analyses (Neumann et al., 2018), could inform a 3D mechanical model of the TEB. This may provide insight into how distinct behaviours of the three major TEB populations lead to TEB progression and bilayer formation.

6.4 Mammary ductal macrophages

The intra-epithelial network of ductal MØs is a major component of mammary ducts and is likely to have a broad range of functions in health and disease. Their distribution, molecular features and behaviour were comprehensively described and a major function during involution was uncovered. These findings provide a foundational base for ongoing research into the role of MØs and the wider immune system in mammary gland development, function and disease.

During revision of this thesis, a paper was published describing MØ localisation throughout development by 3D imaging (Stewart et al., 2019). This study showed that MØs surround and infiltrate the epithelium in embryonic, pubertal, adult, lactating and involuting glands, including observation of intra-epithelial MØs. While this paper did not differentiate MØ populations, it provides valuable information that complements our work, particularly by mapping stromal MØs in greater detail, which will facilitate future dissection of their functions. An additional recent study also observed intra-epithelial cells using CD45 and MHCII, noting their intimate association with myoepithelial cells in lactation, but did not identify these cells as MØs (Hitchcock et al., 2019).

6.4.1 MØ function during involution

The regular positioning of DMs over alveoli in lactation poises them for their phagocytic role during involution. In addition to phagocytosis, MØs are critical for induction of alveolar cell death (O'Brien et al., 2012). A specific role for DMs in induction of alveolar cell death is possible but may be difficult to tease apart due the tight link between death and rapid phagocytosis. IVM may be useful in revealing phenotypes in DM-specific gene knock-out mice during this highly dynamic phase. To investigate this, RNA was collected from DMs at 3 days of involution to identify molecular features of DMs as alveolar cell death is initiated. These samples were of poor quality and could not be used, potentially because of high levels of lysosomal enzymes in DMs.

DMs phagocytose cells during the second phase of involution that is initiated by systemic factors (Lund et al., 1996). This large-scale cell death is complex and involves lysosomal leakage; factors involved in this process could be explored in the context of DMs, such as LIF and Tgfβ3 (Watson and Kreuzaler, 2011). Phagocytosis of alveolar cells by DMs might be stimulated by alveolar cell death or DMs may respond to systemic factors and contribute to induction of alveolar cell death. Studying how cell death mechanisms and remodelling are perturbed following DM depletion at different timepoints throughout involution could address these questions. The long-term consequences of DM depletion during involution were not determined and would be of interest for future investigation using mouse models that allow long-term DM depletion. Further research

into DM function during involution will be of great interest, considering the influence this phase has on MØ-associated tumour progression (Stanford et al., 2014).

6.4.2 The function of DMs in development

To explore a function for DMs in puberty, DCs and DMs were depleted using the *CD11c-DTR* mouse model. This only resulted in minor reduction in growth and branching that could not be specifically attributed to any of DC1/DC2 or DMs. Furthermore, specific depletion of DMs in *CD11c-Cre/Cx3cr1*$^{DTR/+}$ mice did not produce a phenotype. These data differ from the well-established and critical role for MØs in puberty (Gouon-Evans et al., 2000; Nguyen and Pollard, 2002) but it is plausible that stromal MØs play a more significant role in morphogenesis than DMs. Mice without MØs have abnormal collagen organisation around TEBs (Ingman et al., 2006), a phenotype presumably associated with stromal MØs. Specific depletion of stromal MØs in puberty to investigate their function (potentially using the *CD169-DTR* mouse model) may resolve this issue. Specific depletion of DMs and SMs in pregnancy would also be of interest to untangle potentially diverse roles for MØs in alveolar morphogenesis.

DM response to epithelial damage was only briefly explored through induction of precise laser damage during IVM. This may be a useful approach to further investigate the cells and mechanisms involved in repair of the mammary epithelium. It remains to be determined how long the epithelium takes to recover from these lesions and whether DMs are required for efficient repair. Use of additional fluorescence reporter mice such as E-Cadherin-GFP (Erami et al., 2015) might provide more insight into the epithelial dynamics during repair, and specific depletion of DMs in CD11c-Cre/Cx3cr1$^{DTR/+}$ mice prior to IVM and laser ablation could help to further define their role.

6.4.3 The role of DMs in disease

DMs may also play an important role in control of infection in mastitis. A similar MØ population in the liver capsule recruits neutrophils to prevent liver dissemination of bacterial infection in the peritoneum (Sierro et al., 2017). A similar function for DMs could be explored in a mammary

gland infection model combined with specific depletion of DMs, as well as IVM to observe cell dynamics.

MØs promote early metastasis of breast cancers (Linde et al., 2018) and DM-like TAMs aid tumour growth (Franklin et al., 2014), suggesting an important function for DMs in different stages of tumourigenesis. Preliminary experiments were performed by depleting DMs during the early hyperplastic stage in *MMTV-PyMT* mice, but no effect was seen. The degree of hyperplasia and timing of tumour onset in *MMTV-PyMT* mice is highly variable, so this may not be suitable for discerning a subtle influence of DMs.

DM monitoring of the entire epithelium could facilitate a role in detection and elimination of abnormal or transformed cells. This could be investigated by *in vivo* transformation of rare epithelial cells by intraductal injection of viruses carrying CRISPR guides against tumour suppressors into Cas9-expressing mice. Simultaneous DM depletion together with IVM and 3D imaging could reveal the response of DMs to transformation and determine their influence on cancer initiation.

The pervasion of DMs throughout the tumour epithelium could be exploited in cancer therapies. While TAMs generally promote tumorigenesis, they can work against cancer in some cases (Qian and Pollard, 2010). The abundance of tumour DMs could make manipulation of these to promote cytotoxic lymphocyte and DC activation an effective strategy (Figure 6.2). Additionally, DMs appear to be primed to phagocytose mammary epithelial cells during normal remodelling. Inhibition of 'don't eat me' signals that can activate tumour cell phagocytosis (Barkal et al., 2019) — a better understanding of the regulation of DM-mediated phagocytosis of mammary epithelial cells may enable more efficient induction of tumour phagocytosis by targeted therapies (Figure 6.2).

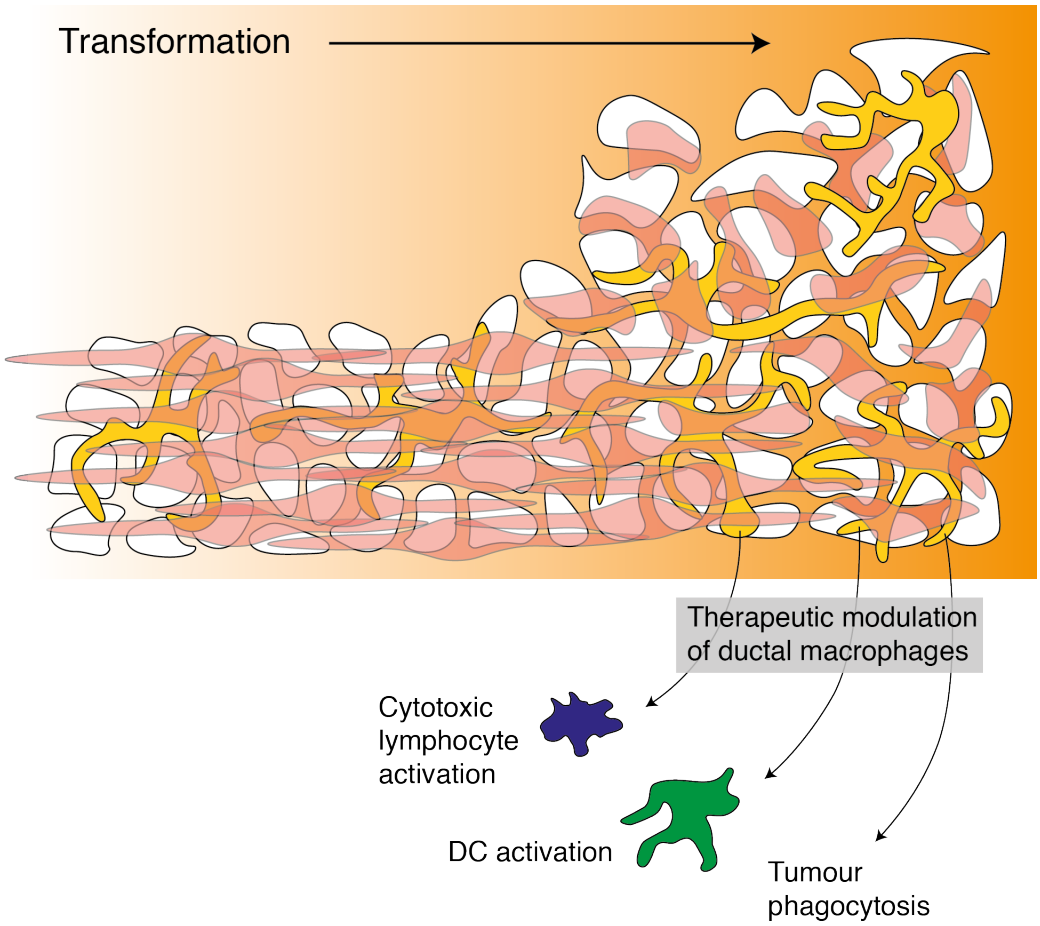

Figure 6.2: Targeting ductal macrophages during tumourigenesis

Ductal macrophages (yellow) are abundant within the epithelium throughout tumourigenesis and are promising therapeutic targets. DM modulation may increase activation of cytotoxic lymphocytes and DCs, which collaborate to control tumour growth. Embedding of DMs within the tumour epithelium suggests that induction of DM phagocytosis of tumour cells may be an effective treatment strategy.

6.5 Concluding remarks

In summary, the work presented in this thesis advances our knowledge of mammary gland formation and cell-cell interactions. Organogenesis is controlled and accomplished by the behaviour and organisation of individual cells. Recent technological advances have made it possible to image mammalian gastrulation and early organogenesis at the single cell level (le et al., 2018). However, the later stages of organ formation are currently inaccessible due to the size of the embryo, limitations in imaging depth and the difficulty of maintaining physiological embryogenesis *ex vivo*. Post-natal morphogenesis of the mammary gland provides a unique opportunity to observe *in vivo* organogenesis in full flight. Thus, the data presented here, while important for understanding the mammary gland, also have broader implications for mammalian organogenesis with achievement of *in vivo* single cell tracking during a key morphogenic phase. Future combination of TEB IVM with genetic and pharmacalogic manipulation informed by single cell transcriptomics is an exciting opportunity to deepen our understanding of mammalian organogenesis.

Identifying the diversity of cells that directly interact with the mammary epithelium, as well as the dynamics and outcomes of these interactions, is essential for a more complete knowledge of mammary gland biology. The intimate relationship between DMs and the mammary epithelium now represents a key interaction that should be considered. While a role for these was demonstrated during involution, the data may only scratch the surface of this fascinating cell type. In the context of the broader tissue-resident MØ field, the characterisation of a novel population adds to a growing list of unique MØs that are highly adapted for niche-specific functions. Of these, DMs are the only population to be identified in a non-essential organ. Thus, the mammary gland may emerge as a dominant model for the study of tissue–MØ crosstalk, due to its amenability for *ex vivo* genetic manipulation and transplantation. Further exploration of DM function is a promising avenue and this work provides a strong foundation for ongoing research in this direction.

Bibliography

Abdala-Valencia, H., Coden, M.E., Chiarella, S.E., Jacobsen, E.A., Bochner, B.S., Lee, J.J., and Berdnikovs, S. (2018). Shaping eosinophil identity in the tissue contexts of development, homeostasis, and disease. J Leukocyte Biol *104*, 95–108.

Ahmed, F., Wyckoff, J., Lin, E., Wang, W., and Wang, Y. (2002). GFP expression in the mammary gland for imaging of mammary tumor cells in transgenic mice. Cancer Res *62*, 7166–7169.

van Amerongen, R., Bowman, A., and Nusse, R. (2012). Developmental stage and time dictate the fate of Wnt/β-catenin-responsive stem cells in the mammary gland. Cell Stem Cell *11*, 387–400.

Andres, A.-C., and Strange, R. (1999). Apoptosis in the estrous and menstrual cycles. J Mammary Gland Biol *4*, 221–228.

Arendt, L.M., and Kuperwasser, C. (2015). Form and function: how estrogen and progesterone regulate the mammary epithelial hierarchy. J Mammary Gland Biol *20*, 9–25.

Asselin-Labat, M., Vaillant, F., Sheridan, Pal, B., and Wu, D. (2010). Control of mammary stem cell function by steroid hormone signalling. Nature *465,* 798-802.

Asselin-Labat, M.-L., Sutherland, K.D., Barker, H., Thomas, R., Shackleton, M., Forrest, N.C., Hartley, L., Robb, L., Grosveld, F.G., van der Wees, J., et al. (2006). Gata-3 is an essential regulator of mammary-gland morphogenesis and luminal-cell differentiation. Nat Cell Biol *9*, 201–209.

Asselin-Labat, M.-L., Sutherland, K.D., Vaillant, F., Gyorki, D.E., Wu, D., Holroyd, S., Breslin, K., Ward, T., Shi, W., Bath, M.L., et al. (2011). Gata-3 negatively regulates the tumor-initiating capacity of mammary luminal progenitor cells and targets the putative tumor suppressor Caspase-14. Mol Cell Biol *31*, 4609–4622.

Atwell, K., Qin, Z., Gavaghan, D., Kugler, H., Hubbard, J.E., and Osborne, J.M. (2015). Mechano-logical model of C. elegans germ line suggests feedback on the cell cycle. Development *142*, 3902–3911.

Bai, L., and Rohrschneider, L. (2010). s-SHIP promoter expression marks activated stem cells in developing mouse mammary tissue. Gene Dev *24*, 1882.

Bain, C.C., Bravo-Blas, A., Scott, C.L., Perdiguero, E., Geissmann, F., Henri, S., Malissen, B., Osborne, L.C., Artis, D., and Mowat, A. (2014). Constant replenishment from circulating monocytes maintains the macrophage pool in the intestine of adult mice. Nat Immunol *15*, 929–937.

Barbareschi, M., Pecciarini, L., Cangi, G.M., Macrì, E., Rizzo, A., Viale, G., and Doglioni, C. (2001). p63, a p53 homologue, is a selective nuclear marker of myoepithelial cells of the human breast. Am J Surg Pathology *25*, 1054–1060.

Barkal, A.A., Brewer, R.E., Markovic, M., Kowarsky, M., Barkal, S.A., Zaro, B.W., Krishnan, V., Hatakeyama, J., Dorigo, O., Barkal, L.J., et al. (2019). CD24 signalling through macrophage Siglec-10 is a target for cancer immunotherapy. Nature *572*, 392–396.

Bayarmagnai, B., Perrin, L., Pourfarhangi, K., and Gligorijevic, B. (2018). Intravital imaging of tumor cell motility in the tumor microenvironment context. Cell Migration. *1749*, 175–193.

Beleut, M., Rajaram, R., Caikovski, M., Ayyanan, A., Germano, D., Choi, Y., Schneider, P., and Brisken, C. (2010). Two distinct mechanisms underlie progesterone-induced proliferation in the mammary gland. Proc Natl Acad Sci *107*, 2989–2994.

Betts, C.B., Pennock, N.D., Caruso, B.P., Ruffell, B., Borges, V.F., and Schedin, P. (2018). Mucosal immunity in the female murine mammary gland. J Immunol *201*, 734–746.

Bingle, L., Brown, N., and Lewis, C. (2002). The role of tumour-associated macrophages in tumour progression: implications for new anticancer therapies. J Pathol *196* 254-265.

Blaas, L., Pucci, F., Messal, H.A., dersson, A., Ruiz, J.E., Gerling, M., Douagi, I., Spencer-Dene, B., Musch, A., Mitter, R., et al. (2016). Lgr6 labels a rare population of mammary gland progenitor cells that are able to originate luminal mammary tumours. Nat Cell Biol *18*, 1346–1356.

Bladström, A., Anderson, H., and Olsson, H. (2003). Worse survival in breast cancer among women with recent childbirth: Results from a swedish population-based register study. Clin Breast Cancer *4*, 280–285.

Bocchinfuso, W., and Korach, K. (1997). Mammary gland development and tumorigenesis in estrogen receptor knockout mice. J Mammary Gland Biol Neoplasia *2,* 323-334.

Brisken, C., Park, S., Vass, T., Lydon, J.P., O'Malley, B.W., and Weinberg, R.A. (1998). A paracrine role for the epithelial progesterone receptor in mammary gland development. Proc Natl Acad Sci *95*, 5076–5081.

Brisken, C., Kaur, S., Chavarria, T.E., Binart, N., Sutherland, R.L., Weinberg, R.A., Kelly, P.A., and Ormandy, C.J. (1999). Prolactin controls mammary gland development via direct and indirect mechanisms. Dev Biol *210*, 96–106.

Brisken, C., Heineman, A., Chavarria, T., Elenbaas, B., Tan, J., Dey, S.K., McMahon, J.A., McMahon, A.P., and Weinberg, R.A. (2000). Essential function of Wnt-4 in mammary gland development downstream of progesterone signaling. Gene Dev *14*, 650–654.

Brown, C.E., Alizadeh, D., Starr, R., Weng, L., Wagner, J.R., Naranjo, A., Ostberg, J.R., Blanchard, S.M., Kilpatrick, J., Simpson, J., et al. (2016). Regression of glioblastoma after chimeric antigen receptor T-cell therapy. N Engl J Med *375*, 2561–2569.

Broz, M.L., Binnewies, M., Boldajipour, B., Nelson, A.E., Pollack, J.L., Erle, D.J., Barczak, A., Rosenblum, M.D., Daud, A., Barber, D.L., et al. (2014). Dissecting the tumor myeloid compartment reveals rare activating antigen-presenting cells critical for T cell immunity. Cancer Cell *26*, 638–652.

Burnett, S.H., Kershen, E.J., Zhang, J., Zeng, L., Straley, S.C., Kaplan, A.M., and Cohen, D.A. (2004). Conditional macrophage ablation in transgenic mice expressing a Fas-based suicide gene. J Leukocyte Biol *75*, 612–623.

Buske, P., Galle, J., Barker, N., Aust, G., Clevers, H., and Loeffler, M. (2011). A comprehensive model of the spatio-temporal stem cell and tissue organisation in the intestinal crypt. Plos Comput Biol *7*, e1001045.

Calabro, S., Liu, D., Gallman, A., Nascimento, M., Yu, Z., Zhang, T., Chen, P., Zhang, B., Xu, L., Gowthaman, U., et al. (2016). Differential intrasplenic migration of dendritic cell subsets tailors adaptive immunity. Cell Reports *16*, 2472–2485.

Carroll, D.K., Carroll, J.S., Leong, C.-O., Cheng, F., Brown, M., Mills, A.A., Brugge, J.S., and Ellisen, L.W. (2006). p63 regulates an adhesion programme and cell survival in epithelial cells. Nat Cell Biol *8*, 551–561.

Chaffer, C., and Weinberg, R. (2011). A perspective on cancer cell metastasis. Science *331,* 1559-1564.

Chakarov, S., Lim, H., Tan, L., Lim, S., See, P., Lum, J., Zhang, X.-M., Foo, S., Nakamizo, S., Duan, K., et al. (2019). Two distinct interstitial macrophage populations coexist across tissues in specific subtissular niches. Science *363*, eaau0964.

Chakrabarti, R., Celià-Terrassa, T., Kumar, S., Hang, X., Wei, Y., Choudhury, A., Hwang, J., Peng, J., Nixon, B., Grady, J.J., et al. (2018). Notch ligand Dll1 mediates cross-talk between mammary stem cells and the macrophageal niche. Science eaan4153.

Chen, L., and Flies, D.B. (2013). Molecular mechanisms of T cell co-stimulation and co-inhibition. Nat Rev Immunol *13*, 227–242.

Chen, Y., Lun, A.T., and Smyth, G.K. (2014). Differential expression analysis of complex RNA-seq experiments using edgeR. In Statistical analysis of next generation sequencing data, Datta, S., and Nettleton, D., eds. (Springer, Cham), pp. 51–74.

Chiossone, L., Dumas, P.-Y., Vienne, M., and Vivier, E. (2018). Natural killer cells and other innate lymphoid cells in cancer. Nat Rev Immunol *18*, 671–688.

Chistiakov, D.A., Bobryshev, Y.V., Kozarov, E., Sobenin, I.A., and Orekhov, A.N. (2015). Intestinal mucosal tolerance and impact of gut microbiota to mucosal tolerance. Front Microbiol *5*, 781.

Choi, Y., Chakrabarti, R., Escamilla-Hernandez, R., and Sinha, S. (2009). Elf5 conditional knockout mice reveal its role as a master regulator in mammary alveolar development: Failure of Stat5 activation and functional differentiation in the absence of Elf5. Dev Biol *329*, 227–241.

Chua, A., Hodson, L., Moldenhauer, L., Robertson, S., and Ingman, W. (2010). Dual roles for macrophages in ovarian cycle-associated development and remodelling of the mammary gland epithelium. Development *137*, 4229–4238.

Chung, K., Wallace, J., Kim, S.-Y., Kalyanasundaram, S., Andalman, A.S., Davidson, T.J., Mirzabekov, J.J., Zalocusky, K.A., Mattis, J., Denisin, A.K., et al. (2013). Structural and molecular interrogation of intact biological systems. Nature *497*, 332–337.

Ciarloni, L., Mallepell, S., and Brisken, C. (2007). Amphiregulin is an essential mediator of estrogen receptor α function in mammary gland development. Proc Natl Acad Sci *104*, 5455–5460.

Colbert, D.C., McGarry, M.P., O'neill, K., Lee, N.A., and Lee, J.J. (2005). Decreased size and survival of weanling mice in litters of IL-5-/ -mice are a consequence of the IL-5 deficiency in nursing dams. Contemp Top Lab Anim Sci *44*, 53–55.

Condeelis, J., and Segall, J. (2003). Intravital imaging of cell movement in tumours. Nat Rev Cancer *3*, 921-930.

Cruz-Muñoz, M., Valenzuela-Vázquez, L., Sánchez-Herrera, J., and Tapia, J. (2019). From the "missing self" hypothesis to adaptive NK cells: Insights of NK cell-mediated effector functions in immune surveillance. J Leukocyte Biol *105*, 955–971.

Daniel, C., Ome, D.K., Young, J., Blair, P., and Faulkin, L. (1968). The in vivo life span of normal and preneoplastic mouse mammary glands: a serial transplantation study. Proc of the Natl Acad Sci *61*, 53–60.

Danielian, P.S., Muccino, D., Rowitch, D.H., Michael, S.K., and McMahon, A.P. (1998).

Modification of gene activity in mouse embryos in utero by a tamoxifen-inducible form of Cre recombinase. Curr Biol *8*, 1323-S2.

Davis, F.M., Lloyd-Lewis, B., Harris, O.B., Kozar, S., Winton, D.J., Muresan, L., and Watson, C.J. (2016). Single-cell lineage tracing in the mammary gland reveals stochastic clonal dispersion of stem/progenitor cell progeny. Nat Commun *7*, 13053.

DeNardo, D.G., and Ruffell, B. (2019). Macrophages as regulators of tumour immunity and immunotherapy. Nat Rev Immunol *19,* 369-382.

DeOme, K., Faulkin, L., Bern, H., and Blair, P. (1959). Development of mammary tumors from hyperplastic alveolar nodules transplanted into gland-free mammary fat pads of female C3H mice. Cancer Res *19*, 515–520.

DeSantis, C.E., Ma, J., Sauer, A., Newman, L.A., and Jemal, A. (2017). Breast cancer statistics, 2017, racial disparity in mortality by state. Ca Cancer J Clin *67*, 439–448.

Diaspro, A., Chirico, G., and Collini, M. (2005). Two-photon fluorescence excitation and related techniques in biological microscopy. Q Rev Biophys *38*, 97–166.

Dulbecco, R., Henahan, M., and mstrong (1982). Cell types and morphogenesis in the mammary gland. Proc Natl Acad Sci *79*, 7346–7350.

Dunn, S.-J., Näthke, I.S., and Osborne, J.M. (2013). Computational models reveal a passive mechanism for cell migration in the crypt. Plos One *8*, e80516.

Eisenbarth, S. (2018). Dendritic cell subsets in T cell programming: location dictates function. Nat Rev Immunol *19*, 1.

Ellenbroek, S., and van Rheenen, J. (2014). Imaging hallmarks of cancer in living mice. Nat Rev Cancer *14,* 406-418.

Epelman, S., Lavine, K., Beaudin, A., Sojka, D., Carrero, J., Calderon, B., Brija, T., Gautier, E., Ivanov, S., Satpathy, A., et al. (2014). Embryonic and adult-derived resident cardiac macrophages are maintained through distinct mechanisms at steady state and during inflammation. Immunity *40*, 91–104.

Erami, Z., Herrmann, D., Warren, S.C., Nobis, M., McGhee, E.J., Lucas, M.C., Leung, W., Reischmann, N., Mrowinska, A., Schwarz, J.P., et al. (2015). Intravital FRAP imaging using an E-cadherin-GFP mouse reveals disease- and drug-dependent dynamic regulation of cell-cell junctions in live tissue. Cell Rep *14*, 152–167.

Ewald, A.J., Brenot, A., Duong, M., Chan, B.S., and Werb, Z. (2008). Collective epithelial migration and cell rearrangements drive mammary branching morphogenesis. Dev Cell *14*, 570.

Ewald, A.J., Werb, Z., and Egeblad, M. (2011a). Preparation of mice for long-term intravital imaging of the mammary gland. Cold Spring Harbor Protoc. *2011*, 168–173.

Ewald, A.J., Werb, Z., and Egeblad, M. (2011b). Monitoring of vital signs for long-term survival of mice under anesthesia. Cold Spring Harbor Protoc. *2011*, 174–177.

Ewald, A.J., Huebner, R.J., Palsdottir, H., Lee, J.K., Perez, M.J., Jorgens, D.M., Tauscher, A.N., Cheung, K.J., Werb, Z., and Auer, M. (2012). Mammary collective cell migration involves transient loss of epithelial features and individual cell migration within the epithelium. J Cell Sci *125*, 2638.

Fan, A., Cassidy, J., Carthew, R.W., and Hilgenfeldt, S. (2015). Two-dimensional mapping of 3D data from confocal microscopy. Biorxiv 019133.

Fata, J.E., Kong, Y.-Y., Li, J., Sasaki, T., Irie-Sasaki, J., Moorehead, R.A., Elliott, R., Scully, S., Voura, E.B., Lacey, D.L., et al. (2000). The osteoclast differentiation factor osteoprotegerin-ligand is essential for mammary gland development. Cell *103*, 41–50.

Fata, J.E., Chaudhary, V., and Khokha, R. (2001). Cellular turnover in the mammary gland is correlated with systemic levels of progesterone and not 17-estradiol during the estrous cycle. Biol Reprod *65*, 680–688.

Feng, J., Wang, H., in, D.-M., Masiuk, M., Qi, C.-F.F., and Morse, H.C. (2011). IFN regulatory factor 8 restricts the size of the marginal zone and follicular B cell pools. J Immunol *186*, 1458–1466.

Fernandez-Gonzalez, R., Illa-Bochaca, I., Welm, B.E., Fleisch, M.C., Werb, Z., Ortiz-de-Solorzano, C., and Barcellos-Hoff, M. (2008). Mapping mammary gland architecture using multi-scale in situ analysis. Integr Biol *1*, 80.

Fornetti, J., Flanders, K., Henson, P., and Tan, A. (2016). Mammary epithelial cell phagocytosis downstream of TGF-β3 is characterized by adherens junction reorganization. Cell Death Differ *23,* 185-196.

Franklin, R.A., Liao, W., Sarkar, A., Kim, M.V., Bivona, M.R., Liu, K., Pamer, E.G., and Li, M.O. (2014). The cellular and molecular origin of tumor-associated macrophages. Science *344*, 921–925.

Fu, N., Rios, A.C., Pal, B., Soetanto, R., Lun, A.T., Liu, K., Beck, T., Best, S.A., Vaillant, F., Bouillet, P., et al. (2015). EGF-mediated induction of Mcl-1 at the switch to lactation is essential for alveolar cell survival. Nat Cell Biol 365–375.

Fu, N., Rios, A.C., Pal, B., Law, C.W., Jamieson, P., Liu, R., Vaillant, F., Jackling, F., Liu, K., Smyth, G.K., et al. (2017). Identification of quiescent and spatially restricted mammary stem cells that are hormone responsive. Nat Cell Biol *19*, 164–176.

van Furth, R., and Cohn, Z.A. (1968). The origin and kinetics of mononuclear phagocytes. J Exp Med *128*, 415–435.

Gajewski, T.F., Schreiber, H., and Fu, Y.-X. (2013). Innate and adaptive immune cells in the tumor microenvironment. Nat Immunol *14*, 1014–1022.

Gautier, E.L., Shay, T., Miller, J., Greter, M., Jakubzick, C., Ivanov, S., Helft, j., Chow, A., Elpek, K.G., Gordonov, S., et al. (2012). Gene-expression profiles and transcriptional regulatory pathways that underlie the identity and diversity of mouse tissue macrophages. Nature *13*, 1118–1128.

Germain, Robey, E., and Cahalan (2012). A decade of imaging cellular motility and interaction dynamics in the immune system. Science *336,* 1676-1681.

Gibbings, S., Thomas, S., Atif, S., McCubbrey, A., Desch, A., Danhorn, T., Leach, S., Bratton, D., Henson, P., Janssen, W., et al. (2017). Three unique interstitial macrophages in the murine lung at steady state. Am J Respir Cell Mol Biol *57*, 66-76.

Gilbert, N., Lucas, L., Klein, C., Menager, M., Bonnet, N., and Ploton, D. (1995). Three-dimensional co-location of RNA polymerase I and DNA during interphase and mitosis by confocal microscopy. J Cell Sci *108 (Pt 1)*, 115–125.

Ginhoux, F., and Guilliams, M. (2016). Tissue-resident macrophage ontogeny and homeostasis. Immunity *44*, 439-449.

Ginhoux, F., Liu, K., Helft, J., Bogunovic, M., Greter, M., Hashimoto, D., Price, J., Yin, N., Bromberg, J., Lira, S.A., et al. (2009). The origin and development of nonlymphoid tissue CD103+ DCs. J Exp Med *206*, 3115–3130.

Ginhoux, F., Greter, M., Leboeuf, M., Nandi, S., and See, P. (2010). Fate mapping analysis reveals that adult microglia derive from primitive macrophages. Science *330*, 841-845.

Giraddi, R.R., Shehata, M., Gallardo, M., Blasco, M.A., Simons, B.D., and Stingl, J. (2015). Stem and progenitor cell division kinetics during postnatal mouse mammary gland development. Nat Commun *6*, 8487.

Gordon, S. (2016). Phagocytosis: An immunobiologic process. Immunity *44*, 463–475.

Gordon, S., and Plüddemann, A. (2017). Tissue macrophages: heterogeneity and functions. BMC Biol. *15*, 53.

Gouon-Evans, V., Rothenberg, M.E., and Pollard, J.W. (2000). Postnatal mammary gland development requires macrophages and eosinophils. Development *127*, 2269–2282.

Green, K.A., and Lund, L.R. (2005). ECM degrading proteases and tissue remodelling in the mammary gland. Bioessays *27*, 894–903.

Grimbaldeston, M.A., Chen, C.-C., Piliponsky, A.M., Tsai, M., Tam, S.-Y., and Galli, S.J. (2005). Mast cell-deficient W-sash c-kit mutant Kit W-sh/W-sh mice as a model for investigating mast cell biology in vivo. Am J Pathol *167*, 835–848.

Guerriero, J.L., Sotayo, A., Ponichtera, H.E., Castrillon, J.A., Pourzia, A.L., Schad, S., Johnson, S.F., Carrasco, R.D., Lazo, S., Bronson, R.T., et al. (2017). Class IIa HDAC inhibition reduces breast tumours and metastases through anti-tumour macrophages. Nature *543*, 428–432.

Gugliotta, P., Sapino, A., Macrí, L., Skalli, O., Gabbiani, G., and Bussolati, G. (1988). Specific demonstration of myoepithelial cells by anti-alpha smooth muscle actin antibody. J Histochem Cytochem *36*, 659–663.

Guilliams, M., and Scott, C.L. (2017). Does niche competition determine the origin of tissue-resident macrophages? Nat Rev Immunol *17*, 451–460.

Guilliams, M., Dutertre, C.-A., Scott, C.L., McGovern, N., Sichien, D., Chakarov, S., Van Gassen, S., Chen, J., Poidinger, M., De Prijck, S., et al. (2016). Unsupervised high-dimensional analysis aligns dendritic cells across tissues and species. Immunity *45*, 669–684.

Guilliams, M., Mildner, A., and Yona, S. (2018). Developmental and functional heterogeneity of monocytes. Immunity *49*, 595–613.

Gyorki, D.E., Asselin-Labat, M.-L., van Rooijen, N., Lindeman, G.J., and Visvader, J.E. (2009). Resident macrophages influence stem cell activity in the mammary gland. Breast Cancer Res. *11*, R62.

Hanahan, D., and Weinberg, R. (2011). Hallmarks of cancer: the next generation. Cell *144*, 646-674.

Hannezo, E., Scheele, C., Moad, M., Drogo, N., Heer, R., Sampogna, R.V., van Rheenen, J., and Simons, B.D. (2017). A unifying theory of branching morphogenesis. Cell *171*, 242-255.e27.

Hennighausen, L. (2000). Mouse models for breast cancer. Breast Cancer Res *2*, 2.

Heuser, J.E. (2000). Membrane traffic in anaglyph stereo. Traffic *1*, 35–37.

Hirsch, M., and Kramer, T. (1999). Neuroanatomy, 3D-stereoscopic atlas of the human brain. (Springer, Berlin Heidelberg).

Hitchcock, J.R., Hughes, K., Harris, O.B., and Watson, C.J. (2019). Dynamic architectural interplay between leucocytes and mammary epithelial cells. FEBS J *287*, 250–266.

Hodson, L.J., Chua, A., Evdokiou, A., Robertson, S.A., and Ingman, W.V. (2013). Macrophage phenotype in the mammary gland fluctuates over the course of the estrous cycle and is regulated by ovarian steroid hormones. Biol Reprod *89*, Article 65, 1-8.

Hoeffel, G., and Ginhoux, F. (2015). Ontogeny of tissue-resident macrophages. Front Immunol *6*, 486.

Hoeffel, G., Chen, J., Lavin, Y., Low, D., Almeida, F., See, P., Beaudin, A., Lum, J., Low, I., Forsberg, E., et al. (2015). C-Myb+ erythro-myeloid progenitor-derived fetal monocytes give rise to adult tissue-resident macrophages. Immunity *42*, 665-678.

Hor, J.L., Whitney, P.G., Zaid, A., Brooks, A.G., Heath, W.R., and Mueller, S.N. (2015). Spatiotemporally distinct interactions with dendritic cell subsets facilitates CD4+ and CD8+ T cell activation to localized viral infection. Immunity *43*, 554–565.

Hoshino, K., and Gardner, W.U. (1967). Transplantability and life span of mammary gland during serial transplantation in mice. Nature *213*, 193–194.

Howard, B.A., and Gusterson, B.A. (2000). Human breast development. J Mammary Gland Biol *5*, 119–137.

Huebner, R.J., Neumann, N.M., and Ewald, A.J. (2016). Mammary epithelial tubes elongate through MAPK-dependent coordination of cell migration. Development *143*, 983–993.

Hughes, K., Wickenden, J.A., Allen, J.E., and Watson, C.J. (2012). Conditional deletion of Stat3 in mammary epithelium impairs the acute phase response and modulates immune cell numbers during post-lactational regression. J Pathol *227*, 106–117.

Hulsmans, M., Clauss, S., Xiao, L., Aguirre, A.D., King, K.R., Hanley, A., Hucker, W.J., Wülfers, E.M., Seemann, G., Courties, G., et al. (2017). Macrophages facilitate electrical conduction in the heart. Cell *169*, 510-522.e20.

Ingman, W.V., Wyckoff, J., Gouon-Evans, V., Condeelis, J., and Pollard, J.W. (2006). Macrophages promote collagen fibrillogenesis around terminal end buds of the developing mammary gland. Dev Dynam *235*, 3222–3229.

Jaitin, D., Adlung, L., Thaiss, C.A., Weiner, A., Li, B., Descamps, H., Lundgren, P., Bleriot, C., Liu, Z., Deczkowska, A., et al. (2019). Lipid-associated macrophages control metabolic homeostasis in a Trem2-dependent manner. Cell *178*, 686-698.e14.

Jenkins, S.J., Ruckerl, D., Thomas, G.D., Hewitson, J.P., Duncan, S., Brombacher, F., Maizels, R.M., Hume, D.A., and Allen, J.E. (2013). IL-4 directly signals tissue-resident macrophages to proliferate beyond homeostatic levels controlled by CSF-1. J Exp Med *210*, 2477–2491.

Jensen, R.G., and Newburg, D.S. (1995). Handbook of milk composition. 543–575.

Jiang, J., Tang, Y., and Liang, X. (2011). EMT: A new vision of hypoxia promoting cancer progression. Cancer Biol Ther *11*, 714–723.

Johnston, A., Rae, J., Ariotti, N., Bailey, B., Lilja, A., Webb, R., Ferguson, C., Maher, S., Davis, T.P., Webb, R.I., et al. (2018). Journey to the centre of the cell: Virtual reality immersion into scientific data. Traffic *19*, 105–110.

Kahlon, K.S., Brown, C., Cooper, L.J., Raubitschek, A., Forman, S.J., and Jensen, M.C. (2004). Specific recognition and killing of glioblastoma multiforme by interleukin 13-zetakine redirected cytolytic T cells. Cancer Res *64*, 9160–9166.

Ke, M.-T., Fujimoto, S., and Imai, T. (2013). SeeDB: a simple and morphology-preserving optical clearing agent for neuronal circuit reconstruction. Nat Neurosci *16*, 1154–1161.

Kedrin, D., Gligorijevic, B., Wyckoff, J., Verkhusha, V.V., Condeelis, J., Segall, J.E., and Rheenen, J. (2008). Intravital imaging of metastatic behavior through a mammary imaging window. Nat Methods *5*, 1019–1021.

Keller, R. (2002). Shaping the vertebrate body plan by polarized embryonic cell movements. Science *298*, 1950–1954.

Keymeulen, A., Rocha, A., Ousset, M., Beck, B., Bouvencourt, G., Rock, J., Sharma, N., Dekoninck, S., and Blanpain, C. (2011). Distinct stem cells contribute to mammary gland development and maintenance. Nature *479*, 189.

Keymeulen, A., Fioramonti, M., Centonze, A., Bouvencourt, G., Achouri, Y., and Blanpain, C. (2017). Lineage-restricted mammary stem cells sustain the development, homeostasis, and regeneration of the estrogen receptor positive lineage. Cell Rep *20*, 1525–1532.

Khialeeva, E., Lane, T.F., and Carpenter, E.M. (2011). Disruption of reelin signaling alters mammary gland morphogenesis. Development *138*, 767–776.

Kim, H., Pang, M.-F., Varner, V.D., Kojima, L., Miller, E., Radisky, D.C., and Nelson, C.M. (2015). Localized smooth muscle differentiation is essential for epithelial bifurcation during branching morphogenesis of the mammalian lung. Dev Cell *34*, 719–726.

Koboldt, D.C., Fulton, R.S., McLellan, M.D., Schmidt, H., Kalicki-Veizer, J., McMichael, J.F., Fulton, L.L., Dooling, D.J., Ding, L., Mardis, E.R., et al. (2012). Comprehensive molecular portraits of human breast tumours. Nature *490*, 61–70.

Kondo, H., Saito, K., Grasso, J.P., and Aisen, P. (1988). Iron metabolism in the erythrophagocytosing Kupffer cell. Hepatology *8*, 32–38.

Kordon, E., and Smith, G. (1998). An entire functional mammary gland may comprise the progeny from a single cell. Development *125*, 1921–1930.

Kotsuma, M., Parashurama, N., Smith, B.R., Wo, J., Ito, K., and Gambhir, S.S. (2012). Nondestructive, serial in vivo imaging of a tissue-flap using a tissue adhesion barrier. IntraVital *1*, 69–76.

Kouros-Mehr, H., orach, E., Sternlicht, M.D., and Werb, Z. (2006). GATA-3 Maintains the differentiation of the luminal cell fate in the mammary gland. Cell *127*, 1041–1055.

Krasnova, Y., Putz, E., Smyth, M.J., and Souza-Fonseca-Guimaraes, F. (2017). Bench to bedside: NK cells and control of metastasis. Clin Immunol *177*, 50–59.

Kreuzaler, P.A., Staniszewska, A.D., Li, W., Omidvar, N., Kedjouar, B., Turkson, J., Poli, V., Flavell, R.A., Clarkson, R.W., and Watson, C.J. (2011). Stat3 controls lysosomal-mediated cell death in vivo. Nat Cell Biol *13*, 303.

Kritikou, E.A., Sharkey, A., Abell, K., Came, P.J., Anderson, E., Clarkson, R.W., and Watson, C.J. (2003). A dual, non-redundant, role for LIF as a regulator of development and STAT3-mediated cell death in mammary gland. Development *130*, 3459–3468.

Lafkas, D., Rodilla, V., Huyghe, M., and Mourao, L. (2013). Notch3 marks clonogenic mammary luminal progenitor cells in vivo. J Cell Biol *203*, 47–56.

Lavin, Y., and Merad, M. (2013). Macrophages: gatekeepers of tissue integrity. Cancer Immunol Res *1*, 201–209.

Lavin, Y., Winter, D., Blecher-Gonen, R., David, E., Keren-Shaul, H., Merad, M., Jung, S., and Amit, I. (2014). Tissue-resident macrophage enhancer landscapes are shaped by the local microenvironment. Cell *159*, 1312–1326.

Leung, G., Cool, T., Valencia, C., Worthington, A., Beaudin, A., and Forsberg, C. (2019). The lymphoid-associated interleukin 7 receptor (IL-7R) regulates tissue resident macrophage development. BioRxiv 534859.

Li, W., Germain, R.N., and Gerner, M.Y. (2017). Multiplex, quantitative cellular analysis in large tissue volumes with clearing-enhanced 3D microscopy (Ce3D). Proc Natl Acad Sci *114*, E7321–E7330.

Li, Y., Pang, Z., Dong, X., Liao, X., Deng, H., Liao, C., Liao, Y., Chen, G., and Huang, L. (2018). MUC1 induces M2 type macrophage influx during postpartum mammary gland involution and triggers breast cancer. Oncotarget *9*, 3446–3458.

Liao, Y., Smyth, G.K., and Shi, W. (2013). The Subread aligner: fast, accurate and scalable read mapping by seed-and-vote. Nucleic Acids Res. *41*, e108.

Liao, Y., Smyth, G.K., and Shi, W. (2014). featureCounts: an efficient general purpose program for assigning sequence reads to genomic features. Bioinformatics *30*, 923–930.

Liberzon, A., Subramanian, A., Pinchback, R., Thorvaldsdóttir, H., Tamayo, P., and Mesirov, J.P. (2011). Molecular signatures database (MSigDB) 3.0. Bioinformatics *27*, 1739–1740.

Lilja, A.M., Rodilla, V., Huyghe, M., Hannezo, E., Landragin, C., Renaud, O., Leroy, O., Rulands, S., Simons, B.D., and Fre, S. (2018). Clonal analysis of Notch1-expressing cells reveals the existence of unipotent stem cells that retain long-term plasticity in the embryonic mammary gland. Nat Cell Biol *20*, 677–687.

Lilla, J., and Werb, Z. (2010). Mast cells contribute to the stromal microenvironment in mammary gland branching morphogenesis. Dev Biol *337*, 124–133.

Lim, H.Y., Lim, S.Y., Tan, C.K., Thiam, C.H., Goh, C.C., Carbajo, D., Chew, S.H.S., See, P., Chakarov, S., Wang., X.N., et al., (2018). Hyaluronan receptor LYVE-1-wxpressing macrophages maintain arterial tone through hyaluronan-mediated regulation of smooth muscle cell collagen. Immunity *49* 326-341.

Lin, E., Nguyen, A., and Russell, R. (2001). Colony-stimulating factor 1 promotes progression of mammary tumors to malignancy. J Exp Med *193,* 727-740.

Linde, N., Casanova-Acebes, M., Sosa, M.S., Mortha, A., Rahman, A., Farias, E., Harper, K., Tardio, E., Torres, I.R., Jones, J., et al. (2018). Macrophages orchestrate breast cancer early dissemination and metastasis. Nat. Commun. *9*, 21.

Liu, Z., Gu, Y., Chakarov, S., Bleriot, C., Kwok, I., Chen, X., Shin, A., Huang, W., Dress, R.J., Dutertre, C.-A., et al. (2019). Fate mapping via Ms4a3-expression history traces monocyte-derived cells. Cell *178*, 1509-1525.e19.

Lloyd-Lewis, B., vis, F., Harris, O.B., Hitchcock, J.R., Lourenco, F.C., Pasche, M., and Watson, C.J. (2016). Imaging the mammary gland and mammary tumours in 3D: optical tissue clearing and immunofluorescence methods. Breast Cancer Res *18*, 127.

Lloyd-Lewis, B., vis, F., Harris, O.B., Hitchcock, J.R., and Watson, C.J. (2018). Neutral lineage tracing of proliferative embryonic and adult mammary stem/progenitor cells. Development *145*, dev164079.

Loladze, A.V., Stull, M.A., Rowzee, A.M., DeMarco, J., Lantry, J.H., Rosen, C.J., LeRoith, D., Wagner, K.-U., Hennighausen, L., and Wood, T.L. (2006). Epithelial-specific and stage-specific functions of insulin-like growth factor-i during postnatal mammary development. Endocrinology *147*, 5412–5423.

Lu, P., Zhou, T., Xu, C., and Lu, Y. (2019). Mammary stem cells, where art thou? Wiley Interdiscip Rev Dev Biol e357.

Lucas, L., Gilbert, N., Ploton, D., and Bonnet, N. (1996). Visualization of volume data in confocal microscopy: comparison and improvements of volume rendering methods. J Microsc-Oxford *181*, 238–252.

Lund, L., Rømer, J., Thomasset, N., Solberg, H., Pyke, C., Bissell, M., Danø, K., and Werb, Z. (1996). Two distinct phases of apoptosis in mammary gland involution: proteinase-independent and -dependent pathways. Development *122*, 181–193.

Lydon, J., DeMayo, F., Funk, C., Mani, S., Hughes, A., Montgomery, C., Shyamala, G., Conneely, O., and O'Malley, B. (1995). Mice lacking progesterone receptor exhibit pleiotropic reproductive abnormalities. Genes Dev *9*, 2266–2278.

Lyons, T.R., O'Brien, J., Borges, V.F., Conklin, M.W., Keely, P.J., Eliceiri, K.W., Marusyk, A., Tan, A.-C.C., and Schedin, P. (2011). Postpartum mammary gland involution drives progression of ductal carcinoma in situ through collagen and COX-2. Nat Med *17*, 1109–1115.

Macias, H., and Hinck, L. (2012). Mammary gland development. Wiley Interdiscip Rev Dev Biol *1*, 533.

Mailleux, A.A., Overholtzer, M., Schmelzle, T., Bouillet, P., Strasser, A., and Brugge, J.S. (2007). BIM regulates apoptosis during mammary ductal morphogenesis, and its absence reveals alternative cell death mechanisms. Dev Cell *12*, 221–234.

Mallepell, S., Krust, A., Chambon, P., and Brisken, C. (2006). Paracrine signaling through the epithelial estrogen receptor α is required for proliferation and morphogenesis in the mammary gland. P Natl Acad Sci Usa *103*, 2196–2201.

Martinson, H., Jindal, S., Durand-Rougely, C., Borges, V., and Schedin, P. (2015). Wound healing-like immune program facilitates postpartum mammary gland involution and tumor progression. Int J Cancer *136*, 1803-1813.

Masedunskas, A., Chen, Y., and Stussman, R. (2017). Kinetics of milk lipid droplet transport, growth, and secretion revealed by intravital imaging: lipid droplet release is intermittently stimulated by oxytocin. Mol Biol Cell *28,* 935-946.

McCarthy, D.J., Chen, Y., and Smyth, G.K. (2012). Differential expression analysis of multifactor RNA-Seq experiments with respect to biological variation. Nucleic Acids Res *40*, 4288–4297.

McDaniel, S.M., Rumer, K.K., Biroc, S.L., Metz, R.P., Singh, M., Porter, W., and Schedin, P. (2006). Remodeling of the mammary microenvironment after lactation promotes breast tumor cell metastasis. Am J Pathol *168*, 608–620.

McDole, K., Guignard, L., Amat, F., Berger, A., Malandain, G., Royer, L.A., Turaga, S.C., Branson, K., and Keller, P.J. (2018). In toto imaging and reconstruction of post-implantation

mouse development at the single-cell level. Cell *175*, 859-876.e33.

Medzhitov, R., and Janeway, C. (2000). Innate immune recognition: mechanisms and pathways. Immunol Rev *173*, 89–97.

Merad, M., Sathe, P., Helft, J., Miller, J., and Mortha, A. (2013). The dendritic cell lineage: Ontogeny and function of dendritic cells and their subsets in the steady state and the inflamed setting. Annu Rev Immunol *31*, 563–604.

Miller, A.B., and Bulbrook, R.D. (1980). The epidemiology and etiology of breast cancer. N Engl J Med *303*, 1246–1248.

Miller, J.C., Brown, B.D., Shay, T., Gautier, E.L., Jojic, V., Cohain, A., Pandey, G., Leboeuf, M., Elpek, K.G., Helft, J., et al. (2012). Deciphering the transcriptional network of the dendritic cell lineage. Nat Immunol *13*, 888–899.

Miller, M.J., Wei, S.H., Cahalan, M.D., and Parker, I. (2003). Autonomous T cell trafficking examined in vivo with intravital two-photon microscopy. Proc Natl Acad Sci *100*, 2604–2609.

Mills, A.A., Zheng, B., Wang, X.-J., Vogel, H., Roop, D.R., and Bradley, A. (1999). p63 is a p53 homologue required for limb and epidermal morphogenesis. Nature *398*, 19531.

Minsky, M. (1988). Memoir on inventing the confocal scanning microscope. Scanning *10*, 128–138.

Miyake, K., and Kaisho, T. (2014). Homeostatic inflammation in innate immunity. Curr Opin Immunol *30*, 85–90.

Monks, J., Rosner, D., Geske, F., Lehman, L., Hanson, L., Neville, M., and Fadok, V. (2005). Epithelial cells as phagocytes: apoptotic epithelial cells are engulfed by mammary alveolar epithelial cells and repress inflammatory mediator release. Cell Death and Differ *12*, 107–114.

Mukherjee, A., yal, S., Li, J., Ying, Y., He, B., DeMayo, F.J., and Lydon, J.P. (2010). Targeting RANKL to a specific subset of murine mammary epithelial cells induces ordered branching morphogenesis and alveologenesis in the absence of progesterone receptor expression. Faseb J *24*, 4408–4419.

Mulac-Jericevic, B., Lydon, J.P., DeMayo, F.J., and Conneely, O.M. (2003). Defective mammary gland morphogenesis in mice lacking the progesterone receptor B isoform. Proc Natl Acad Sci *100*, 9744–9749.

Neumann, N.M., Perrone, M.C., Veldhuis, J.H., Huebner, R.J., Zhan, H., Devreotes, P.N., Brodland, W.G., and Ewald, A.J. (2018). Coordination of receptor tyrosine kinase signaling and interfacial tension dynamics drives radial intercalation and tube elongation. Dev Cell *45*, 67-82.e6.

Nguyen, A., and Pollard, J. (2000). Transforming growth factor beta3 induces cell death during the first stage of mammary gland involution. Development *127*, 3107–3118.

Nguyen, A., and Pollard, J.W. (2002). Colony stimulating factor-1 is required to recruit macrophages into the mammary gland to facilitate mammary ductal outgrowth. Dev Biol *247*, 11–25.

Oakes, S.R., Naylor, M.J., Asselin-Labat, M.-L., Blazek, K.D., Gardiner-Garden, M., Hilton, H.N., Kazlauskas, M., Pritchard, M.A., Chodosh, L.A., Pfeffer, P.L., et al. (2008). The Ets transcription factor Elf5 specifies mammary alveolar cell fate. Gene Dev *22*, 581.

O'Brien, J., and Schedin, P. (2009). Macrophages in breast cancer: do involution macrophages

account for the poor prognosis of pregnancy-associated breast cancer? J Mammary Gland Biol Neoplasia *14*, 145–157.

O'Brien, J., Lyons, T., Monks, J., Lucia, S.M., Wilson, S.R., Hines, L., Man, Y., Borges, V., and Schedin, P. (2010). Alternatively activated macrophages and collagen remodeling characterize the postpartum involuting mammary gland across species. Am J Pathol *176*, 1241–1255.

Stewart, T.A., Hughes, K., Hume, D.A., and Davis, F.M. (2019). Developmental stage-specific distribution of macrophages in mouse mammary gland. Front Cell Dev Biol *7*, 250.

O'Brien, J., Martinson, H., Durand-Rougely, C., and Schedin, P. (2012). Macrophages are crucial for epithelial cell death and adipocyte repopulation during mammary gland involution. Development *139*, 269–275.

Oftedal, O. (2012). The evolution of milk secretion and its ancient origins. Animal *6*, 355.

Oftedal, O.T. (2002). The mammary gland and its origin during synapsid evolution. J Mammary Gland Biol Neoplasia *7*, 225–252.

Ohtsuka, T., Imayoshi, I., Shimojo, H., and Nishi, E. (2006). Visualization of embryonic neural stem cells using Hes promoters in transgenic mice. Mol Cellul Neurosci *31,* 109-122.

Orth, A., Ploschner, M., Wilson, E., Maksymov, I., and Gibson, B. (2019). Optical fiber bundles: Ultra-slim light field imaging probes. Sci Adv *5*, eaav1555.

Paine, I., Chauviere, A., Landua, J., Sreekumar, A., Cristini, V., Rosen, J., and Lewis, M.T. (2016). A geometrically-constrained mathematical model of mammary gland ductal elongation reveals novel cellular dynamics within the terminal end bud. PLoS Comput Biol *12*, e1004839.

Pal, B., Bouras, T., Shi, W., Vaillant, F., Sheridan, J., Fu, N., Breslin, K., Jiang, K., Ritchie, M.E., Young, M., et al. (2013). Global changes in the mammary epigenome are induced by hormonal cues and coordinated by Ezh2. Cell Rep *3*, 411–426.

Pal, B., Chen, Y., Vaillant, F., Jamieson, P., Gordon, L., Rios, A.C., Wilcox, S., Fu, N., Liu, K.H., Jackling, F.C., et al. (2017). Construction of developmental lineage relationships in the mouse mammary gland by single-cell RNA profiling. Nat Commun *8*, 1627.

Pardoll, D.M. (2012). The blockade of immune checkpoints in cancer immunotherapy. Nat Rev Cancer *12*, 252.

Perdiguero, E., Klapproth, K., Schulz, C., Busch, K., Azzoni, E., Crozet, L., Garner, H., Trouillet, C., de Bruijn, M.F., Geissmann, F., et al. (2014). Tissue-resident macrophages originate from yolk-sac-derived erythro-myeloid progenitors. Nature *518*, 547–551.

Perou, C.M., Sørlie, T., Eisen, M.B., van de Rijn, M., Jeffrey, S.S., Rees, C.A., Pollack, J.R., Ross, D.T., Johnsen, H., Akslen, L.A., et al. (2000). Molecular portraits of human breast tumours. Nature *406*, 747.

Phipson, B., Lee, S., Majewski, I.J., Alexander, W.S., and Smyth, G.K. (2016). Robust hyperparameter estimation protects against hypervariable genes and improves power to detect differential expression. Ann Appl Stat *10*, 946–963.

Pidhorskyi, S., Morehead, M., Jones, Q., Spirou, G., and Doretto, G. (2018). syGlass: Interactive exploration of multidimensional images using virtual reality head-mounted displays. arXiv 1804.08197v4.

Pike, M., Krailo, Henderson, B., Casagrande, J., and Hoel, D. (1983). 'Hormonal' risk factors, 'breast tissue age' and the age-incidence of breast cancer. Nature *303*, 303767a0.

Plaks, V., Boldajipour, B., Linnemann, J.R., Nguyen, N.H., Kersten, K., Wolf, Y., Casbon, A.-J., Kong, N., van den Bijgaart, R.J.E., Sheppard, D., et al. (2015). Adaptive immune regulation of mammary postnatal organogenesis. Dev. Cell *34*, 493–504.

Plaks, V., Brenot, A., Lawson, D., Linnemann, J., Kappel, E., Wong, K., Sauvage, F., Klein, O., and Werb, Z. Lgr5-expressing cells are sufficient and necessary for postnatal mammary gland organogenesis. Cell Rep *3*, 70.

Pollard, J. (2004). Tumour-educated macrophages promote tumour progression and metastasis. Nat Rev Cancer *4,* 71-78.

Pollard, J.W. (1997). Role of colony-stimulating factor-1 in reproduction and development. Mol Reprod Dev *46*, 54–61.

Pollard, J.W., and Hennighausen, L. (1994). Colony stimulating factor 1 is required for mammary gland development during pregnancy. Proc Natl Acad Sci *91*, 9312–9316.

Postek, M.T., and Steffens, W. (1979). Red/green anaglyph preparation technique for the presentation of stereo electron microscopy. T Am Microsc Soc *98*, 515.

Prater, M.D., Petit, V., Russell, A.I., Giraddi, R.R., Shehata, M., Menon, S., Schulte, R., Kalajzic, I., Rath, N., Olson, M.F., et al. (2014). Mammary stem cells have myoepithelial cell properties. Nat Cell Biol *16*, 942–950.

Qian, B.-Z., and Pollard, J.W. (2010). Macrophage diversity enhances tumor progression and metastasis. Cell *141*, 39–51.

Quaglino, A., Salierno, M., Pellegrotti, J., Rubinstein, N., and Kordon, E.C. (2009). Mechanical strain induces involution-associated events in mammary epithelial cells. BMC Cell Biol *10*, 55.

Rantakari, P., Jäppinen, N., Lokka, E., Mokkala, E., Gerke, H., Peuhu, E., Ivaska, J., Elima, K., Auvinen, K., and Salmi, M. (2016). Fetal liver endothelium regulates the seeding of tissue-resident macrophages. Nature *538*, 392–396.

Rao, K.N., and Brown, M.A. (2008). Mast cells. Ann Ny Acad Sci *1143*, 83–104.

Reed, J.R., and Schwertfeger, K.L. (2010). Immune cell location and function during post-natal mammary gland development. J Mammary Gland Biol *15*, 329–339.

Ricard, C., and Debarbieux, F. (2014). Six-color intravital two-photon imaging of brain tumors and their dynamic microenvironment. Front Cell Neurosci *8*, 57.

Richards, G.R., Klotz, D.M., Walker, M.P., and DiAugustine, R.P. (2004). Mammary gland branching morphogenesis is diminished in mice with a deficiency of insulin-like growth factor-I (IGF-I), but not in mice with a liver-specific deletion of IGF-I. Endocrinology *145*, 3106–3110.

Richardson, D., and Lichtman, J. (2015). Clarifying tissue clearing. Cell *162*, 246–257.

Rios, A.C., Fu, N.Y., Lindeman, G.J., and Visvader, J.E. (2014). In situ identification of bipotent stem cells in the mammary gland. Nature *506*, 322–327.

Rios, A.C., Fu, N.Y., Jamieson, P.R., Pal, B., Whitehead, L., Nicholas, K.R., Lindeman, G.J., and Visvader, J.E. (2016a). Essential role for a novel population of binucleated mammary epithelial cells in lactation. Nat Commun *7*, 11400.

Rios, A.C., Fu, N., Cursons, J., Lindeman, G.J., and Visvader, J.E. (2016b). The complexities and caveats of lineage tracing in the mammary gland. Breast Cancer Res *18*, 116.

Rios, A.C., Capaldo, B.D., Vaillant, F., Pal, B., van Ineveld, R., Dawson, C.A., Chen, Y., Nolan, E., Fu, N.Y., Group, 3DTCL, et al. (2019). Intraclonal plasticity in mammary tumors revealed through large-scale single-cell resolution 3D imaging. Cancer Cell *35*, 618-632.e6.

Risau, W. (1997). Mechanisms of angiogenesis. Nature *386*, 671–674.

Ritchie, M.E., Phipson, B., Wu, D., Hu, Y., Law, C.W., Shi, W., and Smyth, G.K. (2015). limma powers differential expression analyses for RNA-sequencing and microarray studies. Nucleic Acids Res *43*, e47.

Ritsma, L., Ellenbroek, S.I., Zomer, A., Snippert, H.J., de Sauvage, F.J., Simons, B.D., Clevers, H., and van Rheenen, J. (2014). Intestinal crypt homeostasis revealed at single-stem-cell level by in vivo live imaging. Nature *507*, 362–365.

Rizzo, A., Koenig, S., and Talbot, T.B. (2019). Clinical results using virtual reality. J Technol Hum Serv 1–24.

Rodilla, V., Dasti, A., Huyghe, M., Lafkas, D., Laurent, C., Reyal, F., and Fre, S. (2015). Luminal progenitors restrict their lineage potential during mammary gland development. Plos Biol *13*, e1002069.

Rohrschneider, L.R., Custodio, J.M., Anderson, T.A., Miller, C.P., and Gu, H. (2005). The intron 5/6 promoter region of the ship1 gene regulates expression in stem/progenitor cells of the mouse embryo. Dev Biol *283*, 503–521.

Rojas, G.M., Gálvez, M., Potler, N., Craddock, C.R., Margulies, D.S., Castellanos, X.F., and Milham, M.P. (2014). Stereoscopic three-dimensional visualization applied to multimodal brain images: clinical applications and a functional connectivity atlas. Front Neurosci *8*, 328.

Rosa, P.C., Bolasco, G., Pagani, F., Maggi, L., Scianni, M., Panzanelli, P., Giustetto, M., Ferreira, T.A., Guiducci, E., Dumas, L., et al. (2011). Synaptic pruning by microglia is necessary for normal brain development. Science *333*, 1456–1458.

Rosner, B., Colditz, G.A., and Willett, W.C. (1994). 94144079 Reproductive risk factors in a prospective study of breast cancer: The nurses' health study. Maturitas *20*, 224.

Rossetti, S., Corlazzoli, F., Gregorski, A., Azmi, N.A., and Sacchi, N. (2012). Identification of an estrogen-regulated circadian mechanism necessary for breast acinar morphogenesis. Cell Cycle *11*, 3691–3700.

Ruffell, B., and Coussens, L.M. (2015). Macrophages and therapeutic resistance in cancer. Cancer Cell *27*, 462–472.

Russo, J., and Russo, I.H. (2004). Development of the human breast. Maturitas *49*, 2–15.

Russo, J., Tay, L.K., and Russo, I.H. (1982). Differentiation of the mammary gland and susceptibility to carcinogenesis. Breast Cancer Res Tr *2*, 5–73.

Ruthensteiner, B., Baeumler, N., and Barnes, D.G. (2010). Interactive 3D volume rendering in biomedical publications. Micron *41*, 886.e1-886.e17.

Safadel, P., and White, D. (2019). Facilitating molecular biology teaching by using augmented reality (AR) and protein data bank (PDB). Techtrends *63*, 188–193.

Samokhvalov, I.M., Samokhvalova, N.I., and Nishikawa, S. (2007). Cell tracing shows the contribution of the yolk sac to adult haematopoiesis. Nature *446*, 1056.

Sandahl, M., Hunter, D.M., Strunk, K.E., Earp, S.H., and Cook, R.S. (2010). Epithelial cell-directed efferocytosis in the post-partum mammary gland is necessary for tissue homeostasis and future lactation. BMC Dev Biol *10*, 122.

Sargeant, T., Lloyd-Lewis, B., Resemann, H., Ramos-Montoya, A., Skepper, J., and Watson, C. (2014). Stat3 controls cell death during mammary gland involution by regulating uptake of milk fat globules and lysosomal membrane permeabilization. Nat Cell Biol *16*, 1057–1068.

Schafer, D.P., Lehrman, E.K., Kautzman, A.G., Koyama, R., Mardinly, A.R., Yamasaki, R., Ransohoff, R.M., Greenberg, M.E., Barres, B.A., and Stevens, B. (2012). Microglia sculpt postnatal neural circuits in an activity and complement-dependent manner. Neuron *74*, 691–705.

Schedin, P., O'Brien, J., Rudolph, M., Stein, T., and Borges, V. (2007). Microenvironment of the involuting mammary gland mediates mammary cancer progression. J Mammary Gland Biol Neoplasia *12*, 71–82.

Scheele, C., Maynard, C., and van Rheenen, J. (2016). Intravital insights into heterogeneity, metastasis, and therapy responses. Trends Cancer *2*, 205–216.

Scheele, C.L., Hannezo, E., Muraro, M.J., Zomer, A., Langedijk, N.S., van Oudenaarden, A., Simons, B.D., and van Rheenen, J. (2017). Identity and dynamics of mammary stem cells during branching morphogenesis. Nature *542*, 313.

Schepper, S., Verheijden, S., Aguilera-Lizarraga, J., Viola, M., Boesmans, W., Stakenborg, N., Voytyuk, I., Smidt, I., Boeckx, B., de Casterlé, I., et al. (2018). Self-maintaining gut macrophages are essential for intestinal homeostasis. Cell. *175*, 400-415.e13.

Schindelin, J., Arganda-Carreras, I., Frise, E., Kaynig, V., Longair, M., Pietzsch, T., Preibisch, S., Rueden, C., Saalfeld, S., Schmid, B., et al. (2012). Fiji: an open-source platform for biological-image analysis. Nat Methods *9*, 676.

Schönig, K., Schwenk, F., Rajewsky, K., and Bujard, H. (2002). Stringent doxycycline dependent control of CRE recombinase in vivo. Nucleic Acids Res *30*, e134–e134.

Schumacher, T.N., and Hacohen, N. (2016). Neoantigens encoded in the cancer genome. Curr Opin Immunol *41*, 98–103.

Schwertfeger, K., Rosen, J., and Cohen, D. (2006). Mammary gland macrophages: pleiotropic functions in mammary development. J. Mammary Gland Biol. Neoplasia *11*, 229–238.

Scott, C., Bain, C., Wright, P., Sichien, D., Kotarsky, K., Persson, E., Luda, K., Guilliams, M., Lambrecht, B., Agace, W., et al. (2015). CCR2+CD103− intestinal dendritic cells develop from DC-committed precursors and induce interleukin-17 production by T cells. Mucosal Immunol *8*, 327–339.

Scott, C., Zheng, F., De Baetselier, P., Martens, L., Saeys, Y., De Prijk, S., Lippens, S., Abels, C., Schoonooghe, S., Raes, G., et al. (2016). Bone marrow-derived monocytes give rise to self-renewing and fully differentiated Kupffer cells. Nature Commun *7*, 10321.

Shackleton, M., Vaillant, F., Simpson, K.J., Stingl, J., Smyth, G.K., Asselin-Labat, M.-L.L., Wu, L., Lindeman, G.J., and Visvader, J.E. (2006). Generation of a functional mammary gland from a single stem cell. Nature *439*, 84.

Shan, S., Sorg, B., and Dewhirst, M.W. (2003). A novel rodent mammary window of orthotopic breast cancer for intravital microscopy. Microvasc Res *65*, 109–117.

Shehata, M., Teschendorff, A., Sharp, G., Novcic, N., Russell, A.I., Avril, S., Prater, M., Eirew,

P., Caldas, C., Watson, C.J., et al. (2012). Phenotypic and functional characterisation of the luminal cell hierarchy of the mammary gland. Breast Cancer Res *14*, R134.

Shehata, M., van Amerongen, R., Zeeman, A.L., Giraddi, R.R., and Stingl, J. (2014). The influence of tamoxifen on normal mouse mammary gland homeostasis. Breast Cancer Res *16*, 411.

Sheng, J., Ruedl, C., and Karjalainen, K. (2015). Most tissue-resident macrophages except microglia are derived from fetal hematopoietic stem cells. Immunity *43*, 382–393.

Sheridan, J.M., Ritchie, M.E., Best, S.A., Jiang, K., Beck, T.J., Vaillant, F., Liu, K., Dickins, R.A., Smyth, G.K., Lindeman, G.J., et al. (2015). A pooled shRNA screen for regulators of primary mammary stem and progenitor cells identifies roles for Asap1 and Prox1. BMC Cancer *15*, 221.

Shihavuddin, A., etama Basu, Rexhepaj, E., Delestro, F., Menezes, N., goillot, S., Nery, E., Selimi, F., Spassky, N., and Genovesio, A. (2017). Smooth 2D manifold extraction from 3D image stack. Nat Commun *8*, ncomms15554.

Sierro, F., Evrard, M., Rizzetto, S., Melino, M., Mitchell, A.J., Florido, M., Beattie, L., Walters, S.B., Tay, S.S., Lu, B., et al. (2017). A liver capsular network of monocyte-derived macrophages restricts hepatic dissemination of intraperitoneal bacteria by neutrophil recruitment. Immunity *47*, 374-388.e6.

Silberstein, G., and Daniel, C. (1987). Reversible inhibition of mammary gland growth by transforming growth factor-beta. Science *237*, 291–293.

Silberstein, G.B., and Daniel, C.W. (1982). Glycosaminoglycans in the basal lamina and extracellular matrix of the developing mouse mammary duct. Dev Biol *90*, 215–222.

Snippert, H., Flier, L., Sato, T., Es, J., Born, M., Kroon-Veenboer, C., Barker, N., Klein, A., Rheenen, J., Simons, B., et al. (2010). Intestinal crypt homeostasis results from neutral competition between symmetrically dividing Lgr5 stem cells. Cell *143*, 134–144.

Sobolik, T., Su, Y.-J., Ashby, W., Schaffer, D.K., Wells, S., Wikswo, J.P., Zijlstra, A., and Richmond, A. (2016). Development of novel murine mammary imaging windows to examine wound healing effects on leukocyte trafficking in mammary tumors with intravital imaging. IntraVital *5*, e1125562.

Song, W., Wang, R., Jiang, W., Yin, Q., Peng, G., Yang, R., Yu, Q., Chen, J., Li, J., Cheung, T.H., et al. (2019). Hormones induce the formation of luminal-derived basal cells in the mammary gland. Cell Res *29*, 206–220.

Souza-Fonseca-Guimaraes, F., Cursons, J., and Huntington, N.D. (2019). The emergence of natural killer cells as a major target in cancer immunotherapy. Trends Immunol *40*, 142–158.

Soyal, S.M., Mukherjee, A., Lee, K., Li, J., Li, H., DeMayo, F.J., and Lydon, J.P. (2005). Cre-mediated recombination in cell lineages that express the progesterone receptor. Genesis *41*, 58–66.

Spike, B.T., Engle, D.D., Lin, J.C., Cheung, S.K., La, J., and Wahl, G.M. (2012). A mammary stem cell population identified and characterized in late embryogenesis reveals similarities to human breast cancer. Cell Stem Cell *10*, 183–197.

Sreekumar, A., Toneff, M.J., Toh, E., Roarty, K., Creighton, C.J., Belka, G.K., Lee, D.-K., Xu, J., Chodosh, L.A., Richards, J.S., et al. (2017). WNT-mediated regulation of FOXO1 constitutes a critical axis maintaining pubertal mammary stem cell homeostasis. Dev Cell *43*, 436-448.e6.

Srinivasan, K., Strickland, P., Valdes, A., Shin, G., and Hinck (2003). Netrin-1/Neogenin

interaction stabilizes multipotent progenitor cap cells during mammary gland morphogenesis. Dev Cell *4*, 371–382.

Stanford, J.C., Young, C., Hicks, D., Owens, P., Williams, A., Vaught, D.B., Morrison, M.M., Lim, J., Williams, M., Brantley-Sieders, D.M., et al. (2014). Efferocytosis produces a prometastatic landscape during postpartum mammary gland involution. J Clin Inv *124*, 4737–4752.

Stein, T., Morris, J., Davies, C., Weber-Hall, S., Duffy, M., Heath, V., Bell, A., Ferrier, R., Sandilands, G., and Gusterson, B. (2003). Involution of the mouse mammary gland is associated with an immune cascade and an acute-phase response, involving LBP, CD14 and STAT3. Breast Cancer Res *6*, 75–91.

Stevenson, A.J., Vanwalleghem, G., Stewart, T.A., Condon, N.D., Lloyd-Lewis, B., Marino, N., Putney, J.W., Scott, E.K., Ewing, A.D., and vis, F. (2019). Multiscale activity imaging in the mammary gland reveals how oxytocin enables lactation. Biorxiv 657510.

Stingl, J., Eirew, P., Ricketson, I., Shackleton, Vaillant, F., Choi, D., Li, H.I. and Eaves, C.J. (2006). Purification and unique properties of mammary epithelial stem cells. Nature *439*, 993997

Stoliar, O.A., Pelley, R.P., Klaus, M.H., Kaniecki-Green, E., and Carpenter, C.C.J. (1976). Secretory IgA against enterotoxins in breast-milk. Lancet *307*, 1258–1261.

Sun, X., Robertson, S., and Ingman, W. (2013). Regulation of epithelial cell turnover and macrophage phenotype by epithelial cell-derived transforming growth factor beta1 in the mammary gland. Cytokine *61*, 377–388.

Susaki, E.A., Tainaka, K., Perrin, D., Kishino, F., Tawara, T., Watanabe, T.M., Yokoyama, C., Onoe, H., Eguchi, M., Yamaguchi, S., et al. (2014). Whole-brain imaging with single-cell resolution using chemical cocktails and computational analysis. Cell *157*, 726–739.

Tainaka, K., Kubota, S.I., Suyama, T.Q., Susaki, E.A., Perrin, D., Ukai-Tadenuma, M., Ukai, H., and Ueda, H.R. (2014). Whole-body imaging with single-cell resolution by tissue decolorization. Cell *159*, 911–924.

Takaki, R. (2005). Can morphogenesis be understood in terms of physical rules? J Biosci *30*, 87–92.

Tamoutounour, S., Henri, S., Lelouard, H., de Bovis, B., de Haar, C., van der Woude, J.C., Woltman, A.M., Reyal, Y., Bonnet, D., Sichien, D., et al. (2012). CD64 distinguishes macrophages from dendritic cells in the gut and reveals the Th1-inducing role of mesenteric lymph node macrophages during colitis. Eur J Immunol *42*, 3150–3166.

Teplova, I., Lozy, F., Price, S., Singh, S., Barnard, N., Cardiff, R.D., Birge, R.B., and Karantza, V. (2013). ATG proteins mediate efferocytosis and suppress inflammation in mammary involution. Autophagy *9*, 459–475.

Tharmapalan, P., Mahendralingam, M., Berman, H.K., and Khokha, R. (2019). Mammary stem cells and progenitors: targeting the roots of breast cancer for prevention. Embo J *38*, e100852.

Tober, J., Yzaguirre, A.D., Piwarzyk, E., and Speck, N.A. (2013). Distinct temporal requirements for Runx1 in hematopoietic progenitors and stem cells. Development *140*, 3765–3776.

Tymoszuk, P., Evens, H., Marzola, V., Wachowicz, K., Wasmer, M., Datta, S., Müller-Holzner, E., Fiegl, H., Böck, G., van Rooijen, N., et al. (2014). In situ proliferation contributes to accumulation of tumor-associated macrophages in spontaneous mammary tumors. Eur J

Immunol *44*, 2247–2262.

Varol, C., Mildner, A., and Jung, S. (2015). Macrophages: development and tissue specialization. Annu Rev Immunol *33*, 643–675.

Ved, N., Curran, A., Ashcroft, F., and Sparrow, D. (2019). Tamoxifen administration in pregnant mice can be deleterious to both mother and embryo. Lab Anim 002367721985691.

Visvader, J.E. (2009). Keeping abreast of the mammary epithelial hierarchy and breast tumorigenesis. Genes Dev *23*, 2563–2577.

Visvader, J.E. (2011). Cells of origin in cancer. Nature *469*, 314.

Visvader, J.E., and Stingl, J. (2014). Mammary stem cells and the differentiation hierarchy: current status and perspectives. Genes Dev *28*, 1143.

Wagner, M., Aßmus, B., Hartman, A., Hutzler, P., and Amann, R. (1994). In situ analysis of microbial consortia in activated sludge using fluorescently labelled, rRNA-targeted oligonucleotide probes and confocal scanning laser microscopy. J Microsc-Oxford *176*, 181–187.

Wang, C., Christin, J.R., Oktay, M.H., and Guo, W. (2017). Lineage-biased stem cells maintain estrogen-receptor-positive and -negative mouse mammary luminal lineages. Cell Reports *18*, 2825–2835.

Wang, D., Cai, C., Dong, X., Yu, Q., Zhang, X.-O., Yang, L., and Zeng, Y. (2015). Identification of multipotent mammary stem cells by protein C receptor expression. Nature *517*, 81–84.

Wang, E., Babbey, C., and Dunn, K. (2005). Performance comparison between the high-speed Yokogawa spinning disc confocal system and single-point scanning confocal systems. J Microsc-Oxford *218*, 148–159.

Wang, H., Yan, M., Sun, J., Jain, S., Yoshimi, R., Abolfath, S.M., Ozato, K., Coleman, W.G., Ng, A.P., Metcalf, D., et al. (2014). A reporter mouse reveals lineage-specific and heterogeneous expression of IRF8 during lymphoid and myeloid cell differentiation. J Immunol *193*, 1766–1777.

Wang, Y., Szretter, K.J., Vermi, W., Gilfillan, S., Rossini, C., Cella, M., Barrow, A.D., Diamond, M.S., and Colonna, M. (2012). IL-34 is a tissue-restricted ligand of CSF1R required for the development of Langerhans cells and microglia. Nat Immunol *13*, 753.

Watson, C.J., and Kreuzaler, P.A. (2011). Remodeling mechanisms of the mammary gland during involution. Int J Dev Biol *55*, 757–762.

Williams, J.M., and Daniel, C.W. (1983). Mammary ductal elongation: differentiation of myoepithelium and basal lamina during branching morphogenesis. Dev Biol *97*, 274–290.

Willingham, S.B., Volkmer, J.-P., Gentles, A.J., Sahoo, D., Dalerba, P., Mitra, S.S., Wang, J., Contreras-Trujillo, H., Martin, R., Cohen, J.D., et al. (2012). The CD47-signal regulatory protein alpha (SIRPa) interaction is a therapeutic target for human solid tumors. Proc Natl Acad Sci *109*, 6662–6667.

Woods, D.M., Laino, A., Villagra, A., and Sotomayor, E.M. (2014). Molecular pathways in antigen-presenting cells involved in the induction of antigen-specific T-cell tolerance. In Tumor-induced immune suppression, mechanisms and therapeutic reversal, Gabrilovich D., and Hurwitz A., eds. (Springer, New York, NY), pp. 411–433.

Wu, D., and Smyth, G.K. (2012). Camera: a competitive gene set test accounting for inter-gene correlation. Nucleic Acids Res. *40*, e133.

Wuidart, A., Ousset, M., Rulands, S., Simons, B.D., Keymeulen, A., and Blanpain, C. (2016). Quantitative lineage tracing strategies to resolve multipotency in tissue-specific stem cells. Genes Dev *30*, 1261–1277.

Wuidart, A., Sifrim, A., Fioramonti, M., Matsumura, S., Brisebarre, A., Brown, D., Centonze, A., Dannau, A., Dubois, C., Keymeulen, A., et al. (2018). Early lineage segregation of multipotent embryonic mammary gland progenitors. Nat Cell Biol *20*, 666–676.

Wyckoff, J., Stanley, E., Graf, T., Pollard, J., Segall, J., and Condeelis, J. (2004). A paracrine loop between tumor cells and macrophages is required for tumor cell migration in mammary tumors. Cancer Res *64*, 7022–7029.

Wynn, T.A., Chawla, A., and Pollard, J.W. (2013). Macrophage biology in development, homeostasis and disease. Nature *496*, 445–455.

Xu, J., Chen, C., Jiang, X., Xu, R., Tambe, D., Zhang, X., Liu, L., Lan, B., Cai, K., and Deng, L. (2011). Effects of micropatterned curvature on the motility and mechanical properties of airway smooth muscle cells. Biochem Bioph Res Co *415*, 591–596.

Yang, A., Schweitzer, R., Sun, D., Kaghad, M., Walker, N., Bronson, R.T., Tabin, C., Sharpe, A., Caput, D., Crum, C., et al. (1999). p63 is essential for regenerative proliferation in limb, craniofacial and epithelial development. Nature *398*, 19539.

Yona, S., Kim, K.-W., Wolf, Y., Mildner, A., Varol, D., Breker, M., Strauss-Ayali, D., Viukov, S., Guilliams, M., Misharin, A., et al. (2013). Fate mapping reveals origins and dynamics of monocytes and tissue macrophages under homeostasis. Immunity *38*, 1073–1079.

Yu, M., Gerkins, V., Henderson, B., Brown, J., and Pike, M. (1981). Elevated levels of prolactin in nulliparous women. Brit J Cancer *43*, 826.

Zhang, F., Gradinaru, V., Adamantidis, A.R., Durand, R., Airan, R.D., de Lecea, L., and Deisseroth, K. (2010). Optogenetic interrogation of neural circuits: technology for probing mammalian brain structures. Nat Protoc *5*, 439–456.

Zhou, J., Chehab, R., Tkalcevic, J., Naylor, M.J., Harris, J., Wilson, T.J., Tsao, S., Tellis, I., Zavarsek, S., Xu, D., et al. (2005). Elf5 is essential for early embryogenesis and mammary gland development during pregnancy and lactation. Embo J *24*, 635–644.